Prediction of the Flow and Heat Transfer between a Rotating and a Stationary Cone

Nicholas Edward May

Submitted to the Council for National Academic Awards in partial fulfilment for the Degree of Doctor of Philosophy

Sponsoring Establishment:

Polytechnic South West

Department of Mathematics and Statistics

Collaborating Establishment:

Rolls-Royce plc.

July 1990

Prediction of the flow and Heat Transfer between a Rotating and a Stationary Cone

by

Nicholas Edward May

Abstract

This thesis is concerned with the development of a theoretical method for predicting the turbulent flow and heat transfer in the cavity between a rotating and a stationary cone. The motivation for the work stems from the need, in the design process for the gas turbine aero-engine, for a fast and reliable predictive method for such flows. The method developed here is the integral method, which reduces the governing partial differential equations to ordinary differential equations. A number of solution methods for these equations are described, and the optimum in terms of speed and accuracy is indicated. Predicted moment coefficients compare well with experimental data for half cone angles greater than approximately 60°, but poorly for half cone angles less than approximately 45°. The poor agreement for small cone angles is thought to be due to the presence of Taylor-type vortices, which cannot be incorporated into the integral method. Heat transfer is incorporated into the method using the Reynolds analogy. Due to the lack of experimental data, heat transfer predictions are compared with those from a finite difference program and show encouraging agreement.

A computer program which solves the full Reynolds-averaged Navier-Stokes and energy equations in steady and axisymmetric form, using a finite difference method is modified for use in the conical geometry. Comparison of the predicted moment coefficients with experimental data shows no marked improvement over the integral method. Examination of the secondary flow predicted by the program shows it to be similar to that of the integral method. The failure of the program to predict Taylor-type vortices may be attributed to the fact that they are non-axisymmetric and/or unsteady. The assumptions underlying the integral method are investigated via the finite difference program and it is concluded that they are valid for half cone angles as small as 15°. Based on the results of the finite difference program, the integral method is modified to allow for a rectangular outer shroud, and a new model for the stator is described.

It is concluded that both the integral method and the finite difference program can be used safely in rotor-stator systems where the half cone angle is greater than about 60°.

ACKNOWLEDGMENTS

I would like to thank Dr. Phil James and Dr. John Chew for their continued help and advice throughout the duration of this project. I am grateful for the award granted by the SERC and for the considerable support from Roll-Royce plc, both financially and by way of access to their resources. I am appreciative of the help given by the staff of the computing centre at Polytechnic South West. I would also like to thank Mrs Sharon Ward for her help with the typing and A.R.A. Ltd for their assistance in the completion of this thesis. Finally, thanks to Gillian for her encouragement and patience throughout the duration of the project.

CONTENTS

CHAPTER 1

INTRODUCTION

1.1 MOTIVATION, OBJECTIVES AND APPROACH

The need to improve design techniques for gas turbine aero-engines has resulted in considerable effort being put into the development of methods for predicting the flow and heat transfer processes which occur in these engines. Such predictions play an essential part in the design of the internal air system of an aero-engine. This system has several important functions to perform, one of which is to cool certain internal components of the engine to ensure that they do not absorb heat to such an extent that their safe operation is jeopardised. The aero-engine designer requires estimates of quantities such as the torque and heat transfer experienced by components, such as turbine discs, and theoretical techniques are often used to provide such estimates since the temperatures in the engine are too great to be reproduced in the laboratory.

The main features of the internal air flow occuring in a typical aero-engine are shown in Figure 1.1. Due to the complex geometries involved, as well as the high rotational velocities of many of the components, such as the compressors and turbine discs, the flow patterns are complex and diverse. The task of predicting the flow and heat transfer is further complicated by phenomena such as tubulence, compressibility and possibly time-dependence. However as a first approximation, many of the flows which occur may be satisfactorily

modelled using fairly simple geometric configurations. Examples of such configurations are rotating disc systems, which may consist of either the co-rotating disc system (two parallel discs rotating about the same axis with equal angular velocities) or the rotor-stator disc system (a disc rotating next to a parallel stationary disc), both of which may be used to model flows occuring in the compressor and turbine. A consequence of the importance of rotating disc systems in aero-engines is that much effort has been put into developing theoretical techniques for predicting the flow and heat transfer in such systems. Another example of a simple configuration which may be used to model some of the internal air flows is that of a rotor-stator cone system; a configuration which has received relatively little attention. The objective of the work described in this thesis is to provide a theoretical method for the prediction of flow and heat transfer in the cavity formed between a rotating and a stationary cone.

Ideally, for efficient design, a predictive method should be fast and accurate. In practice, this is not always achievable, but designers may still use theoretical predictions for guidance since even a qualitative understanding of the main factors influencing the flow is of value. A flow and heat transfer calculation for a conical rotor-stator system may only form a small part of a far more extensive computation, in which case a predictive technique that takes days to produce results is of little use. Depending on the situation, different compromises between speed and accuracy are required and so the development of a variety of predictive techniques would be beneficial. In this thesis, the emphasis is placed on the development of a fast technique for the prediction of the flow and heat transfer in a rotor-stator cone system. The technique is known as the 'integral method'. The integral method has been used in fluid dynamics for many

years and it provides fast predictions since it only requires the solution of a system of ordinary differential equations rather than the solution of the full momentum, energy and continuity equations. This reduction to ordinary differential equations is possible when the flows considered exhibit a boundary layer character and it relies on the use of empirically based velocity profiles and surface shear stress formulae. In spite of the inherent limitations, the integral method has been used very successfully to provide the theoretical predictions for a variety of rotating flows, as will be seen from the discussion in §2.3.2.

A secondary aim of the work presented in this thesis is to modify a computer program which solves the full (axisymmetric and steady) Reynolds-averaged Navier-Stokes and energy equations using a finite difference technique, so that it can be used for the conical geometry. Such programs are considerably slower than integral method programs, but since less assumptions are made, they have the advantage of having a wider range of application and, in general of being more accurate. The finite difference results will be used to provide further insight into the flow and heat transfer mechanisms which the integral method alone can not provide. A summary of previous work using finite difference methods for rotating flows will be given in §2.3.3.

The only way to effectively assess the predictive capability of a theoretical method is to compare its predictions with experiment. However, there is a scarcity of experimental data concerning rotor-stator cone systems. Experimentally obtained data for the moment experienced by the rotating cone appears, in fact, to be restricted to one source and there appears to be no relevant heat transfer data for rotor-stator disc or cone systems. To compensate for the lack of

experimental data, reliance is placed on the accuracy of the finite difference results to assess the predictive capability of the integral method. Clearly, this is not ideal and further experimental work is necessary to make a thorough assessment of both the integral method and the finite difference method.

1.2 OUTLINE OF THESIS

In chapter 2, three types of commonly occuring rotating disc systems are classified and the flows which are known to occur in such systems are described. Rotating disc systems are of relevance here, since they are a special case of a general cone system, and in developing the integral method, the flow pattern occuring in a rotor-stator cone system is assumed to be similar to that occuring in a rotor-stator disc system. Relevant theoretical work on the prediction of flow in rotating disc and cone systems is then reviewed so that the present methods may be put into context.

In chapters 3,4 and 5 an integral method to predict the flow and heat transfer in a rotor-stator cone system is developed. In chapter 3, the isothermal flow equations are derived and the assumptions required for the integral method are described. In this thesis, unlike previous authors, extra terms are included when modelling the flow in a narrow-angled rotor-stator system. Chapter 4 is concerned with the methods of solution of the isothermal flow equations derived in chapter 3. A number of methods are described in the chapter, and the preferable method which optimises accuracy and speed is indicated. The chapter is also concerned with assessing the effect of the extra terms retained in the governing equations and the problem of indeterminacy

of initial conditions is considered by examining asymptotic solutions to the equations. The chapter concludes with an assessment of the predictive capability of the method by comparing its predictions with available experimental data.

In chapter 5, heat transfer is incorporated into the isothermal integral method described in chapters 3 and 4. This is achieved by using the 'Reynolds analogy' which relates the surface heat flux to the surface shear stress. Also in chapter 5 a review of previous authors' work on modifying the Reynolds analogy in order to generalise its applicability is carried out. The work in this chapter represents the first attempt at using the Reynolds analogy to predict the heat transfer in rotor-stator disc or cone systems where the specified flow rate through the cavity is relatively small. To the author's knowledge, there is no relevant experimental data with which to verify the heat transfer method described in chapter 5, and so the chapter concludes by assessing the predictive capability of the method by comparing its predictions with those obtained from the finite difference program.

Chapter 6 describes the use of a finite difference method to solve the Reynolds-averaged Navier-Stokes and energy equations in the cavity between a rotating and a stationary cone. The work involves the modification of a computer program which solves the equations describing flow and heat transfer in rotating plane disc systems. Included in the chapter is a description of the program along with a section describing the consistency checks made to ensure the modifications were coded correctly. The chapter concludes with a comparison of the predicted results with the available experimental data and a comparison of the results with those predicted by the integral method in chapter 4.

In chapter 7, the results of the finite difference program are used to assess the validity of the assumptions used in the integral method described in chapter 3, and in particular, to assess whether the assumptions which are based on those used in rotor-stator disc systems may also be used in rotor-stator cone systems. Modelling of the stator boundary layer in the integral method has caused some difficulty in the past and an alternative model based on the present finite difference results is described in chapter 7. The chapter concludes with a simple modification to the integral method to account for the effect of varying the shape of the outer-shroud which channels fluid from the rotor to the stator.

Finally in chapter 8, the important conclusions which may be drawn from the work presented in the thesis are summarised and recommendations for further work are stated.

CHAPTER 2

THEORETICAL METHODS FOR THE PREDICTION OF ROTATING FLOWS

2.1 INTRODUCTION

In this chapter, three rotating flow geometries of particular relevance to rotor-stator cone systems will be classified, and the flow patterns encountered in each case will be described. The flow patterns have features in common and this has led to similarities in the attempts to descibe them by the integral method. Theoretical work related to the three types of flow is then reviewed in §2.3, where it is seen that the integral method has been improved and extended by various authors in a logical way. The review provides a basis for the particular type of integral method to be used for rotor-stator cone systems in chapter 3 and also enables the finite difference method of attack on the problem to be set in context.

2.2 CLASSIFICATION OF ROTATING FLOW SYSTEMS

There are essentially three related flow problems of relevance to the work contained in this thesis which have received both theoretical and experimental attention. These configurations are (i) free-rotating systems, (ii) co-rotating systems and (iii) rotor-stator systems. Most of the published theoretical and experimental

work on these systems has been confined to a consideration of plane discs and so the descriptions of the flows which occur in the three configurations will be restricted to plane disc flows. It will be assumed in chapter 3 that the secondary flow pattern which occurs in a rotor-stator cone system is the same as that which occurs in a rotor-stator disc system. The results from the finite difference method described in chapter 6 will be used to support this assumption. The above three configurations will now be defined and the flows which occur in each case will be described.

(i) Free-rotating systems.

Here the disc is rotating in an otherwise undisturbed fluid of infinite expanse.

The fluid near to the surface of a rotating disc rotates because of the no-slip condition and it moves both radially and circumferentially along the surface in a spiral motion. The outward radial motion is compensated for by flow in the axial direction which is entrained into a boundary layer on the disc. This entrained fluid is then in turn carried and ejected centrifugally. A diagram of this flow induced by a free-rotating disc, which is known as the 'disc pumping effect' is shown in Figure 2.1(a).

(ii) Co-rotating systems.

Here two identical and parallel discs are rotating with the same constant angular velocity about the same axis. Fluid is pumped between the discs or cones at a specified constant flow rate.

For an isothermal co-rotating disc system, the flow pattern which occurs between the discs has been well established by theory and experiment (see for example Owen and Pincombe (1980) and Chew, Owen

and Pincombe (1984)) and is shown in Figure 2.1(b). The source region, is defined by $a < r \leq r_e$, where a is the inner radius of the discs, r is the local radius and r_e denotes the radial location of the end of the source region. In this region, incoming fluid is entrained into boundary layers on the discs in a manner similar to the entrainment described above for a free-rotating disc. In the source region, the mass flow rate increases continually with increasing r in the boundary layers until the sum of the mass flow rates in the two boundary layers equals the mass inflow rate, $\dot{m}$. This criterion is reached at the radial location denoted by r_e. In the core region, defined by $r > r_e$, the boundary layers are non-entraining, i.e. the mass flow rate in the boundary layers is constant. Between these boundary layers and the sink boundary layer which forms over the outer shroud, there is a rotating core of fluid in which the axial and radial velocity components can be taken to be approximately zero.

(iii) Rotor-stator systems.

Here a disc rotates next to a stationary, parallel disc with a constant angular velocity.

The isothermal flow pattern which occurs in the cavity formed by a rotor-stator disc system has been studied theoretically and experimentally by, for example, Daily and Nece (1960), Daily et al (1964) and Chew (1987), and is shown in Figure 2.1(c). In the source region, $a < r \leq r_e$, which occurs when there is a non-zero throughflow rate, fluid is entrained into a boundary layer on the rotor in a manner similar to that described above for a free-rotating disc. In the source region, the stator does not significantly influence the flow. The source region extends to the point where all of the specified throughflow is entrained into the rotor boundary layer.

Beyond this point, for $r > r_e$, there is the core region where, in contrast to the co-rotating system, there is a continual entrainment of fluid into the rotor boundary layer. In the core region, then, the outflow rate on the rotor is greater than the throughflow rate at the inlet. At r=b, the fluid on the rotor is channelled across the outer shroud into a stator boundary layer. This fluid then travels radially inwards back down the stator and thus compensates for the surplus mass outflow on the rotor. In the core region, between the boundary layers on the rotor, stator and outer shroud there is a rotating core of fluid in which there is a weak axial flow from the stator to the rotor, but, to a good approximation, there is again no radial flow.

When the throughflow rate is zero, there is no source region and the core region fills the entire cavity. In this case it is known from experiment (Daily and Nece (1960)) that the fluid core between the boundary layers rotates almost as a solid body at about 40% to 50% of the rotor angular velocity. When there is a non-zero throughflow rate, the finite difference results of Chew (1987) show that the rotational speed of the core may vary quite strongly with radius. If the throughflow rate is high enough, the source region shown in Figure 2.1(c) will extend so as to fill the entire cavity and the core region will not exist.

2.3 PREDICTIVE METHODS

The problem of predicting the flows which occur in the above three configurations has attracted the attention of workers for many years. Early workers confined their attention to exact solutions to simplified forms of the governing equations, but more recently with

the advances in computer power, attention has switched to numerical solutions of the full flow and energy equations.

The nature of the rotating flows has made possible the application of certain assumptions to simplify the governing equations. Firstly, it is often assumed that the flows are axisymmetric. Secondly, it is normally assumed that a steady state has been reached, so that all the terms involving time derivatives may be omitted. Thirdly, due to the boundary layer character of the flows adjacent to the surfaces, 'boundary layer theory' may be used to further simplify the equations.

In the next three sub-sections, important theoretical contributions to problems of predicting the flows occuring in the three configurations described in §2.2 will be discussed. The three sub-sections are concerned with three different theoretical techniques: analytical solutions for laminar flow, integral method solutions for turbulent flow and finite difference solutions of the Navier-Stokes equations for both laminar and turbulent flow (using Reynolds-averaging and a turbulence model in the latter case).

2.3.1 Analytical Solutions of the Laminar Equations

Analytical solutions to the laminar flow equations are not normally directly relevant to the aero-engine environment, where, due to high rotational speed, the flows are usually turbulent. Nevertheless, analytical solutions can give a useful insight into the flow.

Von Karman (1921) obtained a set of ordinary differential equations from the partial differential equations governing the

steady, axisymmetric, incompressible, laminar flow over a free-rotating disc. He achieved this by assuming that the velocity components and pressure were separable into arbitrary functions of the independent variables, r and z, where r denotes the radial co-ordinate and z the axial co-ordinate in a cylindrical polar co-ordinate system. After substituting for the velocity components and pressure, von Karman recognised that for simple functions of r, the equations reduced to a set of ordinary differential equations with z as the independent variable. This resulting set of ordinary differential equations was later solved numerically by Cochran (1934). The von Karman-Cochran solution is now regarded as one of the classical solutions of the Navier-Stokes equations and it has been extended by Wu (1959) to apply to the flow over a free-rotating cone. For a free-rotating cone with a large cone angle, Wu showed that the boundary layer equations were reducible to a set of ordinary differential equations identical to those obtained by von Karman (1921), with the exception of the equation governing the pressure field. Wu concluded that Cochran's (1934) numerical solution may be applied to the cone equations and that the pressure equation may be solved separately.

In laminar flow the heat transfer from a heated free-rotating cone has been studied theoretically by Tien (1960) and Hering and Grosh (1963), using an approach similar to the isothermal approach of von Karman (1921). Tien assumed that the temperature in the boundary layer energy equation was separable into a function of r and a function of z. Substituting for this function of r, Tien similarly reduced the energy equation to an ordinary differential equation along with the continuity and momentum equations. Tien deduced that the incompressible solutions are also valid in the compressible case

provided viscous dissipation has a negligible effect in the energy equation. Hering and Grosh (1963) extended the analysis of Tien (1960) to cases where the cone has a small rotational speed so that bouyancy forces have a significant effect.

The above solutions have been confined to free-rotating systems. However, another important solution was given by Ekman (1905) which is relevant to co-rotating and rotor-stator systems where, in the core region, the tangential velocity at the boundary layer edge is significant. Ekman obtained solutions to the laminar boundary layer equations when the flow is assumed to be a small perturbation from solid body rotation. The approximate solutions he obtained have been shown by comparison with experiment to have a surprisingly large range of validity.

2.3.2 Integral Methods in Turbulent Flow

Integral methods have been used to predict turbulent rotating flows for many years. The attractions of these methods is that they produce results very quickly compared with finite difference methods and that analytical solutions are possible in certain cases. The methods can also be readily extended to include heat transfer, although detailed discussion of this aspect of the methods will be left until chapter 5. The review in this section will again be carried out with reference to the flow configuarations (i), (ii) and (iii) described in §2.2, since the approaches used by many of the authors cited are extensions of von Karman's (1921) solution for the free-rotating disc.

(i) Free-rotating systems

The first integral method solution to the equations governing the incompressible, turbulent boundary layer flow induced by a free-rotating disc was that of von Karman (1921). Von Karman integrated the boundary layer equations across the boundary layer to obtain a set of simultaneous ordinary differential equations. He achieved this by assuming power law velocity profiles and surface shear stress formulae which were obtained empirically from experiments on pipe flows. A detailed discussion of the derivation of these relations will be given in §3.4. For the case of a disc with a zero inner radius, von Karman then obtained exact analytical solutions to the set of ordinary differential equations.

Despite the apparently questionable assumption of using empirical relationships based on experiments for pipe flows, von Karman's method has proved to be very successful and it has been extended to predict the flow in a variety of rotating systems. In particular, von Karman's analysis has been extended to investigate the incompressible, turbulent boundary layer flow over a free-rotating cone by Kreith (1966) and Chew (1985a). Chew shows that for sufficiently large cone angles, the boundary layer equations describing the flow over a free-rotating cone may be integrated to give an identical set of ordinary differential equations to those obtained by von Karman for the free-rotating disc, provided the cone angle is accounted for in the non-dimensionalisation of the equations. Chew thus concluded that the free-rotating disc solutions may be applied directly to the free-rotating cone.

Notable alternative approaches to that of von Karman are those of Goldstein (1935) and Murthy (1973). Rather than use power law velocity profiles, Goldstein assumed that logarithmic velocity

profiles were valid within the incompressible, turbulent boundary layer formed over a free-rotating disc. The disadvantage of his method is that the set of ordinary differential equations obtained is complicated and simple solutions are only possible for a special case. Murthy examined the incompressible turbulent boundary layer formed over a free-rotating cone. He claims that there is a disagreement between the theoretically predicted and experimentally obtained radial velocity over a free-rotating disc and thus uses an alternative expression to that used by von Karman or Goldstein for the velocity distribution. Murthy uses Van Driest's (1955) expression for eddy diffusivity to find the velocity distribution across the boundary layer, but he makes the assumption that the shear stress within the boundary layer equals the value obtained at the cone surface. This assumption seems to be questionable, since, by definition, the shear stress at the edge of the boundary layer is zero. Nevertheless, Murthy obtains some excellent agreement with experiment for heat transfer calculations.

(ii) Co-Rotating Systems

The integral method has been used to predict the turbulent flow occuring in the cavity formed between co-rotating discs by Owen et al (1985) and by Chew and Rogers (1988). Both these publications are based on an extension of the work of von Karman (1921), since von Karman's velocity profiles and surface shear stress formulae (suitably modified to allow for a non-zero boundary layer edge velocity) are assumed to be valid in the boundary layers formed on the two discs.

Owen et al (1985) examined solutions to both the linear and the non-linear boundary layer equations. These authors define 'Ekman-layer' solutions as the solutions to the boundary layer equations in

which the non-linear inertial and centrifugal terms have been neglected. The resulting linear equations are then solved exactly using von Karman's velocity profiles and shear stress formulae. The non-linear equations, i.e. the unsimplified integrated boundary layer equations were obtained by Owen et al by integrating the momentum equations across the boundary layer again using von Karman's velocity profiles and surface shear stress formulae. These non-linear ordinary differential equations were then solved numerically. Owen et al found that for small values of the core rotation, the numerical solutions to the full integrated boundary layer equations showed a better agreement with experiment than the linear 'Ekman-layer' solutions. However, in Owen et al's non-linear approach, the terms involving axial velocities in the boundary layer equations were omitted. This is not justified from the usual boundary layer simplifications and these terms were included in the analysis of Chew and Rogers (1988). Chew and Rogers also extended the method of Owen et al to include heat transfer.

(iii) Rotor-Stator Systems

Integral methods have been applied by several workers to incompressible, turbulent flow in the space between a rotating and a stationary disc. Early workers, i.e. Schultz-Grunow (1935), Daily and Nece (1960) and Dorfman (1963) confined their attention to sealed rotor-stator systems in which there is zero net radial outflow. These authors use von Karman's velocity profiles and surface shear stress formulae, suitably modified to allow for the different boundary conditions, for both the rotor and stator boundary layers. Daily and Nece use slightly modified versions of the radial velocity profiles in both the rotor and the stator boundary layers. These authors assume that the core between the boundary layers is rotating with a constant

angular velocity and calculate its value from an overall angular momentum balance. Schultz-Grunow (1935) and Dorfman (1963) neglect the effects of the outer shroud on the angular momentum balance whereas Daily and Nece include its effect by assuming the boundary layer thickness on the outer shroud is the same as that occuring on the rotor at the same radial location. All the above mentioned authors neglect the axial velocity terms in the boundary layer equations, an assumption which, again, is not justified from the usual boundary layer assumptions.

More recently, Polowski (1984) and Owen (1988) have considered rotor-stator systems allowing for a net radial outflow of fluid. Polowski again assumes that the core rotates with a constant angular velocity and uses an overall angular momentum balance to calculate its value. He assumes that the shear stress on the outer shroud is the same as that on the rotor or stator (depending on whether the shroud is rotating or stationary) at the same radius. Polowski claims to have included all the axial velocity terms in the boundary layer equations, but it appears that some of these terms have still been omitted. Owen's approach is similar to that of Owen et al (1985) in that he uses a linear 'Ekman-layer' solution for the flow over the stator. Owen neglects the variation of the core angular velocity with radius and finds its value from a consideration of conservation of mass within the rotor and stator boundary layers. Owen does not account for the influence of the outer shroud and does not justify his linear approach for the stator. Nevertheless, he, and the other authors mentioned above do find some good agreement with experiment.

Based on an analysis of analytical solutions to the integrated boundary layer equations and finite difference results (Chew (1987)), Chew (1989) argues that von Karman's (1921) radial velocity profile is

inappropriate for the stator boundary layer. These considerations led to Chew developing an integral method for rotor-stator disc systems employing a modified treatment for the stator boundary layer. In his model, the radial momentum equation for the stator is dropped and it is replaced by an equation which fixes the limiting flow angle as the stator surface is approached. Chew allows for a variation of the core velocity with radius and finds the values of this velocity at a number of radial locations using an iterative procedure which solves for mass conservation at each location. Chew incorporates the effects of the outer shroud into his model by using a constant friction factor which he calculates from the rotor boundary layer at the radial location of the outer shroud. The important aspects of Chew's (1989) work will be described in detail in chapter 3.

2.3.3 Finite Difference Methods

In recent years, there has been an increase in the number of publications concerning the use of numerical techniques to solve the Navier-Stokes and energy equations governing both laminar and turbulent flow (using Reynolds-averaging and turbulence modelling in the turbulent case) in rotating systems. To date most of the published work has been for plane disc geometries where the flow is assumed to be steady and axisymmetric; assumptions which result in a considerable saving in computer time. The difficulties encountered in applying numerical techniques to rotating disc flows have been caused mainly by numerical problems associated with the strong coupling that exists between the radial and tangential momentum equations in these flows and also by difficulties with the turbulence model. The more common

turbulence models used and some of the difficulties encountered will be briefly mentioned below. A more thorough discussion of numerical methods which have been used to solve the full governing equations may be found in Chew (1990), but some of the recent work of relevance to the development of the finite difference program described in chapter 6 will now be briefly discussed.

Many workers have used variations of Patankar and Spalding's (1972) finite difference (or finite volume) pressure correction method to study axisymmetric steady flow in both laminar and turbulent regimes. To improve the convergence properties of the algorithm a number of measures in addition to the use of standard under-relaxation have been employed. Gosman et al (1976a) introduced an extra damping term in the radial momentum equation which may be shown to act as a distributed under-relaxation factor on the radial velocity. This extra term has been found by other workers to improve convergence. The accuracy to which the pressure correction equation is solved has also been shown to affect convergence (Chew (1984a)). Further large improvements in computing time have resulted from the use of multigrid acceleration techniques (Lonsdale (1988), Vaughan et al (1989)).

The mixing length model of turbulence based on that adopted by Koosinlin et al (1974) for boundary layer flows on free-rotating discs and cones has proved to be successful for flow predictions in co-rotating systems and rotor-stator disc systems. In this model, computations extend into the viscous sub-layer regions adjacent to the walls. The model has been shown to give reasonable agreement with experiment for flow predictions in co-rotating disc systems and rotor-stator disc systems (see Chew (1985b, 1987), Vaughan and Turner (1987) and Chew and Vaughan (1988)). The Koosinlin et al turbulence model will be described in §6.3.

The k-ϵ turbulence model has been used to predict turbulent rotating flows with varying degrees of success. A high turbulence Reynolds number version of the k-ϵ model with the use of logarithmic wall function in the near-wall region was used by Gosman et al (1976a, 1976b) for rotor-stator disc systems. These authors obtained some encouraging results, but Chew (1984b) later found the disc moment predictions to be sensitive to the near-wall mesh spacing. Poor results were obtained by Morse (1988) when using the model to predict the radial outflow between co-rotating discs. A low turbulence Reynolds number version of the k-ϵ model has been applied with mixed results to rotating disc flows. Launder and Sharma (1974) and Sharma (1977) obtain very good agreement with experiment for flow and heat transfer predictions for a free-rotating disc, but Chew (1984b) and Ong (1988) report that the model predicts laminar flow in conditions known from experiment to be turbulent. Morse (1988, 1989a, 1989b) has developed k-ϵ models for co-rotating disc and rotor-stator disc systems including transitional flows. Agreement with experiment is generally good although some fine tuning of the model is necessary.

2.4 SUMMARY AND CONCLUSIONS

A review of relevant theoretical work on the prediction of rotating flows has been carried out. It is evident from the integral method work mentioned in §2.3.2 that the most common and successful approaches have been based on extensions of von Karman's (1921) free-rotating disc method. Previous work in conical rotating systems has been limited to investigations of the flow induced by a free-rotating cone, and the analysis has been based on a recognition

of the fact that, for large cone angles, there is a similarity between the disc and cone equations of motion. In studying the flow occuring in co-rotating and rotor-stator disc systems, most authors have assumed that von Karman's velocity profiles and surface shear stress formulae may be applied to the boundary layers in these cases. However, in the case of rotor-stator systems, the analysis of many of the authors is questionable since they have neglected certain terms in the boundary layer equations. Chew (1989) includes these terms in his analysis and he concludes that some aspects of von Karman's model are unsatisfactory for the stator boundary layer. Chew's alternative stator model has the advantage over previous models of being based on the evidence of finite difference solutions to the full momentum equations. The integral method adopted by Chew would seem to be the most sophisticated to date, since some justification is given for most of the assumptions made. The same method is used here in chapter 3 and it is assumed that the model may be generalised to a conical geometry. The results from the finite difference method described in chapter 6 will be used to support this assumption.

In solving the full momentum equations for rotating flows, the mixing length turbulence model has been found to be particularly successful in reproducing experimental results. The model also has the advantage over other models (such as the k-ϵ model) of requiring less equations to be solved and therefore of being computationally more efficient. The finite difference program described in chapter 6 is that of Vaughan et al (1989), which has been modified here to solve the equations describing the flow in a conical geometry. The program uses various techniques to improve convergence, such as the use of the extra under-relaxation term of Gosman et al (1976) and the use of multigrid acceleration techniques (Lonsdale (1988)). Compared with the

integral method, the finite difference method requires less assumptions to be made about the flow and is therefore expected to produce better predictions. In view of this, the results of the finite difference program will be used to examine the flows in more detail than the integral method solutions alone can provide.

CHAPTER 3

FORMULATION OF THE ISOTHERMAL EQUATIONS

3.1 INTRODUCTION

The purpose of this chapter is to explain the theory and assumptions leading to the derivation of the integrated boundary layer equations describing turbulent flow in the cavity between a rotating and a stationary cone. The method of solution of the equations will be left until chapter 4. The work described in this chapter is an extension of the work of Chew (1989) on the flow between a rotating and a stationary disc. Chew assumes the flow to be fully turbulent and assumes that the gap width between the discs is sufficiently large for two distinct boundary layers to form on the discs. A straightforward extension of von Karman's (1921) method is used by Chew to formulate the integrated boundary layer equations for the rotor, but he concludes the method is unsatisfactory for the stator. Chew uses results obtained from finite difference work and experiment to improve the model for the stator.

In §3.2, the full governing equations are presented and in §3.3 the standard boundary layer assumptions are described and they are applied to a conical surface. Two sets of boundary layer equations are derived; one of these accounts for the case where the inner radius or the cone angle is large and the other accounts for the case where the cone angle and inner radius of the cone are both small. In §3.4, the velocity profiles and shear stress formulae necessary for the implementation of the integral method are derived and the assumptions

made by von Karman (1921) in deriving these equations are explained. Some important aspects of the postulated flow pattern in a rotor-stator cone system are described in §3.5, and their consequences on the boundary conditions are explained. In §3.6, the integrated rotor boundary layer equations are obtained and in §3.7 Chew's (1989) stator model is explained, and thus the integrated stator boundary layer equations are derived. Finally in §3.8, the treatment of the outer shroud which channels fluid from the rotor to the stator is described.

3.2 GOVERNING EQUATIONS

The geometry of the rotor-stator cone system considered is shown in Figure 3.1. The outer radius of the cone is of length b and the inner radius is of length a (which may be zero). The perpendicular distance between the rotor and stator is d. The rotor is rotating about an axis at $r = 0$ with constant angular velocity Ω and a 'tilted' cylindrical polar co-ordinate system (s,θ,n) is used. The half cone angle is denoted by λ.

Throughout this chapter, the flow is assumed to be fully turbulent and all quantities have been averaged over a suitably small time scale so that they denote turbulent mean quantities. The mean components of velocity are denoted by (u,v,w), the mean pressure by p and the mean density by ρ. The shear stresses shown below are the sum of laminar stresses and Reynolds stresses. The shear stresses are written in component form, so for example, τ_{sn} is the stress which acts on the surface whose normal is in the s-direction and which acts in the n-direction. For generality the equations have been derived for compressible flow, although in later sections of this chapter

incompressibility will be assumed. The continuity and momentum equations which describe the flow in the cavity between the rotor and stator may then be written as

$$\frac{\partial \rho}{\partial t} + \frac{1}{r}\frac{\partial}{\partial s}(\rho r u) + \frac{1}{r}\frac{\partial}{\partial \theta}(\rho v) + \frac{1}{r}\frac{\partial}{\partial n}(\rho r w) = 0 \ , \qquad (3.2.1)$$

$$\rho\left[\frac{\partial u}{\partial t} + u\frac{\partial u}{\partial s} + \frac{v}{r}\frac{\partial u}{\partial \theta} + w\frac{\partial u}{\partial n} - \frac{v^2}{r}\sin\lambda\right]$$

$$= -\frac{\partial p}{\partial s} + \frac{1}{r}\frac{\partial}{\partial \theta}\tau_{s\theta} - \frac{\sin\lambda}{r}\tau_{\theta\theta} + \frac{1}{r}\frac{\partial}{\partial s}(r\tau_{ss}) + \frac{1}{r}\frac{\partial}{\partial n}(r\tau_{sn}) \ , \qquad (3.2.2)$$

$$\rho\left[\frac{\partial v}{\partial t} + u\frac{\partial v}{\partial s} + \frac{v}{r}\frac{\partial v}{\partial \theta} + w\frac{\partial v}{\partial n} + \frac{uv}{r}\sin\lambda + \frac{wv}{r}\cos\lambda\right]$$

$$= -\frac{1}{r}\frac{\partial p}{\partial \theta} + \frac{1}{r}\frac{\partial}{\partial \theta}\tau_{\theta\theta} + \frac{1}{r^2}\frac{\partial}{\partial s}(r^2\tau_{\theta s}) + \frac{1}{r^2}\frac{\partial}{\partial n}(r^2\tau_{\theta n}) \ , \qquad (3.2.3)$$

$$\rho\left[\frac{\partial w}{\partial t} + u\frac{\partial w}{\partial s} + \frac{v}{r}\frac{\partial w}{\partial \theta} + w\frac{\partial w}{\partial n} - \frac{v^2}{r}\cos\lambda\right]$$

$$= -\frac{\partial p}{\partial n} + \frac{1}{r}\frac{\partial \tau_{n\theta}}{\partial \theta} - \frac{\cos\lambda}{r}\tau_{\theta\theta} + \frac{1}{r}\frac{\partial}{\partial s}(r\tau_{ns}) + \frac{1}{r}\frac{\partial}{\partial n}(r\tau_{nn}) \ . \qquad (3.2.4)$$

Following Boussinesq (1877), the Reynolds stresses of the above equations may be expressed in terms of gradients of the mean velocity components and a 'turbulent' viscosity. This turbulent viscosity may then be found from an application of a turbulence model, such as the

mixing length model or k-ε model. The resulting equations would be very complex and they would be very expensive to solve numerically. However certain simplifications may be made to the above equations due to the nature of the flows encountered in rotor-stator cone systems which are of practical interest here. Firstly the flows can be assumed to be axisymmetric and steady, so that all terms involving derivatives of θ and t will be zero.† Secondly due to the high rotational velocity of the rotor, boundary layers will be formed over the solid surfaces. This means that boundary layer theory may be used to simplify the above equations.

3.3 APPLICATION OF BOUNDARY LAYER THEORY TO A CONICAL SURFACE

The concept of a fluid forming a boundary layer when it flows over a solid surface was first described by Prandtl in 1904 and is supported by many experimental observations. Boundary layer theory is now well established and only a brief description of it will be given here. The novelty of this chapter is the application of boundary layer theory to a conical geometry and in particular its application to cases where the cone angle and inner radius are small.

A boundary layer will be formed when the flow is at near zero incidence and is at a high velocity relative to the bounding surface so that the influence of viscosity is confined to a thin layer in the

† These assumptions are certainly justified when examining flows in a rotor-stator disc system (the limiting case when $\lambda = 90^{\circ}$) where the experimental and numerical work supports these assumptions. For the cases where λ takes small values ($< 60^{\circ}$) certain types of flow may occur which would violate these assumptions. The occurence of these types of flows will be discussed in §6.4.

immediate neighbourhood of the surface. The boundary layer is the region in which the relative fluid velocity makes a transition from zero at the boundary to a finite 'free-stream' velocity in the main flow. The definition of the boundary layer thickness, δ, is not precise but may be expressed as the distance from the solid boundary to the point where the boundary layer velocity attains a certain percentage of the free-stream velocity.

As stated above within the boundary layer, tangential fluid velocities will be much larger than those normal to the boundary. Since the relative fluid velocity changes from zero at the boundary to a finite value over a small distance of the order of the boundary layer thickness, spatial gradients of velocity in the normal direction will be larger than those in the tangential direction. These are the major simplifying assumptions of boundary layer theory, and they will now be applied to the flow close to the rotating or stationary surfaces in a rotor-stator cone system.

In terms of the variables used to describe the flow in the boundary layer formed over the rotating or stationary cone, the following relationships are assumed:

$$\frac{\partial}{\partial n} \gg \frac{\partial}{\partial s} , \qquad v \gg w . \tag{3.3.1}$$

For rotationally dominated flow, within the boundary layer v is expected to be larger than u. However, since their relative orders of magnitude are not precisely known, it is assumed that

$$u \lesssim v , \tag{3.3.2}$$

where the $\sim$ symbol means 'of the same order of magnitude'.

The variables of equations (3.2.1) - (3.2.4) may be non-dimensionalised as follows:

$$u = Uu' , \qquad \rho = \tilde{\rho}\rho' , \qquad s = Ss' ,$$
$$v = Vv' , \qquad r = Rr' , \qquad p = \tilde{p}p' , \qquad (3.3.3)$$
$$w = Ww' , \qquad n = Nn' ,$$

where, for example, V has the dimensions of velocity and has a magnitude of a typical tangential velocity within the boundary layer. The dashed variables are therefore dimensionless and are of equal orders of magnitude.

Relationships (3.3.1) and (3.3.2) then translate to

$$S >> N, \quad U >> W, \quad U \lesssim V . \qquad (3.3.4)$$

The boundary layer flow is now assumed to be axisymmetric and steady. Substitution of the above variables into the continuity equation (3.2.1) leads to

$$W \sim \frac{UN}{S} . \qquad (3.3.5)$$

The shear stress terms in equations (3.2.2) - (3.2.4) are scaled by first writing them in terms of their velocity components and effective viscosity, so that, for example, τ_{ss} is scaled as

$$\tau_{ss} = \left[\frac{U}{S}\right] \mu_e \left[2 \frac{\partial u'}{\partial s'} - \frac{2}{3r'}\left[\frac{\partial}{\partial s'} (r'u') + \frac{\partial}{\partial n'} (r'w')\right]\right] = \left[\frac{U\tilde{\mu}}{S}\right] \tau_{ss}' , \qquad (3.3.6)$$

where μ_e is the effective viscosity and $\tilde{\mu}$ has the dimensions of viscosity and the magnitude of a typical viscosity within the boundary layer.

Substitution of equations (3.3.3) into the momentum equations (3.2.2) - (3.2.4) yields, on setting U = V,

$$\rho' \left[u' \frac{\partial u'}{\partial s'} + w' \frac{\partial u'}{\partial n'} - \frac{v'^2}{r'} \sin\lambda \left[\frac{S}{R} \right] \right] = - \frac{\partial p'}{\partial s'} \frac{\tilde{p}}{\rho U^2}$$

$$+ \frac{1}{Re^*} \left[\frac{1}{r'} \frac{\partial}{\partial s'} (r'\tau'_{ss}) + \left[\frac{S}{N} \right]^2 \frac{1}{r'} \frac{\partial}{\partial n'} (r'\tau'_{sn}) - \left[\frac{S}{R} \right] \sin\lambda \frac{\tau'_{\theta\theta}}{r'} \right] , \qquad (3.3.7)$$

$$\rho' \left[u' \frac{\partial v'}{\partial s'} + w' \frac{\partial v'}{\partial n'} + \left[\frac{S}{R} \right] \sin\lambda \frac{u'v'}{r'} + \left[\frac{N}{R} \right] \cos\lambda \frac{w'v'}{r'} \right] =$$

$$\frac{1}{Re^*} \left[\frac{1}{r'^2} \frac{\partial}{\partial s'} (r'^2 \tau'_{\theta s}) + \left[\frac{S}{N} \right]^2 \frac{1}{r'^2} \frac{\partial}{\partial n'} (r'^2 \tau'_{\theta n}) \right] , \qquad (3.3.8)$$

$$\rho' \left[u' \frac{\partial w'}{\partial s'} + w' \frac{\partial w'}{\partial n'} - \left[\frac{S}{N} \right]^2 \left[\frac{N}{R} \right] \cos\lambda \frac{v'^2}{r'} \right] = - \frac{\partial p'}{\partial n'} \left[\frac{S}{N} \right]^2 \frac{\tilde{p}}{\rho U^2}$$

$$- \frac{1}{Re^*} \left[\frac{S}{N} \right]^2 \left[\frac{N}{R} \right] \cos\lambda \frac{\tau'_{\theta\theta}}{r'} + \frac{1}{Re^*} \left[\frac{S}{N} \right]^2 \left[\frac{1}{r'} \frac{\partial}{\partial s'} (r'\tau'_{ns}) + \frac{1}{r'} \frac{\partial}{\partial n'} (r'\tau'_{nn}) \right]$$

(3.3.9)

where Re^* is a Reynolds number for the flow which is defined as

$$Re^* = \tilde{\rho} \frac{US}{\mu} , \qquad (3.3.10)$$

and it is assumed that $Re^* \gg 1$.

An order of magnitude analysis may now be carried out on the individual terms of equations (3.3.7) - (3.3.9) provided that the magnitudes of the terms $(S/N)^2$, $(S/R)\sin\lambda$ and $(N/R)\cos\lambda$ relative to Re^* may be estimated. For boundary layer flow induced by either the rotor or stator, the relative sizes of S, N and R will depend on the geometry of the cone considered. N represents the distance over which velocities change significantly in the normal direction and may be represented by the boundary layer thickness, δ. S represents the distance over which velocities change significantly in the longitudinal direction and may be represented by the longitudinal dimension of the cone, ℓ.

As can be seen from Figure 3.1, $r = s\sin\lambda + n\cos\lambda$, so the following relationship between the scales S, N and R may be assumed

$$R \sim S\sin\lambda + N\cos\lambda \ . \qquad (3.3.11)$$

The size of R compared with S and N will therefore depend on the size of the cone angle, λ, and since S depends on the inner radius, R will also depend on a. Two cone geometries, which are assumed to be realistic models for practical purposes are considered to facilitate the comparison of R with S and N. These two cases will now be examined individually and a different set of boundary layer equations will be derived for each case.

Case (i)

The cone angle and/or the inner radius are not small. In this case within most of the boundary layer, except maybe near the inner radius, $S\sin\lambda \gg N\cos\lambda$, so that

$$R \sim S\sin\lambda, \tag{3.3.12}$$

and the following relationship holds:

$$\frac{N}{S\tan\lambda} \ll 1 \ . \tag{3.3.13}$$

Setting $R \sim S\sin\lambda$ in equations (3.3.7) - (3.3.9) gives

$$\rho' \left[u' \frac{\partial u'}{\partial s'} + w' \frac{\partial u'}{\partial n'} - \frac{v'^2}{r'}\right] = - \frac{\tilde{p}}{\rho U^2} \frac{\partial p'}{\partial s'}$$

$$+ \frac{1}{Re}*\left[\frac{1}{r'} \frac{\partial}{\partial s'} (r'\tau_{ss}') + \left[\frac{S}{N}\right]^2 \frac{1}{r'} \frac{\partial}{\partial n'} (r'\tau_{sn}') - \frac{\tau_{\theta\theta}'}{r'}\right] \ , \tag{3.3.14}$$

$$\rho' \left[u' \frac{\partial v'}{\partial s'} + w' \frac{\partial v'}{\partial n'} + \frac{u'v'}{r'} + \frac{N}{S\tan\lambda} \frac{w'v'}{r'}\right] =$$

$$\frac{1}{Re}*\left[\frac{1}{r'^2} \frac{\partial}{\partial s'} (r'^2\tau_{\theta s}') + \left[\frac{S}{N}\right]^2 \frac{1}{r'^2} \frac{\partial}{\partial n'} (r'^2\tau_{\theta n}')\right] \ , \tag{3.3.15}$$

$$\rho' \left[u' \frac{\partial w'}{\partial s'} + w' \frac{\partial w'}{\partial n'} - \left[\frac{S}{N}\right]^2 \frac{N}{S\tan\lambda} \frac{v'^2}{r'}\right] = - \frac{p}{\rho U^2} \left[\frac{S}{N}\right]^2 \frac{\partial p'}{\partial n'}$$

$$- \frac{1}{Re}*\left[\frac{S}{N}\right]^2 \frac{N}{S\tan\lambda} \frac{\tau_{\theta\theta}'}{r'} + \frac{1}{Re}*\left[\frac{S}{N}\right]^2 \left[\frac{1}{r'} \frac{\partial}{\partial s'} (r'\tau_{ns}') + \frac{1}{r'} \frac{\partial}{\partial n'} (r'\tau_{nn}')\right]. \tag{3.3.16}$$

In equation (3.3.14) all the terms on the left hand side will then be of order of magnitude unity. On the right hand side, the pressure term and the middle stress term will be of order of magnitude unity if

$\tilde{p} \sim \tilde{\rho}U^2$ and $\left\{\frac{S}{N}\right\}^2 \sim Re^*$. The other two stress terms will be of order of magnitude $1/Re^*$. In equation (3.3.15) all the terms on the left hand side will be of order of magnitude unity except the last term which will be very small. On the right hand side the first stress term will be of order of magnitude $1/Re^*$ whereas the second stress term will be of order of magnitude unity. In equation (3.3.16), the dominant term will be the pressure term which will be of order of magnitude Re^*, whereas the other terms will be of order of magnitude unity or less.

If terms of order of magnitude unity are neglected compared with terms of order of magnitude Re^*, and $\frac{N}{S\ \tan\lambda}$ is assumed to be of order of magnitude $1/Re^*$, the following boundary layer equations may be obtained from equations (3.2.1) - (3.2.4):

$$\frac{1}{r}\frac{\partial}{\partial s}(\rho r u) + \frac{1}{r}\frac{\partial}{\partial n}(\rho r w) = 0 , \qquad (3.3.17)$$

$$\frac{1}{r}\frac{\partial}{\partial s}(\rho r u^2) + \frac{1}{r}\frac{\partial}{\partial n}(\rho r u w) - \frac{\rho v^2}{r}\sin\lambda + \frac{\partial p}{\partial s} = \frac{1}{r}\frac{\partial}{\partial n}(r\tau_s) , \qquad (3.3.18)$$

$$\frac{1}{r^2}\frac{\partial}{\partial s}(\rho r^2 u v) + \frac{1}{r}\frac{\partial}{\partial n}(\rho r w v) = \frac{1}{r^2}\frac{\partial}{\partial n}(r^2\tau_\theta) , \qquad (3.3.19)$$

$$\frac{\partial p}{\partial n} = 0 , \qquad (3.3.20)$$

where $\tau_s \equiv \tau_{sn}$, $\tau_\theta \equiv \tau_{\theta n}$.

Case (ii)

Both the cone angle and the inner radius are small. In this case within most of the boundary layer $S\sin\lambda \sim N\cos\lambda$, so that

$$R \sim S\sin\lambda \ , \tag{3.3.21}$$

and the following relationship holds

$$\frac{N}{S\tan\lambda} \sim 1 \ . \tag{3.3.22}$$

In an 'extreme' case, i.e when both the cone angle and the inner radius are very small, then theoretically we may have $N\cos\lambda \gg S\sin\lambda$ and $R \sim N\cos\lambda$. This extreme case is however considered to be too unrealistic to be used as a model for an aero-engine problem and is not considered here. Substituting $R \sim S\sin\lambda$ into equations (3.3.7) - (3.3.9) gives equations (3.3.14) - (3.3.16) as before.

An order of magnitude analysis may now be carried out on the terms in equations (3.3.14) - (3.3.16). If terms of order of magnitude unity are again neglected compared with terms of order Re^*, equations (3.3.14) will produce boundary layer equation (3.3.18) as before. In equation (3.3.15) all the terms on the left hand side will be of order of magnitude unity. On the right hand side the first stress term will be of order of magnitude $1/Re^*$ whereas the second stress term will be of order of magnitude unity. In equation (3.3.16), the dominant terms will be the pressure term and the $v/r\cos\lambda$ term which will both be of order of magnitude Re^*, whereas the other terms will be of order of magnitude unity or less. If terms of order of magnitude unity are neglected when compared with terms of order of magnitude Re^*, the following alternative boundary layer equations are obtained from equations (3.3.15) and (3.3.16):

θ-momentum (case (ii))

$$\frac{1}{r^2}\frac{\partial}{\partial s}(\rho r^2 uv) + \frac{1}{r^2}\frac{\partial}{\partial n}(\rho r^2 wv) - \frac{1}{r^2}\frac{\partial}{\partial n}(r^2\tau_\theta) , \qquad (3.3.23)$$

n-momentum (case (ii))

$$-\rho\frac{v^2}{r}\cos\lambda + \frac{\partial p}{\partial n} = 0 . \qquad (3.3.24)$$

3.4 VELOCITY PROFILES AND THEIR RELATIONSHIP WITH SHEAR STRESS

What follows is a derivation of a relationship between surface shear stress and velocity for flow through a pipe of circular cross-section. An empirical relationship based on experiment is then used to find the velocity distribution across the boundary layer. Prandtl made the fundamental assumption that the velocity distribution in the boundary layer formed over a flat plate is identical to that between the axis and the surface in the flow inside a circular pipe (see Schlichting (1968)). According to Schlichting (1968), this assumption has been verified by experimental studies. The description of the above work is fairly well known, but its inclusion is necessary here for an understanding of the more unusual approach used for rotating flows. This approach is that of von Karman (1921) who assumed the flat plate velocity distribution may also be applied to a free rotating disc. He also assumed that the above mentioned relationship between surface shear stress and velocity was valid for a free rotating disc. As discussed in §2.3.2, many authors have since used von Karman-type assumptions for other types of rotating disc

flows and they are used here for rotor-stator cone system flows.

The assumed velocity profiles will obviously not be an exact representation of the true velocity profiles. This fact is clearly illustrated by the infinite shear stress that the assumed profiles predict at the boundary. However, the experimental results from which the power law profiles were obtained often involved integrals of the velocity. The integral method involves integrating the velocities across the boundary layer too, and so the power law profiles should provide good estimates for the purposes they are used for here.

Consider the fully developed, turbulent flow of a fluid through a straight pipe of circular cross-section and diameter D. In a fluid cylinder of length L, the equilibrium of forces due to the shear stress τ_0 on the circumference and pressure difference P_1-P_2 on the end faces gives:

$$\pi DL\tau_0 = \frac{\pi D^2}{4} (P_1-P_2) , \qquad (3.4.1)$$

so that

$$\tau_0 = \frac{(P_1-P_2)}{L} \frac{D}{4} . \qquad (3.4.2)$$

where the subscript '0' represents values at the pipe surface.

Empirically determined 'laws of friction' for turbulent pipe flow are commonly stated in terms of the dimensionless coefficient of resistance, Λ, where

$$\frac{P_1-P_2}{L} = \frac{\Lambda\rho U_m}{2D} , \qquad (3.4.3)$$

and U_m is the mean velocity of the fluid, defined as

$$U_m = \frac{4Q}{\pi D^2} \quad , \tag{3.4.4}$$

where Q is the volumetric flow rate.

Comparison of expressions (3.4.2) and (3.4.3) gives

$$\tau_0 = \frac{\Lambda}{8} \rho U_m^2 \quad . \tag{3.4.5}$$

In 1911, Blasius made a survey of the then existing experimental results and established the following empirical equation

$$\Lambda = 0.3164 \left[\frac{U_m D}{\nu} \right]^{-\frac{1}{4}} \quad , \tag{3.4.6}$$

where ν is the kinematic viscosity ($=\mu/\rho$), and which is known as the Blasius formula.

Equations (3.4.5) and (3.4.6) may now be used to relate τ_0 to the mean velocity U_m. In 1932, Nikuradse carried out a very thorough experimental investigation into the laws of friction and velocity profiles in smooth pipes over a wide range of Reynolds numbers ($4 \times 10^3 < U_m D/\nu < 3.2 \times 10^6$). Schlichting (1968) shows plots of u/U_{max} (where U_{max} is the maximum velocity in the cross section) against $2y/D$ (where y is the distance measured radially inwards from the wall surface) from Nikuradse's results and shows that the following empirical equation is a close representation of the velocity profiles

$$\frac{u}{U_{max}} = \left[\frac{2y}{D} \right]^{1/m} \quad , \tag{3.4.7}$$

where the exponent m varies slightly with Reynolds number. From this

equation, the ratio of the mean to the maximum velocity can be shown to be

$$\frac{U_m}{U_{max}} = \frac{2m^2}{(m+1)(2m+1)} = F(m) \quad . \tag{3.4.8}$$

Substitution of equation (3.4.6) into equation (3.4.5) gives

$$\tau_0 = 0.03325\rho U_m{}^{7/4} \left[\frac{2\nu}{D} \right]^{\frac{1}{4}} \quad . \tag{3.4.9}$$

Throughout this chapter, m will be taken as 7, although in §7.2.3, the effect of using other power laws will be discussed. The Blasius formula (3.4.6) was established for Reynolds numbers (calculated with the mean velocity and diameter of the pipe) up to a maximum of 10^5 since at that time, measurements for higher Reynolds numbers were not available. For a Reynolds number of 10^5, Schlichting (1968) recommends using F(m) = 0·8, which corresponds approximately to m = 7. If U_m is obtained from equation (3.4.8) and substituted into equation (3.4.9) the following relationship is obtained:

$$\tau_0 = 0.0225\rho U_{max}{}^{7/4} \left[\frac{2\nu}{D} \right]^{\frac{1}{4}} \quad . \tag{3.4.10}$$

Von Karman (1921) assumed that for a free rotating disc a similar expression to (3.4.10) was valid near to the rotating surface. It is assumed here that a similar expression is valid near the surface of the rotor and stator in a rotor-stator cone system. For the rotor or stator, D/2 is replaced by the normal distance near to the surface and U_{max} is replaced by the resultant relative velocity (U_{res}) near to the surface. Thus, for example, the resultant surface

shear stress for the rotor is given by

$$\tau_0 = 0.0225\rho \lim_{n\to 0} \left\{ U_{res}{}^{7/4} \left[\frac{\nu}{n}\right]^{\frac{1}{4}} \right\} \quad . \tag{3.4.11}$$

Finally, following Von Karman (1921), it is assumed that near the wall, the direction of the shear stress is that of the resultant velocity relative to the wall. Hence it is assumed that

$$\frac{\tau_{s,n}}{\tau_{\theta,0}} = \lim_{n\to 0} \left[\frac{u}{v-v_0} \right] . \tag{3.4.12}$$

Von Karman (1921) assumed that the velocity profile (3.4.7) was valid for the skewed boundary layer formed over a rotating disc. Other authors have since used similar profiles for the velocities in a variety of rotating disc flows. In particular, similar profiles where used by Chew (1989) for the velocities in the boundary layer formed over the rotating disc in a rotor-stator disc system. Chew (1989) claims that his finite difference results indicate that these assumed profiles give a good representation of the velocity profiles on the rotating disc. The same profiles are used here for the boundary layer formed over the rotating cone in a rotor-stator cone system and it will be shown in §7.2.4 that finite difference results support the use of such power law profiles. For reasons discussed in §3.7, it is not at this stage assumed that the velocity profile (3.4.7) is valid for the boundary layer formed over the stator.

The velocity components u(s,n) and v(s,n) in the rotor boundary layer are obtained following von Karman's (1921) method for a free-rotating disc. Von Karman assumed that in the boundary layer formed over a free-rotating disc, the radial and tangential velocity

components were separable into a function of s and a function of n, and that the function of n took the form of a power law profile. Von Karman assumed that the profile for the tangential velocity was of a 1/7th power law form similar to equation (3.4.7) but where the radius of the pipe, D/2, is replaced by the boundary layer thickness, δ. He also assumed that the radial velocity component obeyed a 1/7th power law near to the disc surface and used a simple multiplying factor to force the radial velocity to zero at the boundary layer edge. In the next section, it will be shown from a consideration of the flow outside the boundary layer in a rotor-stator cone system that u(s,n) should not be zero at the boundary layer edge. However inclusion of a non-zero u(s,n) at the boundary layer edge leads to considerable complication of the governing equations and as an approximation it will be neglected. The magnitude of u(s,n) at the boundary layer edge is expected to be small relative to the velocity within the boundary layers since it results from a weak axial flow across the cavity, and this view will be supported by finite difference results in §7.2.1. The tangential velocity at the boundary layer edge in a rotor-stator disc or cone system will however be of a comparable size to the rotor velocity (see the experimental results of Daily and Nece (1960)) and is therefore not neglected here. The following boundary conditions for u(s,n) and v(s,n) are used for the rotor boundary layer:

$$u(s,0) = u(s,\delta) = 0, \quad v(s,0) = v_0(s), \quad v(s,\delta) = \bar{v}(s), \qquad (3.4.13)$$

where the overbar denotes a value at the boundary layer edge. Following von Karman, D/2 in equation (3.4.7) is replaced by δ and m is set to 7 as appropriate for the 1/7th power law. Considering the boundary conditions of equation (3.4.13), the velocity components may

be written as:

$$u(s,\eta) = \tilde{u}(s)f(\eta) \ , \tag{3.4.14}$$

$$v(s,\eta) = \bar{v}(s) - [\bar{v}(s)-v_0(s)]g(\eta) \ , \tag{3.4.15}$$

where

$$f(\eta) = \eta^{1/7}(1-\eta), \quad g(\eta) = 1 - \eta^{1/7} \ , \tag{3.4.16}$$

and

$$\eta = n/\delta \ .$$

The surface shear stress components for the rotor in the rotor-stator cone system may now be obtained from equations (3.4.11) and (3.4.12), where the resultant velocity relative to the cone may be obtained from equations (3.4.14) and (3.4.15). Using

$$\tau_0^2 = \tau_{s,0}^2 + \tau_{\theta,0}^2 \ , \tag{3.4.17}$$

the following stress components may be obtained:

$$\tau_{\theta,0} = -0.0225\rho \left[\frac{\nu}{\delta} \right]^{\frac{1}{4}} (v_0-\bar{v}) \left[\tilde{u}^2+(v_0-\bar{v})^2\right]^{3/8}, \tag{3.4.18}$$

and

$$\tau_{s,0} = - \frac{\tilde{u}}{v_0-\bar{v}} \tau_{\theta,0} \ . \tag{3.4.19}$$

3.5 THE FLOW PATTERN AND BOUNDARY CONDITIONS

The assumed velocity profiles (3.4.14) and (3.4.15) and the shear stress equations (3.4.18) and (3.4.19) allow the integration of

the boundary layer equations (3.3.17), (3.3.18), (3.3.19) and (3.3.20) or equations (3.3.17), (3.3.18), (3.3.23) and (3.3.24) through the boundary layer on the rotor. However, in equation (3.4.15), $\bar{v}(s)$ is unknown and the boundary layer equations describing the flow over the stator have not been derived. In this section information will be obtained which will enable the derivation of the stator equations in §3.7, and enable the required relationships for $\bar{v}(s)$ to be deduced.

The postulated flow pattern in the cavity formed between a rotating and a stationary cone is shown in Figure 3.2. It is assumed that the flow develops in a similar way to the flow between a rotating and a stationary disc, and in §7.2 it will be shown that finite difference results support this assumption. The pattern assumed to occur in the disc case has been confirmed by experimental work (Daily and Nece (1960), Daily, Ernst and Asbedian (1964)) and by finite difference results (Chew (1987)) and is shown in Figure 2.1(c). In the source region, fluid is entrained into a boundary layer on the rotor, any flow on the stator up to this point being negligible. In the core region, fluid is 'centrifuged' up the rotor and back down the stator. Between these two boundary layers, there is a rotating core, in which there is a weak axial velocity and negligible radial velocity. If there is no throughflow then there is no source region and the core region fills the entire cavity (except for a thin boundary layer over the outer shroud). In this case the core between the rotor and stator boundary layers rotates with an approximately constant angular velocity. In the flow external to the boundary layers, viscous effects are not so important and it is consistent with previous authors, eg. Owen, Pincombe and Rogers (1985) and Chew (1989) to treat the flow in these regions as inviscid.

In the inviscid source region outside the boundary layer on the

rotor, it is assumed that the flow obeys conservation of angular momentum and is incompressible. (Incompressibility will be assumed throughout the cavity in the next section and a discussion of this will be given there). At the boundary layer edge, therefore, the following relationship may be obtained:

$$r\bar{v}(r) = av_{in}(a) \ , \qquad a \leq r \leq r_e \qquad (3.5.1)$$

where the subscript 'in' indicates the inlet value, and r_e marks the edge of the source region.

If it is assumed that in the core region between the rotor and stator boundary layers, the flow is inviscid, incompressible and rotationally dominated, then coriolis and centrifugal forces dominate inertial forces. There is therefore a balance between the 'centrifugal' and pressure forces in equations (3.2.2) and (3.2.4) and coriolis forces dominate in equation (3.2.3). The following relationships may thus be obtained from equations (3.2.2) - (3.2.4):

$$-\rho \frac{v^2}{r} \sin\lambda = -\frac{\partial p}{\partial s} \ , \qquad (3.5.2)$$

$$\rho \frac{v}{r} (u \sin\lambda + w \cos\lambda) = 0 \ , \qquad (3.5.3)$$

$$-\rho \frac{v^2}{r} \cos\lambda = -\frac{\partial p}{\partial n} \ . \qquad (3.5.4)$$

It is now convenient to use the 'standard' polar coordinate system (r,θ,z) shown in Figure 3.1. In this system, equations (3.5.2) - (3.5.4) can be combined to give

$$\rho \frac{v^2}{r} - \frac{\partial p}{\partial r} , \tag{3.5.5}$$

$$\rho \frac{u_r v}{r} = 0 , \tag{3.5.6}$$

$$\frac{\partial p}{\partial z} = 0 , \tag{3.5.7}$$

where $u_r(r,z)$ is the radial velocity component. Equation (3.5.7) shows that the pressure is a function of r only. Equation (3.5.5) may be differentiated with respect to z to obtain

$$2\rho \frac{v}{r} \frac{\partial v}{\partial z} = 0 . \tag{3.5.8}$$

From equations (3.5.6) and (3.5.8) it may be deduced that

$$\frac{\partial v}{\partial z} = 0 , \tag{3.5.9}$$

and

$$u_r = 0 . \tag{3.5.10}$$

Equation (3.5.10) shows that there is no radial flow in the central core so that all radial flow is confined to the two boundary layers. Equation (3.5.9) shows that the tangential velocity in the central rotating core is constant at a fixed radial position. This means that the tangential velocities at the boundary layer edges on the rotor and stator are equal at the same radial positions. Thus equation (3.5.9) provides important information for the solution of the boundary layer equations on the rotor and stator by effectively reducing the number of unknowns by one.

3.6 THE INTEGRATED BOUNDARY LAYER EQUATIONS FOR THE ROTOR

In §3.3, two alternative sets of equations describing the flow in the boundary layer formed over a cone were derived. In §3.4, the theory and assumptions which led to the particular formulation of the velocity components for the rotor boundary layer, i.e. equations (3.4.14) and (3.4.15) were explained. In this section, the velocity profiles will be substituted into the two sets of boundary layer equations which will then be integrated across the boundary layer. First it is necessary to discuss assumptions concerning compressibility.

Throughout the rest of this chapter, it is assumed that the flow is incompressible. According to Schlichting (1968), a gaseous flow may be considered to be incompressible, if for isothermal flow:

$$\tfrac{1}{2} M^2 \ll 1 \qquad (3.6.1)$$

where M is the Mach number (= v/c, where v is the speed of the flow and c is the speed of sound). For a rotationally dominated flow such as the flow in a rotor-stator cone system, v may be taken as the magnitude of the maximum tangential velocity of the flow. Schlichting suggests that a value of $\frac{1}{2}M^2$ of 0·05 may be taken as an upper limit for a flow to be considered as incompressible. For flows with high Reynolds numbers, such as may occur in many practical situations for which a cone rotor-stator system could be used as a model, this value may be exceeded. Chew and Rogers (1988), however, conclude that in the flow between co-rotating discs, the effect of density variations across the boundary layers is negligible. Since the boundary layers in rotor-stator systems are similar to those in co-rotating systems, it

is reasonable to assume that density variations will also by negligible across the isothermal boundary layers considered in this thesis. In the present analysis, it is also assumed that density variations longitudually through the boundary layer are negligible, although in chapter 5, longitudinal density variations will be accounted for in non-isothermal flows. The effect of the present assumption of incompressibility will be assessed using the finite difference program in §7.2.2.

Case (i)

When integrating equations (3.3.17) - (3.3.20) across the boundary layer it will be assumed that r is independent of n. This is consistent with the boundary layer arguments of §3.3 which were used to derive the case (i) equations.

Equation (3.3.20) states that the pressure is independent of n in the boundary layer. If equation (3.3.18) is evaluated at the boundary layer edge the following equation is obtained:

$$\frac{dp}{ds} = \rho \frac{\bar{v}^2}{r(s)} \sin\lambda \ . \qquad (3.6.2)$$

Integrating equation (3.3.17) across the boundary layer gives

$$\bar{w} = - \frac{1}{\rho r_0} \frac{d}{ds} [\rho r_0 \tilde{u} \delta] \int_0^1 f(\eta) d\eta \ . \qquad (3.6.3)$$

By using equations (3.6.2) and (3.6.3) in the integration of equations (3.3.18) and (3.3.19) across the boundary layer the following eqution may be obtained:

$$\frac{I_{ff}}{r_0}\ \frac{d}{ds}\left[\rho r_0\tilde{u}^2\delta\right] - \rho\,\frac{\delta}{r_0}\sin\lambda\left[\bar{v}^2-2\bar{v}(\bar{v}-v_0)I_g + (\bar{v}-v_0)^2 I_{gg}\right]$$

$$+\ \rho\,\frac{\bar{v}^2}{r_0}\,\delta\sin\lambda = -\tau_{s,o} \qquad (3.6.4)$$

and

$$\frac{1}{r_0^2}\ \frac{d}{ds}\left\{\rho r_0^2\delta\left[\tilde{u}\bar{v}I_f-\tilde{u}(\bar{v}-v_0)I_{fg}\right]\right\} - \frac{\bar{v}}{r_0}\,I_f\,\frac{d}{ds}\left[\rho r_0\tilde{u}\delta\right]$$

$$= -\tau_{\theta,o}\ , \qquad (3.6.5)$$

where

$$I_f = \int_0^1 f(\eta)d\eta\ , \qquad I_g = \int_0^1 g(\eta)d\eta\ ,$$

$$I_{fg} = \int_0^1 f(\eta)g(\eta)d\eta\ , \qquad I_{ff} = \int_0^1 f^2(\eta)d\eta\ , \qquad I_{gg} = \int_0^1 g^2(\eta)d\eta. \quad (3.6.6)$$

The integrals are constants, $\tau_{s,o}$ and $\tau_{\theta,o}$ may be obtained from equations (3.4.18) and (3.4.19) and $r_0 = s\sin\lambda$.

Case (ii)

When integrating equations (3.3.17), (3.3.18), (3.3.23) and (3.3.24) across the boundary layer, the variation of r across the boundary layer will be included. This is consistent with the boundary layer arguments of §3.3 which were used to derive the case (ii) equations.

Integration of equation (3.3.24) across the boundary layer from a general point within the boundary layer to the boundary layer edge gives

$$p(s,n) = \bar{p} - \int_n^{\delta} \rho \frac{v^2(s,n')}{r(s,n')} \cos\lambda \, dn' \quad . \tag{3.6.7}$$

If equation (3.6.7) is differentiated with respect to s the following equation is obtained:

$$\frac{\partial p}{\partial s} = \frac{\partial \bar{p}}{\partial s} - \frac{\partial}{\partial s} \int_{\alpha}^{\delta} \rho \frac{v^2(s,n')}{r(s,n')} \cos\lambda \, dn' \quad . \tag{3.6.8}$$

Equation (3.3.18) may be evaluated at the boundary layer edge to obtain

$$\frac{\partial \bar{p}}{\partial s} = \rho \frac{\bar{v}^2}{\bar{r}(s)} \sin\lambda \quad , \tag{3.6.9}$$

and a substitution of equation (3.6.9) into equation (3.6.8) gives

$$\frac{\partial p}{\partial s} = \rho \frac{\bar{v}^2}{\bar{r}(s)} \sin\lambda - \frac{\partial}{\partial s} \int_n^{\delta} \rho \frac{v^2(s,n')}{r(s,n')} \cos\lambda \, dn' \quad . \tag{3.6.10}$$

Equation (3.3.17) may be integrated across the boundary layer to obtain

$$\bar{w} = - \frac{1}{\rho(s\sin\lambda+\delta\cos\lambda)} \frac{d}{ds} \left[\rho\tilde{u}\delta(I_{f}s\sin\lambda+\delta I_{f\eta}\cos\lambda)\right] \quad . \tag{3.6.11}$$

Equations (3.6.10) and (3.6.11) may be used in the integration of equations (3.3.18) and (3.3.23) across the boundary layer to obtain

$$\frac{I_{ff}}{s}\frac{d}{ds}(\rho s\tilde{u}^2\delta) + \frac{I_{ff\eta}}{s\tan\lambda}\frac{d}{ds}(\rho\tilde{u}^2\delta^2) + \frac{\rho\delta}{s}[2\bar{v}(\bar{v}-v_0)I_g-(\bar{v}-v_0)^2 I_{gg}]$$

$$+ \left[1 + \frac{\alpha\delta}{s\tan\lambda}\right]\frac{d}{ds}\left[\frac{\rho\delta^2}{(s\tan\lambda+\alpha\delta)}\left\{-\frac{\bar{v}^2}{2} - 2\bar{v}(\bar{v}-v_0)I_G+(\bar{v}-v_0)^2 I_{GG}\right\}\right]$$

$$= -\tau_{s,o} \quad , \tag{3.6.12}$$

and

$$\frac{1}{s^2}\frac{d}{ds}[\rho\tilde{u}s^2\delta\{\bar{v}I_f-(\bar{v}-v_0)I_{fg}\}] + \frac{2}{s^2\tan\lambda}\frac{d}{ds}[\rho\tilde{u}s\delta^2\{\bar{v}I_{f\eta}-(\bar{v}-v_0)I_{fg\eta}\}]$$

$$+ \frac{1}{s^2\tan^2\lambda}\frac{d}{ds}[\rho\tilde{u}\delta^3\{\bar{v}I_{f\eta\eta}-(\bar{v}-v_0)I_{fg\eta\eta}\}] - \left\{1 + \frac{\delta}{s\tan\lambda}\right\}I_f\frac{\bar{v}}{s}\frac{d}{ds}(\rho\tilde{u}s\delta)$$

$$- \left[\frac{1}{\tan\lambda} + \frac{\delta}{s\tan^2\lambda}\right] I_{f\eta}\frac{\bar{v}}{s}\frac{d}{ds}(\rho\tilde{u}\delta^2) = -\tau_{\theta,o} \quad , \tag{3.6.13}$$

where $0 \leq \alpha \leq 1$ and

$$I_G = \int_0^1\int_1^\eta g(\eta')\,d\eta'\,d\eta, \qquad I_{GG} = \int_0^1\int_1^\eta g^2(\eta')\,d\eta'\,d\eta,$$

$$I_{f\eta} = \int_0^1 \eta f(\eta)\,d\eta, \qquad I_{f\eta\eta} = \int_0^1 \eta^2 f(\eta)\,d\eta,$$

$$I_{fg\eta} = \int_0^1 \eta\, f(\eta)\, g(\eta)\,d\eta, \qquad I_{fg\eta\eta} = \int_0^1 \eta^2 f(\eta)\, g(\eta)\,d\eta,$$

$$I_{ff\eta} = \int_0^1 \eta\, f^2(\eta)\,d\eta \quad .$$

The constant α appears in equation (3.6.12) as a result of an application of the mean value theorem in the integration of the second term on the right hand side of equation (3.6.10) across the boundary layer.

After substituting for the surface shear stresses from equations (3.4.18) and (3.4.19), the two sets of boundary layer equations may be non-dimensionalised as follows:

$$u_1 = \frac{\tilde{u}}{\beta r_0} , \quad \bar{V} = \frac{\bar{v}}{\beta r_0} , \quad V_0 = \frac{v_0}{\beta r_0} , \quad \delta_1 = \frac{\delta}{r_0} Re_\theta^{1/5} \sin\lambda ,$$

$$Re_\theta = \frac{\beta b^2}{\nu \sin\lambda} , \quad x = \frac{r_0}{b} , \qquad (3.6.14)$$

where β is a representative angular velocity, and $r_0 \equiv s\sin\lambda$.

The particular non-dimensionalisation used in equations (3.6.14) ensures that the resulting case(i) equations are independent of Re_θ and λ. The integrated boundary layer equations for case (i) (equations (3.6.4) and (3.6.5)) become

$$\frac{I_{ff}}{x^3} \frac{d}{dx} (x^4 \delta_1 u_1^2) + \delta_1 [2\bar{V}(\bar{V}-V_0) I_g - (\bar{V}-V_0)^2 I_{gg}]$$

$$= - \frac{0.0225}{(x^2\delta_1)^{\frac{1}{4}}} u_1 [u_1^2 + (V_0-\bar{V})^2]^{3/8} , \qquad (3.6.15)$$

and

$$\frac{I_{fg}}{x^4} \frac{d}{dx} [x^5 u_1 \delta_1 (V_0-\bar{V})] + \frac{\delta_1 u_1}{x} I_f \frac{d}{dx} (x^2 \bar{V})$$

$$= \frac{0.0225}{(x^2\delta_1)^{\frac{1}{4}}} (V_0-\bar{V}) [u_1^2 + (V_0-\bar{V})^2]^{3/8} \qquad (3.6.16)$$

The integrated boundary layer equations for case (ii) (equations (3.6.12) and (3.6.13)) become

$$\frac{1}{x^3}\left[I_{ff} + \frac{\delta_1 I_{ff\eta}}{Re_\theta^{1/5}\tan\lambda}\right] \frac{d}{dx}(u_1^2\delta_1 x^4) + \frac{I_{ff\eta}\, u_1^2\delta_1 x}{Re_\theta^{1/5}\tan\lambda} \frac{d\delta_1}{dx}$$

$$+ \delta_1[2\bar{v}(\bar{v}-v_0)I_g - (\bar{v}-v_0)^2 I_{gg}]$$

$$+ \frac{1}{x^3\tan\lambda Re_\theta^{1/5}} \frac{d}{dx}\left[x^4\delta_1^2\left\{-\frac{\bar{v}^2}{2} - 2\bar{v}(\bar{v}-v_0)I_G + (\bar{v}-v_0)^2 I_{GG}\right\}\right]$$

$$- \frac{\delta_1^2\left[-\frac{\bar{v}^2}{2} - 2\bar{v}(\bar{v}-v_0)I_G + (\bar{v}-v_0)^2 I_{GG}\right]}{\alpha\delta_1 + Re_\theta^{1/5}\tan\lambda}\left[1 + \frac{\alpha}{Re_\theta^{1/5}\tan\lambda}\frac{d}{dx}(x\delta_1)\right]$$

$$= -\frac{0.0225}{(x^2\delta_1)^{\frac{1}{4}}} u_1 [u_1^2 + (v_0-\bar{v})^2]^{3/8}, \qquad (3.6.17)$$

and

$$\frac{1}{x^4}\frac{d}{dx}[\delta_1 x^5 u_1(\bar{v}I_f - (\bar{v}-v_0)I_{fg})] + \frac{2}{x^4 Re_\theta^{1/5}\tan\lambda}\frac{d}{dx}$$

$$[x^5\delta_1^2 u_1(\bar{v}I_{f\eta} - (\bar{v}-v_0)I_{fg\eta})]$$

$$+ \frac{1}{x^4\tan^2\lambda Re_\theta^{2/5}}\frac{d}{dx}[\delta_1^3 x^5 u_1(\bar{v}I_{f\eta\eta} - (\bar{v}-v_0)I_{fg\eta\eta})]$$

$$- \frac{\bar{v}}{x^2}\left[1 + \frac{\delta_1}{Re_\theta^{1/5}\tan\lambda}\right]\left[\left[I_f + \frac{I_{f\eta}\delta_1}{\tan\lambda Re_\theta^{1/5}}\right]\frac{d}{dx}(u_1\delta_1 x^3) +\right.$$

$$\left.\frac{I_{f\eta} u_1\delta_1 x^3}{\tan\lambda Re_\theta^{1/5}}\frac{d\delta_1}{dx}\right]$$

$$= -\frac{0.0225}{(x^2\delta_1)^{1/4}}(v_0-\bar{v})[u_1^2 + (v_0-\bar{v})^2]^{3/8}. \qquad (3.6.18)$$

The integrated boundary layer equations for case (i) (equations (3.6.15) and (3.6.16)) do not show an explicit dependence on the cone angle λ. These equations are in fact identical to the equations obtained by Chew (1989) to describe the flow over the rotor in a rotor-stator disc system, except in his case the scaling parameters involved r instead of $r_0(\equiv s\sin\lambda)$. This similarity between the cone equations in case (i) and the disc equations is important in the next section, where the stator equations are derived via analytical solutions to an infinite cone rotor-stator system. The case (ii) equations will reduce to the case (i) equations if $\lambda = 90^{\circ}$, which is to be expected since the boundary layer assumptions which result in the extra terms being present will not then be valid. The effects the extra terms in the case(ii) equations and the unknown parameter, α, have on the solutions to the equations will be discussed in §4.5.

3.7 THE INTEGRATED BOUNDARY LAYER EQUATIONS FOR THE STATOR

The formulation of the stator equations in this section is the same as that of Chew (1989) for the stator boundary layer equations in a rotor-stator disc system. The same method is possible here due to the similarity between the cone rotor equations for case (i) and the disc rotor equations derived by Chew. The formulation of the equations is based on the evidence of experimental results of Daily and Nece (1960) and the finite difference results of Chew (1987) for rotor-stator disc systems. At present it is assumed that these results are also applicable to rotor-stator cone systems and in §7.3 finite difference results will be used to help validate this assumption. The approach used by Chew (1989) which is described here

is to consider the flow in a rotor-stator system of infinite radius with no throughflow. This approach is convenient because analytical solutions are then possible for the rotor equations and the mechanism of the flow over an outer shroud connecting the rotor to the stator need not be considered.

It has been observed experimentally by Daily and Nece (1960) that in a finite rotor-stator disc system with no throughflow, two boundary layers develop on the rotor and stator separated by an inviscid core rotating with approximately a constant angular velocity. It is assumed that a similar flow pattern occurs in a fictitious infinite rotor-stator system. Further, following the experiments of Daily and Nece (1960) it is assumed that the core in the infinite case rotates with an experimentally obtained typical value of 0.42 times the rotor speed. Using this model it will be shown that analytical solutions may be obtained for the rotor equations but the same approach used for the stator produces meaningless solutions. From this, Chew (1989) concluded that the velocity profiles used for the rotor, ie. equation (3.4.16), were not valid for the stator, a conclusion which he suspected from his finite difference results (Chew (1987)). He then uses his finite difference results, as described here, to formulate an alternative set of equations valid for the stator boundary layer.

Assuming that in an infinite rotor-stator cone system, the rotor and stator boundary layers are separated by a uniformly rotating cone, the method of Newman (1983) may be used to find analytical solutions to the integrated rotor boundary layer equations. The boundary conditions for the tangential velocity are then given by

$$v_0 = \Omega r_0 \quad \text{and} \quad \bar{v} = k\Omega r_0 \ , \tag{3.7.1}$$

where k is a constant. Choosing $\beta = (1-k)\Omega$, analytical solutions may be found to equations (3.6.15) and (3.6.16) in which u_1 = constant, $\delta_1 \propto x^{-0.4}$. These are

$$u_1^2 = \frac{2I_g k+(1-k)I_{gg}}{3.6I_{ff}(1-k)+4.6I_{fg}(1-k)+2I_f k} \quad , \tag{3.7.2}$$

and

$$(\delta_1 x^{0.4})^{5/4} = \frac{0.0225(1-k)(1+u_1^2)^{3/8}}{u_1[2I_f k+4.6I_{fg}(1-k)]} \quad . \tag{3.7.3}$$

It would seem logical now to assume that equations (3.6.15) and (3.6.16) are valid for the stator boundary layer and to look for similar analytical solutions for the equations describing the flow over a stationary cone under a uniformly rotating fluid. In this case $v_0 = 0$ and it is found that

$$u_1^2 = \frac{k^2(I_{gg}-2I_g)}{(3.6I_{ff}+4.6I_{fg}-2I_f)(1-k)^2} \quad . \tag{3.7.4}$$

From equations (3.6.6), $I_{gg} = 1/36$, $I_g = 1/8$, $I_{ff} = 343/1656$, $I_{fg} = 49/720$ and $I_f = 49/120$. Thus $u_1^2 < 0$, so no real solutions exist for u_1.

The fact that this solution is physically impossible suggests that the velocity profiles assumed for the rotor, (3.4.14) and (3.4.15), may not be a good representation of the stator velocity profiles. Finite difference results obtained by Chew (1987) for rotor-stator disc systems suggest that the rotor radial velocity profile gives a particularly poor representation of the profile in the

stator boundary layer. This would mean that some of the constants in equations (3.6.6) which were obtained by integrating the radial velocity profile across the boundary layer would be incorrect for the flow over the stator. The same finite difference results suggest that the 1/7th power law for the tangential velocity is a good fit for most of the boundary layer on the stator. Thus the same tangential velocity profile used on the rotor, i.e. equation (3.4.15), is used for the stator. The radial velocity profile on the stator is replaced by the following more general form:

$$u^s = \tilde{u}^s f^s(\eta^s) \ , \qquad (3.7.5)$$

where the superscript 's' is used to denote a stator value and $\eta^s = (d-n)/\delta^s$. To satisfy the boundary conditions, it is required that

$$f^s(0) = f^s(1) = 0 \ . \qquad (3.7.6)$$

In order that the stress relations (3.4.18) and (3.4.19) hold for the stator, the following relationship is required:

$$f^s(\eta^s) \to (\eta^s)^{1/7} \quad \text{as} \quad \eta^s \to 0 \ . \qquad (3.7.7)$$

No attempt at finding the explicit form of $f^s(\eta^s)$ will be made; instead values of the constants $I_f{}^s$ and $I_{fg}{}^s$ will be found by ensuring that analytical solutions to the stator equations obey conservation of mass in the infinite rotor-stator system.

From the velocity equations (3.4.14), (3.4.15) and (3.7.5) it may be deduced that close to the cone surface both on the rotor and stator, the fluid velocity relative to the cone is at a limiting flow

angle γ, such that

$$\tan\gamma = \frac{\tilde{u}}{v_0 - \bar{\bar{v}}} \ . \qquad (3.7.8)$$

At high Reynolds numbers and away from the outer shroud, Chew (1988) suggests his finite difference results predict that γ for both the rotor and stator is approximately 20°. For the stator, the following boundary conditions must be satisfied:

$$v_0 = 0 \ , \quad \bar{v} = k\Omega r \ , \qquad (3.7.9)$$

and using a similar form of non-dimensionalisation as for the rotor, i.e. using equations (3.6.14), the following equation may be obtained from equation (3.7.8):

$$u_1{}^s = \frac{k\Omega}{\beta^s} \tan 20^\circ \ . \qquad (3.7.10)$$

For the rotor, the boundary conditions are given by (3.7.1), so equation (3.7.8) gives

$$u_1 = \frac{(\Omega - k\Omega)}{\beta} \tan 20^\circ \ . \qquad (3.7.11)$$

From equation (3.5.10), it is apparent that there is no radial flow in the core region. The mass outflow in the rotor boundary layer must therefore exactly balance the mass inflow in the stator boundary layer. The mass flow rate in a boundary layer is given by

$$\dot{m} = \int_0^{\delta} 2\pi\rho r u \, dn \ , \tag{3.7.12}$$

so the mass balance requirement gives

$$I_f \, u_1 \delta_1 + I_f^s \, u_1^s \, \delta_1^s = 0 \ , \tag{3.7.13}$$

where $\beta^s = \beta$. Substitution of u_1 and u_1^s from equations (3.7.10) and (3.7.11) gives

$$I_f \, \delta_1 (1-k) = I_f^s \, k \delta_1^s \ . \tag{3.7.14}$$

The experimental results of Daily and Nece (1960) suggest that a typical value for k is 0.42 and that $\delta_1^s > \delta_1$. Choosing $I_f^s = I_f$ gives $\delta_1^s = 1.38\delta_1$, which is in reasonable agreement with experiments of Daily and Nece (1960) and the finite difference results of Chew (1988).

Using equation (3.7.10) to find u_1^s, an analytical solution of the tangential momentum equation (3.6.16) is possible for the stator boundary layer, in which, again $\delta_1^s \propto x^{-0.4}$. It is found that with k = 0.42, the mass balance equation (3.7.14) is satisfied if $I^s_{fg} = I_{fg}/2$. With $\beta^s = k\Omega$, the stator solution is then

$$u_1^s = -0.364 \ , \tag{3.7.15}$$

and

$$(\delta_1^s \, x^{0.4})^{5/4} = \frac{0.0225[1+(u_1{}^s)^2]^{\ 3/8}}{u_1{}^s(4.61^s_{fg} - 2I_f{}^s)} \ . \tag{3.7.16}$$

Analytical solutions for an infinite rotor-stator cone system without throughflow have now been obtained. Equations will now be derived for

the stator in a finite, shrouded rotor-stator cone system with or without throughflow. The finite difference results presented by Chew (1988) show that for small throughflow rates γ^s has a large value at lower radii but tends to level off at about 20°, although for high throughflow rates γ^s is more erratic. In §7.3 it will be shown that finite difference results for a general cone angle show a similar behaviour of γ^s as presented by Chew (1988). It is also assumed that for all cases, $I^s_{fg} = I_{fg}/2$ and $I_f{}^s = I_f$. If, for general cases the constant β^s is set to Ω, the stator equations may then be derived from equations (3.7.10) and (3.6.16) as

$$u_1^s = -0.364\bar{V}^s \tag{3.7.17}$$

and

$$\frac{d\delta_1^s}{dx} = -\frac{0.0225[1+(0.364)^2]^{3/8}}{0.364 I^s_{fg}(V^s)^{\frac{1}{4}}(x^6\delta_1)^{\frac{1}{4}}} + \frac{\delta_1^s}{x}\left[\frac{2I_f{}^s - 5I^s_{fg}}{I^s_{fg}}\right]$$

$$- \frac{d\bar{V}^s}{dx}\ \frac{\delta_1^s}{V^s}\left[\frac{2I^s_{fg} - I_f{}^s}{I^s_{fg}}\right]. \tag{3.7.18}$$

Equation (3.7.18) is an integrated boundary layer equation for the stator derived under the assumption that the variation of r with n is negligible (i.e. the case (i) boundary layer arguments of §3.3). To derive a stator equation which allows for the variation of r with n (i.e. the case (ii) boundary layer arguments), then equation (3.6.18) is required in place of equation (3.6.16). However, assuming the analysis of Chew (1989) to be valid, equation (3.6.18) will still contains the unknown constants $I^s_{f\eta}$, $I^s_{fg\eta}$, $I^s_{fg\eta\eta}$ and $I^s_{f\eta\eta}$. Since it is assumed that $I^s_f = I_f$ and $I^s_{fg} = I_{fg}/2$, at this stage corresponding assumptions will be made about the other unknown constants so that the

following will be assumed: $I^s_{f\eta} = I_{f\eta}$, $I^s_{fg\eta} = I_{fg\eta}/2$, $I^s_{f\eta\eta} = I_{f\eta\eta}$ and $I^s_{fg\eta\eta} = I_{fg\eta\eta}/2$. The stator equation under the case (ii) boundary layer arguments then becomes

$$\frac{d\delta^s_1}{dx}\left[1 - \frac{4(I^s_{f\eta}-I^s_{fg\eta})\delta^s_1}{I^s_{fg}Re_\theta{}^{1/5}\tan\lambda} + \frac{3(I^s_{f\eta\eta}-I^s_{fg\eta\eta})\delta^s_1}{I^s_{fg}(Re_\theta{}^{1/5}\tan\lambda)^2} + \frac{I^s_{f\eta}\delta^s_1}{I^s_{fg}Re_\theta{}^{1/5}\tan\lambda}\right.$$

$$\left.\left[1 + \frac{\delta^s_1}{Re_\theta{}^{1/5}\tan\lambda}\right]\right.$$

$$\left. + \frac{I^s_{f\eta}\delta^s_1}{I^s_{fg}Re_\theta{}^{1/5}\tan\lambda}\left[1 + \frac{\delta^s_1}{Re_\theta{}^{1/5}\tan\lambda}\right] + \frac{I^s_f\delta^s_1}{I^s_{fg}Re_\theta{}^{1/5}\tan\lambda}\right]$$

$$= -\frac{0.0225[1+(0.364)^2]^{3/8}}{I^s_{fg}(x^6\delta^s_1\bar{v})^{\frac{1}{4}}0.364} + \frac{5(I^s_f-I^s_{fg})\delta^s_1}{I^s_{fg}x} + \frac{10(I^s_{f\eta}-I^s_{fg\eta})(\delta^s_1)^2}{I^s_{fg}xRe_\theta{}^{1/5}\tan\lambda}$$

$$- \frac{5(I^s_{f\eta\eta}-I^s_{fg\eta\eta})(\delta^s_1)^3}{I^s_{fg}x(Re_\theta{}^{1/5}\tan\lambda)^2} - \frac{3\delta^s_1}{xI^s_{fg}}\left[1 + \frac{\delta^s_1}{Re_\theta{}^{1/5}\tan\lambda}\right]\left[I^s_f + \frac{I^s_{f\eta}\delta^s_1}{Re_\theta{}^{1/5}\tan\lambda}\right]$$

$$+ \frac{d\bar{v}}{dx}\frac{\delta^s_1}{\bar{v}I^s_{fg}}\left[2(I^s_f-I^s_{fg}) + \frac{4\delta^s_1(I^s_{f\eta}-I^s_{fg\eta})}{Re_\theta{}^{1/5}\tan\lambda} - \frac{2(I^s_{f\eta\eta}-I^s_{fg\eta\eta})(\delta^s_1)^2}{(Re_\theta{}^{1/5}\tan\lambda)^2}\right.$$

$$\left. - \left[1 + \frac{\delta^s_1}{Re_\theta{}^{1/5}\tan\lambda}\right]\left[I^s_f + \frac{I^s_{f\eta}\delta^s_1}{Re_\theta{}^{1/5}\tan\lambda}\right]\right] . \qquad (3.7.19)$$

It may be noted that if $\lambda = 90^\circ$ is substituted into equation (3.7.19) then equation (3.7.18) is obtained as expected. The effect of using the more elaborate equation (3.7.19) rather than equation (3.7.18) will be investigated in §4.4.

3.8 THE SHROUD TREATMENT

In §3.6, the integrated boundary layer equations describing the flow over the rotor were derived and in §3.7, the integrated boundary layer equations describing the flow over the stator were derived. To close the problem the effect of the gap width, d (see Figure 3.1), between the rotor and the stator needs to be included. This is accomplished by using conservation of angular momentum in the outer shroud boundary layer and the method used here is that used by Chew (1989).

As shown in Figure 3.2, the shroud serves to channel fluid from the rotor boundary layer into the stator boundary layer. The assumptions made are that the mass flow rate in the shroud boundary layer is constant, its thickness is negligibly small compared with the outer radius of the rotor, b, and that the tangential shear stress on the shroud surface can be estimated using a constant friction factor, F, estimated from the rotor.

It is convenient in this section to use the standard cylindrical polar co-ordinate system (r,θ,z). Defining $v_m(z)$ to be the mass averaged and boundary layer integrated (i.e. averaged through the shroud boundary layer) tangential velocity in the shroud boundary layer (i.e. at r=b), it follows that

$$v_m(z) = \frac{a_m}{\dot{m}b} , \qquad (3.8.1)$$

where $\dot{m}$ is the mass flow rate and a_m is the angular momentum in the boundary layer. The tangential shear stress on the shroud is calculated using a constant friction factor as

$$\tau_{\theta,z} = -\tfrac{1}{2}\rho F|\Omega_b b - v_m(z)|(\Omega_b b - v_m(z)) \qquad (3.8.2)$$

where Ω_b is the angular velocity of the shroud. The friction factor, F, is calculated from the rotor boundary layer at r=b. Thus, if the rotor is situated at n = 0 and the stator at n = d, then

$$F = -\frac{\tau_{\theta,o}\big|_{r=b}}{\tfrac{1}{2}\rho(\Omega b - v_m(0))|\Omega b - v_m(0)|} , \qquad (3.8.3)$$

but

$$v_m(0) = \Omega b \left[\bar{V} + (1-\bar{V}) \frac{I_{fg}}{I_f} \right] , \qquad (3.8.4)$$

and so

$$F = \frac{0.045[u_1^2+(1-\bar{V})^2]^{3/8} I_f^2}{(R_{e\varphi}^{0.8}\delta_1)^{\frac{1}{4}}(1-\bar{V})(I_f-I_{fg})^2} . \qquad (3.8.5)$$

A balance of angular momentum for the flow in the shroud boundary layer leads to

$$\dot{m}_b v_m(z) = \dot{m}_b v_m(0) - 2\pi b \int_o^z \tau_{\theta,z'}\, dz' , \qquad (3.8.6)$$

where $\dot{m}_b$ is the mass flow rate in the shroud boundary layer (i.e. the difference between the mass flow rate in the rotor boundary layer at r=b and any flow which leaves at r=b). Substitution of equation (3.8.2) into equation (3.8.6) and integration from z = 0 to z=d/sinλ gives

$$v_m(d/\sin\lambda) = \Omega_b b - \frac{\dot{m}_b(\Omega_b b - v_m(0))}{[\dot{m}_b + \pi\rho F b d/\sin\lambda|\Omega_b b - v_m(0)|]} . \qquad (3.8.7)$$

Now

$$\nu_m(d/\sin\lambda) = \Omega b\bar{V}^s \left[-1 - \frac{I^s_{fg}}{I^s_f} \right] , \qquad (3.8.8)$$

and so use of equation (3.8.7), evaluated at r=b, enables the value of $\bar{V}^s$ at r=b to be calculated from values of the rotor variables at this point.

3.9 SUMMARY

In §3.6 and §3.7, two sets of integrated boundary layer equations were derived to describe the flow over the rotor and stator respectively. The second set contained extra terms to allow for the fact that near the cone apex of a small angled cone, the distance from the axis of rotation to the cone surface may be of a comparable size to the boundary layer thickness. The effect these extra terms have on the solutions to the flow problems will be discussed in the next chapter.

In §3.8, the effects of the shroud were accounted for which led to the derivation of an equation which enables the starting conditions for the stator boundary layer to be obtained from the conditions at the end of the rotor boundary layer.

The above equations, together with an equation derived from conservation of mass between the two boundary layers and equations (3.5.1) and (3.5.9) constitute all the required relations to obtain the solutions to rotor-stator cone problems. In the next chapter several methods of solution of the system of coupled equations will be described.

CHAPTER 4

SOLUTION OF THE ISOTHERMAL INTEGRATED BOUNDARY LAYER EQUATIONS

4.1 INTRODUCTION

In this chapter several methods of solving the integrated boundary layer equations derived in chapter 3 will be explained. All the relevant equations will first be derived in terms of variables chosen for the final numerical calculations. With reference to Figure 3.2, to solve the equations when there is a specified throughflow rate, the cavity between the rotor and stator will be divided into a source region and a core region. When there is no throughflow, the cavity will be assumed to consist of a core region only. In § 4.2 the solution procedure for the source region and two alternative methods of solution for the core region will be described. In § 4.3 the advantages and disadvantages of the two core region methods will be discussed and the reasons for a preference will be explained.

In chapter 2, two sets of rotor and stator equations were derived; the second of these had extra terms which are expected to have an influence when the cone angle and the inner hub radius are small. The effect these extra terms have on the solutions to the equations will be discussed in § 4.4. In § 4.5 to improve the treatment of the initial conditions, the governing equations will be re-derived in terms of asymptotic variables. These new governing equations are amenable to treatment by similar solution methods, and they will provide an alternative system for the solution of flow

problems. Finally in § 4.6, the predicted results will be compared with available experiment data.

4.2 SOLUTION METHODS

4.2.1 Governing Equations and an outline of the solution procedure

In chapter two, the integrated boundary layer equations governing the flow over the rotor and stator were derived in terms of the non-dimensional dependent variables δ_1, u_1, $\bar{V}$, δ_1^s and $\bar{V}^s$. For the purposes of solving the equations, they will be re-written in terms of the following new dependent variables:

$$Y_1(x) = u_1\delta_1 x^3 \ , \quad Y_2(x) = \delta_1 x \ . \tag{4.2.1}$$

The reasons for this change of variables will now be discussed. The boundary layer thickness on the rotor, δ, is given in equations (3.6.14) which show that δ is proportional to $\delta_1 x$. The mass flow rate in a boundary layer is given by equation (3.7.12) which, when evaluated for the rotor and allowing for a variation of r across the boundary layer, becomes

$$\dot{m} = 2\pi\rho\mu b(Re_\phi)^{4/5}\, u_1\delta_1 x^3 \left[I_f + \frac{\delta_1 I_{f\eta}}{(Re_\phi)^{1/5}\tan\lambda} \right] . \tag{4.2.2}$$

Thus Y_1 and Y_2 are proportional to the mass flow rate and the boundary layer thickness respectively and so they represent physical quantities. The idealised initial conditions are that the boundary layer thickness is zero and the mass flow rate in the boundary layer is zero. The constants I_f and $I_{f\eta}$ in equation (4.2.2) are positive

and the boundary layer thickness cannot be negative, so $\dot{m}$ is zero only when $u_1\delta_1 x^3 = 0$. For a cone with inner radius a and outer radius b, the idealised initial conditions are then

$$u_1\delta_1 \left[\frac{a}{b}\right]^3 = 0 \quad \text{and} \quad \delta_1 \left[\frac{a}{b}\right] = 0 \ . \tag{4.2.3}$$

If $a \neq 0$, then equations (4.2.3) indicate that initially δ_1 should be zero and that u_1 need not have any specific initial value but it should be finite. If $a = 0$, then equations (4.2.3) indicate that both δ_1 and u_1 need not have any specific value but they should both be finite. There is then an ambiguity in the required initial values of δ_1 and u_1 and a more sensible choice of variables would be Y_1 and Y_2 in equations (4.2.1) which ideally for any value of a should both have initial values of zero.

These may now be substituted into the case (ii) equations (the case (i) equations are not used explicitly since these are really a special case of the case (ii) equations and may be obtained by putting $\lambda = 90^\circ$).

Putting $\beta = \Omega$ in equations (3.6.14), then $V_0 = 1$ and equations (3.6.17) and (3.6.18) become

$$\frac{dY_1}{dx} 2Y_1Y_2 \left[I_{ff} + \frac{I_{ff}\eta Y_2}{xRe_\theta{}^{1/5}\tan\lambda}\right]$$

$$+ \frac{dY_2}{dx} \left\{\frac{Y_2{}^3x^2}{\tan\lambda Re_\theta{}^{1/5}}\left[2x - \frac{Y_2\alpha}{\left[Re_\theta{}^{1/5}\tan\lambda + \frac{\alpha Y_2}{x}\right]}\right]\left[-\frac{\bar{V}^2}{2} - 2\bar{V}(\bar{V}-1)I_G + (\bar{V}-1)^2 I_{GG}\right]\right.$$

$$\left. - I_{ff}Y_1{}^2\right\}$$

$$= -0.0225\, Y_1 x^{7/4} \left[\left[\frac{Y_1}{x^2}\right]^2 + Y_2^2(1-\bar{V})^2\right]^{3/8} + \frac{Y_1^2 Y_2}{x}\left[I_{ff} + \frac{2Y_2 I_{ffn}}{x\tan\lambda Re_\theta^{1/5}}\right]$$

$$- Y_2^3 x^3 \left[2\bar{V}(\bar{V}-1)I_g - (\bar{V}-1)^2 I_{gg}\right]$$

$$- \frac{x^2 Y_2^4}{\tan\lambda Re_\theta^{1/5}}\left\{\left[2 - \frac{1}{\left[Re_\theta \tan\lambda + \frac{\alpha Y_2}{x}\right]}\right]\left[-\frac{\bar{V}^2}{2} - 2\bar{V}(\bar{V}-1)I_G + (\bar{V}-1)^2 I_{GG}\right]\right.$$

$$\left. + 2x\frac{d\bar{V}}{dx}\left[-\frac{\bar{V}^2}{2} + (1-2\bar{V})I_G + (\bar{V}-1)I_{GG}\right]\right\}, \qquad (4.2.4)$$

and

$$\frac{dY_1}{dx}\left\{1 + \frac{Y_2}{I_{fg}\tan\lambda Re_\theta^{1/5}}\left[\frac{2I_{fg\eta}}{x} + \frac{Y_2 I_{fg\eta\eta}}{\tan\lambda Re_\theta^{1/5}}\right]\right.$$

$$\left. - \frac{\bar{V}Y_2}{x(1-V)I_{fg}Re_\theta^{1/5}\tan\lambda}\left[I_f - I_{f\eta} + \frac{Y_2(I_{f\eta} - I_{f\eta\eta})}{x\tan\lambda Re_\theta^{1/5}}\right]\right\}$$

$$+ \frac{dY_2}{dx}\frac{Y_1}{x\tan\lambda Re_\theta^{1/5} I_{fg}(1-V)}\left\{2\left[\bar{V}I_{f\eta} + (1-\bar{V})I_{fg\eta}\right] + \frac{2Y_2}{x}\left[\bar{V}I_{f\eta\eta} + (1-\bar{V})I_{fg\eta\eta}\right]\right.$$

$$\left. - \bar{V}I_{f\eta}\left[1 + \frac{Y_2}{xRe_\theta^{1/5}\tan\lambda}\right]\right\}$$

$$= \frac{0.0225x^{7/4}}{I_{fg}Y_2}\left[\left[\frac{Y_1}{x^2}\right]^2 + Y_2^2(1-\bar{V})^2\right]^{3/8}$$

$$- \frac{d\bar{V}}{dx}\frac{Y_1}{I_{fg}(1-V)}\left[I_f - I_{fg} + \frac{2Y_2}{x\tan\lambda Re_\theta^{1/5}}(I_{f\eta} - I_{fg\eta}) + \frac{Y_2^2}{\tan^2\lambda Re_\theta^{2/5}}(I_{f\eta\eta} - I_{fg\eta\eta})\right]$$

$$- \frac{Y_1}{xI_{fg}(1-V)}\left[2\left[I_f\bar{V} + I_{fg}(1-\bar{V}) + \frac{2Y_2}{x\tan\lambda Re_\theta^{1/5}}\left[I_{f\eta}\bar{V} + I_{fg\eta}(1-\bar{V})\right]\right.\right.$$

$$+ \frac{Y_2 I_f \eta^V}{x \tan\lambda Re_\theta^{1/5}} \left[1+ \frac{Y_2}{x \tan\lambda Re_\theta^{1/5}}\right]\right] \quad . \tag{4.2.5}$$

In addition to the above integrated boundary layer equations and the stator equations, i.e. equations (3.7.17) and (3.7.19), two further equations are used in the solution method. The first of these concerns conservation of mass in the core region of the flow.

Equation (3.5.10) shows that there is no radial flow in the central core, and so the net mass flow rate in the rotor and stator boundary layers must equal the specified mass throughflow rate. Using equation (3.7.12) to evaluate the mass flow rate in the boundary layers, this condition gives

$$Y_1 - 0.364\bar{V}^S \delta_1^S x^3 + \frac{I_{f\eta}}{Re_\theta^{1/5} I_f \tan\lambda}\left[\frac{Y_1 Y_2}{x} - 0.364\bar{V}^S (\delta_1^S)^2 x^3\right] = \frac{Cq}{2\pi I_f Re_\theta^{4/5}} \ , \tag{4.2.6}$$

where Cq is the non-dimensional mass flow rate ($Cq = \dot{m}/\mu b$).

The second additional equation is the outer shroud equation, i.e. equation (3.8.7). This equation which is valid at $r_0 = b$ may be written as:

$$D\bar{V}^S = \frac{\Omega_b}{\Omega} - \frac{(Y_1 - E)AB}{(Y_1 - E)B + (d/b)C|A|} \ , \tag{4.2.7}$$

where

$$A = \frac{\Omega_b}{\Omega} - \left[\bar{V} + (V_0 - \bar{V})\frac{I_{fg}}{I_f}\right] \ , \qquad B = Y_2^{1/4}(V_0 - \bar{V})(I_f - I_{fg})^2 \ ,$$

$$C = 0.0225\ I_f \left[\left[\frac{Y_1}{Y_2}\right]^2 + (V_0 - \bar{V})^2\right]^{3/8} \ ,$$

$$D = 1 - \frac{I^s_{fg}}{I^s_f} \quad \text{and} \quad E = \frac{C_q}{2\pi(Re_\phi)^{4/5}} \ .$$

Equations (4.2.4), (4.2.5), (3.7.17), (3.7.19) and (4.2.7) along with the core region condition which links the rotor solution to the stator solution and will be described below are sufficient to describe the isothermal flow in the cavity formed between a rotating and a stationary cone. As stated in § 3.5, the flow calculation may be divided into a source region and a core region. A sketch of the flow is shown in Figure 3.2. The source region will exist when there is a flow through the cavity: it is the region where fluid is entrained into a boundary layer on the rotor. This region will extend up to the point where the specified mass flow rate is fully entrained into the rotor boundary layer. Beyond this point, the mass flow rate will continue to increase on the rotor, and will be compensated for by a boundary layer flow in the opposite direction down the stator. Fluid will flow from the stator boundary layer across the central rotating core and into the rotor boundary layer. Equation (3.5.9) shows that in the core region

$$\bar{V}^s(x) = \bar{V}(x) \ , \tag{4.2.8}$$

and both of the solution methods described in the next section attempt to ensure that this relationship holds. All of the methods described in the next section involve the solution of simultaneous ordinary differential equations and this was achieved using a variable order, variable step length NAG library routine for the solution of a stiff system of ordinary differential equations.

It is now convenient to define the moment coefficient, Cm, which

is a non-dimensional parameter that effectively measures the torque experience by the rotating cone. The moment coefficient is the parameter most often used to compare the present theoretical results with experimental data; it is defined here as

$$Cm = \frac{2M\sin\lambda}{\rho\Omega^2 b^5} \quad , \tag{4.2.9}$$

where M is the moment on the rotor, which is calculated from

$$M = -\int_{a/\sin\lambda}^{b/\sin\lambda} 2\pi r_0^2 \, \tau_{\theta,o} \, ds \quad . \tag{4.2.10}$$

From equations (4.2.9) and (4,2,10) the following equation may be obtained:

$$Cm = 0.09\pi Re_{\phi}^{-0.2} \int_{a/b}^{1} \frac{x^{15/4}(1-\bar{V})}{Y_2^{1/4}} \left[\left[\frac{Y_1}{Y_2 x^2}\right]^2 + (1-\bar{V})^2\right]^{3/8} dx. \tag{4.2.11}$$

4.2.2 Source Region

In the source region, fluid is entrained into a boundary layer on the rotor; the flow on the stator in this region is assumed to be negligible. Outside the rotor boundary layer, the fluid is assumed to obey conservation of angular momentum, so that $\bar{v}(r)$ satisfies equation (3.5.1). This equation may be non-dimensionalised using relations (4.6.14) to obtain

$$\bar{V}(x) = \left[\frac{a}{b}\right]^2 \frac{\varphi}{x^2} \quad , \tag{4.2.12}$$

where φ ($= \bar{v}_{in}/\Omega a$) is a constant and a measure of the inlet swirl. If equation (4.2.12) is substituted into equations (4.2.4) and (4.2.5) two ordinary differential equations for the two unknowns Y_1 and Y_2 are obtained.

As stated in the previous section the idealised initial conditions are that both Y_1 and Y_2 are zero. Equations (4.2.4) and (4.2.5) may be re-arranged so that it is clear that numerical difficulties will be encountered if either x, Y_1 or Y_2 are zero. The initial value of x gives the ratio of the rotor inner radius to outer radius, i.e. a/b. To avoid numerical difficulties a lower bound of 10^{-5} was set for the initial value of x, even in cases when a/b is zero (in practice it is arguable whether the inner radius of a cone can ever be precisely zero). The initial conditions for Y_1 and Y_2 were set to 10^{-10}. A full discussion of the problems encountered with the initial conditions will be given in § 4.5. It is assumed that the inlet swirl parameter, φ, may vary between 0 and 1, a value of 1 indicating that the tangential velocity of the fluid at the inlet is equal to the rotor velocity. From equation (3.2.5) it can be seen that numerical difficulties will be encountered if $\bar{V} = 1$; an upper-bound of 0.99 was therefore set for φ.

Given the parameters necessary to carry out a source region calculation, i.e. a/b, the throughflow rate parameter, Cq and the inflow swirl parameter, φ, equations (4.2.4) and (4.2.5) may be solved from $x = a/b$. The ordinary differential equation routine was stopped when the specified throughflow rate was fully entrained into the rotor boundary layer. From equation (4.2.6), this condition was achieved when

$$Y_1 \left[1 + \frac{Y_2 I_f \eta}{x I_f \tan\lambda Re_\theta^{1/5}}\right] = \frac{Cq}{2\pi I_f (Re_\theta)^{4/5}} \cdot \qquad (4.2.13)$$

The x value reached when equation (4.2.13) is satisfied marks the end of the source region and the beginning of the core region and is denoted by x_e.

4.2.3 The Core Region Calculation (Method 1)

The main feature of this method is that the equations are solved in the direction of the secondary flow. The two rotor equations, (4.2.4) and (4.2.5) are therefore solved from $x = x_e$ to $x = 1$ and the stator equation (3.7.19) is then solved from $x = 1$ to $x = x_e$. The two sets of equations are linked with equation (4.2.8) and an iterative method is used to find the correct $\bar{V}(x)$ distribution such that the mass balance equation (4.2.6) is satisfied.

If there is a throughflow in the cavity, then the starting conditions for Y_1 and Y_2 are obtained from the values of Y_1 and Y_2 at the end of the source region, i.e. at $x = x_e$. If there is no throughflow, then the starting conditions for Y_1 and Y_2 are set to 10^{-10}. The core region is discretised into N radial locations, denoted by x_i, i=1,...,N and initially $\bar{V}(x_i)$ are guessed at each point. A curve is then fitted through the $\bar{V}(x_i)$ values using a library routine which interpolated the discrete values using cubic splines. Using this $\bar{V}$ distribution, the rotor equations (4.2.4) and (4.2.5) are solved from $x = x_e$ to $x = 1$.

The values of Y_1, Y_2 and $\bar{V}$ at $x = 1$ are then substituted into the shroud equation (4.2.7), from which $\bar{V}^s(x_N)$ is obtained. Using this value together with the other $\bar{V}(x_i)$ (i=1,...,N-1), a $\bar{V}^s(x_i)$

distribution is obtained using the same curve fitting routine as before. The δ_1^s value at the start of the stator calculation, $x = 1$ is obtained from the mass balance equation (4.2.6). The stator equation is then solved from $x = 1$ to $x = x_e$.

The values of $Y_1(x_i)$ obtained from the rotor equations and the values of $\delta_1^s(x_i)$ obtained from the stator equation at the radial locations $i = 1$ to N-1 are then substituted into equation (4.2.6). The error in this equation at each x_i (i=1,...,N-1) is denoted by $F_i(\bar{V}_i,\ldots,\bar{V}_N)$ (which will be written as $F_i(\bar{V})$), where

$$F_i(\bar{V}) = \frac{Y_1(x_i) - 0.364\bar{V}^s(x_i)\delta_1{}^s(x_i)x^3}{Y_1(x_i)}$$

$$+ \frac{I_{f\eta}}{I_f Re_\theta{}^{1/5}\tan\lambda}\left[\frac{Y_1Y_2}{x} - 0.364\bar{V}^s(x_i)\delta_1{}^s(x_i)^2x^3\right] - \frac{C_q}{2\pi I_f(Re_\theta)^{4/5}} \cdot \qquad (4.2.14)$$

A final equation for $i = N$ is obtained from equation (4.2.8) evaluated at $x = 1$ as

$$F_N(\bar{V}) = \frac{\bar{V}^s(x_N) - \bar{V}(x_N)}{\bar{V}(x_N)} \quad . \qquad (4.2.15)$$

Thus the initial guessed $\bar{V}(x_i)$ distribution leads to a system of N simultaneous non-linear algebraic equations of the form

$$F_i(\bar{V}) = 0 \ , \qquad \text{for } i = 1,2,\ldots,N \quad . \qquad (4.2.16)$$

These equations are solved iteratively for $\bar{V}(x_i)$, each iteration

requiring the solution of the rotor equations and the stator equation using the up-graded $\bar{V}(x_i)$ distribution.

The accuracy and computational speed of this method would be expected to depend on the following factors:

(i) The numerical method used to find the correct $\bar{V}(x_i)$ distribution such that equations (4.2.16) are satisfied within a certain error band and the size of the error band chosen.

(ii) The number of points, N.

(iii) The distance between x_e and the first point, x_1. It is assumed that the rest of the points are spaced at equal intervals between x_1 and x_N. Thus, as the first point moves further from x_e, effectively the condition that the mass flow rate in the stator boundary layer at $x = x_e$ is exactly zero is relaxed.

The above three factors will now be considered separately.

(i) Three schemes were attempted to find the $\bar{V}(x_i)$ distribution which satisfied equations (4.2.16).

The first scheme used a standard NAG library routine which solved a system of N non-linear functions in N variables. The N variables in this case were $\bar{V}(x_i)$, i=1,...,N, and the N non-linear functions were given by equation (4.2.16). This scheme was found to be slow to converge and therefore not very efficient. A typical run with N = 10 would take about 150 iterations and about 20 minutes processing time on a Prime 6350. A relative error of 10^{-6} was specified for each $\bar{V}(x_i)$, which produced an average error in the mass balance (i.e. $|F_i|$ of equation (4.2.16)) of about 10^{-3}. If the relative error in $\bar{V}(x_i)$ was set larger than this, say 10^{-5}, it was found that F_i

(i=1,...,N) could vary between 0.1 and 0.8. These results indicate that the mass balance equations are highly dependent on the $\bar{V}$ distribution and suggest that the equations may be ill-conditioned. The rate of convergence did not seem to depend on the initial guessed values of $\bar{V}(x_i)$; a $\bar{V}$ distribution estimated from a method 2 calculation (see § 4.2.4) did not improve the convergence rate. The main draw-back of the scheme was that it was not very robust. Often the routine would fail with an error message indicating that the iteration procedure was not making good progress. Also the routine would sometimes produce 'unreasonable' $\bar{V}(x_i)$ values, i.e. negative or rapidly varying values which would create problems with the O.D.E solver.

The second scheme attempted used a library routine which found a minimum of the function $G(\bar{V}(x_1), \bar{V}(x_2), \ldots, \bar{V}(x_N))$ where

$$G = |F_1| + |F_2| + \ldots + |F_N| \quad . \tag{4.2.17}$$

This scheme had the advantage over the previous scheme that constraints could be placed on the $\bar{V}(x_i)$ which avoided unreasonable values being produced by the routine. However, the scheme generally took longer to converge (about 250 iterations corresponding to about 30 mins processing time on a Prime 6350 when N = 10) and again it was not very robust.

The third scheme tried was a simple iterative method. The value of $\bar{V}(x_i)$ for the j^{th} iteration was obtained from equations (4.2.16) as follows:

$$\bar{V}^{j}(x_i) = \bar{V}^{j-1}(x_i) + \omega\bar{V}^{j-1}(x_i)F_i(\bar{V}) \quad , \qquad (4.2.18)$$

where ω is a constant under-relaxation factor (see appendix A for the motivation for equation (4.2.18)). Numerical experiments suggested that an optimum value of ω for a zero throughflow case was about 0.5 and for a case with throughflow was about 0.8. The factor $\bar{V}j^{-1}(x_i)$ appears multiplied by ω on the right hand side of equation (4.2.18) to prevent negative $\bar{V}j(x_i)$ values being obtained when $\bar{V}j^{-1}(x_i)$ was close to zero. For a zero throughflow case, initial values of $\bar{V}(x_i)$ were all set to 0.4. For a throughflow case, initial values were set as follows:

$$\bar{V}(x_1) = 0.02, \quad \bar{V}(x_i) = \bar{V}(x_{i-1}) + 0.01, \quad i = 2,...N... \qquad (4.2.19)$$

These initial values were chosen because they gave the approximate variation and magnitudes of $\bar{V}(x_i)$ which could be expected in the final solutions. The method was found to be robust and to converge quickly, a typical case taking about 25 iterations and using 30 seconds processing time on a Prime 6350. This method was therefore favoured over the previous two and was the method used in determining the effects of varying T_1, N and x_1-x_e below.

The effect the tolerance, T_1, defined as $\max|F_i(\bar{V})|$ (i=1,...,N), in equation (4.2.16) has on the moment coefficient, Cm and the number of iterations required is shown in Table 4.1(a). The moment coefficients shown in these tables and quoted throughout this thesis are given a three significant figure accuracy. The reasons for not quoting more significant

figures are:

(a) Greater accuracy cannot be justified in view of the assumptions made in the integral method.

(b) The experimental data with which the moment coefficient predictions will be compared cannot be expected to justify more accurate readings.

(c) The moment coefficient was calculated numerically from equation (4.2.11) using a library routine and the integrand error is normally such that the moment coefficient will be accurate to about three signficant figures.

Table 4.1(a) shows that Cm is very insensitive to T_1 over the range shown with an error between the predicted value for $T_1 = 10^{-1}$ and $T_1 = 10^{-4}$ of only 1.3%. A value of $T_1 = 10^{-2}$ was set for all subsequent problems.

(ii) The effect the number of points, N, has on the moment coefficient and the number of iterations required is shown in Table 4.1(b). The table shows that the solution is very insensitive to N with an error between the predicted values for N = 4 and N = 40 of less than 1%. A value of 10 was used for all subsequent problems. For the runs producing Tables 4.1, the core region filled approximately half the cavity. For lower throughflow rates, the core region would become larger and it may be expected that N would need to increase to produce the same degree of accuracy. However, Figure 4.1 shows that as the throughflow rate decreases then the $\bar{V}$ distribution becomes flatter so that increasing N would not greatly improve the accuracy of the solution.

(iii) The effect the distance x_1-x_e has on the moment coefficient and number of iterations is shown in Table 4.1(c). The table shows that the solution is very insensitive to this distance over the range considered. However, the processing time taken in all cases are comparatively small, so that there is no significant saving to be made by choosing a large value of x_1-x_e. A value of 0.05 was chosen for all subsequent problems.

4.2.4 The Core Region Calculation (Method 2)

The main feature of this method is that all the equations are solved simultaneously in the same direction, i.e. from $x = x_e$ to $x = 1$. The mass balance equation (4.2.6) may be differentiated with respect to x to obtain

$$\frac{dY_1}{dx}\left[1+\frac{I_f\eta}{I_fRe_\theta^{1/5}\tan\lambda}\right]+\frac{dY_2}{dx}\left[\frac{I_f\eta Y_1}{I_fRe_\theta^{1/5}\tan\lambda}\right]-\frac{d\delta_1^s}{dx}\left[0.364x^3\bar{V}\left[1+\frac{2\delta_1^s I_f\eta}{I_fRe_\theta^{1/5}\tan\lambda}\right]\right]$$

$$-\frac{d\bar{V}}{dx}\left[0.364x^3\delta_1^s\left[1+\frac{\delta_1^s I_f\eta}{I_fRe_\theta^{1/5}\tan\lambda}\right]\right]-1.092\delta_1^s x^2\bar{V}\left[1+\frac{\delta_1^s I_f\eta}{I_fRe_\theta^{1/5}\tan\lambda}\right]$$

$$-\frac{Y_1Y_2}{x^2}\frac{I_f\eta}{I_fRe_\theta^{1/5}\tan\lambda}=0 \quad . \qquad (4.2.20)$$

Equations (4.2.4), (4.2.5), (3.7.19) and (4.2.20) are four ordinary differential equations for the four variables Y_1, Y_2, δ_1^s and $\bar{V}$. The original mass balance equation (4.2.6) is used to calculate initial conditions at the start of the core region. Ideally, the starting conditions for the four variables should be obtained from the end of

the source region, i.e. at $x = x_e$. However, from the mass balance equation (4.2.6) evaluated at $x = x_e$, either δ_1^s or $\bar{V}$ will be zero, which will result in $d\delta_1^s/dx$ being infinite at $x = x_e$ (see equations (3.7.18) and (3.7.19)). In practice therefore the source region calculation is continued for a short distance Δx_e past x_e. The values of Y_1 and Y_2 at $x = x_e+\Delta x_e$ are then substituted into equation (4.2.6) and the value of δ_1^s at $x = x_e+\Delta x_e$ is calculated using a guessed value of $\bar{V}$ at $x = x_e+\Delta x_e$. Using these four starting conditions, the four ordinary differential equations are solved from $x = x_e+\Delta x_e$ to $x = 1$. At $x = 1$, the values of Y_1, Y_2 and $\bar{V}$ are substituted into the shroud equation (4.2.7). This equation yields a value of $\bar{V}^s$ at $x = 1$ which may be compared with the $\bar{V}$ value obtained from the solution to the ordinary differential equations. An iterative procedure is then used on the guessed value of $\bar{V}$ at $x = x_e+\Delta x_e$ which is continued until $\bar{V}$ and $\bar{V}^s$ at $x = 1$ are equal (to within a specified tolerance). The iterative procedure used is the method of bisection, so that two initial $\bar{V}$ guesses are required, one producing a $\bar{V}$ at $x = 1$ such that $\bar{V} > \bar{V}^s$, the other producing a $\bar{V}$ such that $\bar{V} < \bar{V}^s$.

The accuracy and computational speed of this method would be expected to depend on the following factors:

(i) The size of Δx_e. As Δx_e becomes smaller, then the solutions should become more accurate, since the solution will more closely represent the postulated flow pattern shown in Figure 3.2.

(ii) The error tolerated in $\bar{V}-\bar{V}^s$ at $x = 1$, i.e.

$$T_2 = \frac{|\bar{V}-\bar{V}^s|}{\bar{V}} \quad . \tag{4.2.21}$$

As with method 1, a series of calculations were performed to determine suitable values for the parameters Δx_e and T_2.

(i) The effect Δx_e has on the moment coefficient and computational speed is shown in Table 4.2(a). The table shows that varying Δx_e does appear to have a fairly significant effect on the solution. The smallest value of Δx_e shown in the table is 0.0017, since if Δx_e was smaller than this (to four decimal places) then a solution could not be obtained for any value of T_2 tested (i.e. $T_2 > 10^{-6}$). The reasons for this will be discussed in § 4.3. The size of Δx_e chosen for subsequent problems was 0.005.

(ii) The effect the tolerance, T_2, defined in equation (4.2.21) has on the moment coefficient and computational speed is shown in Table 4.2(b). The table shows that the solution is not sensitive to T_2 when $T_2 < 0.1$ and a value of 10^{-3} was chosen for subsequent problems.

4.3 COMPARISON OF THE TWO CORE REGION METHODS

To determine which of the above two core region methods is superior, the efficiency, reliability and accuracy of both of them need to be considered. These three criteria will now be discussed separately.

Excluding the extreme cases shown in Tables 4.1(a)-(c), i.e. the cases where T_1 and x_1-x_e are smallest and N is largest, Tables 4.1(a)-(c) and Tables 4.2(a) and (b) show that both methods use

approximately the same amount of processing time.

By the reliability of each method is meant whether the method is prone to failure for one reason or another. Method 1 will fail if the under-relaxation factor, ω, in equation (4.2.18) is too large, such that the errors in the mass balance, $|F_i|$, do not decrease as the iteration process procedes, or such that the iteration procedure produces an erratic V distribution which can cause problems with the ordinary differential equation solver. Also, if ω is too large then the iteration procedure often may not converge within a reasonable number, say 200, iterations. If ω was given a maximum value as indicated in § 4.2.3 then a solution was found in all tried cases. If ω is reduced then the reliability will be increased, although more iterations will be required.

Method 2 requires two initial values of $\bar{V}$ at $x = x_e+\Delta x_e$, one producing $\bar{V} > \bar{V}^s$, the other $\bar{V} < \bar{V}^s$ at $x = 1$. The method of bisection is then used until a $\bar{V}$ at $x_e+\Delta x_e$ is obtained which produces $\bar{V} = \bar{V}^s$ (to within a specified accuracy) at $x = 1$. If however Δx_e is too small, then to machine accuracy, the bisection method will eventually produce an unchanging $\bar{V}$ at $x_e+\Delta x_e$, but still either $\bar{V} > \bar{V}^s$ or $\bar{V} < \bar{V}^s$ at $x = 1$. This indicates that equations (3.7.19) and (4.2.20) are very sensitive to their initial conditions, i.e. small changes in δ_1^s and $\bar{V}$ at $x_e+\Delta x_e$ produce relatively large changes in δ_1^s and $\bar{V}$ at $x = 1$. As stated in § 4.2.4, however, the method should succeed provided Δx_e is given a value no less than 0.005.

Ideally it should be possible to choose small enough or large enough values of the parameters shown in tables 1 and 2 such that methods 1 and 2 predict exactly the same value for C_m.
Tables 4.1(a)-(c) show that method 1 is very insensitive to the precise values of T_1, N and x_1-x_e, which indicates that the moment

coefficient should not change from 3.84×10^{-3} even if T_1 and x_1-x_e were reduced further or if N was increased further. Table 4.2(a) shows, however, that method 2 is more sensitive to the precise value of Δx_e and it was found that a solution could not be obtained for $\Delta x_e < 0.0017$ for any value of T_2 (≤ 0.1). Thus the value of Cm = 3.81×10^{-3} (which differs from the above value for method 1) may not be the correct unchanging value.

A comparison of the moment coefficient predicted by both methods using the chosen values for T_1, N, x_1-x_e, T_2, Δx_e stated in the previous section is shown in Table 4.3. The table shows that a very good agreement is obtained between the methods with the relative error always being less than 2%. Figure 4.2 shows graphs of $\bar{V}$ predicted by the two methods for two throughflow rates. Both graphs show a good agreement which explains the close agreement between the moment coefficient predictions. What is noticable in Figure 4.2 is that the $\bar{V}$ distribution predicted by method 2 has a physically unrealistic jump when transferring from the source region to the core region; this jump causes the library routine to produce a larger error when integrating the Cm equation (4.2.11) than the error produced by method 1.

Clearly, the differences between the two methods in terms of efficiency, reliability and accuracy are not great, and it is not immediately apparent which method is superior. However, if a choice between the two methods was required then Method 1 would seem to be preferable for the following reasons.

(i) Method 2 is more sensitive to the parameter Δx_e than method 1 is to all its relevant parameters shown in Tables 4.1(a)-(c).

(ii) The jump in the $\bar{V}$ distribution predicted by method 2 tends to

cause a greater error in evaluating Cm than the other $\bar{V}$ distribution predicted by method 1.

Of relevance here is a comparison of the performance of the preferred method 1 calculation procedure with that of Chew (1989). Chew solved the equations governing the flow in a rotor-stator disc system and his equations may be obtained by putting $\lambda = 90^{\circ}$ in equations (3.7.19), (4.2.4), (4.2.5) and (4.2.6). For the core region calculation, Chew again discretised the region into N radial locations but he assumed a linear variation of $\bar{V}$ between these points rather than fitting a curve through these points as in the present method. He found that it was required to take N = 40 for grid independent solutions which is far greater than the required value found here (see Table 4.1(b)). Chew solved the system of equations (4.2.16) using a library routine for the solution of a system of simultaneous non-linear equations. Assuming this solver to be similar to the one used in the first attempted scheme described in the method 1 calculation here, it may be concluded that the present method of solution using the simple iterative scheme (equation (4.2.18)) and using cubic splines to interpolate $\bar{V}(x_i)$, results in a considerable saving in processing time. A comparison of the moment coefficient predicted by the present method with the moment coefficient predicted by Chew (1988) will be made in § 4.6.

4.4 THE EFFECT OF THE TERMS CONTAINING tanλ

The terms containing tanλ in equations (3.7.19), (4.2.4) and (4.2.5) complicate the equations considerably and so it would be

desirable to neglect them. This section is concerned with determining whether or not their neglect is justified and this is achieved by assessing the effect of the terms on the solutions to the equations. From the analysis of § 3.3, the terms containing tanλ are expected to have an effect when $\delta \simeq r$ (or $\delta^s \simeq r$ for the stator) and this is most likely to occur when both a and λ are small. The effect of the tanλ terms on the solutions to the equations will therefore be assessed by comparing the solutions as λ decreases for various values of the ratio (a/b). The equations governing the flow over the rotor, i.e. equations (4.2.4) and (4.2.5), and the equation governing the flow over the stator, i.e. equation (3.7.19) will be examined separately and so the present section will now be divided into the two appropriate sub-sections, with a further sub-section added for a discussion.

(i) Rotor Equations

The constant α appears in equation (4.2.4) as a result of an application of the mean value theorem to one of the terms in the boundary layer equations. The constant α may take any value between 0 and 1 and the solutions to equations (4.2.4) and (4.2.5) when $\alpha = 0$ and $\alpha = 1$ is shown in Figure 4.3. The results show that α has no noticable effect on $\delta_1 x$ ($=Y_2$) except when $\lambda = 1^\circ$. It was found that α had even less effect on the solution for Y_1 and so it was concluded that α may be set to zero for all subsequent problems.

The effect varying λ has on the solutions to equations (4.2.4) and (4.2.5) is shown in Figures 4.4(a)-(c) and Figure 4.5. In Figures 4.4, $\bar{V}$ is set to zero and the ratio of the inner to outer radius, a/b, is varied between 0.001 and 0.75. The three graphs show that the tanλ terms only have an appreciable affect on the solution

when λ is less than about 15°. The graphs also show that the discrepancies are fairly independent of a/b. In Figure 4.5, a/b is set to 0.001 and $\bar{V}$ is set to 0.42 which is the approximate value which may be expected for a rotor-stator disc case without throughflow. Again the graphs show that the tanλ terms only have an appreciable effect when λ is less than about 15°.

(ii) Stator Equation

The effect of varying λ on the solutions to equation (3.7.19) is shown in Figures 4.6(a) and (b). The $\bar{V}$ distributions chosen were fairly typical for a zero throughflow case and for a case where C_q has a value of about 3000 in which cases δ_1^s at $x = 1$ is set at 0.1, a typical value. As is consistent with the results from the rotor equations, the graphs show that the tanλ terms only have an appreciable effect when λ is less than about 15°.

(iii) Discussion

Figures 4.4, 4.5 and 4.6 suggest that the tanλ terms may be omitted from the case (ii) integrated boundary layer equations (thus reducing them to the case (i) equations) without noticably effecting the solutions unless λ is as small as about 10°. In chapter 6, the experimental results will be discussed which provide evidence that for $\lambda < 45^{\circ}$, the secondary flow pattern may change and it may no longer be amenable to the integral method treatment. If this experimental evidence is correct then there is certainly no point in considering rotor-stator equations with λ as small as 10°. It may be concluded that the extra tanλ terms present in the case (ii) equations may be omitted in all rotor-stator cases where the equations and method are expected to be valid.

4.5 ASYMPTOTIC SOLUTIONS

As stated in § 4.2, the idealised initial conditions for the solution of equations (4.2.4) and (4.2.5) are that both Y_1 and Y_2 are zero. From equations (4.2.4) and (4.2.5) it is clear that to avoid numerical difficulties, Y_1 and Y_2 cannot be zero. In § 4.2 it was stated that the initial values of Y_1 and Y_2 were set at 10^{-10}. To be confident that the solutions obtained for a particular problem are the real physical solutions, they need to be independent of the particular starting values. Figure 4.7 shows the effect of using four different starting conditions for Y_1 and Y_2 on the solution for Y_2 ($=\delta_1 x$). The graphs show some variation in the solution with the initial values assigned to Y_1 and Y_2, particularly when they are assigned different values. In Figure 4.7, $\bar{V} = 0$ and $a/b = 0.1$, however, similar affects are observed when different values are assigned to these variables.

In order to provide more confidence in the solutions when Y_1 and Y_2 are given initial values of 10^{-10}, in this section two methods will be described which involve re-formulating equations (4.2.4) and (4.2.5) so as to remove the singularity which occurs when Y_1 and Y_2 are zero. The solutions to the resulting equations for the second method will then be compared with the solutions to the original equations when Y_1 and Y_2 are given starting values of 10^{-10}. In both of these methods it is assumed that the boundary layer grows from $x = a/b$ in a similar way to a boundary layer growing over a free rotating cone from $x = a/b$ (see Appendix B for the special case $a/b = 0$), so that dY_1/dx and dY_2/dx are infinite at $x = a/b$.

The first method is to set Y_1 and Y_2 at $x = a/b$ to zero and to simply approximate dY_1/dx and dY_2/dx with a very large positive number at $x = a/b$. The method does not work as the solutions are strongly

dependent on the approximation to dY_1/dx and dY_2/dx and on the precise distance from $x = a/b$ over which the approximation is used. Effectively, all this method does is to replace a guess of Y_1 and Y_2 with a guess of dY_1/dx and dY_2/dx at $x = a/b$.

The second method involves a change of variables such that the assumed singularity in dY_1/dx and dY_2/dx at $x = a/b$ is removed. The method was motivated by the work of Rogers (1988) who applied a similar method to obtain an approximate solution for the stator in a rotor-stator disc system. The variables Y_1 and Y_2 are re-written in the following forms:

$$Y_1 = \epsilon^{\xi_1} F_1(\epsilon), \quad Y_2 = \epsilon^{\xi_2} F_2(\epsilon) \ , \tag{4.5.1}$$

where $0 < \xi_1 < 1$, $0 < \xi_2 < 1$ and $\epsilon = x - a/b$.

As $x \to a/b$, we assume that F_1 and F_2 have the following asymptotic expansions

$$F_1(\epsilon) = a_0 + a_1\epsilon + a_2\epsilon^2 + \ldots \ , \tag{4.5.2}$$

$$F_2(\epsilon) = b_0 + b_1\epsilon + b_2\epsilon^2 + \ldots \ , \tag{4.5.3}$$

where $a_0, a_1, \ldots$ and $b_0, b_1, \ldots$ are constants.

Equations (4.5.1) ensure that Y_1 and Y_2 are zero at $x = a/b$ and that dY_1/dx and dY_2/dx are infinite at $x = a/b$. In the source region, $\bar{V}(x)$ takes the form of equation (4.2.12) which may be written, as $x \to a/b$, as

$$\bar{V} = \varphi \left[1 - 2\epsilon \frac{a}{b} + \ldots\right] \ . \tag{4.5.4}$$

If equations (4.5.1) are substituted into equations (4.2.4) and (4.2.5) two ordinary differential equations for F_1 and F_2 are obtained. The values of ξ_1 and ξ_2 may then be obtained by comparing the lowest powers of ε in the equations. This comparison ensures that all the terms in the ordinary differential equations for F_1 and F_2 are finite at $x = a/b$ (ε=0). It is found that for the case (i) equations (i.e. the equations formed when the tanλ terms are omitted in equations (4.2.4) and (4.2.5)), if $\xi_1 = 9/10$ and $\xi_2 = 2/5$ then ε in the two ordinary differential equations occured in integer powers (or the terms could be expanded such that ε occurred in integer powers). For the case (ii) equations however, no values of ξ_1 and ξ_2 could be found which left only integer powers of ε in the ordinary differential equations. The assumed asymptotic expansions (i.e. equations (4.5.2) and (4.5.3)) could not therefore be correct for the case (ii) solutions.

Putting $\xi_1 = 9/10$ and $\xi_2 = 2/5$ and substituting equations (4.5.1) into the case (i) boundary layer equations gives

$$10I_{ff}\varepsilon(\varepsilon+a/b)F_1F_2\frac{dF_1}{dx} - 5I_{ff}\varepsilon(\varepsilon+a/b)F_1^2\frac{dF_2}{dx} =$$

$$5I_{ff}\varepsilon F_1^2F_2 - 7I_{ff}(\varepsilon+a/b)F_1^2F_2 - 5(\varepsilon+a/b)^4F_1^3[2I_{g\varphi}(\varphi-1) - I_{gg}(1-\varphi)^2]$$

$$- 0.1125(\varepsilon+a/b)^{5/4}F_1[(\varepsilon+a/b)^4F_2^2(1-\varphi)^2 + \varepsilon F_1^2]^{3/8}, \qquad (4.5.5)$$

and

$$10I_{fg}\varepsilon(\varepsilon+a/b)(1-\varphi)F_1F_2\frac{dF_1}{dx} = -F_1^2F_2I_{fg}[9(\varepsilon+a/b)(1-\varphi)+20\varepsilon]$$

$$+ 0.225(\varepsilon+a/b)^{5/4}(1-\varphi)F_1[(\varepsilon+a/b)^4F_2^2(1-\varphi)^2 + \varepsilon F_1^2]^{3/8}. \qquad (4.5.6)$$

From equations (4.5.2) and (4.5.3),

$$\lim_{\varepsilon\to 0} F_1 = a_0 \quad , \qquad \lim_{\varepsilon\to 0} \frac{dF_1}{dx} = a_1 \quad ,$$

$$\lim_{\varepsilon\to 0} F_2 = b_0 \quad , \qquad \lim_{\varepsilon\to 0} \frac{dF_2}{dx} = b_1 \quad . \tag{4.5.7}$$

If equations (4.5.2) and (4.5.3) are substituted into equations (4.5.5) and (4.5.6), then the coefficients of powers of ε may be equated to find the values of a_0, a_1, b_0 and b_1. If coefficients of ε^0 are equated in equations (4.5.5) and (4.5.6) the following relationships are obtained:

$$a_0 = \left\{\frac{0.033338\left[\frac{a}{b}\right]^{17/8}(1-\varphi)^{3/4}[I_{gg}(1-\varphi)^2-2I_{g\varphi}(\varphi-1)]^{1/8}}{I_{fg}(14I_{ff}+9I_{fg})^{1/8}}\right\}^{4/5} , \tag{4.5.8}$$

and

$$b_0 = a_0\left[\frac{14I_{ff}+9I_{fg}}{10\left[\frac{a}{b}\right]^{3}[I_{gg}(1-\varphi)^2-2I_{g\varphi}(\varphi-1)]}\right]^{1/2} . \tag{4.5.9}$$

If coefficients of ε' in equations (4.5.5) and (4.5.6) are equated, the following relationships are obtained:

$$a_1 = \frac{CE-FB}{AE-DB} , \tag{4.5.10}$$

and

$$b_1 = \frac{DC-FA}{BD-AE} , \tag{4.5.11}$$

where

$$A = 171_{ff}\left[\frac{a}{b}\right]a_0b_0 + 0.1125\left[\frac{a}{b}\right]^{11/4}b_0^{3/4}(1-\varphi)^{3/4} ,$$

$$B = 2I_{ff}\left[\frac{a}{b}\right]a_0^2 + 15\left[\frac{a}{b}\right]^4 b_0^2[2I_g\varphi(\varphi-1)-I_{gg}(1-\varphi)^2]$$

$$+ 0.0844\left[\frac{a}{b}\right]^{11/4}(1-\varphi)^{3/4}\frac{a_0}{b_0^{1/4}} ,$$

$$C = -2I_{ff}\left[\frac{a}{b}\right]a_0^2b_0 + 20\left[\frac{a}{b}\right]^3 b_0^3[2I_g\varphi+I_{gg}(1-\varphi)]$$

$$- \frac{0.0422a_0[a_0+\left[\frac{a}{b}\right]^3 b_0^2 4\varphi(2\varphi-1)+4\left[\frac{a}{b}\right]^3 b_0^2(1-\varphi)^2]}{\left[b_0(1-\varphi)\left[\frac{a}{a}\right]\right]^{5/4}} ,$$

$$D = 28I_{fg}\left[\frac{a}{b}\right]a_0b_0 - 0.225\left[\frac{a}{b}\right]^{11/4}b_0^{3/4}(1-\varphi)^{3/4} ,$$

$$E = 9I_{fg}\left[\frac{a}{b}\right]a_0^2 - 0.1688\left[\frac{a}{b}\right]^{11/4}(1-\varphi)^{3/4}\frac{a_0}{b_0^{1/4}} ,$$

$$F = -I_{fg}a_0^2b_0\left[9 + \frac{20}{(1-\varphi)}\right] + \frac{0.0844a_0\left[a_0\left[\frac{a}{b}\right]^3 b_0^2 4(\varphi(2\varphi-1)+(1-\varphi)^2)\right]}{\left[b_0(1-\varphi)\left[\frac{a}{b}\right]\right]^{5/4}} .$$

Given the physical variables for a particular problem, i.e. a/b and φ, the values of F_1, F_2, dF_1/dx and dF_2/dx at $x = a/b$ may be obtained from equations (4.5.8)-(4.5.11). The values given by equations (4.5.10) and (4.5.11) were given to dF_1/dx and dF_2/dx only at the precise point (to machine accuracy) where $x = a/b$.

A comparison was made between $\delta_1 x$ predicted by equations (4.5.5)

and (4.5.6) along with equations (4.5.8)-(4.5.11) and $\delta_1 x$ predicted by equations (4.2.4) and (4.2.5) with Y_1 and Y_2 given initial values of 10^{-10} for various values of the parameters a/b and φ. As expected, the values of $\delta_1 x$ were identical for each case tried, except when a/b was very small, when as shown in Figure 4.8, the present solution gives a smoother curve at the start of the calculation.

This section presents an alternative solution method for the rotor equations in the source region and appears to overcome the indeterminacy in the initial conditions. The method is only applicable to the case (i) equations, but could perhaps be extended to the case (ii) equations if the change of variables in equations (4.5.1) are re-defined or the expansions of F_1 and F_2 in equations (4.5.2) and (4.5.3) are altered. From a practical point of view, there is perhaps little to be gained by adopting the procedure in this section; its main purposes is to check the previously obtained solutions.

4.6 RESULTS

4.6.1 Comparision with Experiment

In this section the moment coefficient predicted by the integral method will be compared with available experimental data. In the source region of the flow, which will exist when there is a throughflow, equations (4.2.4) and (4.2.5) will be solved for the flow on the rotor along with equation (4.2.12) for $\bar{V}$. In the core region, equations (4.2.4) and (4.2.5) will be solved on the rotor and equation (3.7.19) will be solved on the stator; method 1 described in § 4.2.3 will be used to couple these solutions.

The sources of experimental data used in this section may be

divided into those applicable for rotor-stator disc flows only (i.e. the special case of a cone when $\lambda = 90^{\circ}$) and those applicable to rotor-stator cone systems. For rotor-stator disc systems, the data of Daily and Nece (1960), Daily et al (1964) and Yamada and Ito (1975) are used; and for rotor-stator cone systems, to the authors knowledge, the only known experimental data concerning moment coefficient calculations is that of Yamada and Ito (1975) and (1979). In all cases the authors report to measure (or calculate indirectly) the moment coefficient experienced by one side of the rotor only.

Daily and Nece (1960) investigated the flow in a rotor-stator disc system without throughflow in both the laminar and turbulent flow regimes. For the types of flow investigated theoretically by the integral method in this chapter (i.e. two separated, fully turbulent boundary layers), Daily and Nece obtained the following empirical formula from their data

$$Re_\theta^{0.2}\, Cm = 0.051(d/b)^{0.1}, \quad 0.06 < d/b < 0.2 \quad . \qquad (4.6.1)$$

Daily et al (1964) investigated the flow in a rotor stator disc system with throughflow and obtained the following empirical formula from their data

$$Cm = \left[8.75\, \frac{C_q}{Re_\theta^{0.8}} + 1\right] Cm_0, \quad 0 < \frac{C_q}{Re_\theta^{0.8}} < 0.06, \quad 0.0138 < d/b < 0.1241. \qquad (4.6.2)$$

where Cm_0 is the moment coefficient for a zero throughflow case. Yamada and Ito (1975) correlated their data for the moment coefficient in a rotor-stator disc system with no throughflow and for fully turbulent, separated boundary layers obtained the following empirical formula

$$Re_\theta^{0.2}\, Cm = 0.050(d/b)^{1/14}, \quad 0.016 < d/b < 0.24 \ . \qquad (4.6.3)$$

For rotor-stator cone systems with and without throughflow, Yamada and Ito (1975) and (1979) did not give a correlation for the moment coefficient, and so the data used in this section are read from their graphs. The moment coefficient is a difficult quantity to measure experimentally, and a relative error between theory and experiment of less than 5% will be referred to as a very good fit, and a relative error of less than 10% but greater than 5% will be referred to as a reasonable fit.

Figures 4.9(a) and (b) compare the moment coefficient for a rotor-stator disc system with zero throughflow with equations (4.6.1) and (4.6.3). The factor $Re_\phi^{0.2}$ is multiplied by Cm in these graphs, since from equation (4.2.11) this quantity is independent of Reynolds number. (Equations (4.2.4) and (4.2.5) are also independent of Reynolds number when $\lambda = 90^\circ$). The maximum relative error in Figures 4.9(a) and (b) occurs at the top end of the (d/b) range and is 1.4% and 5.9% respectively. Over most of the (d/b) range, the comparison with Daily and Nece and Yamada and Ito is excellent.

Figure 4.9(c) compares the moment coefficient for a rotor-stator disc system with a specified throughflow rate with equation (4.6.2), where Cm_0 is given by the present theoretical work, so that the trends produced by increasing the flow rate may be compared. The factor $Re_\theta^{0.8}$ appears multiplied by Cq, since equation (4.2.6) is then independent of Reynolds number (when $\lambda=90^0$). The graphs are in excellent agreement, for example the largest error is about 5% when $\varphi = 0.99$. Two values of the inlet swirl, φ, are assumed since it is unclear from Daily et al's (1964) paper which is appropriate. In their experiment, there was an axial inlet at the base of the stator,

whereas the present integral method assumes a uniform radial inlet. At higher values of $CqRe_{\phi}^{0.8}$, this difference in inlet conditions may affect the moment coefficient, since some of the inlet air may not influence the rotor which would have the effect of reducing the moment coefficient. Also shown in Figures 4.9(a) and 4.9(c) are graphs of data taken from Chew (1988), which as expected show a very close agreement with the present results.

Figures 4.10-4.12 shows comparisons of the predicted moment coefficient with the data of Yamada and Ito (1975, 1979) for various cone angles and flow parameters. Note that finite difference results are also shown in some of these figures, which will be referred to later in chapter 6. Figures 4.10(a)-(f) show the variation of the moment coefficient with cone angle for zero throughflow cases. The gap width parameter, d/b, decreases from 0.24 in Figure 4.10(a) to 0.008 in Figure 4.10(f). The graphs show that for $d/b > 0.016$ the agreement between the integral method and experiment is excellent for $\lambda > 60^{\circ}$, with a relative error between theory and experiment always less than 5%. For $\lambda < 45^{\circ}$, the agreement is generally poor, the relative error achieving a minimum value of 5% for $\lambda = 45^{\circ}$ and $d/b = 0.08$. When d/b is as small as 0.008, Figure 4.10(f) shows a poor agreement for all values of λ with a minimum relative error of 17%.

Figures 4.11(a)-(c) show the variation of moment coefficient with Reynolds number for three different cone angles (90°, 60° and 30°) for $d/b = 0.08$. Figure 4.11(a) shows a good agreement between the integral method and experiment in the 90° case for $Re > 2 \times 10^5$ with the relative error being less than 8%. Figure 4.11(b) shows excellent agreement between the integral method and experiment in the 60° case for $Re > 10^5$ with the error always being less than 5%. Figure 4.11(c) shows that the agreement between the integral method

and experiment is poor for all values of Reynolds number for a cone angle of 30°, with a relative error being greater than 13% at each point.

Figures 4.12(a)-(e) show the variation of moment coefficient with the throughflow rate parameter, Cq, for cone angles of 45°, 30° and 15°. The agreement between the integral method and experiment is poor but the agreement generally improves as the throughflow rate is increased. For example in Figure 4.12(c) the relative error at Cq = 0 is 12% and at Cq = 8000 it is 5% and in Figure 4.12(e) the relative error at Cq = 0 is 11% and at Cq = 10000 it is 2%.

4.6.2 Discussion

Figures 4.10(a)-(e) show an excellent agreement between the predictions of the integral method and the experimental data for $\lambda > 60°$, but a poor agreement for $\lambda < 45°$. From visual flow studies and examination of data trends, Yamada and Ito (1975) report that when $\lambda > 60°$ any secondary flows present will always be of the large scale (disc-type) such as assumed by the integral method and shown in Figure 3.2. The same visual flow studies and examination of data trends led Yamada and Ito (1975) to report that when $\lambda < 45°$, the secondary flow may consist of both disc-type flow and 'Taylor-type' vortices similar to those which are known to occur under certain conditions in a rotor-stator cylinder system. A complete discussion of this phenomenon will be given in § 6.4, but it may be noted that Yamada and Ito (1975) report the presence of Taylor-type vortices in the flow result in an increase in the moment coefficient. The occurence of secondary flows other than the disc-type flow would explain the poor

agreement between theory and experiment for $\lambda < 45^{\circ}$. Another possible reason for the poor agreement for $\lambda < 45^{\circ}$ is that the assumed velocity profiles, i.e. equations (3.4.16) may not be valid for small cone angles. This possibility will be investigated using the finite difference results in §7.2.4. Figure 4.10(f) shows a poor agreement between theory and experiment for all values of λ. Since the present integral method assumes the rotor and stator boundary layers to be separated by a rotating core, this is consistent with the findings of Yamada and Ito (1975) who found that for a rotor stator disc system the boundary layers on the rotor and stator may be considered turbulent and merged for $d/b = 0.008$ if $Re > 2.75 \times 10^5$.

The poor agreement between theory and experiment shown in Figure 4.11(c) for all Reynolds numbers at $\lambda = 30^{\circ}$ is to be expected considering the above discussion. Figure 4.11(a) shows a good agreement between theory and experiment for $Re > 2 \times 10^5$ and Figure 4.11(b) shows good agreement for $Re > 10^5$. The improved agreement at the lower Reynolds number for the smaller cone angle could be due to the flow becoming turbulent at lower values of Re as the cone angle is reduced. This was the conclusion of Kreith et al (1963) who studied the transition Reynolds numbers for free-rotating cones of various vertex angles. This phenomenon has not been studied in rotor-stator systems but the above conclusion is given further evidence in § 6.4.

Figures 4.12(a)-(e) show that the agreement between theory and experiment generally improves as the throughflow rate is increased. This may be explained by the findings of Yamada and Ito (1979) who found that if for a particular case with zero throughflow, Taylor-type vortices would be expected in the secondary flow, then the application of a throughflow suppresses the formation of the vortices.

The results have indicated that the present integral method is

adequate to predict the flows occuring in rotor-stator cone systems when the cone angle, λ, is greater than or equal to 60°. Figures 4.10(a)-(e) show that the experimental trend of moment coefficient with cone angle is very similar to the integral method trend for $\lambda > 60^{\circ}$; this is to be expected since Yamada and Ito (1975) report the secondary flow to be similar to the assumed disc-type in these cases. For cone angles less than 60°, the experimental trends change and the moment coefficient begins to increase as λ decreases. This trend change is indicative of a change of flow pattern and it is hoped that the finite difference program which will be described in chapter 6 will detect such changes. In theory, the finite difference program has the advantage over the integral method of not being constrained to predicting disc-type secondary flows and it is hoped that its results will help to clarify the types of secondary flows which occur in the flow for small cone angles.

4.7 SUMMARY

In § 4.2 the methods of solution of the integrated boundary layer equations governing the isothermal flow between a rotating and a stationary cone were described. The preferred method of solution is the core region results in a considerable saving in processing time when compared with the solution method of Chew (1989).

In § 4.4 it was shown that the extra terms containing $\tan\lambda$ in the case (ii) equations had no appreciable effect on the solutions to the equations for values of λ where the flows would be expected to be amenable to the integral method. It was therefore concluded that these terms may be omitted from the equations reducing them to the far

simpler case (i) equations.

In § 4.5 the rotor equations were re-formulated so as to avoid the problem of the indeterminacy of the initial conditions. The solutions to the resulting equations were found to be identical to the original solutions confirming that the latter were sufficiently insensitive to their initial conditions.

In § 4.6 the present integral method was shown to give excellent predictions for the moment coefficient compared with the available experimental data provided $\lambda > 60^{\circ}$. A possible reason for the poor agreement for values of λ less than this is thought to be the occurence of Taylor-type vortices in the secondary flow, which will be discussed in more detail in §6.4.

CHAPTER 5

AN INTEGRAL METHOD FOR THE PREDICTION OF HEAT TRANSFER

5.1 INTRODUCTION

The objective of the method described in this chapter is the prediction of the heat transfer rate between either the rotor or the stator and the surrounding fluid in a rotor-stator cone system. For fully turbulent flow in the cavity between a rotating and a stationary cone as shown in Figure 3.2, this quantity may be found from the relation

$$q_0(s) = - \left[k_e(s,n) \frac{\partial T(s,n)}{\partial n} \right]_{n=o} \qquad (5.1.1)$$

where $k_e(s,n)$ is the effective thermal conductivity, $T(s,n)$ is the mean temperature and the co-ordinate system shown in Figure 3.1 is employed.

It is common to express the heat transfer rate in terms of the Nusselt number, Nu, which is a non-dimensional measure of the ratio of heat transferred by conduction to heat transferred by convection. It is defined here as

$$Nu(s) = \frac{r_0(s) q_0(s)}{k \Delta T(s)} \quad , \qquad (5.1.2)$$

where k is the laminar thermal conductivity and $\Delta T(s)$ is a temperature difference. $\Delta T(s)$ is usually defined as the difference between either

the surface temperature and the temperature at the boundary layer edge or the surface temperature and the adiabatic surface temperature.

To calculate the Nusselt number directly using equation (5.1.1), the fluid temperature gradient at the solid boundary is required. It is not possible to predict this gradient using the integral method, and this chapter is concerned with finding an expression which can replace the right hand side of equation (5.1.1) with one which contains quantities which the integral method can predict. This is achieved by using the Reynolds analogy which was first published by Osborne Reynolds in 1874 and concerns the equivalence of the mechanisms of momentum and heat transfer in fluid flows. Previous authors (for example Dorfman (1963)) have used the Reynolds analogy to calculate the heat transfer from a free-rotating disc directly using the analytical solutions shown in Appendix B. This approach has been extended to rotor-stator disc flow systems in which there is a very high throughflow rate (see for example Kapinos (1965) and Owen (1971)). In such flows the source region will fill the entire cavity, so that the re-circulating core region will not exist, thus enabling considerable simplifications of the heat transfer method to be made. The Reynolds analogy approach has also been used by Chew and Rogers (1988) to calculate heat transfer in co-rotating disc systems.

In §5.2 the boundary layer energy equation valid in either the rotor or stator boundary layer of a conical rotor-stator system is derived and integrated across the boundary layer. A review of previous authors' modifications and extensions of the Reynolds analogy is carried out in §5.3 which leads to the derivation of an expression for q_0 in equation (5.1.1). The review attempts to explain the extensions in a rational order and the analysis involved is quite detailed since many of the derivations of are complicated and previous

authors do not clarify many of the assumptions. In an attempt to assist in the reading of this chapter, some of the more tedious, although not trivial derivations are written in appendices. The novelty of the analysis in §5.3 is the derivation of equations which are valid in either the rotor or stator boundary layer of a rotor-stator cone system. In §5.4 a method of incorporating the energy equations into the integral method is described. In implementing the method described in §5.4, difficulties were encountered in obtaining numerical solutions to the stator energy equation. These difficulties were found to be caused by the sensitivity of the solutions to their initial conditions; an insight into the likely reasons for this sensitivity is provided in §5.5. The predictive capability of the heat transfer method is then assessed in §5.6 by comparing predicted Nusselt number calculations with available experimental data and results predicted by the finite difference method which will be described in chapter 6.

5.2 DERIVATION AND INTEGRATION OF THE BOUNDARY LAYER ENERGY EQUATION

For steady, axisymmetric and fully turbulent flow, the Reynolds averaged equation describing conservation of energy may be written in terms of the fixed (s,θ,n) co-ordinate system shown in Figure 3.1 as

$$\frac{1}{r}\frac{\partial}{\partial s}(\rho r u H) + \frac{1}{r}\frac{\partial}{\partial n}(\rho r w H) = \frac{1}{r}\frac{\partial}{\partial s}\left[r k_e \frac{\partial T}{\partial s}\right] + \frac{1}{r}\frac{\partial}{\partial n}\left[r k_e \frac{\partial T}{\partial n}\right]$$

$$+ \frac{1}{r}\frac{\partial}{\partial s}\left[r(u\tau_{ss}+v\tau_{s\theta}+w\tau_{ns})\right] + \frac{1}{r}\frac{\partial}{\partial n}\left[r(u\tau_{sn}+v\tau_{n\theta}+w\tau_{nn})\right] , \qquad (5.2.1)$$

where the fluid is assumed to be a perfect gas and the stagnation enthalpy H is defined as

$$H = C_pT + \tfrac{1}{2}(u^2+v^2+w^2) \ . \qquad (5.2.2)$$

C_p is the specific heat at constant pressure.

By analogy with the assumption of the formation of a momentum boundary layer over a conical surfaced described in §3.3, a thermal boundary layer is also expected to form over such surfaces. The thermal boundary layer is the region near to the rotor or stator surface which is affected by the surface temperature. Within the thermal boundary layer, there will be a very steep temperature gradient normal to the wall and the thermal boundary layer thickness, δ_T, may be defined as the distance from the wall to the point where the temperature is within a certain percentage of the external temperature. Thus within the thermal boundary layer it is assumed that

$$\frac{\partial T}{\partial n} \gg \frac{\partial T}{\partial s} \ . \qquad (5.2.3)$$

The case (i) boundary layer arguments of §3.3 may be applied to equation (5.2.1) and in addition to the scales listed in equations (3.3.3), a scale N_T is introduced for the normal derivatives of temperature such that

$$n = N_T n' \ , \qquad (5.2.4)$$

where n' is dimensionless and N_T represents a distance over which the temperature changes significantly in the normal direction. It is assumed that $N_T \sim \delta_T$. From equation (5.2.2), H may be scaled using C_pT

or v^2 depending on which is the larger; but for generality it is assumed that C_pT is of the same order as v^2.

The relative sizes of the thermal and momentum boundary layer thicknesses, i.e. δ_T and δ, can be estimated from a comparison of the convective terms on the left hand side of equation (5.2.1) with the second conductive term on the right hand side. For these terms to have an equal order of magnitude, the following relationship is required

$$\frac{\delta_T}{\delta} \sim \frac{1}{\sqrt{P_r^*}} \quad , \tag{5.2.5}$$

where P_r^* is a characteristic Prandtl number for the flow defined as

$$P_r^* = \frac{\tilde{\mu}\, C_p}{k} \quad , \tag{5.2.6}$$

where $\tilde{\mu}$ and $\tilde{k}$ have the dimensions and magnitudes of a typical viscosity and thermal conductivity within the boundary layer respectively.The experimental data quoted by Schlichting (1968) may be used to estimate the size of P_r^*. The laminar Prandtl number, P_r, defined as $P_r = \mu C_p/k$ depends only on the properties of the fluid and for air this quantity is fairly independent of temperature. The turbulent Prandtl number, P_{rt}, defined as $P_{rt} = \mu_t C_p/k_t$ is more difficult to measure and will vary with position. According to Schlichting (1968), P_r for air may vary between 0.71 at 0°C to 0.72 at 300°C whereas P_{rt} may typically vary between 0.9 near to a solid wall to 0.5 away from the wall (P_{rt} is often given the approximate value of one). Using the above figures to approximate values for P_r and P_{rt} a direct estimate of P_r^* from equation (5.2.6) is not possible. However,

from the above figures it is reasonable to assume that P_r^* is of order of magnitude unity, and so δ and δ_T will be of the same order of magnitude. As an approximation it will further be assumed that $\delta_T = \delta$.

The energy equation (5.2.1) may now be simplified in a similar way to the momentum equations in §3.3. The Reynolds number, Re^*, is defined as in equation (3.3.10) and if terms of order of magnitude unity are neglected when compared with terms of order of magnitude Re^* in equation (5.2.1), the following boundary layer version of the energy equation is obtained

$$\frac{1}{r}\frac{\partial}{\partial s}(\rho ruH) + \frac{1}{r}\frac{\partial}{\partial n}(\rho rwH) = -\frac{1}{r}\frac{\partial}{\partial n}[r(q-u\tau_{sn}-v\tau_{n\theta})], \qquad (5.2.7)$$

where

$$q \equiv q(s,n) = -k_e(s,n)\frac{\partial T(s,n)}{\partial n} . \qquad (5.2.8)$$

In integrating equation (5.2.7) across the boundary layer, the same u(s,n) velocity profiles are assumed as in chapter 3, i.e. equation (3.4.14) for the rotor and equation (3.7.5) for the stator. The following more general enthalpy profile is assumed for H in the boundary layer on the rotor

$$H(\eta,s) = H_0(s) - [H_0(s)-\bar{H}(s)]h(\eta,s) \qquad (5.2.9)$$

where $h(\eta,s)$ satisfies $h(0,s) = 0$ and $h(1,s) = 1$.

The assumed enthalpy profile for the stator boundary layer is similar to that for the rotor given by equation (5.2.9) except that $h(\eta,s)$ is replaced by $h^s(\eta^s,s)$. When integrating equation (5.2.7) across the boundary layer, the variation of r with n is neglected as

in the case (i) boundary layer assumptions of §3.3. Equation (5.2.7) may be integrated across the boundary layer to obtain the following equation for the rotor

$$\frac{d}{ds}\left[\rho u s\delta \sin\lambda\{H_0 I_f-(H_0-\bar{H})I_{fh}\}\right] - \bar{H}\frac{d}{ds}\left[\rho u\delta s I_f \sin\lambda\right]$$

$$= s(\sin\lambda)(q_0-v_0\tau_{\theta,o}) \quad , \qquad (5.2.10)$$

where

$$I_{fh}(s) = \int_0^1 f(\eta)h(\eta,s)d\eta \quad . \qquad (5.2.11)$$

An equation similar to equation (5.2.10) may also be obtained for the stator. The following section is concerned with estimating $q_0(s)$ and $q_0^s(s)$ so that equation (5.2.10) (together with the corresponding equation for the stator) may be incorporated into the integral method described in chapters 3 and 4.

5.3 REVIEW OF THE REYNOLDS ANALOGY APPROACH

5.3.1 The Basic Reynolds Analogy

In 1874, Reynolds published a paper in which he suggested that for turbulent flows, momentum and heat in a fluid are transferred in a similar way. The important results he obtained from this suggestion are summarised by von Karman (1939) and are given in this sub-section for completeness.

Consider a steady, turbulent flow relative to a rectangular (x,y) co-ordinate system in which the Reynolds averaged flow is one dimensional and parallel to the x-axis and the mean velocity, u is a

function of y only. A plane wall parallel to the x-axis is situated at y = 0. The shear stress acting on an arbitrary plane perpendicular to the y axis may be expressed as a sum of the laminar stress and the Reynolds stress. If the Reynolds stress is expressed in terms of a turbulent viscosity, the following expression is obtained

$$\tau(y) = (\mu+\mu_t(y)) \frac{du(y)}{dy} \quad , \tag{5.3.1}$$

where μ and $\mu_t(y)$ are the laminar and turbulent viscosities respectively. If the temperature, T, of the fluid is also a function of y only, then the heat flux across the same plane as above may be expressed as the sum of two terms in a similar form to equation (5.3.1). The first term of this heat flux expression consists of the contribution from molecular heat conduction and the second part consists of turbulent heat transfer due to the fluctuations of velocity and temperature. Hence the total heat transfer rate is given by

$$q(y) = -(k + \rho C_p \varepsilon_t(y)) \frac{dT(y)}{dy} \quad , \tag{5.3.2}$$

where k is the molecular thermal conductivity and $\varepsilon_t(y)$ is the turbulent diffusivity of heat. Defining the laminar kinematic viscosity as $\nu = \mu/\rho$, the turbulent kinematic viscosity as $\nu_t(y) = \mu_t(y)/\rho$, and the molecular thermal diffusivity as $\varepsilon = k/\rho C_p$, equations (5.3.1) and (5.3.2) may be written as

$$\frac{\tau(y)}{\rho} = (\nu+\nu_t(y)) \frac{du(y)}{dy} \quad , \tag{5.3.3}$$

and

$$\frac{q(y)}{\rho C_p} = -(\epsilon+\epsilon_t(y))\,\frac{dT(y)}{dy} \quad . \tag{5.3.4}$$

The anology suggested by Reynolds is that the turbulent diffusivities in equations (5.3.3) and (5.3.4) are equal, i.e. $\nu_t(y) = \epsilon_t(y)$. This statement is equivalent to stating that the turbulent Prandtl number, ν_t/ϵ_t is unity. Reynolds went further to say that if the laminar Prandtl number, ν/ϵ is unity, then for incompressible flow equations (5.3.3) and (5.3.4) may be integrated from the wall to an arbitrary point giving

$$u(y) - u_0 = \frac{1}{\rho}\int_0^y \frac{\tau(y')dy'}{(\nu+\nu_t(y'))} \quad , \tag{5.3.5}$$

and

$$T(y) - T_0 = -\frac{1}{\rho C_p}\int_0^y \frac{q(y')dy'}{(\nu+\nu_t(y'))} \quad . \tag{5.3.6}$$

If $\tau(y)/q(y)$ is independent of y, i.e if $\tau(y) = \tau_0 f(y)$ and $q(y) = q_0 f(y)$, then it follows from equations (5.3.5) and (5.3.6) that

$$q_0 = -C_p\tau_0\,\frac{(T-T_0)}{(u-u_0)} \quad , \tag{5.3.7}$$

which is the original result obtained by Reynolds.

It should be emphasised that in order to obtain equation (5.3.7) it has been assumed that:

(i) $\tau(y)$ and $q(y)$ vary with y according to the same law, which can only be an approximation;

(ii) the laminar Prandtl number is unity: $Pr = \nu/\varepsilon = 1$;

(iii) the turbulent Prandtl number is unity: $Pr_t = \nu_t/\varepsilon_t = 1$.

5.3.2 The Reynolds Analogy applied to a Rotor-Stator Cone System

Dorfman (1963) placed the Reynolds analogy described in the preceeding sub-section on a firmer mathematical basis for the case of a free-rotating disc. He showed that if friction and compressive heating effects are neglected then a strong similarity exists between the resulting boundary layer energy equation and the tangential momentum equation. Dorfman's analysis has been extended to include the effects of friction and compressive work by Owen (1971), who considered rotating disc flows and by Chew (1985c) who considered flows over axisymmetric surfaces of small curvature.

The work of the above authors is extended here to demonstrate the similarity between the boundary layer energy and tangential momentum equations in the rotor and stator boundary layers in a rotor-stator cone system. It will also be shown here that the similarity exists in the inviscid rotating core between the rotor and stator boundary layers in the core region (see Figure 3.2) so that an analogy (which is not strictly the Reynolds analogy but will be referred to as such here) may be applied to the entire cavity between a rotating and a stationary cone.

Assuming steady, axisymmetric flow, the boundary layer energy equation (5.2.7) may be written (see appendix C) as

$$\rho \left[u \frac{\partial H}{\partial s} + w \frac{\partial H}{\partial n} \right] = \frac{\partial}{\partial n} \left[\frac{k_e}{c_p} \frac{\partial H}{\partial n} \right] , \qquad (5.3.8)$$

where it has been assumed that the effective Prandtl number (defined as $Pr_e = \mu_e C_p/k_e$) is unity. If the effects of friction and compressive work in the boundary layer energy equation are neglected, then equation (5.2.4) may be written (see appendix C) as

$$\rho \left[u \frac{\partial T}{\partial s} + w \frac{\partial T}{\partial n}\right] = \frac{\partial}{\partial n} \left[\frac{k_e}{C_p} \frac{\partial T}{\partial n}\right] . \qquad (5.3.9)$$

The boundary layer tangential momentum equation (3.3.19) may be written as

$$\rho \left[u \frac{\partial v}{\partial s} + w \frac{\partial v}{\partial n} + \frac{uv}{r} \sin\lambda\right] = \frac{\partial}{\partial n} \left[\mu_e \frac{\partial v}{\partial n}\right] . \qquad (5.3.10)$$

In the rotating core between the rotor and stator boundary layers it is assumed that viscous effects are negligible (see §3.3), so that the right hand sides of equations (5.3.8)-(5.3.10) may be set to zero.

If the following non-dimensional variables are introduced:

$$\Phi_v = \frac{crv}{\Omega b^2} , \quad \Phi_T = \frac{T-T_{ref}}{T_{ref}} , \quad \Phi_H = \frac{H-H_{ref}}{H_{ref}} , \qquad (5.3.11)$$

where c is an arbitrary constant, T_{ref} is a constant reference temperature and H_{ref} is a constant reference enthalpy ($=C_pT_{ref}$), then for an effective Prandtl number of unity, equations (5.3.8)-(5.3.10) may be represented by the common equation

$$\rho \left[u \frac{\partial \Theta}{\partial s} + w \frac{\partial \Theta}{\partial n}\right] = \frac{\partial}{\partial n} \left[\mu_e \frac{\partial \Theta}{\partial n}\right] , \qquad (5.3.12)$$

where Θ represents either Φ_v, Φ_T or Φ_H. In the inviscid core, the

boundary layer energy and tangential momentum equations may similarly be represented by the common equation

$$\rho \left[u \frac{\partial \theta}{\partial s} + w \frac{\partial \theta}{\partial n} \right] = 0 \ . \qquad (5.3.13)$$

In both the boundary layers and the inviscid rotating core, the equations for Φ_V, Φ_T and Φ_H are thus identical and if the boundary conditions are the same then the solutions for Φ_V, Φ_T and Φ_H will be identical. If friction and compressive work are neglected then identical boundary conditions may be obtained by equating Φ_V and Φ_T. This requires that the rotor and stator surface temperatures satisfy

$$\text{rotor:} \quad T_0 = T_{ref} \left[1 + c \left[\frac{r}{b} \right]^2 \right] \ , \qquad (5.3.14)$$

$$\text{stator:} \quad T_0^s = T_{ref} \ . \qquad (5.3.15)$$

At the edge of either the rotor or stator boundary layers, assuming $\bar{v}(s) = \bar{v}^s(s)$, the boundary conditions will be identical if the temperature satisfies

$$\bar{T} = T_{ref} \left[1 + \frac{cr\bar{v}}{\Omega b^2} \right] \ . \qquad (5.3.16)$$

If the effects of friction and compressive work are included, then identical boundary conditions may be obtained by equating Φ_V and Φ_H. This requires that the enthalpy satisfies

$$H_0 = H_{ref} \left[1 + c \left[\frac{r}{b} \right]^2 \right] \ , \qquad (5.3.17)$$

$$H_0^s = H_{ref} \ , \tag{5.3.18}$$

$$\bar{H} = H_{ref} \left[1 + \frac{cr\bar{v}}{\Omega b^2}\right] \ . \tag{5.3.19}$$

If the Reynolds analogy is applied in the rotor and stator boundary layers, then the boundary layer edge conditions (equations (5.3.16) or (5.3.19)) need to be satisfied. It may be noted that if the Reynolds analogy is applied throughout the entire cavity between the rotor and stator, then these boundary conditions need not be satisfied. However, to apply the Reynolds analogy throughout the entire cavity equation (5.3.12) or equation (5.3.13) will need to be valid in the region adjacent to the outer shroud and at the inlet. If it is assumed that a boundary layer forms over the outer shroud, then an equation similar to (5.3.12) will be valid in this region and the required boundary conditions on the surface of the shroud will be similar to those for the rotor or stator depending on whether the shroud is rotating or stationary. In the source region, the flow external to the rotor boundary layer is assumed to be inviscid (see §3.5), so that the inviscid equations (5.3.13) will describe the flow. At the inlet, the tangential velocity $\bar{v}$ is prescribed, so that the required boundary conditions for T and H may be obtained from equation (5.3.16) or equation (5.3.19).

Clearly, the application of the Reynolds analogy throughout the entire cavity or just in the rotor and stator boundary layers requires very restrictive temperature or enthalpy boundary conditions, and this illustrates one obvious weakness in trying to use the Reynolds analogy in more general conditions. Using the equality of Φ_v and Φ_T or Φ_H the surface heat flux on either the rotor or stator may be calculated from equations (5.3.11). If friction and compressive work are neglected

the heat transfer rates will be

$$\text{rotor:}\quad q_0 = -\frac{C_p \tau_{\theta,o}}{(v_0-\bar{v})}(T_0-\bar{T}) \ , \tag{5.3.20}$$

$$\text{stator:}\quad q_0^s = \frac{C_p \tau^s_{\theta,o}}{\bar{v}^s}(T_0{}^s-\bar{T}^s) \ . \tag{5.3.21}$$

If the effects of friction and compressive work are included, the heat transfer rates will be

$$\text{rotor:}\quad q_0 = -\frac{C_p \tau_{\theta,o}}{(v_0-\bar{v})}\left[(T_0-\bar{T}) - \frac{\bar{U}^2}{2C_p}\right] \ , \tag{5.3.22}$$

$$\text{stator:}\quad q_0{}^s = C_p \frac{\tau^s_{\theta,o}}{\bar{v}^s}\left[(T_0{}^s-\bar{T}^s) - \frac{(\bar{U}^s)^2}{2C_p}\right] \ , \tag{5.3.23}$$

where

$$\bar{U}^2 = \bar{u}^2 + (\bar{v}-v_0)^2 + \bar{w}^2 \ . \tag{4.3.24}$$

In this sub-section it has been shown that the surface heat fluxes on both the rotor and stator may be calculated from equations (5.3.20)-(5.3.23) provided the following conditions are satisfied:

(i) The boundary layer assumptions leading to the case (i) equations of §3.3 are valid.

(ii) The rotor surface temperature varies quadratically with radius (see equations (5.3.14) and (5.3.17)) and the stator surface temperature is constant (see equations (5.3.15) and (5.3.18)).

(iii) If the Reynolds analogy is applied across the boundary layers

only, then the boundary layer edge temperature distribution (equation (5.3.16) or (5.3.19)) must also be satisfied.

(iv) The effective Prandtl number is unity.

In the next three sub-sections, the effects of relaxing conditions (ii) and (iv) on the Reynolds analogy will be discussed. This involves extending previous authors' work so that it applies to either the rotor or stator boundary layer in rotor-stator cone systems. The effect of relaxing condition (iii), is not considered here and so the resulting expression for the surface heat flux which will be given in equation (5.3.54) can only be an approximation when used in rotor-stator systems.

5.3.3 Extension to include a Non-unity Laminar Prandtl Number

In this section a factor is incorporated into the surface heat flux expressions to account for a non-unity laminar Prandtl number, although the turbulent Prandtl number is still assumed to be unity in this sub-section. The analysis follows that of Dorfman (1963) who extended his unity Prandtl number work described in §5.3.2. Dorfman's analysis is based on the boundary layer flow over a free rotating disc when the effects of friction and compressive work on heat transfer are neglected. His work is extended here to boundary layer flows over both a rotating and a stationay cone with an arbitrary tangential velocity at the boundary layer edge. The analysis is explained in a fairly detailed manner, as Dorfman omitted many of his assumptions which consequently made some of his work confusing.

The approach used here is to find a relationship between the tangential velocity profile and the temperature profile so that the surface heat flux may be determined in terms of the surface shear stress. Following Dorfman, a dimensionless length, ζ, velocity, v^*, and temperature, T^* are defined for the (s,θ,n) co-ordinate system shown in Figure 3.1 by

$$\zeta = \frac{nv^*}{\nu} , \quad v^* = \sqrt{\frac{|\tau_{\theta,o}|}{\rho}} , \quad T^* = \frac{q_n}{\rho C_p v^*} . \qquad (5.3.25)$$

The following assumptions were made by Dorfman and are also made here for both the rotor and stator cone boundary layers:

(i) Within the rotor boundary layer, the quantity $(v_0-v)/v^*$ is independent of s and is thus only a function of the dimensionless distance, ζ, i.e

$$v_0 - v = v^*F(\zeta) . \qquad (5.3.26)$$

(Similarly within the stator boundary layer, the tangential velocity is of the form $v^s = (v^*)^sF(\zeta)$).

(ii) The turbulent boundary layer may be divided into the usual three layers (see for example Schlichting (1968)) namely

viscous sub-layer: $0 < \zeta < 5$ where $F(\zeta) = \zeta$ (5.3.27)

transition layer: $5 < \zeta < 30$ where $F(\zeta) = 5\left[\ell n\left[\frac{\zeta}{5}\right] + 1\right]$

(5.3.28)

fully turbulent layer : $\zeta > 30$, where molecular transport processes are negligible compared with turbulent transport processes. For the present purposes, an explicit formula for $F(\zeta)$ in the fully turbulent layer is not required.

A necessary condition for equations (5.3.27) and (5.3.28) to hold is that the shear stress, τ_θ is constant within the viscous sub-layer and transition layer (see for example Laundau and Lifshitz (1987)). It is also assumed that the heat flux, q, is constant within these layers (again see Laundau and Lifshitz (1987)).

By analogy with the shear stress and heat flux equations (5.3.3) and (5.3.4) and assuming a turbulent Prandtl number of unity the shear stress and heat flux within the rotor boundary layer may be written as

$$\frac{\tau_\theta}{\rho} = (\nu+\nu_t)\,\frac{\partial v}{\partial n} \qquad (5.3.29)$$

and

$$\frac{q}{\rho C_p} = -(\varepsilon+\nu_t)\,\frac{\partial T}{\partial n}\ . \qquad (5.3.30)$$

From equations (5.3.25), (5.3.29) and (5.3.30) the following equations valid in the viscous sub-layer and transition layer may be obtained

$$v^{*2} = (\nu+\nu_t)\left|\frac{\partial v}{\partial n}\right|\ , \quad v^*T^* = -(\varepsilon+\nu_t)\,\frac{\partial T}{\partial n}\ . \qquad (5.3.31)$$

If equation (5.3.26) is differentiated with respect to 'n' and the resulting expression for $\partial v/\partial n$ is substituted into equation (5.3.29) the following equation is obtained:

$$\nu_t = \nu \left[\frac{1}{F'(\zeta)} - 1\right] , \qquad (5.3.32)$$

where the prime denotes differentiation with respect to ζ and the density is assumed to be constant. If equation (5.3.32) is used to substitute for ν_t into the second of equations (5.3.31) the following equation valid in the viscous sub-layer and transition layer is obtained:

$$\frac{\partial T}{\partial n} = - \frac{q_0}{\rho C_p \nu \left[\frac{1}{P_r} + \frac{1}{F'(\zeta)} - 1\right]} . \qquad (5.3.33)$$

Equation (5.3.33) may be integrated across the boundary layer from the cone surface to a general point within the viscous sub-layer or transition region of the boundary layer to obtain

$$T_0 - T = T^* G(\zeta) , \qquad (5.3.34)$$

where

$$\frac{1}{G'(\zeta)} = \frac{1}{P_r} + \frac{1}{F'(\zeta)} - 1 . \qquad (5.3.35)$$

By analogy with the velocity equation (5.3.26), Dorfman (1963) assumes that equation (5.3.34) is valid throughout the boundary layer.

Applying the three layer scheme of assumption (ii), equation (5.3.35) may be used to find the function $G(\zeta)$ in the three regions of the boundary layer (see appendix D). In particular in the outer fully turbulent region of the boundary layer, the following relationships are obtained

$$F(\zeta) = G(\zeta) - \Sigma(P_r) , \qquad (5.3.36)$$

where

$$\Sigma(P_r) = 5(P_r-1) + 5\ell n\left[\frac{5P_r+1}{6}\right] . \qquad (5.3.37)$$

If the expressions for $F(\zeta)$ and $G(\zeta)$ from equations (5.3.26) and (5.3.34) are substituted into equation (5.3.36) the resulting equation may be evaluated at the boundary layer edge to obtain

$$q_0 = -C_p\, \tau_{\theta,o}\, \frac{(T_0-\bar{T})}{(v_0-\bar{v})}\left[1 + \frac{\Sigma(P_r)}{|v_0-\bar{v}|}\sqrt{\frac{|\tau_{\theta,o}|}{\rho}}\right]^{-1} . \qquad (5.3.38)$$

Equation (5.3.38) gives an expression for the surface heat flux valid for the rotor, and an equivalent expression valid for the stator may be obtained by setting $v_0 = 0$.

Comparison of equation (5.3.38) with equation (5.3.20) shows that if friction and compressive work are neglected, the effect of a non-unity laminar Prandtl number is to multiply the heat flux when Pr = 1 by the factor in square brackets.

5.3.4 Extension to include Non-unity Laminar and Turbulent Prandtl numbers

Equation (5.3.38) was derived by neglecting the effects of frictional heating and compressive work on heat transfer and assuming the turbulent Prandtl number to be unity. In this section an empirical factor will be introduced to account for the effects of both a non-unity laminar and turbulent Prandtl number when frictional heating and compressive work effects are included.

A comparison of equations (5.3.20) and (5.3.21) with equations (5.3.22) and (5.3.23) shows that the effects of frictional heating and

compressive work may be accounted for by including the term $\bar{U}^2/2C_p$ or $(\bar{U}^s)^2/2C_p$ in the surface heat flux expressions derived when the effects were neglected. It will now be shown that these extra terms are related to adiabatic temperature differences, thus allowing the introduction of an experimentally determined correction factor to allow for non-unity laminar and turbulent Prandtl numbers. By setting q_0 and q_0^s equal to zero in equations (5.3.22) and (5.3.23), the following expressions for the adiabatic temperature difference across the boundary layers may be obtained:

$$\text{rotor:} \qquad T_{o,ad} - \bar{T}_{ad} = \frac{\bar{U}^2}{2C_p} , \tag{5.3.39}$$

$$\text{stator:} \qquad T^s_{o,ad} - \bar{T}^s_{ad} = \frac{(\bar{U}^2)^2}{2C_p} , \tag{5.3.40}$$

where the subscript 'ad' refers to adiabatic values. In turbulent flow, experimental results (Schlichting (1968)) have led to the inclusion of a 'recovery factor', R_c, into equations (5.3.39) and (5.3.40) to account for non-unity laminar and turbulent Prandtl numbers. The recovery factor appears on the right hand sides of equations (5.3.39) and (5.3.40), so for example, to allow for non-unity laminar and turbulent Prandtl numbers, the adiabatic temperature difference for the rotor becomes

$$T_{o,ad} - \bar{T}_{ad} = \frac{R_c\bar{U}^2}{2C_p} . \tag{5.3.41}$$

The experimental results reproduced in Schlichting (1968), show that in fully turbulent flow R_c may vary betweeen 0.875 and 0.890 and since

for dry air, the laminar Prandtl number may vary between 0.71 at 0°C and 0.72 at 300°C Schlichting approximates R_c by

$$R_c = P_r^{1/3} \ . \qquad (5.3.42)$$

To account for a non-unity laminar and turbulent Prandtl number, when the effects of frictional heating and compressive work on heat transfer are included, equation (5.3.41) is used in place of equation (5.3.39) and this may be incorporated into equation (5.3.38) as follows

$$q_0 = - \frac{C_p \tau_{\theta,o}}{(v_0 - \bar{v})} \left[(T_0 - \bar{T}) - \frac{R_c \bar{U}^2}{2C_p} \right] \left[1 + \frac{\Sigma(Pr)}{|v_0 - \bar{v}|} \sqrt{\frac{|\tau_{\theta,o}|}{\rho}} \right]^{-1} \ . \qquad (5.3.43)$$

A similar expression may be obtained for the stator. The same recovery factor was used by Chew and Rogers (1988) for heat transfer calculations in co-rotating disc systems, but the effects of using it for the present applications will be discussed in §5.6.1.

5.3.5 Extension to include an arbitrary Temperature Distribution

The heat flux expressions (5.3.20)-(5.3.23) were derived under the assumptions that the rotor temperature distribution varies quadratically with radius and the stator temperature is constant. In this section an attempt is made at finding approximate heat flux expressions for arbitrary surface temperature distributions and non-unity laminar and turbulent Prandtl numbers. The analysis follows the method of Chew and Rogers (1988) for the heat transfer in co-rotating disc systems. Their method was a generalisation of the

work by Dorfman (1963) who examined the heat transfer from a free-rotating disc when the effects of friction and compressive work were neglected. The following section represents an extension of the work of Chew and Rogers (1988) to either the rotor or stator boundary layers in a rotor-stator cone system.

It is assumed that for an arbitrary surface temperature and arbitrary laminar and turbulent Prandtl numbers, the surface heat flux on either the rotor or stator may be expressed in the form

$$\frac{q_0}{C_p} = -\chi \left[T_0 - \bar{T} - R_c \frac{(v_0-\bar{v})^2}{2C_p}\right] \frac{\tau_{\theta,o}}{(v_0-\bar{v})} \quad , \qquad (5.3.44)$$

where it has been assumed that $(v_0-\bar{v})^2 \gg \bar{w}^2$ and $(v_0-\bar{v})^2 \gg \bar{u}^2$. In equation (5.3.44) it is assumed that χ depends on the laminar Prandtl number and the cone temperature distribution. Defining the Nusselt number as

$$Nu = \frac{r_0 q_0}{k[T_0-\bar{T}-R_c(v_0-\bar{v})^2/2C_p]} \quad , \qquad (5.3.45)$$

it follows that

$$Nu = -\frac{P_r \chi r_0 \tau_{\theta,o}}{\mu(v_0-\bar{v})} \quad . \qquad (5.3.46)$$

Dorfman assumed the following relationship for the Nusselt number (the basis for the relationship is not clear, although it may be an empirical relationship based on experimental results for free-rotating discs)

$$Nu = F(P_r)\, R_{e\ell}\, R_T^{\beta} \quad , \qquad (5.3.47)$$

where $F(P_r)$ is a universal function of the laminar Prandtl number, β is a universal constant and $R_{e\ell}$ and R_T are a local Reynolds number and thermal Reynolds number respectively. In terms of the notation of this thesis, $R_{e\ell}$ and R_T are defined by

$$R_{e\ell} = \rho[\tilde{u}^2+(v_0-\bar{v})^2]^{\frac{1}{2}} \frac{r_\Omega}{\mu} , \qquad (5.3.48)$$

and

$$R_T = \frac{\rho}{\mu} [\tilde{u}^2+(v_0-\bar{v})^2]^{\frac{1}{2}} \int_0^\delta \frac{u}{\bar{u}} \left|\frac{(H-\bar{H})}{(H_0-\bar{H})}\right| dn . \qquad (5.3.49)$$

Using the enthalpy expression (5.2.9) and the velocity profile (3.4.14), equation (5.3.49) becomes

$$R_T = \frac{\rho}{\mu} [\tilde{u}^2+(v_0-\bar{v})^2]^{\frac{1}{2}} \delta|I_f-I_{fh}| . \qquad (5.3.50)$$

Note that in equation (5.2.9), $h(\zeta,s)$ is a function of s, so that I_{fh} in equation (5.3.50) is a function of s. In the special conditions when the temperature boundary conditions satisfy the Reynolds analogy condition, then as illustrated by equation (E3) of Appendix E, I_{fh} is a constant $(=I_f-I_{fg})$. Since $F(P_r)$ and β are assumed to be universal, they may be found by considering the special cases of §5.3.2 and §5.3.3. It may be shown (see appendix E) that

$$\beta = -1/4 \quad \text{and} \quad F(P_r) = 0.0225 Pr \xi^{5/4} I_{fg}^{1/4} , \qquad (5.3.51)$$

where

$$\xi = \left[1 + \frac{\Sigma(P_r)}{|v_0-\bar{v}|} \sqrt{\frac{|\tau_{\theta,n}|}{\rho}}\right]^{-1} . \qquad (5.3.52)$$

The unknown χ may now be found from equations (5.3.46) and (5.3.47) as

$$\chi = \left[\frac{\xi^5 I_{fg}}{|I_f - I_{fh}|}\right]^{\frac{1}{4}} . \qquad (5.3.53)$$

The final assumed form for the surface heat flux on the rotor or stator may then be obtained from equation (5.3.44) as

$$\frac{q_0}{C_p} = - \left[\frac{\xi^5 I_{fg}}{|I_f - I_{fh}|}\right]^{\frac{1}{4}} \left[T_0 - \bar{T} - Rc \frac{(v_0 - \bar{v})^2}{2C_p}\right] \frac{\tau_{\theta,o}}{(v_0 - \bar{v})} . \qquad (5.3.54)$$

The key assumptions which led to the derivation of equation (5.3.54) are that the effects of an arbitrary cone surface temperature distribution may be accounted for by the multiplicative factor χ present in equation (5.3.44) and that the Nusselt number may be expressed in the form (5.3.47). The first of these assumptions leads to a form of equation similar to equation (5.3.38) which was obtained at the end of §5.3.2, and which indicated that the effect of a non-unity laminar Prandtl number was simply to multiply the heat flux expression by the factor shown in equation (5.3.38). It is not clear how equation (5.3.47) is justified and if it is based on experimental results for free-rotating systems, then its application to more general flow regimes will be questionable. However, in §5.6.1 an assessment will be made of the relative merits of the use of equation (5.3.54) over eqution (5.3.43) in heat transfer predictions.

5.4 A METHOD FOR PREDICTING THE HEAT TRANSFER IN A ROTOR-STATOR CONE-SYSTEM

5.4.1 Formulation of the Equations

The surface heat flux equation (5.3.54) may be substituted into the integrated boundary layer energy equation (5.2.10) to obtain an equation valid for the rotor and a similar equation may be obtained for the stator. These equations may then be solved along with the boundary layer momentum equations derived in §3.6, but the inclusion of compressibility inherent in the derivation of equation (5.3.54) is also necessary. The effects of compressibility will be assessed using the finite difference results in §5.6.2, but at present it is assumed that the effects of density variations across the boundary layers is negligible. This assumption follows the recommendations of Chew and Rogers (1988) who concluded that allowing for density variations across the boundary layers in a co-rotating disc system did not significantly affect the Nusselt number calculations. Compressibility is accounted for longitudinally within the boundary layers by use of the perfect gas law:

$$p(s) = \rho(s)\, R_G\, T_m(s) \quad , \tag{5.4.1}$$

where R_G is the gas constant and T_m is the mean temperature across the boundary layer at a particular radial location (i.e. $T_m = (T_0+\bar{T})/2$ and $T_m{}^s = (T_0{}^s+\bar{T}^s)/2$). Differentiating equation (5.4.1) and using equation (3.6.2) the following equation is obtained:

$$\frac{d}{ds}\left[\frac{\rho}{\rho_i}\right] = \frac{\rho}{\rho_i T_m}\left[\frac{\bar{V}^2}{rR_G}\sin\lambda - \frac{dT_m}{ds}\right] \quad , \tag{5.4.2}$$

where ρ_i is a constant inlet or reference density. Re-defining the non-dimensional variables (3.6.14) as

$$u_1 = \frac{u}{\beta r} , \quad \bar{V} = \frac{\bar{v}}{\beta r} , \quad V_0 = \frac{v_0}{\beta r} , \quad \delta_1 = \frac{\rho \delta Re\phi^{1/5} \sin\lambda}{\rho_i r} ,$$

$$Re\phi = \frac{\beta b^2 \rho_i}{\mu \sin\lambda} , \quad x = \frac{r}{b} , \qquad (5.4.3)$$

the rotor momentum equations (3.6.15) and (3.6.16) become

$$\frac{I_{ff}}{x^3} \frac{d}{dx} (u_1^2 \delta_1 x^4) + \delta_1 [2\bar{V}(\bar{V}-V_0) I_g - (\bar{V}-V_0)^2 I_{gg}]$$

$$= - \frac{0.0225}{(x^2\delta_1)^{1/4}} u_1 [u_1^2 + (V_0-\bar{V})^2]^{3/8} \frac{\rho}{\rho_i} , \qquad (5.4.4)$$

and

$$\frac{I_{fg}}{x^4} \frac{d}{dx} [x^5 u_1 \delta_1 (V_0-\bar{V})] + \frac{\delta_1 u_1}{x} I_f \frac{d}{dx} (x^2 \bar{V})$$

$$= \frac{0.0225}{(x^2\delta_1)^{1/4}} (V_0-\bar{V}) [u_1^2 + (V_0-\bar{V})^2]^{3/8} \frac{\rho}{\rho_i} , \qquad (5.4.5)$$

and the stator equations (3.7.17) and (3.7.18) become

$$u_1^s = -0.364 V^s , \qquad (5.4.6)$$

and

$$\frac{d\delta_1^s}{dx} = \frac{\delta_1^s}{x} \left[\frac{2I_f^s - 5I_{fg}^s}{I_{fg}^s}\right] - \frac{d\bar{V}^s}{dx} \frac{\delta_1^s}{\bar{V}^s} \left[\frac{2I_{fg}^s - I_f^s}{I_{fg}^s}\right]$$

$$- \frac{0.0225}{0.364 I_{fg}^s} \frac{[1+(0.364)^2]^{3/8}}{(\bar{V}^s)^{1/4} [x^6 (\delta_1^s)^2]^{1/4}} \frac{\rho^s}{\rho_i} . \qquad (5.4.7)$$

Hence the only effect of longitudinal compressibility on the momentum equations is to multiply the stress terms by the factor ρ/ρ_i.

The boundary layer energy equation for the rotor becomes

$$\frac{d}{dx}\left[u_1\delta_1 x^3(I_f H_0-(H_0-\bar{H})I_{fh})\right] - \bar{H}I_f\frac{d}{dx}(u_1\delta_1 x^3) =$$

$$0.0225\left[\frac{x^{14}}{\delta_1}\right]^{\frac{1}{4}}[u_1^2+(1-\bar{V})^2]^{3/8}\left[\left\{\frac{\xi^5 I_{fg}}{(I_f-I_{fh})}\right\}^{\frac{1}{4}}\right.$$

$$\left.\times \quad \left\{H_0-\bar{H}+((1-\bar{V})-\tfrac{1}{2}(1-\bar{V}^2+Rc(1-\bar{V})^2))(\Omega xb)^2\right\}\right]\frac{\rho}{\rho_i} \quad , \qquad (5.4.8)$$

and the boundary layer energy equation for the stator becomes

$$-0.364\frac{d}{dx}\left[\bar{V}^s\delta_1^s x^5(I_f^s H_0^s-(H_0^s-H^s)I_{fh}^s)\right] + 0.364 I_f\bar{H}^s\frac{d}{dx}(\bar{V}^s\delta_1^s x^3)$$

$$- 0.0236\left[\frac{x^{14}}{\delta_1^s}\right]^{\frac{1}{4}}(\bar{V}^s)^{\frac{3}{4}}\left[\frac{\xi^5 I_{fg}^s}{(I_f^s-I_{fh}^s)}\right]^{\frac{1}{4}}\left[H_0^s-\bar{H}^s+\left[\frac{(\bar{V}^s)^2}{2}(1-Rc)\right](\Omega bx)^2\right]\frac{\rho}{\rho_i} \; .$$

(5.4.9)

The quantity ρ/ρ_i was found by integrating equation (5.4.2). Using the non-dimensional variables (5.4.3), the quantity ρ/ρ_i at a particular location x within either the rotor or stator boundary layer may then be found from

$$\frac{\rho(x)}{\rho_i} = \exp\left\{\int_{a/b}^{x}\frac{1}{T_m}\left[\frac{(\Omega b)^2}{R_G}\bar{V}^2 - \frac{dT_m}{dx'}\right]dx'\right\} . \qquad (5.4.10)$$

5.4.2 The Solution Procedure

The momentum equations (5.4.4)-(5.4.7) and the energy equations (5.4.8) and (5.4.9) are coupled via the density relationship (5.4.10). The solution method described here, however, involves solving the momentum equations and energy equations separately and using an iterative procedure to find the density field. The iterative procedure is as follows:

(i) Assume $\rho(x) = \rho_1$, $\rho^S(x) = \rho_1$.

(ii) Solve the momentum equations (5.4.4)-(5.4.7) in the manner described in chapter 3.

(iii) Use $\delta_1(x)$, $u_1(x)$, $\delta_1{}^S(x)$ and $\bar{V}(x)$ from (ii) to solve the energy equations (4.4.8) and (4.4.9) in the manner described below.

(iv) Use the solutions from (ii) and (iii) to find $\rho(x)/\rho_1$ and $\rho^S(x)/\rho_1$, from equation (5.4.10).

(v) Calculate the moment coefficient, Cm and the average Nusselt number, Nu_{av} (see §5.6), go to (ii) and repeat until Cm and Nu_{av} are unchanging (to a specified tolerance).

In all the examples tested, Cm and Nu_{av} were unchanging (to three significant figures) after four of the above iterations.

To proceed with the solution of the energy equations (5.4.8) and (5.4.9), the following important result which follows from the assumptions about the flow in §3.5 is required. Outside the boundary layers in both the source region and the core region, viscous terms are assumed to be negligible so that the right hand side of the energy equation (5.2.1) will be zero. The resulting equation may be written as

$$(\underline{u}.\nabla)H = 0 \qquad (5.4.11)$$

Physically, equation (5.4.11) means that the enthalpy is constant along streamlines. In the source region, streamlines enter from the inlet, so that the enthalpy at the edge of the boundary layer will take the known inlet value and will remain constant up to the end of the source region. In the core region, assuming the flow structure is as shown in Figure 3.2, streamlines leave the stator boundary layer and enter the rotor boundary layer at constant radial locations. At equal radial positions therefore, the enthalpy at the edge of the boundary layers will be equal, or

$$\bar{H}(x) = \bar{H}^s(x) , \qquad x = r/b. \qquad (5.4.12)$$

To find the heat flux from either the rotor or stator in a given rotor-stator system it is assumed that the inlet temperature and the rotor and stator surface temperatures are known. Thus $H_0(x)$ and $H_0^s(x)$ will be known and from the above argument, $\bar{H}(x)$ will be known in the source region.

The proposed method of solution of the energy equations may be divided into a source region calculation and a core region calculation as follows:

Source Region

There is assumed to be no boundary layer on the stator in this region (see chapter 3). On the rotor $H_0(x)$ will be specified and $\bar{H}(x)$ will be known from the inlet conditions, so that equation (5.4.8) may be solved for the one unknown $I_{fh}(x)$. The starting condition may be obtained from the Reynolds analogy result, i.e. equation (E3) of

Appendix E.

Core Region

In this region, equations (5.4.8) and (5.4.9) will be coupled via equation (5.4.12). Assuming $H_0^s(x)$ is also known, equations (5.4.8) and (5.4.9) then contain the three unknowns $\bar{H}(x)$, $I_{fh}(x)$ and $I_{fh}^s(x)$. To close the problem an additional assumption is therefore required and it is assumed thatthe Reynolds analogy result (equation (E(3) of Appendix E) holds on the stator, so that

$$I_{fh}^s = I_f^s - I_{fg}^s \quad . \tag{5.4.13}$$

Using assumption (5.4.13), equations (5.4.8) and (5.4.9) may be solved simultaneously for $\bar{H}(x)$ and $I_{fh}(x)$. $I_{fh}(x)$ is assumed to be continuous from the source region, which specifies the value for $I_{fh}(x_e)$ at the start of the core region. It would seem reasonable to assume $\bar{H}(x)$ is also continuous from the source region, however using this value of $\bar{H}(x)$ at $x = x_e$ produced unreasonable results, i.e. $\bar{H}(x)$ would become very large or very small as the integration proceeded to $x = 1$. The reason for this was found to be that the solutions to the stator energy equation (5.4.9) were sensitive to their initial conditions; this sensitivity will be investigated in the next section. Instead of assuming $\bar{H}(x)$ is continuous from the source region, $\bar{H}(x_e)$ is allowed to have a discontinuity at $x = x_e$ and an iterative procedure is used to find $\bar{H}(x_e)$ such that when the energy equations have been solved overall energy is conserved in the rotor-stator system. Physically, this discontinuity in $\bar{H}(x_e)$ that results at $x = x_e$ is unrealistic. However, it may be reasonable that $\bar{H}(x)$ will change abruptly at a value of x around $x = x_e$, since at this

point, fluid will flow across from the stator boundary layer to the rotor boundary layer with an enthalpy which will depend on the temperature of the stator. In theory, this fluid will meet with fluid from the inlet at $x = x_e$ and depending on the inlet conditions there may be an abrupt change in enthalpy at this point. In §5.6.2, finite difference results will help to verify whether or not a sudden change in enthalpy does occur.

The requirement of an overall energy balance in the system may be expressed using a rate of energy deficit, $\dot{E}$, defined as

$$\dot{E} = \int_{a/\sin\lambda}^{b/\sin\lambda} 2\pi r_0 q_0 \, ds + \int_{r_e/\sin\lambda}^{b/\sin\lambda} 2\pi r_0 q_0^s \, ds$$

$$+ \int_{a/\sin\lambda}^{r_e/\sin\lambda} 2\pi r_0 q_0^s \, ds + 2\pi b d q_{shroud} + \Omega M$$

$$+ \dot{m}(H_{in} - H_{out}) \, , \qquad (5.4.14)$$

where M is the moment exerted by the fluid on the rotor, defined in equation (4.2.10), $\dot{m}$ is the specified mass throughflow rate, H_{in} is the enthalpy at the inlet, H_{out} is the enthalpy at the outlet and q_{shroud} is the surface heat flux from the outer shroud.

The first two integrals in equation (5.4.14) may be calculated directly using equation (5.3.54). The flow over the outer shroud will be of a boundary layer character and assuming the shroud is stationary and has the same temperature as the stator at $x = 1$, then q_{shroud} may be estimated as having the same value as q_0^s at $x = 1$. The inlet enthalpy, H_{in}, will be specified by the temperature and swirl of the

fluid at the inlet and if the outlet is situated next to the rotor as shown in Figure 3.2, the outlet enthalpy, H_{out}, may be estimated as the mean enthalpy, i.e. $(H_0+\bar{H})/2$ at $x = 1$. The third integral in equation (5.4.14) is not so straightforward to estimate since for $a < r < r_e$, it is assumed in chapter 3 that the flow over the stator is negligible and neither a flow calculation nor a heat transfer calculation is performed. The proposed method of calculating q_0^s for $a < r < r_e$ is by use of the heat transfer coefficient, h_c, in an equation of the form:

$$q_0^s = -h_c(\bar{T}-T_0{}^s) \quad . \tag{5.4.15}$$

The heat transfer coefficient, h_c varies according to the particular situation being examined and is normally calculated empirically from experimental data. According to Rogers and Mayhew (1967), for dry gases h_c may vary between 0.5 kW m^{-2} $^{\circ}K$ and 1000 kW m^{-2} $^{\circ}K$, however the finite difference results used in §5.6.2 will help to provide a better estimate for the particular types of problem considered here. It may be noted that for zero throughflow cases when there is no source region, the difficulty in estimating q_0^s from equation (5.4.15) does not arise.

If overall energy is conserved then $\dot{E}$ in equation (5.4.14) will be zero, but in practice this criterion is taken to be satisfied when $\dot{E}$ is within 1% of the rate of energy flow across the rotor. The method of finding $\bar{H}(x_e)$ such that this criterion is satisfied is the method of bisection, so that two starting guesses for $\bar{H}(x_e)$ are requried, one producing $\dot{E} > 0$ and the other producing $\dot{E} < 0$. Typically, the procedure took about 20-30 iterations to converge.

5.5 A SENSITIVITY ANALYSIS OF THE SOLUTIONS TO THE ENERGY EQUATIONS

In the previous section it was stated that the solutions to the stator energy equation (5.4.9) were found to be very sensitive to their initial conditions, i.e small changes in $\bar{H}(x_e)$ would produce large changes in $\bar{H}(1)$. It was found, however, that the solutions to the rotor equation (5.4.8) were insensitive to their initial conditions. In this section, approximate analytical solutions will be found to equations (5.4.8) and (5.4.9) which will provide an insight into the reasons for the different sensitivities of the solutions to the two energy equations.

Analytical solutions may only be obtained for $\bar{H}$ and $\bar{H}^S$ in equations (5.4.8) and (5.4.9) if analytical solutions for u_1, δ_1, δ_1^S and $\bar{V}$ are substituted into them. Analytical solutions may be obtained for u_1, δ_1 and δ_1^S when $\bar{V}$ is a constant and are described in §3.7 for $\bar{V}$ = 0.42 (the infinite rotor-stator system with zero throughflow) and in appendix B for $\bar{V}$ = 0 (the free rotating disc or cone). These solutions are only valid when the inner radius of the discs or cones is zero (i.e. a = 0), however, the solutions should provide a good approximation to the solutions of the equations when a ≠ 0†, and they should serve the required purpose of illustrating the general behaviour of the energy equations. For the purposes of obtaining simple solutions to equations (5.4.8) and (5.4.9), it is also assumed

† Evidence of this is given by Chew (1985d), where using an integral method he finds that the moment coefficient experienced by a free-rotating disc with a non-zero inner radius is only weakly dependent on a. The approximate relation he obtains for the moment coeeficient experienced by a disc of arbitrary inner radius a, denoted by Cm, and the moment coefficient experienced by a disc with a zero inner radius, denoted by $Cm,_0$, is $Cm/Cm,_0 = 1 - (a/b)^5$.

that the basic Reynolds analogy result of §5.3.2 holds, so that $P_{re} = 1$, $I_{fh} = I_f - I_{fg}$, and $I^s_{fh} = I^s_f - I^s_{fg}$.

Under the above conditions, the energy equations (5.4.8) and (5.4.9) may both be expressed in the form

$$\frac{d\bar{H}}{dx} + \frac{A\bar{H}}{x} = A\,\frac{H_0}{x} + B\,\frac{dH_0}{dx}\ , \qquad (5.5.1)$$

where for the rotor $B = -0.2$ and $A = 2.14$ when $\bar{V} = 0.42$ and $A = 0.403$ when $\bar{V} = 0$. For the stator $B = -0.0909$ and $A = -2.20$ when $\bar{V} = 0.42$. Solutions may now be obtained to equation (5.5.1) for a given $H_0(x)$ distribution and a specified initial condition for $\bar{H}$ at $x = a/b$. The $H_0(x)$ distributions considered here are $H_0 = H_{ref}$ and $H_0(x) = H_{ref}(1+x^C)$, and the specified initial condition is $\bar{H} = H_{ref}(1+D)$ where H_{ref}, C and D are constants. When $H_0 = H_{ref}$, the solution to equation (5.5.1) is

$$\bar{H}(x) = H_{ref}\left[1 + D\left\{\frac{(a/b)}{x}\right\}^A\right] \qquad (5.5.2)$$

and when $H_0 = H_{ref}(1+x^C)$, the solution to equation (5.5.1) is

$$\bar{H}(x) = H_{ref}\left[1 + x^C\,\frac{(A+BC)}{(A+C)} + \left\{\frac{(a/b)}{x}\right\}^A\left\{D - (a/b)^C\,\frac{(A+BC)}{(A+C)}\right\}\right]\ . \qquad (5.5.3)$$

The sensitivity of the solutions for $\bar{H}(x)$ to their initial conditions may be assessed by considering the sensitivity of the $\bar{H}(x)$ distribution given by equation (5.5.2) or (5.5.3) to the value assigned to the constant D. From an inspection of these equations for $a/b \neq 0$ it is clear that in general this sensitivity will depend on the sign of A and that for a negative value of A, the $\bar{H}(x)$

distribution will become more sensitive to the value of D as the ratio a/b decreases. As stated earlier, for the rotor equation A is positive whereas for the stator equation, A is negative, so it is the solutions to the stator equation which will exhibit greater sensitivity to their initial conditions.

As an example to illustrate the difference in sensitivity, consider the solutions for H(x) given by equation (5.5.2) for a/b = 0.1, when D = 0 and when D = 0.01. For an infinite rotor-stator system, when $\bar{V}$ = 0.42, the appropriate values for A are 2.14 for the rotor and -2.20 for the stator. The rotor solution then gives $\bar{H}(1) = H_{ref}$ when D = 0 and $\bar{H}(1) = 1.00007\ H_{ref}$ when D = 0.01, and the stator solution gives $\bar{H}^s(1) = H_{ref}$ when D = 0 and $\bar{H}^s(1) = 2.58\ H_{ref}$ when D = 0.01. the large difference in the stator solutions compared with the negligible difference of the rotor solutions clearly illustrates the different sensitivities.

The difference in sensitivity to initial conditions illustrated by the above example is also found to occur when solving the energy equations numerically for a variety of flow parameters. As already stated, equations (5.5.2) and (5.5.3) are not strictly valid since they are based on analytical solutions to the flow equations which are only valid if a/b = 0. Nevertheless the behaviour of equations (5.5.2) and (5.5.3) provide a plausible explanation for the different numerical behaviours of the solutions to the rotor and stator energy equtions to be understood.

5.6 COMPARISON WITH EXPERIMENT AND FINITE DIFFERENCE RESULTS

This section is divided into two sub-sections; the first involves a comparison of the predicted surface heat flux, using the Reynolds analogy as described in the previous sections, with the available experimental data for free-rotating discs and cones. This comparison enables an assessment to be made of the applicability of the generalised Reynolds analogy to conical systems. Unfortunately, there appears to be no relevant experimental data concerning heat transfer in rotor-stator disc or cone systems, so that in the second sub-section a comparison is made between the predictions of the present theory with the predictions of a finite difference program to be described in the next chapter. In both sub-sections an assessment will be made of the importance of the various extensions of the Reynolds analogy described in §5.3. The conclusions to be made from the two sub-sections will be given in §5.7.

5.6.1 Free-rotating Systems

To the authors knowledge the only relevant experimental Nusselt number data is that of Kreith (1966), who calculated average Nusselt number values from heat transfer data concerning free-rotating discs and cones. To compare the results from the above theory with this data, the source region method of §5.4.2 was used, with the condition that $\bar{V}(x) = 0$. Equation (5.4.8) was solved from $x = a/b$ to $x = 1$ using the solutions from the rotor flow equations, i.e. equations (5.4.4) and (5.4.5). The solutions for $u_1(x)$ and $\delta_1(x)$ were obtained at 100 equally spaced points between $x = a/b$ and $x = 1$ and were

interpolated by cubic splines. The ratio a/b was set to 0.001 and the Nusselt number was defined as

$$Nu(x) = \frac{r_0(x)q_0(x)}{k[T_0(x)-\bar{T}(x)]} \quad . \tag{5.6.1}$$

To compare average Nusselt numbers with those obtained by Kreith, an average Nusselt number was defined as

$$Nu_{av} = 2\int_{a/b}^{1} Nu(x)\, dx \quad . \tag{5.6.2}$$

Kreith did not mention the temperature of the cone surface or the surroundings, but stated that the cone surface temperature was uniform. However, numerical experiments showed that Nu_{av} calculated from equation (5.6.2) was insensitive to the values assigned to the cone temperature and the ambient temperature, i.e. T_0 and $\bar{T}$ respectively. (When $T_0-\bar{T} = 1000^{\circ}K$, $Nu_{av} = 936.6$ and when $T_0-\bar{T} = 11.2^{\circ}K$, $Nu_{av} = 937.9$ for one particular case considered when $a/b = 0.001$). For the present comparisons, $T_0 - \bar{T}$ was set to $100^{\circ}K$. It may be noted that for a free rotating cone, with constant surface temperature, $T_m(x)$ is constant and hence from equation (5.4.10) $\rho(x)$ is constant. A value of 0.72 for Pr was used here as in Kreith. C_p was set to 1012J kg^{-1} $^{\circ}C$ and μ was set to 1.81×10^{-5} kg m^{-1} sec^{-1} which are taken from Bachelor (1967) as representative values for air at room temperature. Shown in Figures 5.1(a) and (b) are a comparison of Nu_{av} calculated from equation (5.6.2) with that of Kreith. Only one curve is presented for the present theory to represent all the cone angles since the results of §4.4 show that varying λ has very

little effect on the flow variables and the energy equation (5.4.8) is independent of λ.

Figure 5.1(a) also shows the effects on the Nu_{av} calculations of omitting the various extensions to the Reynolds analogy. A calculation of Nu_{av} is shown in which the effects of accounting for a non-quadratic temperature distribution has been omitted, so that $I_{fh}(x)$ has been given a constant value of $I_f - I_{fg}$ in equation (5.3.54). Also shown is a curve of the results for which the effects of a non-unity laminar Prandtl number have been omitted, so that ξ has been set to 1 in equation (5.3.54). The effects of the recovery factor, R_c, in equation (5.3.54) are not shown in Figure 5.1(a), since it was found that the term $R_c(v_0-\bar{v})^2/(2C_p)$ did not have an appreciable effect on Nu_{av}. The term appears in equation (5.3.54) to account for the effect of frictional heating and compressive work (as derived in §5.3.2) and it will only have an effect on the heat transfer when the Eckert number, defined as

$$E_c = \frac{\Omega^2 r^2}{2C_p(T_0-T)} \qquad (5.6.3)$$

is not small compared with unity. The Eckert number will increase as Re_θ increases and it was found that when $Re_\theta = 10^6$ (which is the highest value used by Kreith (1966) and shown in Figure 5.1(a)), $T_0 - \bar{T}$ was required to be as small as 10°C to change the computed values of Nu_{av} by 10%. In an aero-engine environment, the temperature difference between the fluid and metal components is unlikely to be as small as 10^0K, so that high Reynolds numbers (greater than 10^6) will be required for frictional heating and compressive work to have a significant effect on the heat transfer.

Figure 5.1(a) shows that for the free rotating disc ($\lambda = 90°$),

the value of Nu_{av} calculated numerically from equation (5.6.2) shows excellent agreement with Kreith for values of $Re_\theta > 6 \times 10^5$. For $Re_\theta > 6 \times 10^5$, the value of the relative error in Nu_{av} in this case is always less than 5%. For $Re_\theta < 6 \times 10^5$, the error is greater than this, but for these values of Reynolds number the flow may be predominantly laminar. For the case of $\lambda = 40^\circ$, the agreement between Nu_{av} calculated from equation (5.6.2) and Kreith is excellent for $Re_\theta > 4 \times 10^5$, where the relative error is always less than 5%. The agreement for the $\lambda = 30^\circ$ case is excellent for the $Re_\theta < 5 \times 10^5$, where the relative error is less than 5% and reasonable for $Re_\theta > 5 \times 10^5$ where the relative error is less than 10%.

Kreith et al (1963) studied the transition between laminar and turbulent flow for free rotating discs and cones of various vertex angles. They concluded that the transition occurs at progressively smaller values of the Reynolds number as the cone angle is decreased. This could explain the improved agreement between theory and experiment at lower Reynolds numbers for $\lambda = 40^\circ$ and $\lambda = 30^\circ$ compared with the $\lambda = 90^\circ$ case. The close agreement between theory and experiment provides evidence that the application of the Reynolds analogy in this chapter is valid for free-rotating cones with angles as small as 30°. Figure 5.1(a) also indicates that the more elaborate forms of the Reynolds analogy explained in this chapter do improve the model.

Figure 5.1(b) shows a comparison of the average Nusselt number calculated from equation (5.6.2) with Nu_{av} found experimentally by Kreith (1966) for a cone angle of 15°. The Reynolds number variation shown is between 2×10^4 and 10^5. According to Kreith et al (1963), for a 15° cone, the flow begins to become turbulent at a Reynolds number of about 2×10^4. The figure shows a poor agreement between

the predicted and the experimentally obtained values with the relative error in Nu_{av} varying between 18% and 37%. A possible reason for the poor agreement in this case is that for cones with such a small cone angle the boundary layer assumptions and in particular assumption (3.3.1), i.e. $u \gg w$ may not be true for small cone angles. Another possible reason for the poor agreement for the small cone angle cases is that the assumed velocity profiles given by equations (3.4.16) are no longer valid.

5.6.2 Rotor-Stator Systems

As already stated, there is not to the author's knowledge any relevant experimental data concerning rotor-stator disc or cone systems, hence in this section the integral method predictions are compared with finite difference predictions. The finite difference method will be described in detail in the next chapter and only the heat transfer results obtained from the finite difference program will be used here. The finite difference method is expected to give more accurate predictions than the integral method described in this chapter, since the method involves solving the full (axisymmetric and steady) flow and energy equations (with turbulence modelling) within the cavity and far fewer assumptions are made than in the integral method. The comparisons here concentrate on assessing the integral method for a variety of temperature conditions and the configuration of a rotor-stator disc system is used, with the exception of one comparison which was made for a cone system with $\lambda = 45^{\circ}$. The emphasis has been placed on disc systems rather than cone systems, since as stated earlier the integral method solutions are independent of λ and

also it will be shown in chapter 6 that the finite difference results are similarly independent of λ.

The flow within the cavity was assumed to be fully turbulent and the following values were assigned: d/b = 0.12, T_{ref} = 298°K, $Re_\theta = 1.7 \times 10^6/\sin\lambda$, Pr = 0.7, Pr_t = 0.9, Cp = 1012 J kg^{-1} $^0K^{-1}$, $\mu = 1.81 \times 10^{-5}$ kg m^{-1} sec^{-1} and ρ_I = 1.18 kg m^{-3}. Comparisons were made for eight different sets of boundary conditions, labelled (a)-(h), which are described in Table 5.1.

In Table 5.1, T_{IN} refers to the temperature of the inner surface (see Figure 6.1(b) for the finite difference domain) for zero throughflow cases and the temperature of the incoming fluid through a uniform inlet for throughflow cases. In case (b), T_0 is set to $T_{ref} + 1463\ x^2\ ^0K$ since this is the appropriate value for the basic Reynolds analogy condition (5.3.17) to hold.

In all cases, a comparison between the finite difference predictions and the integral method predictions is made by comparing the local Nusselt number, Nu(x) or $Nu^s(x)$, defined by

$$Nu(x) = \frac{r_0(x)q_0(x)}{k[T_0(x)-T_{ref}]} \quad \text{and} \quad Nu^s = \frac{r_0(x)q_0{}^s(x)}{k[T_0(x)-T_{ref}]} . \qquad (5.6.4)$$

Comparisons were also made between predicted average Nusselt numbers, Nu_{av} and $Nu^s{}_{av}$, defined by

$$Nu_{av} = \frac{q_{o,av}\ b}{k(T_{o,av}-T_{ref})} \quad \text{and} \quad Nu^s{}_{av} = \frac{q^s_{o,av}\ b}{k(T_{o,av}-T_{ref})} \qquad (5.6.5)$$

where the subscript 'av' refers to radially weighted average values. Note that for case (c), $T_0(x)$ in equations (5.6.4) is replaced by T^s_0 and $T_{o,av}$ in equations (5.6.5) is replaced by $T^s_{o,av}$, to avoid the

singularity which would occur in equations (5.6.4) and (5.6.5).

A comparison of the average Nusselt numbers predicted by the finite difference method and the integral method for the cases (a)-(h) of Table 5.1 are shown in Table 5.2. The error shown in the table is an error in the average Nusselt number relative to the finite difference method prediction. To obtain solutions for the throughflow cases (f) and (g), an estimate of the heat transfer coefficient, h_c, in equation (5.4.15) is required. As stated in §5.4.2, a value of h_c is required to estimate the surface heat flux in the source region on the stator, where an integral method calculation is not performed. A graph of the variation of h_c with x for case (g) is shown in Figure 5.2. This shows that in the source region of the flow (where x is less than about 0.5), h_c is less than 10 for most of this region shown. It was found, however, that the integral method solutions were fairly insensitive to the value of h_c; the results shown in Table 5.2 were obtained for $h_c = 0$, but when h_c was set to 10, Nu_{av} varied by less than 1% of the value shown.

Apart from case (c), the agreement for the rotor predictions is excellent, whereas the agreement for the stator is more erratic. Figure 5.3(a) shows a comparison of the mid-axial temperature distribution predicted by the two methods for the case (a) boundary conditions. Also shown in the figure is the integral method solution when $\xi = 1$, i.e. the solution when the effect of a non-unity laminar Prandtl number is not accounted for. The graph shows that the integral method predicts the same trend as the finite difference method although the error at larger values of x becomes quite large. The graph also shows that the correction factor for a non-unity laminar Prandtl number, ξ, does seem to improve the agreement. Figure 5.3(b) shows a comparison of the local Nusselt number

predictions evaluated from equations (5.6.4) for the case (a) boundary conditions. The figure shows that setting $\xi = 1$ tends to decrease the Nusselt number, as was the case with the free rotating disc in §5.6.1, but no conclusion may be drawn from the figure as to whether or not the correction factor improves the agreement. It was found, however, that setting $\xi = 1$ resulted in poorer agreement between the average Nusselt numbers predicted by the finite difference program and the integral method.

A comparison between the results for boundary conditions (d) and (e) in Table 5.2 shows that the agreement between the integral method and the finite difference method is worse when the flow is treated as being compressible. Figures 5.4(a) and (b) show graphs comparing the mid-axial temperature difference and local Nusselt numbers on the rotor for these cases. These graphs confirm that the agreement between the methods is better when the flow is assumed to be incompressible. A possible reason for the worse agreement for compressible flows is the assumption in the integral method that the density is constant across the boundary layers. Figure 5.5 shows profile plots of density from the finite difference results for the case (a) and (d) boundary conditions of Table 5.1 taken at three different radial locations. These graphs show a marked variation of density near the rotor which is situated at $n/d = 0$ and at the stator which is situated at at $n/d = 1$, especially for case (d) where the rotor has a higher relative temperature. Unfortunately, the inclusion of density variations across the boundary layers is not straightforward and only an approximation is possible. To include normal density variations into the method described in §5.4 would require a knowledge of the variation of $h(\eta,s)$ and $h^s(\eta,s)$ with η and this variation is only known when $Pr_e = 1$, $T_o - T_{ref} \propto r^2$ and $T_o^s =$

T_{ref}, in which case $h(\eta) = 1-g(\eta)$ and $h^S(\eta) = 1-g^S(\eta)$. Such density variations across the boundary layers were accounted for by Chew and Rogers (1988) for co-rotating disc systems. They showed that for the special case when $Pr_e = 1$ and $T_o - T_{ref} \propto r^2$, the density variations had very little effect on the solutions. They also found that the inclusion of density variations across the boundary layer resulted in computer times being increased by a factor of about ten. Considering these results and the uncertainties involved in accounting for normal density variations under more general surface temperature and Prandtl number conditions, the inclusion of the effect of density variations across the boundary layers would not seem to be worthwhile.

Table 5.2 shows that the comparison of the average Nusselt numbers for the case (c) boundary conditions is quite good for both the rotor and stator with the relative error being less than 10% in both cases. This agreement is surprisingly good since in this case the stator surface temperature varies quadratically with radius and assumption (5.4.13) is only strictly valid when the stator surface temperature is uniform (see appendix E). Assumption (5.4.13) will only be valid if $h^S(\eta) = 1-g^S(\eta)$ within the stator boundary layer, and Figure 5.6(a) shows graphs of $h^S(\eta)$ and $1-g^S(\eta)$ as predicted by the finite difference program at two radial locations adjacent to the stator for the case (c) boundary conditions. The figure shows a good agreement between $h^S(\eta)$ and $1-g^S(\eta)$ at both radial locations, but there is a variation of $h^S(\eta)$ with x. Figure 5.6(b) shows a similar comparison for the case (b) boundary conditions where T_o^S is uniform. As expected, the agreement between $h^S(\eta)$ and $1-g^S(\eta)$ is slightly better and there is less of a variation of $h^S(\eta)$ with x. The above results provide some encouraging evidence that the assumption (5.4.13) may hold in cases where the stator surface temperature is not uniform.

Table 5.2 shows a good comparison for the predicted Nu_{av} for throughflow cases as shown by the results for cases (f) and (g) which were both treated as being incompressible. The agreement for the predicted Nu^{s}_{av} for the case (g) boundary conditions is poor and this is due to the integral method under-predicting the mid-axial temperature in the core region of the flow as shown in Figure 5.7. A noticeable feature of Figure 5.7 is that the finite difference program does predict an abrupt change in temperature when transferring from the source region to the core region. This feature predicted by the finite difference program provides some evidence to support the assumption of a discontinuity in $\bar{H}(x)$ when transferring from the source region to the core region as explained in §5.4.2.

5.7 SUMMARY AND CONCLUSIONS

The work in this chapter represents an extension of heat transfer methods using the Reynolds analogy to the situation of a rotor-stator system where the throughflow rate is sufficiently small for there to be a re-circulating core region in the flow. Previous authors, such as Kapinos (1965) and Owen (1971) have confined their attention to rotor-stator systems with a very high throughflow rate so that the source region shown in Figure 2.1(c) fills the entire cavity and the re-circulating core region does not exist. The calculation of heat transfer between the rotor and the fluid is far simpler in such cases since the temperature of the fluid at the boundary layer edge throughout the cavity is known from the inlet conditions and does not have to be predicted. Owen (1971) confined his attention to rotor-stator disc systems where the distance between the rotor and

stator is sufficiently small for the entire cavity to be treated as one boundary layer. In such cases, the boundary layer edge temperature may be taken as the temperature of the stator and again a temperature prediction is not required.

Chew and Rogers (1988) solved the integrated boundary layer energy equation to find the heat transfer in a symmetrically heated co-rotating disc system. There is no re-circulating region of flow in this case, as shown in Figure 2.1(b), and because both discs have the same temperature distribution there is no interaction between the two boundary layers on the discs. In this case the source region calculation used by Chew and Rogers is similar to the one used here (i.e. the inlet temperature is known and the energy equation is used to calculate $I_{fh}(x)$). In the core region, Chew and Rogers assumed $I_{fh}(x)$ to be constant and used the energy equation to calculate the boundary layer edge temperature. The present method is an extension of the work of Chew and Rogers to rotor-stator systems where there is an interaction between the two boundary layers.

Considering the crude nature of many of the assumptions (e.g. the estimation of some of the terms in the energy balance equation (5.4.14)) and the fact that the heat flux expression (5.3.54) has been developed for flows over a free disc), the method has been surprisingly successful. The comparison of the average Nusselt number solutions for free-rotating cones with experimental results in §5.6.1 provide some evidence that the application of the Reynolds analogy is valid for free-rotating cones with half-angles as small as 30^{0}. It was also shown in §5.6.1 that the extensions of the Reynolds analogy to allow for a varying laminar Prandtl number and arbitrary surface temperature distribution did tend to improve the agreement and there was also some evidence of an improvement in the rotor-stator

predictions when the factor to account for a non-unity laminar Prandtl number was included.

Overall the comparisons with the finite difference results in §5.6.2 show an encouraging agreement. The main draw-back of the method seem to be its restrictiveness in modelling compressibility; improving on this aspect of the model could be an area for further work. The comparisons in §5.6.2 were restricted to rotor-stator disc systems except for one rotor-stator cone system case. However, it will be shown in §7.2 that the finite difference results predict the same flow pattern as assumed in chapter 3 for rotor-stator cone systems and the results also support the use of the integral method assumptions described in these chapters. It would be expected then that the same pattern of results illustrated by Table 5.2 would occur for rotor-stator systems with a general cone angle.

CHAPTER 6

THE FINITE DIFFERENCE METHOD

6.1 INTRODUCTION

In this chapter, the flow between a rotating and stationary cone will be investigated numerically using a finite difference program. There are two reasons for the investigation:

(i) To assess the suitability of the numerical method for predicting rotor-stator cone flows by comparing the results with experimental data.

(ii) To use the numerical results to validate and if necessary to modify the integral method described in previous chapters. This will require examination of the secondary flows to see whether they can be treated by the integral method and if they can, to decide whether modifications are necessary to certain aspects of the model (for example the form of velocity profiles).

The program used here is a modified version of that written by Vaughan, Gilham and Chew (1989) to investigate flows in rotating disc systems. The original program solved the relevant steady, axisymetric equations of motion in a cavity whose geometry is shown in Figure 6.1(a). The present modifications involved 'tilting' the cavity of Figure 6.1(a) through an arbitrary angle, λ, as shown in Figure

6.1(b). The program was written to be very general in its modelling capability and it could be used to investigate a wide range of rotating flows (within the constraints of time independence and axisymmetry). However for the present purposes of modelling rotor-stator cone flows it is sufficient to specify stationary boundaries at $s = a/\sin\lambda$, $s = b/\sin\lambda$ and $n = d$, and a rotating boundary at $n = 0$. With the above boundary conditions, the equations may be solved to describe the flow in a rotor-stator cone system without throughflow. By specifying a uniform inlet at $s = a/\sin\lambda$ and a uniform outlet at $s = b/\sin\lambda$, a model with throughflow may be represented. It may be noted that the solution domain here differs from the domain assumed in the integral method (see Figure 3.1), since the angles that the inner and outer boundaries make with the rotor and stator are not the same in the two cases. The effect of this difference in geometry will be discussed in §6.4.2 and a modification to incorporate a 'rectangular' outer shroud into the integral method will be described in §7.4.

The purpose of the present study is to investigate the predictive capability of the modified version of the program and to analyse the results. The finite difference method used has been accepted and for the present purposes, the model will not be investigated or questioned. However, for completeness, a description of the program and the criteria used to judge whether or not a particular run had converged will be given in §6.2. In §6.3, results will be presented of the studies which were undertaken to ensure that the modifications to the program had been coded correctly. The comparisons of the predicted results with experimental data and the conclusions to be made from the comparisons will be made in §6.4.

6.2 DESCRIPTION OF THE PROGRAM

6.2.1 The Governing Equations

For steady, axisymmetric flow, the Reynolds averaged continuity, momentum, energy and state equations may be written in terms of the coordinate system shown in Figure 6.1(b) as follows

$$\frac{1}{r}\frac{\partial}{\partial s}(\rho r u) + \frac{1}{r}\frac{\partial}{\partial n}(\rho r w) = 0 \ , \tag{6.2.1}$$

$$\frac{1}{r}\frac{\partial}{\partial s}(\rho r u^2) + \frac{1}{r}\frac{\partial}{\partial n}(\rho r u w) = \frac{1}{r}\frac{\partial}{\partial s}\left[\mu_e r \frac{\partial u}{\partial s}\right] + \frac{1}{r}\frac{\partial}{\partial n}\left[\mu_e r \frac{\partial u}{\partial n}\right] + \rho\frac{v^2}{r}\sin\lambda$$

$$- \frac{\partial}{\partial s}(p+\tfrac{2}{3}\mu_e\Delta) + \frac{1}{r}\frac{\partial}{\partial s}\left[\mu_e r \frac{\partial u}{\partial s}\right] + \frac{1}{r}\frac{\partial}{\partial n}\left[\mu_e r \frac{\partial w}{\partial s}\right] - \frac{2\mu_e}{r^2}\sin\lambda\,(u\sin\lambda - w\cos\lambda), \tag{6.2.2}$$

$$\frac{1}{r}\frac{\partial}{\partial s}(\rho r u v) + \frac{1}{r}\frac{\partial}{\partial n}(\rho r w v) = \frac{1}{r}\frac{\partial}{\partial s}\left[\mu_e r \frac{\partial v}{\partial s}\right] + \frac{1}{r}\frac{\partial}{\partial n}\left[\mu_e r \frac{\partial v}{\partial n}\right]$$

$$+ \frac{\rho w v\cos\lambda}{r} + \frac{v\cos\lambda}{r^2}\frac{\partial}{\partial n}(\mu_e r) - \frac{\rho u v\sin\lambda}{r} - \frac{v\sin\lambda}{r^2}\frac{\partial}{\partial s}(\mu_e r) \ , \tag{6.2.3}$$

$$\frac{1}{r}\frac{\partial}{\partial s}(\rho r u w) + \frac{1}{r}\frac{\partial}{\partial n}(\rho r w^2) = \frac{1}{r}\frac{\partial}{\partial s}\left[\mu_e r \frac{\partial w}{\partial s}\right] + \frac{1}{r}\frac{\partial}{\partial n}\left[\mu_e r \frac{\partial w}{\partial n}\right] - \rho\frac{v^2}{r}\cos\lambda$$

$$- \frac{\partial}{\partial n}\left(p+\tfrac{2}{3}\mu_e\Delta\right) + \frac{1}{r}\frac{\partial}{\partial n}\left[\mu_e r \frac{\partial w}{\partial n}\right] + \frac{1}{r}\frac{\partial}{\partial s}\left[\mu_e r \frac{\partial u}{\partial n}\right] + \frac{2\mu_e}{r^2}\cos\lambda\,(u\sin\lambda - w\cos\lambda),$$

(6.2.4)

$$\frac{1}{r}\frac{\partial}{\partial s}(\rho r u H) + \frac{1}{r}\frac{\partial}{\partial n}(\rho r w H) = \frac{1}{r}\frac{\partial}{\partial s}\left[r\frac{k_e}{C_p}\frac{\partial H}{\partial s}\right] + \frac{1}{r}\frac{\partial}{\partial n}\left[r\frac{k_e}{C_p}\frac{\partial H}{\partial n}\right]$$

$$+ \frac{1}{r}\frac{\partial}{\partial s}\left[\left[\mu_e - \frac{k_e}{C_p}\right] r\frac{\partial}{\partial s}\frac{(u^2+v^2+w^2)}{2} - \mu_e r u\tfrac{2}{3}\Delta\right] + \frac{1}{r}\frac{\partial}{\partial s}\left[\mu_e r\left[u\frac{\partial u}{\partial s} + w\frac{\partial u}{\partial n} - \frac{v^2}{r}\sin\lambda\right]\right]$$

$$+ \frac{1}{r}\frac{\partial}{\partial n}\left[\left[\mu_e - \frac{k_e}{C_p}\right] r\frac{\partial}{\partial n}\frac{(u^2+v^2+w^2)}{2} - \mu_e r w\tfrac{2}{3}\Delta\right] + \frac{1}{r}\frac{\partial}{\partial n}\left[\mu_e r\left[w\frac{\partial w}{\partial n} + u\frac{\partial w}{\partial s} + \frac{v^2}{r}\cos\lambda\right]\right],$$

(6.2.5)

$$p = \rho R_G T \,, \tag{6.2.6}$$

where

$$\Delta = \frac{1}{r}\frac{\partial}{\partial s}(ru) + \frac{1}{r}\frac{\partial}{\partial n}(rw) \,, \tag{6.2.7}$$

and

$$H = C_p T + \tfrac{1}{2}(u^2+v^2+w^2) \tag{6.2.8}$$

is the stagnation enthalpy. The vector (u,v,w) represents the mean velocity components in the (s,θ,n) coordinate system, p represents the mean pressure, ρ the mean density, T the mean temperature, μ_e the effective viscosity, ke the effective thermal conductivity, C_p the specific heat at constant pressure and R_G is the gas constant.

For ease of description of the solution procedure the three momentum equations and the energy equation may be represented by the common equation

$$\frac{1}{r}\frac{\partial}{\partial s}(\rho r u\Phi) + \frac{1}{r}\frac{\partial}{\partial n}(\rho r w\Phi) = \frac{1}{r}\frac{\partial}{\partial s}\left[\Gamma r \frac{\partial \Phi}{\partial s}\right] + \frac{1}{r}\frac{\partial}{\partial n}\left[\Gamma r \frac{\partial \Phi}{\partial n}\right] + S_\Phi, \quad (6.2.9)$$

where Φ represents either u,v,w or H, the diffusion coefficient Γ equals μ_e for the momentum equations and k_e/C_p for the energy equation and the source term S_Φ is different for each variable.

The boundary conditions are given by the no-slip and no-penetration conditions on the solid surfaces. The rotor, situated at $n = 0$ is given a constant angular velocity Ω, whereas the other three surfaces are stationary. For a throughflow case, a uniform inlet is assumed at $s = a/\sin\lambda$, $0 \leq n \leq d$ and a uniform outlet is assumed at $s = b/\sin\lambda$, $0 \leq n \leq d_c$, where d_c represents the n location of the end of the solid boundary on the outer shroud at $s = b/\sin\lambda$. For a throughflow case the inlet and outlet boundary conditions are taken to be

$$u = \frac{\dot{m}}{2\pi\rho ad}, \quad v = \Omega r, \quad w = 0 \text{ on } s = a, \quad 0 \leq n \leq d, \quad (6.2.10)$$

$$u = \frac{\dot{m}}{2\pi\rho a(d-dc)}, \quad \frac{\partial}{\partial r}(rv) = 0, \quad w = 0 \text{ on } s = b, \quad 0 \leq n \leq d_c. \quad (6.2.11)$$

6.2.2 The Turbulence Model

The turbulence model used in this program is a mixing length turbulence model based on that applied to the flow over rotating discs and cones by Koosinlin, Launder and Sharma (1974). No allowance is made for the possibility that the flow may be laminar towards the centre of the cavity. This assumption is made by Chew and Vaughan (1988), who found that at high Reynolds numbers it had very little

effect on the results in the main part of the cavity if the boundary layer formed over the inner surface at s = a in a rotor-stator disc system is treated as laminar or turbulent.

The effective viscosity is calculated as the sum of the laminar viscosity, μ and the turbulent viscosity, μ_t:

$$\mu_e = \mu + \mu_t \ . \tag{6.2.12}$$

The turbulent viscosity is calculated from an extension of Prandtl's original mixing length hypothesis as

$$\mu_t = \rho \ell^2 \left[\left[\frac{\partial u_p}{\partial x_n} \right]^2 + \left[r \frac{\partial}{\partial x_n} \left[\frac{v}{r} \right] \right]^2 \right]^{\frac{1}{2}} , \tag{6.2.13}$$

where ℓ is the mixing length, u_p is the velocity component parallel to any of the four surfaces in the s-n plane and x_n is in the direction normal to the surface. A two part specification is used for the distribution of the mixing length. In the region where the presence of the wall affects the turbulence structure, a Van Driest (1956) type of damping factor is used and it is assumed that

$$\ell = 0.42 x_n \left[1 - \exp\left[-\frac{x_n^+ (\tau^+)^e}{26} \right] \right] \tag{6.2.14}$$

where x_n^+ is the non-dimensional distance from the wall ($= x_n (\rho \tau_w)^{\frac{1}{2}} / \mu$), τ_w is the resultant wall shear stress and $\tau^+ (= \tau / \tau_w)$ is a non-dimensional shear stress. Koosinlin et al (1974) recommend the exponent e being given a value of 1.5, however, Chew and Vaughan (1988) found that using this value of e caused numerical difficulties

in rotor-stator disc systems. Following Vaughan et al (1989) the value of e has therefore been set to zero, so that equation (6.2.14) reduces to an identical equation to that used by Van Driest (1956). The effect of using a non-zero value for e on the moment coefficient calculations will be discussed in §6.4.3. In the outer part of each boundary layer, ℓ is given by

$$\ell = 0.085\delta, \tag{6.2.15}$$

where δ is the boundary layer thickness. The factor 0.085 in equation (6.2.15) is used following the recommendations of Koosinlin, Launder and Sharma (1974). The division between the two regions for calculating ℓ is taken as the lowest value of x_n for which equations (6.2.14) and (6.2.15) gave the same value of ℓ.

An appropriate definition of the boundary layer thickness in equation (6.2.15) is the distance from the wall at which the resultant shear stress parallel to the wall becomes 1% of its value at the wall. However it has been suspected that using this definition may cause convergence difficulties and following Chew and Vaughan (1988), the edge of the boundary layer is defined as the point at which

$$\frac{\tau}{\mu_e} = \left[\left[\frac{\partial u_p}{\partial x_n}\right]^2 + \left[r\,\frac{\partial}{\partial x_n}\left[\frac{v}{r}\right]\right]^2\right]^{\frac{1}{2}} \tag{6.2.16}$$

is equal to 0.01 of its value at the wall. In the corners, the value of δ associated with each wall is taken to be the minimum of the 99% boundary layer thickness, as described above for that wall, and the value of x_n for which the distances to the two walls are equal.

Following Koosinlin et al (1974), the influence of rotation on the mixing length is accounted for by use of the Richardson number,

Ri. Accordingly, the mixing length is modified as follows:

$$\ell = \ell_0(1-5Ri), \tag{6.2.17}$$

where ℓ_0 is the mixing length prescribed by equations (6.2.14) and (6.2.15). The factor of 5 in equation (6.2.17) was found by Koosinlin et al (1974) to give the best agreement with experimental data for the moment coefficient and velocity profiles for free-rotating cones and cylinders. The Richardson number is defined as

$$Ri = \frac{\frac{2v}{r^2}\cos\chi\,\frac{\partial}{\partial x_n}(rv)}{\left[\frac{\partial u_p}{\partial x_n}\right]^2 + \left[r\,\frac{\partial}{\partial x_n}\left|\,\frac{v}{r}\right.\right]^2}, \tag{6.2.18}$$

where χ is the angle that the surface makes with the axis of rotation.

To avoid discontinuities in μ_t, the turbulent viscosities calculated for the four walls were averaged as in Chew and Vaughan (1988) as follows:

$$\mu_t = \frac{(x_o x_a x_d)^3\mu_{t,b} + (x_o x_d x_b)^3\mu_{t,a} + (x_a x_b x_o)^3\mu_{t,d} + (x_d x_a x_b)^3\mu_{t,o}}{(x_o x_a x_d)^3 + (x_o x_d x_b)^3 + (x_a x_b x_o)^3 + (x_d x_a x_b)^3}, \tag{6.2.19}$$

where the subscripts o and d refer to the surfaces at n = 0 and n = d respectively and the subscripts a and b refer to the surfaces s = a and s = b respectively. So, for example, x_o represents the normal distance from the wall at n = 0 to the point where the turbulent viscosity is to be calculated. The type of weighting in equation (6.2.19) is chosen by Chew and Vaughan (1988) so as to have a negligible effect in the boundary layers apart from in the corner

regions.

The effective thermal conductivity, k_e, is divided into a laminar and a turbulent part in a similar way as the effective viscosity and is defined as

$$k_e = k + k_t \ . \qquad (6.2.20)$$

The conductivities k and k_t were calculated using a laminar and turbulent Prandtl number, where $Pr = \mu C_p/k$, $Pr_t = \mu_t C_p/k_t$.

6.2.3 The Numerical Method

The derivation of the finite difference equations follows the finite volume approach of Patankar and Spalding (1972) and Patankar (1980). A staggered grid is used as shown in Figure 6.2. The velocity components u and w are calculated at the points marked ↑ and → respectively, which lie mid-way between the main grid points. Other variables are calculated at the main grid points. A control volume is associated with each grid point (shown shaded in Figure 6.2) and the finite difference equations are obtained by integration of the equations of motion over the control volumes.

For a particular control volume, the s and n distances to the points P, N, S, E and W are denoted by s_P, n_P, s_W, n_N etc and to facilitate the integration, the following distances between points are defined:

$$\left.\begin{aligned} Dn_e &= n_E - n_P \ , \\ Dn_w &= n_P - n_W \ , \\ Dn_p &= (n_N - n_S)/2 \ , \\ Ds_n &= s_N - s_P \ , \\ Ds_s &= s_P - s_S \ , \\ Ds_p &= (s_E - s_W)/2 \ , \end{aligned}\right\} \qquad (6.2.21)$$

Smooth expansion factors are used in both the s and n directions, so that grid points could be more closely packed in the regions near to boundaries. Unless otherwise stated, constant radial and axial expansion factors of 1.2 were used throughout. A finite difference representation of equation (6.2.9) for each of the variables at either of the points P shown in Figure 6.2 has the form

$$A_p\Phi_p = \sum_k A_k\Phi_k + (S_1 + S_2\Phi_p) \ , \qquad (6.2.22)$$

where the summation is carried out over the four neighbouring points N, S, E and W. The coefficients associated with u, v, w and H are shown in Appendix F.

The continuity equation (6.2.1), is not included in the above differencing scheme, as this equation requires special treatment. It is used in the iterative pressure-correction method which is the SIMPLEC method of Van Doormal and Raithby (1984).

An iterative, non-linear multigrid method is used to solve the finite difference equations; details of the scheme may be found in Lonsdale (1988) and Vaughan et al (1989). Under-relaxation factors are used for the three velocity components, pressure, enthalpy, turbulent viscosity and multi-grid corrections. The additional so

called Gosman under-relaxation factor, α_G (see Appendix F) is also introduced. Unfortunately, no general rules could be found to assign values to the under-relaxation factors which would provide an optimum convergence rate for a specific case.

6.2.4 Convergence Criteria

To determine whether or not a given numerical calculation had converged, particular aspects of the output were examined; these will now be described.

The Residual

This was calculated for the velocity components, the pressure and the enthalpy (for a non-isothermal case). It is defined as the sum over all grid points, for a particular variable, of the absolute value of the error in the differential equation multiplied by the volume associated with that grid point. From equation (6.2.22), the residual, Res, for a particular variable is defined as

$$\text{Res} = \Sigma \left| (A_p - S_2)\Phi_P - A_n\Phi_N - A_S\Phi_S - A_E\Phi_E - A_W\Phi_W - S_1 \right| \text{Dn}_p\text{Ds}_p \ , \quad (6.2.23)$$

where the summation is carried out over all points of the finest grid before the first coarsening in the multigrid step.

R.M.S. Change

This is calculated for all the variables, and is defined as the root-mean-square of the change of a variable given by the solution procedure on the fine grid, divided by the root-mean-square value for

the variable. The root-mean-square change for a particular variable is therefore defined as

$$\text{R.M.S. change} = \sqrt{\frac{\Sigma(\Delta\Phi)^2}{\Sigma\Phi^2}} \quad , \tag{6.2.24}$$

where Φ represents any variable, $\Delta\Phi$ is the change at a particular grid point and the summation is carried out over all grid points.

Moments

The moment exerted on each of the four surfaces of the cavity by the fluid is calculated at the end of the stipulated number of iterations.

Ideally, as a particular numerical calculation converges, the residuals and root-mean-square changes for each variable will tend to zero. In practice, however, a particular solution may have been judged converged and these parameters would tend to level off at a finite value. If a solution diverges, the residuals become large and the root-mean-square changes approach unity. The performance of a particular iterative solution procedure is dependent on the particular problem considered and the choice of the various input parameters. In determining whether or not a particular numerical calculation has satisfactorily converged, the following factors are taken into account

(i) The values of the root-mean-square changes should be small relative to unity. In practice if a solution had satisfactorily converged, the root-mean-square changes for the velocities and pressure (and enthalpy for a non-isothermal case) would normally

be less than 10^{-4}, although the root-mean-square change for the turbulent viscosity rarely reduced below 10^{-2}.

(ii) The values of the residuals should be small relative to the characteristic values of mass flow, force and energy flow for a particular problem.

(iii) The values of the moments should be unchanging (to 3 significant figures) over single iterations and over 100 to 150 iterations.

(iv) The values of the flow variables at a monitored point should be unchanging (to 4 significant figures) over single iterations and 100 to 150 iterations.

6.3 VERIFICATION OF THE MODIFICATIONS TO THE CODING

To ensure that the program had been modified to model a conical geometry correctly, the results from several pairs of runs which in theory should give exactly the same results will be compared. Since in this section comparisons between numerical results are being made, the accuracy of the solution is not of importance, so to save on computer time, unless otherwise stated, a coarse 17 x 17 grid is used in each case. For isothermal flow the following three pairs of runs are compared.

(R1) Results from a case where $\lambda = 90^{\circ}$, $a = 0$ and the surface at $n = d$ is rotated are compared with results from a case where $\lambda = 0^{\circ}$, $a = 0$ and the surface at $s = 0$ is rotated. The radial and axial dimensions of the cavity in both cases are set to 0.126m and 0.2016m respectively, so that the same rotor-stator disc problem are examined in both cases.

(R2) Results from a case where $\lambda = 70^{\circ}$, the surface at n = 0 is rotated and a = 0 are compared with the results from a case where $\lambda = 110^{\circ}$ and the surface at n = d is rotated. In both cases, the outer radius of the cone, b, is set to 0.126m and the gap width, d, is set to 0.2016m.

(R3) To test the boundary conditions for a throughflow case, the geometries of test (R2) above are used, but a uniform inlet is assumed in place of the surface at s = a and a uniform outlet is assumed in place of the surface at s = b. A mass flow rate of 0.00696kg s^{-1} is assumed.

To test the changes in the energy equation, the results from the following two non-isothermal cases are compared.

(R4) The geometries of the cones are the same as case (R2). The temperature of the rotating surface in each case is set to 500°K and the other three surfaces are given a temperature of 298°K. The laminar Prandtl number is set to 0.7 and the turbulent Prandtl number is set to 0.9.

In all the above cases the flow is treated as turbulent, even if the Reynolds number is sufficiently small to suggest that the flow should be laminar; this ensures that the modifications to the turbulent viscosity calculations are also tested. In all the cases, the flow is considered to be incompressible, since the present modifications did not involve changes to the parts of the program which are concerned with compressibility and the following reference fluid properties are assumed: $\rho_{ref} = 1.18 kg\ m^{-3}$, $\mu_{ref} = 1.84 \times 10^{-5} kg\ m^{-1}\ s^{-1}$, $p_{ref} = 1.01 \times 10^{5} Pa$ and $T_{ref} = 298^{\circ}K$.

The Reynolds number for the flow is calculated as

$$Re = \frac{\rho_{ref}\Omega}{\mu_{ref}} b_2 \ , \qquad (6.3.1)$$

where Ω is the angular velocity of the rotor. Note that the relationship between Re above and Re_θ used in the integral method (equations (3.6.14)) is

$$Re_\theta = Re \sin\lambda \ . \qquad (6.3.2)$$

In non-isothermal cases, the surface area averaged Nusselt number for a bounding surface is calculated from

$$Nu_{av} = \frac{rad\ \Sigma q_n}{k_{ref}(T_m - T_{ref})A} \ , \qquad (6.3.3)$$

where

$$q_0 = -k \frac{\partial T}{\partial x_n} \ , \qquad (6.3.4)$$

and the summation is carried out over all the grid points along the surface. In equation (6.3.3), k_{ref} is the thermal conductivity at reference conditions, A is the area of the surface and T_m is the area-averaged temperature of the sector.

The results for each of the above four pairs of runs are as follows.

(R1) Several values of the Reynolds number were assigned. When $Re = 10^4$, a converged solution was obtained after 210 iterations in both cases and the moments on all four surfaces were identical (to an accuracy of 3 significant figures). The three velocity profiles at the mid-radial location are shown in

Figures 6.3(a)-(c). These show that the profiles are indistinguishable for the two cases. Similar identical profiles were obtained for Re < 10^4. When Re = 10^5 or Re = 10^6, however, convergence difficulties were encountered for the case when $\lambda = 0^\circ$. For Re = 10^6, a converged solution for the $\lambda = 90^\circ$ case was obtained after 377 iterations, but after 1200 iterations the 0° case still had not fully converged. The moment coefficients for the rotor in the $\lambda = 90^\circ$ and $\lambda = 0^\circ$ cases were 9.13×10^{-4} and 9.17×10^{-4} respectively. Figures 6.4(a)-(c) show the three velocity profile plots at the mid-radial location. The tangential velocity profiles are very similar, the radial velocity profiles differ slightly and the axial profiles differ significantly. The only difference in the program for the two cases is the order of execution of the sub-routines concerning the radial and axial momentum equations. This difference must be the cause of the different convergence rates and it was thought possible that this discrepancy may be reduced by using a finer grid. To test this possibility, the Reynolds number was set to 10^6 and a 41 x 41 grid was used. Each case was run for 400 iterations, after which the moment coefficients on the rotor for the $\lambda = 90^\circ$ and $\lambda = 0^\circ$ cases were 3.14×10^{-3} and 3.11×10^{-3} respectively. A comparison of the velocity profiles in the mid-radial position is shown in Figures 6.5(a)-(c). These show that the agreement has definitely been improved by decreasing the grid spacing, indicating that the disagreement in velocity profiles for the coarse mesh was probably due to grid refinement error and not due to an error in the coding.

(R2) A value of Re = 10^6 was assigned. When $\lambda = 70^\circ$, a converged

solution was obtained after 327 iterations and when $\lambda = 110^{\circ}$ a converged solution was obtained after 348 iterations. The moment coefficient on the rotor in both cases was 1.03×10^{-3}. A comparison of the velocity profiles at the mid-radial position is shown in Figures 6.6(a)-(c). As to be expected, the velocity profiles are virtually indistinguishable in all cases.

(R3) Again a value of $Re = 10^6$ was assigned. Each run was given 600 iterations, after which the moment coefficient for the rotor was 1.81×10^{-3} in both cases. A comparison of the velocity profiles at the mid-radial position is shown in Figures 6.7(a)-(c). Again, the velocity profiles are virtually indistinguishable.

(R4) A value of $Re = 10^6$ was also assigned in this case. The 110° run converged after 348 iterations and the 70° case was stopped after 500 iterations. The average Nusselt number for the rotor was 5.38×10^4 in both cases. As expected a comparison of the stagnation enthalpy profiles at the mid-radial position showed that they were indistinguishable.

The evidence of the above four cases gives confidence that the modifications to the program were coded correctly. In the next section the results predicted by the program will be compared with the available experimental data.

6.4 COMPARISON WITH EXPERIMENT

The experimental data concerning moment coefficient calculations in rotor-stator cone systems used in this section is that of Yamada and Ito (1975, 1979). In both papers, the moment coefficient for the rotating cone is calculated; the 1975 paper concerns zero throughflow cases and the 1979 paper concerns rotor-stator systems with an imposed throughflow. The moment coefficient is defined as in equation (4.2.9) and the moment on the cone is calculated numerically using equation (4.2.10). In Yamada and Ito (1975), the values of cone angle investigated are 90° (disc case), 75°, 60°, 45°, 30° and 15°. In Yamada and Ito (1979), the cone angles investigated are 45°, 30° and 15°. The cones used by Yamada and Ito all had a pointed vertex, so that the inner radius is taken to be zero in the subsequent calculations. For the throughflow cases, it is assumed that the flow has zero swirl, so that the tangential velocity at the inlet is set to zero in the program. To make a thorough comparison with experiment, the effects of all the physical parameters, ie. λ, Re, d/b and throughflow rate on the moment coefficient are considered.

The rest of this section is divided into three sub-sections: the first is concerned with laminar flow and the second with turbulent flow. More attention has been given to turbulent flow, however, since these are the types of flow which are expected to occur more often in the aero-engine. The third sub-section concerns conclusions drawn from the previous two.

6.4.1 Laminar Flow

Before comparing the numerical predictions with the experimental results, it is necessary to assess the effect of the grid spacing on the moment coefficient predictions. Table 6.1 shows the results for a run with zero throughflow where $\lambda = 60^{\circ}$, $a = 0$, $Re = 2 \times 10^4$ and $d/b = 0.16$. These results indicate that the moment coefficient is independent of the grid spacing if the mesh has at least 33 x 33 nodes. It is assumed that for subsequent laminar runs a 33 x 33 mesh would give sufficient accuracy.

In Figure 6.8(a), results are compared for a zero throughflow case where $Re = 2 \times 10^4$ and $d/b = 0.16$. For comparison, numerical predictions are also shown in this figure when the flow was treated as being turbulent. The graph shows that the agreement between experiment and the laminar results is good when $\lambda > 45^{\circ}$, where the relative error varies between 5.2% and 1.9%. For $\lambda < 45^{\circ}$, the agreement becomes progressively worse with a 34% error at $\lambda = 15^{\circ}$. Figure 6.8(b) shows results for a case similar to 6.8(a) but where the spacing ratio has been reduced to $d/b = 0.024$. When λ is between 60° and 90°, the relative error is less than 5% and when $\lambda = 30^{\circ}$ or 15°, the relative error is greater than 30%.

One possible reason for the poor agreement in Figures 6.8(a), (b) for smaller cone angles is that the flow is no longer laminar in these cases. As stated in §4.6, the experimental work of Kreith et al (1963) on the transition Reynolds number for free-rotating cones supports the notion that the transition Reynolds number decreases as the cone angle decreases. Figure 6.8(a) shows the results of treating the flow as turbulent, which shows a much better agreement with experiment at lower values of λ, the relative errors being 6.1% when

$\lambda = 15^{\circ}$ and 5.2% when $\lambda = 30^{\circ}$. At higher values of λ, Figure 6.8(a) shows that the agreement between the turbulent flow predictions and experiment is worse than the agreement between the laminar flow predictions and experiment. This difference in agreement provides evidence that the flow laminarises as the cone angle increases. Yamada and Ito (1979) report that the transition Reynolds number is increased as the gap width ratio d/b decreases. This effect is supported by the results shown in Figure 6.8(c) where the gap width ratio is reduced to 0.016 and λ is set to 15°. The graph shows that the agreement at lower Reynolds numbers is excellent with the relative error at $Re = 10^4$ being 1.9% and the relative error at $Re = 2 \times 10^4$ being 3.5%.

Another reason for the poor agreement between the experimental results and the laminar predictions shown in Figures 6.8(a) and (b) for small cone angles is that the mode of secondary flow has changed and the finite difference program is not predicting the flow pattern correctly. For $\lambda \leq 45^{\circ}$, Yamada and Ito (1975) report that the secondary flows may consist of both the large-scale 'disc-type' flow (as assumed in the integral method and shown in Figure 3.2) and 'Taylor-type' vortices which are similar to those which are known to occur under certain conditions in a rotor-stator cylinder system. The presence of these Taylor-type vortices in the flow has been shown by Yamada and Ito (1975) to result in an increase in the moment coefficient. Visual flow studies made by Yamada and Ito showed that the Taylor-type vortices were not a complete ring (as encountered in rotor-stator cylinder systems) but were spiral-shaped. This observation was also made under certain circumstances by Wimmer (1983) who observed spiral-shaped vortices moving from the larger to the smaller radii of the cones. Under other circumstances Wimmer (1983) also observed complete ring 'Taylor-type' vortices being formed

progressively from the outer radius of the cone inwards as the Reynolds number was increased. He observed these vortices travelling axially upwards being driven by the disc-type secondary flow. Wimmer's diagram of these vortices is shown reproduced in Figure 6.9. As the Reynolds number was increased further, Wimmer noticed the gap between the rotor and stator being steadily filled with vortices and the axial speed of the vortices decreasing. Finally, the whole gap was filled with vortices and a steady state was achieved. Wimmer also found that it was possible for the spiral Taylor-type vortices and the ring Taylor-type vortices to exist together side by side at the same time. These observations indicate that the Taylor-type vortices occuring in the flow when $\lambda < 45^{\circ}$ may be both non-axisymetric and non-steady and if so they would not be detected by the finite difference method descibed in this chapter. Yamada and Ito (1975) made another important observation of the flow for a 30° angled rotor-stator system for $d/b = 0.016$; when they observed 'emerging vortices' even in the turbulent flow region ($Re = 1.5 \times 10^6$). This observation has important implications for the explanation of the turbulent flow comparisons which will be described in the next sub-section.

Figures 6.10(a)-(d) show secondary flow streamline plots for four of the results shown in Figures 6.8(a)-(b). Figures 6.10(a), (b) show the results of two runs which used the same specified flow parameters, but in Figure 6.10(a) the flow was treated as being laminar and in Figure 6.10(b) the flow was treated as being turbulent. Both of these streamline plots show the formation of a vortex near the outer shroud rotating in the opposite direction to the main secondary flow. Figures 6.10(c) and (d) (which have been expanded 20 times in the normal direction relative to the gap width to show more detail)

show the formation of what appear to be two vortices near the outer shroud. Streamline plots for the other results shown in Figure 6.8(a)-(d) similarly illustrated the prediction of no more than two such vortices. The occurence of these vortices in the predicted flow pattern does not seem to have a significant effect on the predicted moment coefficient. The vortices shown in Figure 6.10(d) were not present when $Re = 2 \times 10^4$, but Figure 6.8(c) shows the experimental and predicted trends departing at $Re = 4 \times 10^4$. Some of the experimental curves show very significant increases in the moment coefficient as the cone angle becomes small (see Figure 6.8(b) and Figures (4.13(a)-(f)) which are probably due to the influence of Taylor-type vortices. The finite difference program does seem to be capable of predicting some vortices other than the main disc-type flow, but these do not seem to have such a significant effect on the moment coefficient as those which are presumably causing such abrupt changes in the experimental data.

6.4.2 Turbulent Flow

As in §6.4.1, before comparing the numerical predictions with the experimental results, it is necessary to assess the effect of the grid spacing on the solutions. Tables 6.2(a), (b) show the effect of the mesh size and the axial grid expansion factor on the moment coefficient calculations for a system with zero throughflow where $\lambda = 60^{\circ}$, $a = 0$, $Re = 10^6$ and $d/b = 0.16$. The tables show the non-dimensional near-wall grid spacing, YP, at four radial locations in each case, defined as

$$YP = \frac{(\Delta n)_0}{\nu}\sqrt{\frac{|\tau_{\theta,o}|}{\rho}}\,, \qquad (6.4.1)$$

where $(\Delta n)_0$ is the distance between the rotor and the first grid point. For the results shown in Table 6.2(a), the axial expansion factor is held fixed and the mesh size is increased, whereas for the results shown in Table 6.2(b), the mesh size is fixed and the expansion factor is increased. The effect of increasing the mesh size or increasing the expansion factor is to reduce $(\Delta n)_0$ and hence to reduce YP. The Tables show that the moment coefficient (or wall shear stress) is sensitive to the grid spacing and that to achieve a grid-independent solution requires $YP < 1$. This means that the first grid point should be well inside the laminar sub-layer, which would be expected to extend to $YP = 5$ (see equation (5.3.27)). Figure 6.11 shows radial velocity profile plots at $r_0/b = 0.8$, which indicate that only the results for the coarsest two grids are noticably affected by grid refinement error. The above findings are consistent with those of Chew and Vaughan (1988) for a rotor-stator disc system. For subsequent turbulent runs it was ensured that $YP < 1$ at all radial locations.

The experimental data and numerical predictions are compared in Figures 4.10(a), (b), Figures 4.11(a)-(c) and Figures 4.12(a), (b). Overall the agreement between theory and experiment is good, the maximum relative error for all the comparisons is about 14% which occurs in Figure 4.11(c) at the higher Reynolds number. The agreement between theory and experiment generally appears to be worst when $\lambda = 75^\circ$ or 60° (see Figures 4.10(a), (b)). Figures 4.10(a), (b) show that although the overall agreement is good, the trend of the experimental data is different from the trend of results predicted by

the finite difference program. The trend predicted by the finite difference program is in fact similar to the trend predicted by the integral method. Figures 6.12(a)-(f) and Figures 6.13(a), (b) show predicted streamline plots for some of the turbulent cases, which indicate that for all values of λ the predicted secondary flow pattern is of the large scale disc-type as assumed in the integral method (see Figure 3.2). This helps to explain the similar Cm versus λ trends predicted by the integral method and the finite difference program as shown in Figures 4.10(a), (b). It is noticable that for $\lambda > 60^{\circ}$, Figures 4.10(a)-(f) show that the experimental data follow a trend similar to the integral method predictions, but not for $\lambda < 45^{\circ}$. As already stated in the previous sub-section, this difference in trend is likely to be due to the presence of Taylor-type vortices in the flow when $\lambda < 45^{\circ}$. Yamada and Ito (1975) observed vortices emerging even in turbulent flow; this observation is supported by the experimental work of Burkhalter and Koschmeider (1973) who observed Taylor vortices in rotor-stator cylinder systems even in fully turbulent flow. The moment coefficient data and the streamline plots show that the finite difference method is not predicting any form of secondary flow other than the disc-type in the turbulent regime and this would explain the poor agreement for $\lambda < 45^{\circ}$. The failure of the program to predict these vortices could be due to the fact that they are non-axisymmetric (Yamada and Ito (1975) and Wimmer (1983) reported the occurence of spiral shaped vortices) or unsteady.

Figures 4.10(a), (b) indicate that for $\lambda > 60^{\circ}$, both the integral method predictions and the experimental data produce a monotonically increasing moment coefficient trend. In contrast, for $\lambda > 60^{\circ}$, the values for Cm predicted by the finite difference program peak at around 60° to 75°. The experimental apparatus used by Yamada

and Ito (1975, 1979) is such that a half cross-section of the cavity is a parallelogram similar to that assumed by the integral method. The finite difference solution domain is however rectangular and is shown super-imposed on the integral method and experimental domains in Figure 6.14. It can be seen from the figure that in the experimental and integral method domains fluid flows directly from A to B, whereas in the rectangular finite difference domain, the fluid flows across a longer path ACB. Thus the effect of the rectangular domain on the flow is to channel fluid across a further distance causing the fluid to lose more angular momentum. The rectangular domain effectively increases the gap width between the rotor and stator, this effect reaching a maximum at $\lambda = 45^{\circ}$. Figures 4.10(a)-(f) show that Cm increases as the gap width increases, so that for $\lambda < 90^{\circ}$, the finite difference predictions for Cm would be expected to be larger than the integral method predictions and the experimental data. This expected difference in predictions is illustrated by the different Cm versus λ trends shown in Figure 4.10(a), (b). In §7.4 the integral method will be modified to account for the effect of a rectangular outer shroud.

Figure 6.14 shows that the inner boundary at $r = a$ (or $s = a/\sin\lambda$ in the finite difference domain) is also different in each case. In the experiments, this would be a free boundary whereas in the finite difference program the boundary at $s = a/\sin\lambda$ is modelled as a fixed boundary where $u = v = w = 0$. This difference in boundary conditions would not however be expected to contribute to appreciable differences in the moment coefficient, since in the proximity of this boundary, the velocities and distance to the axis of rotation (about which moments are taken) are small. This conclusion is supported by the results of two sets of runs both of which were performed for the $\lambda = 90^{\circ}$ flow conditions which produced the results shown in Figures

4.10(a), (b). For one run, the boundary at $s = a/\sin\lambda$ was treated as fixed ($u = v = w = 0$ at $s = a/\sin\lambda$) and for the other run the boundary was treated as a free-boundary where

$$u = v = 0, \quad \frac{dw}{dr} = 0 \quad \text{at} \quad s = 0 \; . \tag{6.4.2}$$

The moment coefficient was found to be identical (to 3 significant figures) when either the fixed or free-boundary conditions were used.

For $\lambda > 60^{\circ}$ and $Re < 2 \times 10^6$, Figures 4.10(a), (b) and Figures 4.11(a), (b) indicate that the finite difference program is tending to over-estimate the moment coefficient (with the exception of some points shown in figure 4.11(a) where the agreement is excellent anyway). A possible reason for this is the setting of the exponent e in the turbulence model (see equation (6.2.14)) equal to zero. Figure 4.10(b) shows the results of setting $e = 0.75$ for the $\lambda = 30^{\circ}$ and $\lambda = 60^{\circ}$ cases. As can be seen the non-zero value of e has the effect of reducing the moment coefficient by 6.8% and 2.5% respectively. Chew and Vaughan (1988) reported that e has a smaller effect at higher Reynolds numbers; this is supported by the result shown in Figure 4.11(b) where setting $e = 0.75$ at $Re = 4 \times 10^6$ reduced the moment coefficient by only 0.5%. The above results illustrate that a non-zero value of e may result in a slight improvement in the agreement between the predicted and the experimentally determined moment coefficient, although it is not a critical factor, especially at higher Reynolds numbers.

6.4.3 Conclusions

The laminar flow comparisons of §6.4.1 provide evidence for the following conclusions to be drawn about the predictive capability of the program.

(i) In agreement with the experimental work of Kreith et al (1963), the program predicts a decreasing transition Reynolds number with decreasing cone angle.

(ii) The comparisons of predicted moment coefficient with the experimental data of Yamada and Ito (1975) supports their conclusion that the transition Reynolds number increases as the gap width decreases.

(iii) For small cone angles ($\lambda < 45^{\circ}$), Yamada and Ito (1975) report that Taylor-type vortices may be present in the flow which have the effect of increasing the moment coefficient. The finite difference program predicts only a maximum of two extra vortices (other than the main disc-type secondary flow), and these do not seem to significantly increase the predicted moment coefficient.

The turbulent flow comparisons of §6.4.2 provide evidence for the following conclusions.

(i) For $\lambda > 60^{\circ}$, the predicted moment coefficient is in reasonable agreement with the experimental data of Yamada and Ito (1975, 1979). The differences for $\lambda = 60^{\circ}$ and $\lambda = 75^{\circ}$ may be attributed mainly to the differences in the experimental apparatus and the numerical solution domain.

(ii) For $\lambda < 45^{\circ}$, the error between the predicted moment coefficient

and the experimentally obtained values of Yamada and Ito (1975, 1979) indicate a reasonable agreement for any particular value of λ, although there are marked differences in the Cm versus λ trends. This trend difference can be attributed to the failure of the finite difference program to predict Taylor-type vortices in the flow, which is likely to be due to the fact that the vortices are non-axisymmetric or unsteady.

The experimental results have been restricted to one source, so the possibility of experimental error should not be ruled out. The peak in the experimental moment coefficient data for large d/b at $\lambda = 30^{\circ}$ is unexpected since it would seem likely that Taylor-type vortices should have an even larger effect at smaller cone angles. However, this peak is apparent on a number of Yamada and Ito's graphs for a wide range of Reynolds numbers, which suggests some credibility in the results. Further experimental work, particularly concerning more detailed flow visualisations for small angled cones would clearly be benificial.

It is perhaps a little disappointing that the finite difference program described in this chapter failed to provide appreciably better moment coefficient predictions than the integral method described in chapters 3 and 4. As the streamline plots in Figures 6.12(a)-(f) and Figures 6.13(a)-(b) show, the finite difference program has predicted a similar flow pattern for all values of λ tested as assumed in the integral method described in chapter 3. This has resulted in the two methods predicting similar Cm versus λ trends as illustrated in Figures 4.10(a), (b). As already discussed, it is possible that the experimental data is in error, in which case it is worth using the finite difference program results to examine the integral method

assumptions in more detail. This work will be described in the next chapter.

6.5 SUMMARY

This chapter has been concerned with an investigation of the capability of a finite difference program to predict the flow in rotor-stator cone systems.

A brief description of the program was given in §6.2. The original program solved the flow and energy equations in a plane disc geometry. The steps taken to ensure the modifications had been coded correctly were described in §6.3.

The predictive capability of the program was assessed in §6.4 by comparing the predicted results with experimental data and previously obtained integral method results.

CHAPTER 7

MODIFICATIONS TO THE INTEGRAL METHOD

7.1 INTRODUCTION

In §4.6 it was shown that the integral method based on an adaptation of the method of Chew (1989) predicted the moment coefficient in excellent agreement with Yamada and Ito (1975) when $\lambda > 60^{\circ}$. It was also shown that when $\lambda < 45^{\circ}$, the agreement was poor. Ideally, the integral method should be adapted so that the moment coefficient predictions are in better agreement at the smaller cone angles. However, the integral method can only be used if the secondary flows are relatively simple; boundary layers must be formed over the rotor and stator and the radial and tangential velocity components must be capable of being written as a product of a function of s and a function of n (see equations (3.4.14) and (3.4.15)). As discussed in §6.4, the evidence from flow visualisations and plots of experimental moment coefficient versus λ curves suggests that for $\lambda < 45^{\circ}$, the mode of secondary flow changes and Taylor-type vortices are present in the flow. Flows in which Taylor-type vortices are present would not be amenable to analysis by the integral method.

Unfortunately the presence of Taylor-type vortices, or any type of secondary flow other than the disc-type secondary flow has not been confirmed by the finite-difference method (except for the occurence of one or two vortices shown in Figures 6.10 at relatively low Reynolds numbers). As already stated, this could be due to the fact that such

vortices are non-axisymmetric (i.e. spiral-shaped) or unsteady. It is possible, though, that the experimental data referred to is in error for small cone angles, and without further experimental evidence the possibility exists that the finite difference program is correctly predicting the flows at small cone angles. It is worthwhile therefore using the program to examine the assumptions made in the integral method in such cases. There is also the possibility that for $\lambda>60^{\circ}$, the assumptions of the integral method are wrong and that it is giving excellent moment coefficient predictions for other reasons. The finite difference program may then be used to help confirm that for $\lambda>60^{\circ}$ the assumptions are valid. For the above reasons, in §7.2, the results generated by the finite difference program will be used to investigate the integral method assumptions described in chapter 3.

In §7.3 and §7.4, modifications to two aspects of the present integral method will be described. Firstly, in §7.3 an alternative stator model will be described and secondly in §7.4, a simple modification to account for a 'rectangular' outer shroud rather than a shroud parallel to the axis of rotation, as currently assumed in the integral method, will be presented.

7.2. THE INTEGRAL METHOD ASSUMPTIONS

7.2.1 General Flow Structure

The secondary flow pattern which was assumed when using the integral method described in chapter 3 is shown in Figure 3.2. The principal assumptions which were made about the flow will be summarised here again for reference.

(i) For cases with an imposed throughflow, there is a source region where fluid is entrained into a boundary layer on the rotor. This

region continues until the mass flow rate on the rotor equals the specified throughflow rate. Beyond this region there is a core region.

(ii) In the core region, fluid is continually entrained into the rotor boundary layer and is then channelled across the outer shroud and back down in a boundary layer on the stator.

(iii) Between the rotor and stator boundary layers there is an inviscid rotationally dominated core.

(iv) For cases with no throughflow, there is no source region and the core region fills the entire cavity.

The streamline plots shown in Figures 6.12 and 6.13 show that the finite difference program predicts a flow structure very similar to that described above. The u(s,n) and v(s,n) velocity profiles across the cavity at constant s (where $s = r_0 \sin\lambda$) shown in Figures 7.1 (a), (b) and Figures 7.2 (a), (b) confirm the formation of boundary layers on both the rotor and stator, in which the flow is outward on the rotor and inward on the stator. The assumption that in the core region the flow between the rotor and stator is inviscid and rotationally dominated led to the derivation of equations (3.5.9) and (3.5.10). Equation (3.5.9) states that the tangential velocity should be constant between the two boundary layers at constant r (where $r = s \sin\lambda + n \cos\lambda$), and this has been predicted to a good approximation by the finite difference program, as indicated by the examples shown in Figure 7.3. Equation (3.5.10) indicates that at each boundary layer edge, the u(s,n) velocity component should be non-zero for cases when $\lambda \neq 90^{\circ}$. As an approximation these non-zero boundary layer edge components were neglected (see equations (3.4.13) and (3.7.6)). The u(s,n) velocity profiles shown in Figures 7.1 (a), (b) show that if the boundary layers are assumed to extend far enough from the walls, then even for small λ the above approximation appears to be

valid.

7.2.2 Compressibility

In §3.6 it was assumed that the isothermal flows were imcompressible. The validity of this assumption will be assessed using the finite difference program for one particular rotor-stator system for three different Reynolds numbers. The effect of compressibility in non-isothermal systems has already been discussed in chapter 5. In an isothermal system, compressibility will have a greater effect on the flow at higher values of Reynolds number, where pressure differences through the cavity will be greater. A comparison of the moment coefficients predicted by the finite difference program when the flow is treated as incompressible and compressible is shown in Table 7.1, for three different Reynolds numbers for a particular rotor-stator system. The table shows that at the highest Reynolds number the difference in predicted moment coefficients is significant. It may be noted that accounting for compressibility for the $Re = 4 \times 10^6$ case results in a worse agreement with the experimentally obtained value for the moment coefficient of 1.93×10^{-3} (from Yamada and Ito (1975)). The reason for the poorer agreement is to be expected since the test fluid in Yamada and Ito's experiments was either water, a mixture of water and glycerin or spindle oil, all of which would be less susceptible to changes in density compared with the perfect gas assumed in the finite difference program.

Figure 7.4(a) shows profiles of density across the cavity at three radial locations for the $Re = 4 \times 10^6$ case in Table 7.1. All of them confirm that the assumption in §3.6 of constant density across

the boundary layers appears to be valid. Figure 7.4(b) shows longitudinal density plots through the rotor boundary layer at three axial locations. These show a significant density variation which would be responsible for the change in the predicted moment coefficient. Also shown in Figure 7.4(b) is the longitudinal density variation predicted by the integral method when using equation (5.4.10), with T_m constant and $dT_m/dx=0$, to predict the density. The figure shows that the integral method over-estimates the density but it predicts a similar trend to that of the finite difference program. A consequence of this over-estimation is that the integral method over-predicts the moment coefficient, giving a value of 2.48×10^{-3} which corresponds to a 13% error relative to the value of 2.20×10^{-3} predicted by the finite difference program. The reason why the integral method over-estimates the density is that it slightly over-estimates the boundary layer edge velocity, $\bar{V}(x)$, which from equation (5.4.10), results in a higher density prediction.

The examples considered above indicate that the assumption of constant density across the boundary layers is justified but caution is required when assuming a constant longitudinal density at higher Reynolds numbers.

7.2.3 Surface Shear Stress Assumptions

In §3.4 a formula for the surface shear stress on the rotor and stator was found using the empirical Blasius law of friction. The final form of the shear stress relation (equation (3.4.11)) was obtained assuming the boundary layer velocity components obeyed a $1/7^{th}$ power law (i.e. equation (3.4.7) with m = 7). Following

Schlichting (1968), the Blasius law, may be extended to account for a general power index. The surface shear stress relation (3.4.11) may be written as

$$\tau_0(s) = k_m \rho \lim_{n\to 0} \left\{ U_{res}^{2m/(m+1)} \left[\frac{\nu}{n}\right]^{2/(m+1)} \right\} , \qquad (7.2.1)$$

where k_m takes the values 0.0225, 0.0247 and 0.0258 for m = 7,8 and 9 respectively. In general, $f(\eta)$ and $g(\eta)$ in equations (3.4.16) may be replaced by the general power law formulae

$$f(\eta) = \eta^{1/m} (1-\eta) , \qquad g(\eta) = 1-\eta^{1/m} , \qquad (7.2.2)$$

and the limiting behaviour of $f^s(\eta)$ as $\eta \to 0$, i.e. equation (3.7.7), may be replaced by

$$f^s(\eta^s) \to (\eta^s)^{1/m} \quad \text{as } \eta^s \to 0 . \qquad (7.2.3)$$

If equations (7.2.2) are used in the surface shear stress formula (7.2.1), the following shear stress equation for the rotor is obtained:

$$\tau_0(s) = k_m \rho \left[\frac{\nu}{\delta}\right]^{2/(m+1)} \{\tilde{u}^2 + (v_0-\bar{v})^2\}^{m/(m+1)} . \qquad (7.2.4)$$

A similar formula may be obtained for the stator.

The finite difference program may be used to assess the validity of equation (7.2.4) for different values of m. The right hand side of equation (7.2.4) can be calculated using the definition of the boundary layer thickness appropriate to the mixing length in equation (6.2.15). The value of $\bar{v}(s)$ or $\bar{v}^s(s)$ can be obtained from the tangential velocity at this boundary layer edge position and $v_0(s)$ is

the value on the surface of the rotor. From equation (3.4.14), the value of $\tilde{u}(s)$ at a particular s location is given by

$$\tilde{u}(s) = \frac{[u(s,\eta)]_{max}}{f(\eta)_{max}} \quad , \tag{7.2.5}$$

where the subscipt 'max' denotes the maximum value obtained within the boundary layer at a particular s location. From equation (3.7.17) the value of $\tilde{u}^s(s)$ is

$$\tilde{u}^s(s) = -0.364\ \tilde{v}^s(s) \quad . \tag{7.2.6}$$

The left hand side of equation (7.2.4) may be obtained from the actual surface shear stress as predicted by the finite difference program. Thus for the rotor, the left hand side of equation (7.2.4) may be calculated from

$$\tau_0 = \mu \left[\left[\frac{\partial u}{\partial n}\right]^2 + \left\{ r\frac{\partial}{\partial n}\left[\frac{v}{r}\right] \right\}^2 \right]_{n=0}^{1/2} , \tag{7.2.7}$$

and a similar equation may be formulated for the stator.

Use of the finite difference program to evaluate equation (7.2.4) can only lead to an approximate assessment of the validity of the Blasius shear stress law, since through the use of equations (7.2.5) and (7.2.6) it is implicitly assumed that the finite difference program will predict the particular separable forms of the velocity components (equations(3.4.14), (3.4.15) and (3.7.5)). In evaluating equation (7.2.4) a suitable value for the boundary layer thickness is required. The definition of the boundary layer thickness used in the mixing length turbulence model of the finite difference

method is not appropriate for the integral method where a more appropriate definition would be the normal distance from the rotor or stator over which all the flow in the s-direction occurs. Figures 7.1(a), (b) show that next to the region of the flow directed inwards on the stator, there is a region where the flow reverses direction and flows outwards. This region should be accounted for in the stator boundary layer definition used in the integral method since a radial mass flux balance between the rotor and stator boundary layers is essential to the method. The boundary layer definition used by the finite difference method tends to underestimate this distance. In practice, the finite difference method predicts the edge of the boundary layer to be (approximately) at the distance from the stator where the s-velocity first becomes zero. Thus from Figures 7.1(a), (b), this boundary layer thickness could be as small as half of that which is a definition appropriate for the integral method. However, the discrepancy should not have too significant an effect on the Blasius shear stress formula, because of the $2/(m+1)$ index occuring on the right hand side of equation (7.2.4). For the above reasons and for coding simplicity, the boundary layer thickness as predicted by the finite difference method was used in evaluating the shear stress from equation (7.2.4).

Figures 7.5(a), (b) show typical comparisons of the surface shear stress on the rotor predicted by equation (7.2.7) and by equation (7.2.4) for m = 7,8 and 9. The figures show that the Blasius law predictions using equation (7.2.4) exhibit a similar trend to the finite difference predictions using equation (7.2.7). The figures also show that the $1/7^{th}$ law gives the best fit, particularly in Figure 7.5(a) where the Reynolds number is highest ($Re = 4 \times 10^6$ in Figure

7.5(a)). This improved agreement for higher Reynolds numbers is reflected in the moment coefficient comparisons in Figures 4.11 (a) - (c) where the agreement between the integral method and the finite difference program improves as the Reynolds number increases. Figures 7.6(a), (b) show similar comparisons for the stator. Again the $1/7^{th}$ law gives the best predictions, and the comparison is particularly good for the higher Reynolds number as illustrated in Figure 7.6(a).

The comparisons shown in Figures 7.5 and 7.6 can only be used as a rough guide to the validity of the shear stress law, nevertheless very good agreement when using the $1/7^{th}$ power law has been shown, especially at higher Reynolds numbers. This is particularly encouraging since Reynolds numbers of this size and above are likely to be encountered in the aero-engine.

7.2.4 Velocity Profiles

In §3.4 the velocity profiles in the rotor boundary layer were assumed to be generalisations of those used by von Karman (1921), and are given by equations (3.4.14)-(3.4.16). The functional forms of $f(\eta)$ and $g(\eta)$ given by equations (3.4.16) cannot be valid near to the rotor surface since they predict an infinite surface shear stress. However, it would be expected that the profiles are valid throughout most of the remaining boundary layer. It was also assumed in §3.7 that the same tangential velocity profile as that given by equations (3.4.16) was valid in the stator boundary layer. In this sub-section, the finite difference results will be used to assess the validity of the above assumed velocity profiles. The assumptions used to formulate the stator model, in particular the radial velocity in the stator boundary

layer described in §3.7, will be discussed in §7.3.

The validity of the $1/7^{th}$ power law used in the tangential velocity profile in equations (3.4.16) may be most effectively assessed using log plots, where the $1/7^{th}$ law will be represented by a straight line. Some typical profiles across both the rotor and stator boundary layers are shown in Figures 7.7(a)-(d) for a variety of rotor-stator cone systems at three different radial locations. It is apparent from the figures that, even for small cone angles, the $1/7^{th}$ power law is a good representation of the profiles throughout most of the boundary layers (whose thickness will typically be of the order 10% of the gap width, d).

As discussed in §3.4, the simple multiplying factor $(1-\eta)$ present in $f(\eta)$ in equations (3.4.16) was used by von Karman (1921) to force the radial velocity to zero at the boundary layer edge. A more general formula for $f(\eta)$ is

$$f(\eta) = \eta^{1/7} (1-\eta)^M , \qquad (7.2.8)$$

where M is a constant which may be varied in order to determine the value which gives the best agreement with the finite difference results. Figures 7.8(a)-(d) show a selection of finite difference velocity profiles across the rotor boundary layer compared with profiles using equation (7.2.8) with M equal to 0.5, 1 and 2. The boundary layer thickness, δ, in the figures is defined as the distance from the rotor to the point where the radial velocity first becomes approximately zero. The figures show that for all values of λ considered, the value of $M = 1$ in equation (7.2.8), as used by von Karman (1921), appears to give the best agreement with the finite difference results.

The above results show that the assumed velocity profiles of chapter 3 are in good agreement with those predicted by the finite difference method. The comparisons show that even for small cone angles, there is no evidence from the finite difference results to suggest any modifications to these profiles.

7.3 ALTERNATIVE STATOR MODEL

7.3.1 Discussion of the Model used in §3.7

The derivation of the integrated boundary layer equations for the stator boundary layer in §3.7 was based on the method of Chew (1988,1989). The equations were derived from a consideration of analytical solutions to the problem of an infinite rotor-stator cone system with no throughflow. The assumptions which were made about the flow in an infinite system were based on the experiments of Daily and Nece (1960) and the finite difference results of Chew (1987) and for ease of reference are summarised below.

(i) A boundary layer develops on both the rotor and the stator separated by a uniformly rotating inviscid core which rotates with an angular velocity of approximately 0.42 times the rotor angular velocity.

(ii) The fluid velocity relative to both the rotor and stator is at a limiting flow angle γ (or γ^S), such that

$$\tan\gamma = \lim_{n\to 0}\left[\frac{u}{v_0-v}\right] = 0.364 \quad . \tag{7.3.1}$$

(iii) The ratio of the stator boundary layer thickness, δ^S, to the rotor boundary layer thickness, δ, is approximately 1.38 (or, equivalently, $\delta_1^S = 1.38\delta_1$).

The present finite difference results will now be used to discuss the validity of the above three assumptions when applied to cone rotor-stator systems.

(i) Figures 7.9(a), (b) show profiles of $v/(\Omega r)$ against r_0/b where v is evaluated at n=d/2. The graphs show that $v/(\Omega r)$ is approximately constant for all values of λ considered and that the value of $v/(\Omega r)$=0.42 is also a fairly good approximation.

(ii) Profiles of $\tan\gamma$ and $\tan\gamma^S$ against r_0/b are shown in Figures 7.10(a)-(c) and Figures 7.11(a)-(c) respectively. Figures 7.10(a), (b) and Figures 7.11(a), (b) show that for zero throughflow cases, $\tan\gamma$ and $\tan\gamma^S$ tend to attain a constant value at higher values of r_0/b which would correspond to higher values of a local Reynolds number for all values of λ considered. The figures also show that a value of 0.364 ($\approx\tan20^\circ$) is a fairly good approximation to this constant value. Figure 7.11(c) shows that the variation of $\tan\gamma^S$ with r_0/b is more erratic for cases with throughflow, a result also found by Chew (1988).

(iii) Defining the boundary layer thickness as the region within which all the secondary flow occurs, Figures 7.1(a), (b) show that as λ decreases, the boundary layer thicknesses on both the rotor and stator increase in such a way that the ratio δ/δ^S is approximately independent of λ. If the edge of the boundary layers are defined as the points outside of which there is no secondary flow, then Figures 7.1(a) and (b) show that the ratio δ/δ^S should lie between 2 and 3.

It is evident from the above results that the finite difference program predicts values for $\bar{v}/(\Omega r)$, $\tan\gamma$, $\tan\gamma^S$ and δ/δ^S which are fairly independent of λ. This simplifies the stator model since no special considerations are required to account for different cone angles. The results also show that the assumption $\delta^S=1.38\delta$ tends to

underestimate the size of the stator boundary layer. From the finite difference results it appears that the weakest assumption of the model is that $\tilde{u}^s(s)$ in equation (3.7.5) can be calculated from equation (7.3.1) for all throughflow rates. To improve on this aspect of the model, both the radial and tangential momentum equations would need to be retained, instead of replacing the radial momentum equation with equation (7.3.1). This would enable a solution to be found for $u^s(s)$ which could vary according to the problem being considered. To retain both the momentum equations, the radial and tangential velocity components need to be expressed explicitly in a similar way to that shown in equations (3.4.14) and (3.4.15). The following sub-section describes the derivation of explicit profiles for $f^s(\eta^s)$ and $g^s(\eta^s)$ which may be used to express the η^s dependence in the stator radial and tangential velocity components.

7.3.2 Description of the New Model

The particular forms of the profile functions $f^s(\eta^s)$ and $g^s(\eta^s)$ used here are chosen so as to model the profile behaviours evident in Figures 7.1 and 7.2. Examination of the radial profiles adjacent to the stator in Figures 7.1(a), (b) show that the profile function $f^s(\eta^s)$ should change sign to incorporate the region of reverse flow and so it is assumed that the radial velocity in the stator boundary layer, $u(s,\eta^s)$, can be expressed in the form

$$u_s(s,\eta^s) = \tilde{u}^s(s)\ f^s(\eta^s), \qquad (7.3.2)$$

where

$$f^s(\eta^s) = (\eta^s)^{1/7}\ (1-\eta^s)\ (\alpha_1-\eta^s), \qquad \eta^s=(d-n)/\delta^s\ , \qquad (7.3.3)$$

and α_1 is a constant such that $0 < \alpha_1 < 1$.

Examination of the tangential velocity profiles adjacent to the stator in Figures 7.2(a), (b) shows that the tangential velocity profile reaches a maximum which is significantly greater than the core velocity. (It may be noted that a similar phenomenon is observed next to the rotor, although here the difference between the minimum tangential velocity and the core tangential velocity is less significant than in the stator case). To account for this peak in tangential velocity it is assumed that the tangential velocity in the stator boundary layer, $v^s(s,\eta^s)$, can be expressed in the form

$$v^s(s,\eta^s) = \bar{v}^s(s)\ [1-g^s(\eta^s)]\ , \qquad (7.3.4)$$

where

$$g^s(\eta^s) = 1 - \alpha_2(\eta^s)^{1/7} + (\alpha_2-1)\eta^s\ , \qquad (7.3.5)$$

and α_2 is a constant greater than one so that $v^s(s,\eta^s)$ has a maximum above $\bar{v}^s(s)$. The functions $f^s(\eta^s)$ and $g^s(\eta^s)$ shown in equations (7.3.3) and (7.3.5) satisfy the required boundary conditions of $u_s(s,0) = u_s(s,1) = v^s(s,0) = 0$ and $v^s(s,1) = \bar{v}^s(s)$ and they also exhibit a $1/7^{th}$ power law behaviour as $\eta^s \to 0$, so that the Blasius shear stress law (3.4.11) will still hold. Using equations (7.3.3) and (7.3.5), the surface shear stress formulae (3.4.18) and (3.4.19) become

$$\tau^s_{\theta,0} = 0.0225\ \rho \left[\frac{\nu}{\delta^s}\right]^{1/4} \alpha_2\ \bar{v}^s\ [(\alpha_1 u^s)^2 + (\alpha_2 \bar{v}^s)^2]^{3/8} \qquad (7.3.6)$$

and

$$\tau^s_{s,0} = \frac{\alpha_1 u^s}{\alpha_2 \bar{v}^s}\ \tau^s_{\theta,0}\ . \qquad (7.3.7)$$

Substituting the above shear stress formulae into the integrated boundary layer equations (3.6.4) and (3.6.5) and setting $v_0=0$, which is appropriate for the stator, two equations for the stator boundary layer are obtained. Non-dimensionalising these equations using equations similar to (3.6.14) the following equations are obtained:

$$\frac{I^s_{ff}}{x^3}\frac{d}{dx}[x^4(u_1^s)^2\delta_1^s] + \delta_1^s(\bar{V}^s)^2[2I^s_g - I^s_{gg}]$$

$$= -\frac{0.0225\ \alpha_1 u_1^s\ [(u_1^s\alpha_1)^2 + (\alpha_2\bar{V}^s)^2]^{3/8}}{(x^2\delta_1^s)^{1/4}}\ , \qquad (7.3.8)$$

and

$$-\frac{I^s_{fg}}{x^4}\frac{d}{dx}(x^5u_1^s\delta_1^s\bar{V}^s) + \frac{\delta_1^s u_1^s}{x}\ I^s_f\ d\ (x^2\bar{V}^s)$$

$$= \frac{-0.0225\ \alpha_2\bar{V}^s[(\alpha_1u_1^s)^2 + (\alpha_2\bar{V}^s)^2]^{3/8}}{(x^2\delta_1^s)^{1/4}}\ , \qquad (7.3.9)$$

where I^s_f, I^s_g etc. are constants defined in a similar way to those in equations (3.6.6).

The constants α_1 and α_2 which now appear in the expressions for I^s_f, I^s_g etc. and in equations (7.3.8) and (7.3.9) may be calculated using the analytical solutions for an infinite rotor-stator system (c.f. §3.7). Following the approach of §3.7, it is assumed that in an infinite rotor-stator cone system, the rotor and stator boundary layers are separated by a uniformly rotating core. In this case $\bar{v}^s=k\Omega r$ where k is a constant and choosing $\beta^s=k\Omega$, the analytical solutions to equations (7.3.8) and (7.3.9) are

$$(u_1^s) = -\left[\frac{(I^s_{gg}-2I^s_g)\alpha_2}{3.6I^s_{ff}\alpha_2 + (4.6I^s_{fg}-2I^s_f)\alpha_1}\right]^{1/2}\ , \qquad (7.3.10)$$

and

$$(\delta_1^S x^{0.4}) = \left[\frac{0.0225\ \alpha_2[(\alpha_1 u_1^S)^2 + \alpha_2^2]^{3/8}}{u_1^S(4.6I_{fg}^S - 2I_f^S)}\right]^{4/5} \qquad (7.3.11)$$

Two relationships will now be used to find α_1 and α_2. Firstly, the mass balance condition (i.e. mass outflow on the rotor must be balanced by a mass inflow on the stator) gives

$$\frac{\delta_1^S}{\delta_1} = -\frac{(1-k)u_1 I_f}{k u_1^S I_f^S}, \qquad (7.3.12)$$

where u_1 and δ_1 are the analytical solutions to the rotor boundary layer equations and are given by equations (3.7.2) and (3.7.3). Secondly, the limiting flow angle, which has been shown by the present finite difference results to have a fairly constant value for zero throughflow cases, may be derived from equation (7.3.1) as

$$\tan\gamma^S = -\frac{\alpha_1 u_1}{\alpha_2}. \qquad (7.3.13)$$

Given values for $\tan\gamma^S$ and k, equations (7.3.12) and (7.3.13) are two non-linear equations which, provided real solutions exist, may be solved for α_1 and α_2. The method of finding α_1 and α_2 used here though, recognises the fact that the values of $\tan\gamma^S$=0.364 and k=0.42 used previously can only be approximate and the required values of α_1 and α_2 are found numerically as follows.

Firstly upper and lower bounds are placed on α_1 and α_2:

$$0 < \alpha_1 < 1 \ , \tag{7.3.14}$$

and

$$1 < \alpha_2 < 5 \ , \tag{7.3.15}$$

The upper and lower bounds imposed on α_1 follow immediately from equation (7.3.3). The constant α_2 is given an upper bound of 5 since for values larger than this, it may be shown from equation (7.3.5) that the maximum value of $v(s,\eta^s)$ attained within the stator boundary layer is greater than three times $\bar{v}^s(s)$, which from Figures 7.2(a), (b) would seem to be unreasonable. The constants α_1 and α_2 are assigned all values (to a specified accuracy) between the bounds imposed by equations (7.3.14) and (7.3.15) and if real solutions exist, equations (7.3.10) and (7.3.11) are solved for u_1^s and δ_1^s respectively. The values obtained for u_1^s are substituted into equation (7.3.13) to find the value of $\tan\gamma^s$ and if this is within 5% of 0.364, the value of k required to satisfy the mass balance equation (7.3.12) (to a tolerance of 1%) is found. An additional criterion used was that $2 < \delta_1^s/\delta_1 < 3$, which follows from the finite difference results. One value of α_2 and two values of α_1 were found such that $\tan\gamma^s$ was within 5% of 0.364 and $2 < \delta_1^s/\delta_1 < 3$. The final values chosen were α_1= 0.580 and α_2=1.35 which required a value of k= 0.393 to satisfy the mass balance equation (7.3.12) which is reasonably close to the previously chosen value of k=0.42. Using these values for α_1, α_2 and k it was found that $\tan\gamma^s$=0.382 and δ_1^s/δ_1=2.80.

Figures 7.12(a), (b) show graphs comparing the finite difference radial velocity predictions with those from equation (7.3.2) with α_1=0.580 and Figures 7.13(a), (b) show similar comparisons for the tangential velocity with α_2=1.35 in equation (7.3.5). The graphs show

a fairly good agreement between the finite difference predictions and the new velocity profiles. These velocity profiles will now be used in the stator equations to solve general rotor-stator flow problems. With α_1=0.580 and α_2=1.35, the constants in equations (7.3.8) and (7.3.9) take the following values:

I_f^s=8.836 x 10^{-2}, I_g^s=-6.250 x 10^{-3}, I_{ff}^s=2.447 x 10^{-2}, I_{gg}^s=4.833 x 10^{-3} and I_{fg}=4.928 x 10^{-3}.

A comparison between the results obtained using this stator model and the previous model of §3.7 will now be made.

7.3.3 Comparison of the Models

A comparison will be made between the results obtained from the integral method using the old stator model (old integral method) and the integral method using the new stator model (new integral method) with the finite difference results and the experimental results of Yamada and Ito (1975,1979). A stator moment coefficient, C_m^s, is defined in a similar way as the rotor moment coefficient, i.e. C_m^s is defined as

$$C_m^s = \frac{2M^s \sin\lambda}{\rho\Omega^2 b^5} \quad , \tag{7.3.16}$$

where M^s is the moment on the stator which is calculated from

$$M^s = \int_{a/\sin\lambda}^{b/\sin\lambda} 2\pi r_0 \, \tau_{\theta,0}^s \, ds \quad . \tag{7.3.17}$$

The rotor moment coefficients are compared in Figures 7.14(a)-(d) and the stator moment coefficients are compared in Figures

7.15(a)-(d). The agreement for the rotor moment coefficient between those predicted by the finite difference program and the new integral method is shown to be better in all cases except for those shown in Figure 7.14(c) at higher Reynolds numbers. A comparison of the predicted rotor moment coefficients with the experimental results of Yamada and Ito (1975,1979) does not show any marked improvement with the new integral method. In all cases the new integral method predicts a higher rotor moment coefficient than the old integral method, which is a consequence of the new method predicting a lower $\bar{V}(x)$ distribution as shown by the examples in Figures 7.16(a), (b).

Figures 7.15(a)-(d) show that the new integral method tends to produce stator moment coefficients in better agreement with those predicted by the finite difference program than the old method. Figures 7.15(a), (b) show a different trend in Cm^S with λ to that predicted by the finite difference program. This is likely to be caused by differences between the finite difference solution domain and the integral method solution domain (see Figure 6.15). For small values of λ, the outer shroud over which the fluid flows from the rotor to the stator is smaller in the finite difference domain so that the fluid will have lost less angular momentum when it reaches the stator. This will result in an increase in the moment exerted by the fluid on the stator. The discrepancy in the predictions for the stator moment coefficients in throughflow cases may be expected to be larger since the integral method does not calculate the moment exerted on the stator at radial locations within the source region. However, the finite difference results for the surface shear stress shown in Figure 7.17 indicate that the shear stress in this region is much smaller than that in the core region, so that neglecting the contribution to the moment from this region will not greatly affect the overall moment.

A comparison of the predictions for the limiting flow angle, $\tan\gamma^s$, given by equation (7.3.1) is shown in Figures 7.18(a), (b). The zero throughflow case shown in Figure 7.18(a) illustrates that the new integral method gives an improved agreement with the finite difference method and that it correctly predicts the trend at lower radii. However, the throughflow case shown in Figure 7.18(b) indicates that the new integral method over-estimates $\tan\gamma^s$ predicted by the finite difference program at the lower radii.

7.3.4 Discussion

It has been shown that the new integral method tends to predict rotor and stator moment coefficients which are in slightly better agreement with those obtained using the finite difference method and experiment than the old integral method. However, the new integral method does under-predict the core tangential velocity, for which the experimental results of Daily and Nece (1960) for rotor-stator disc systems with zero throughflow provide further evidence of the accuracy of the finite difference predictions. This under-estimation could be a consequence of the values of α_1 and α_2 chosen, which as described in §7.3.2, required a value of k=0.393 (which is lower than the values of k=0.41 to k=0.46 which were obtained by Daily and Nece (1960)), to satisfy the mass balance requirement. It has also been shown that for throughflow cases, the new integral method over-predicts the limiting flow angle apparent from the finite difference results. This over-estimation at lower radii for throughflow cases, as shown in Figure 7.18(b), is perhaps an illustration of the weakness in developing a model from finite difference and experimental results with zero

throughflow and then applying the model to general throughflow cases. Further work will be required to develop an integral method which gives good predictions for quantities such as $\tan\gamma^s$ and Cm^s for general throughflow rates. However, considering the contrast in the fairly constant $\tan\gamma^s$ graphs shown in Figures 7.11(a), (b) compared with the erratic $\tan\gamma^s$ graphs shown in Figure 7.11(c), it is perhaps unlikely that a single simple model will be found which will be valid for cases with throughflow as well as cases with zero throughflow.

Considering the above results and the fact that for $\lambda>60^\circ$, the rotor moment coefficient was satisfactorily predicted by the old integral method, it would seem that the new stator model may only be worthwhile considering in preference to the old model if stator moment coefficient predictions are required.

7.4 THE SHROUD TREATMENT

The outer shroud channels fluid from the rotor boundary layer to the stator boundary layer, as illustrated by Figure 2.1(c) and Figure 3.2, and it has the effect of decreasing or increasing the angular momentum of the fluid as it travels from the rotor to the stator depending on whether it is stationary or rotating. As shown in Figure 3.2, for rotor-stator cone systems, the shroud is assumed to be parallel to the axis of rotation and in this section a simple modification will be explained to allow for the effect of a 'rectangular' outer shroud as assumed in the finite difference method and shown in Figure 6.1(b).

The effect of the rectangular domain is to channel fluid across a further distance, as shown by the dashed arrows in Figure 6.14 . The

rectangular domain effectively increases the gap width between the rotor and stator, which explains the Cm trend differences between the finite difference results and integral method seen for $\lambda > 60^{\circ}$ in Figures 4.10(a), (b). Considering the difference in the geometries of the two domains shown in Figure 6.14, it is clear that the 'apparent' shroud length, d', for the rectangular domain is related to the shroud length, d, of the original integral method domain, by the relation

$$d' = d\,(\cos\lambda + \sin\lambda). \qquad (7.4.1)$$

To account for a rectangular outer shroud in the integral method, the gap width, d, may simply be replaced by d' from equation (7.4.1). This correction should result in the Cm versus λ trend predicted by the finite difference program shown in Figures 4.13(a), (b) and, as shown in Figures 7.19(a), (b), this is found to be the case.

Although the effect of applying correction (7.4.1) is not great (the difference at $\lambda = 45^{\circ}$, where the correction has the greatest effect, for the two integral method solutions shown in Figure 7.19(a) is 4.0%), the principle of accounting for different shroud geometries by changing the gap width may presumably be extended to other situations where the effect may be greater.

7.5 SUMMARY AND CONCLUSIONS

In §7.2 it was shown that the results of the finite difference program have supported the integral method assumptions of chapter 3 and they have shown that the assumptions may be generalised to rotor-stator cone systems. However, as discussed in §6.4, the poor

agreement between the trend of the finite difference results and the trend of the experimental results for $\lambda<45^{\circ}$, raises doubts as to the validity of the finite difference results for small cone angles. Clearly, further experimental work is desirable to clarify the results referred to here which were restricted to one experimental source.

If the above discrepancies are due to the occurence of spiral-shaped or unsteady 'Taylor-type' vortices occuring in the flow when $\lambda<45^{\circ}$, the prediction of such flows will require the numerical solution of non-axisymmetric or unsteady partial differential equations. This will prove more costly. From the experimental evidence available, the conclusion that can be drawn at this stage is that the present integral method may be used with confidence to predict rotor-stator cone flows provided $\lambda>60^{\circ}$.

The treatment of the stator boundary layer in the integral method has proved somewhat difficult in the past and in §7.3 an alternative model to the fairly simple model of Chew (1988,1989) was described. The new model resulted in a slightly improved agreement for the rotor and the stator moment coefficient compared with the finite difference and experimental results. However, the new model tended to under-estimate the rotational speed of the core and did not produce good agreement for the limiting flow angle for throughflow cases compared with the finite difference results. From these results it has been concluded that the new stator model is only worthwhile including if stator shear stress predictions are required.

A simple correction has been proposed to model the effects of a rectangular solution domain. For $\lambda>60^{\circ}$, the correction resulted in the integral method correctly predicting the same Cm versus λ trend as the finite difference results. The model illustrates a method of accounting for other more general shroud geometries.

CHAPTER 8

CONCLUDING REMARKS AND SUGGESTIONS FOR FURTHER WORK

This chapter focusses upon the important conclusions which may be drawn from the work described in this thesis. As most of these conclusions have already been discussed in previous chapters, this chapter serves to summarise and emphasise the most important points. Attention will also be given to recommendations for areas of further work. The chapter is divided into two sections, the first is concerned with the integral method and the second with the finite difference method.

8.1 THE INTEGRAL METHOD

The isothermal predictions for the moment coefficients have been shown to be in very good agreement with experimental results for $\lambda>60^{\circ}$. For $\lambda<45^{\circ}$ and Cq=0, the agreement is poor, which is likely to be caused by the occurence of Taylor-type vortices in the secondary flow. For $\lambda<45^{\circ}$, there is some improvement in the agreement as Cq increases, which may be explained by the fact that the Taylor-type vortices are suppressed by throughflow. Further experimental work concerning rotor-stator cone systems would be useful; particularly detailed flow visualisations to precisely establish the nature of the Taylor-type vortices and the range of parameters (such as Re_{θ}, λ and d/b) over which they occur. Based on the evidence of the available

experimental data, it may be concluded that the present integral method, which is an extension of that developed for rotor-stator disc systems, can be used for flow predictions in rotor-stator cone systems where $\lambda > 60^{\circ}$.

The comparison of the non-isothermal results of chapter 5 with the finite difference results showed encouraging agreement. The effects of compressibility caused modelling difficulties and this could be an area for further work. However, some caution is required, as in certain cases with adverse temperatures, problems may be caused by the effects of bouyancy which can fundamentally change the secondary flow structure. Clearly, experimental work concerning heat transfer in rotor-stator disc or cone systems would be desirable to compare the predicted results and to examine in detail the effects of compressibilty and bouyancy. Some aspects of the model descibed in chapter 5 would benifit from further work; in particular the methods described in §5.4.2 to estimate q_{shroud}, H_{out} and q_0^s. A systematic study of the best ways to estimate these quantities could be achieved more satisfactorily if experimental results were available.

8.2 THE FINITE DIFFERENCE METHOD

The different trends illustrated by the Cm versus λ curves produced by the finite difference results and experiment clearly shows the presence of an experimental effect not being predicted by the finite difference program. As already stated, the experimental evidence suggests that this effect is the occurence of Taylor-type vortices in the secondary flow. For all cone angles considered, the finite difference program predicts a secondary flow pattern similar to

the disc-type secondary flow, except for a few laminar cases, where a second or third small vortex is predicted near to the outer-shroud. The failure of the program to predict Taylor-type vortices may be explained by the fact that they are non-axisymmetric or unsteady. The numerical prediction of non-axisymmetric or unsteady flows (or both) would be very expensive computationally. The results in this thesis show that the finite difference method has a similar range of validity as the integral method, i.e. the finite difference method may be used with confidence to predict the flow in a rotor-stator system provided $\lambda > 60^{\circ}$.

The present finite difference results support the integral method assumptions and they show that the assumptions may be generalised to rotor-stator cone systems. However, the few cases considered indicate that for high Reynolds number isothermal flows, longitudinal compressibility effects should not be neglected.

REFERENCES

Bachelor, G.K.

1967, 'An Introduction to Fluid Dynamics'. Cambridge University Press, Cambridge.

Boussinesq, J.

1877, Mem. Pres. Acad. Sci. XXIII, 46, Paris.

Burkhalter, J.E. and Koschmieder, E.L.

1973, J. Fluid Mech., 58, part 3, 547.

Chew, J.W.

1984a, Int. J. Num. Methods in Fluids, 4, 667.

1984b, ASME paper 84-GT-229.

1985a, Rolls-Royce report TSG0225.

1985b, Proc. Int. Conf. Lam. and Turb. Flow, Swansea, Pineridge Press, 318.

1985c, Trans. of the ASME, 107, 984.

1985d, Rolls-Royce report TSG0155.

1987, Proc. 2nd ASME-JSME Joint Thermal Engineering Conf., Hawaii, 361.

1988, Rolls-Royce report TSG0348.

1989, ASME paper 89-GT-178.

1990, To be presented at 3rd Int. Symposium on Transport Phenomena and Dynamics of Rotating Machinery, Honolulu.

Chew, J.W., Owen, J.M. and Pincombe, J.R.

1984, J. Fluid Mech., 143, 451.

Chew, J.W. and Rogers, R.H.

1988, Int. J. Heat and Fluid Flow, 9, 37.

Chew, J.W. and Vaughan, C.M.

1988, ASME paper 88-GT-127.

Cochran, W.G.

1934, Proc. Cambridge Phil. soc., 30, 365.

Daily, J.W., Ernst, W.D. and Asbedian, V.V.

1964, Report No 64, Hydrodynamics Lab., Massachusetts Inst. Tech.

Daily, J.W. and Nece, R.E.

1960, ASME J. Basic Engineering, 217.

Dorfman, L.A.

1963, 'Hydrodynamic resistance and the heat loss of rotating solids'. Oliver and Boyd Ltd. Edinburgh.

Ekman, V.W.

1905, Ark. Mat. Astr. Fys., 2, 1.

Goldstein, S.

1935, Proc. Cambridge Phil. Soc., 31, part 2, 232.

Gosman, A.D., Koosinlin, M.L., Lockwood, F.C. and Spalding, D.B.

1976a, ASME paper 76-GT-25.

Gosman, A.D., Lockwood, F.C. and Loughhead, J.N.

1976b, J. Mech. Engineering Science, 18, 142.

Hering, R.G. and Grosh, R.J.

1963, ASME J. Heat Trans., 29.

Kapinos, V.M.

1965, Inzhenerno-fizicheskii zhurnal, 8, No. 1, 48.

Karman, T.von.

1921, Z. angeur, Math. Mech., 1, 233.

1939, Trans. ASME, 61, 705.

Koosinlin, M.L., Lauder, B.E. and Sharma, B.I.

1974, ASME J. Heat Trans., 204.

Kreith, F.

1966, Proc. Heat Trans. and Fluid Mech. Inst., Stanford University Press, 29.

Kreith, F., Ellis, D. and Giesing, J.

1963, Appl. sci. res., Section A11, 456.

Landau, L.D. and Lifshitz, E.M.

1987, 'Course of Theoretical Physics', 6, Pergamon Press, Oxford.

Launder, B.E. and Sharma, B.I.

1974, Letters in Heat and Mass Trans., 1, 131.

Lonsdale, G.

1988, J. Comp. Physics, 74, 177.

Morse, A.P.

1988, ASME J. Turbomachinery, 110, 202.

1989a, ASME paper 89-GT-180.

1989b, ASME paper 89-GT-179.

Murthy, V.N.D.

1973, 2nd National Heat and Mass Trans. Conf., I.I.T., Kanpur, India, Paper No. A-1.

Newman, B.G.

1983, AIAA J., 21, 1066.

Ong, C.L.

1988, Report 88/TFMRC/TN67, University of Sussex.

Owen, J.M.

1971, Int. J. Heat Mass trans., 14, 451.

1988, ASME paper 88-GT-293.

Owen, J.M. and Pincombe, J.R.

1980, J. Fluid Mech., 99, 111.

Owen, J.M., Pincombe, J.R. and Rogers, R.H.

1985, J. Fluid Mech., 155, 233.

Pantankar, S.V.

1980, 'Numerical Heat Transfer and Fluid Flow', McGraw-Hill, London.

Pantankar, S.V. and Spalding, D.B.

1972, Int. J. Heat and Mass Trans., 15, 1787.

Polowski, J.W.

1984, Proc. Int. Centre for Heat and Mass trans., Hemisphere, Washington D.C., 16.

Rogers, G.F.C. and Mayhew, Y.R.

1974, 'Engineering Thermodynamics Work and Heat Transfer', Longman Group Ltd, London.

Rogers, R.H.

1988, Report 88/TFMRC/112, University of Sussex.

Schlichiting, H.

1968, 'Boundary-Layer Theory'. McGraw-Hill, London.

Schultz-Grunow, F.

1935, Z. angeur, Math. Mech., 15, 191.

Sharma, B.I.

1977, ASME J. Heat Trans., 151.

Tien, C.L.

1960, J. of Heat Trans., Trans. ASME, 82, series C, 252.

Van Doormal, J.P. and Raithby, G.D.

1984, Num. Heat trans., 7, 147.

Van Driest, E.R.

1955, Heat Trans. and Fluid Mech. Inst. Symposium, University of California, Los Angeles.

Vaughan, C.M., Gilham, S. and Chew, J.W.

1989, Proc. 6th Int. Conf. Num. Meth. Lam. and Turb. Flow. Swansea, Pineridge Press, 63.

Vaughan, C.M. and Turner, A.B.

1987, Proc. 5th Int. Conf. Num. Meth. Lam. and Turb. Flow, Montreal, Pineridge Press, 1640.

Wimmer, M.

1983, Papers of the Taylor vortex working party Conf., Nancy, France.

Wu, C.S.

1959, App. Sci. Res., 8, section A, 140.

Yamada, Y. and Ito, M.

1975, Bulletin of the JSME, 18, No. 123, 1026.

1979, J. of Fluids Engineering, 101, 259.

NOMENCLATURE

a	inner radius
b	outer radius
Cm	moment coefficient ($=2M\sin\lambda/(\rho\Omega^2 b^5)$)
Cp	specific heat at constant pressure
Cq	non-dimensional mass throughflow rate ($=\dot{m}/(\mu b)$)
d	perpendicular distance between the rotor and stator
D	diameter of pipe (see §3.4)
e	exponent in Van Driest (1956) type damping factor (equation (6.2.14))
$\dot{E}$	rate of energy deficit
Ec(s)	Eckert number ($=\Omega^2 r^2/2Cp(T_0-\bar{T})$)
$f(\eta)$	s-velocity profile
F	friction factor
$g(\eta)$	tangential velocity profile
$h(\eta,s)$	stagnation enthalpy profile
H(s,n)	stagnation enthalpy
H_{in}	stagnation enthalpy at inlet
H_{out}	stagnation enthalpy at outlet
h_c	heat transfer coefficient
I_f, I_g, I_{fg}, I_{ff}, I_{gg}, I_G, I_{GG}, $I_{f\eta}$	constants obtained by integrating velocity and enthalpy profiles across the boundary layer

$I_{f\eta\eta}$, $I_{fg\eta\eta}$, $I_{ff\eta}$, I_{fh}

$k(x)$ non-dimensional boundary layer edge tangential velocity ($=\bar{v}/(\Omega r_0)$), used when $\bar{v}$ is constant

k laminar thermal conductivity

k_m constant in Blasius law of friction (equation (7.2.1))

$k_e(s,n)$ effective thermal conductivity ($=k+k_t$)

$k_t(s,n)$ turbulent thermal conductivity

ℓ mixing length

L length of pipe (see §3.4)

m variable exponent in power law velocity profiles

$\dot{m}$ mass flow rate

M moment exerted on rotor

n normal coordinate direction in 'tilted' cylindrical polar system

$Nu(s)$ local Nusselt number

Nu_{av} average Nusselt number

$p(s,n)$ static pressure

Pr laminar Prandtl number

$Pr_e(s,n)$ effective Prandtl number ($=\mu_e Cp/k_e$)

$Pr_t(s,n)$ turbulent Prandtl number ($=\mu_t Cp/k_t$)

Pr^* characteristic Prandtl number

$q(s,n)$ heat flux

q_{shroud} surface heat flux from outer-shroud

Q volumetric flow rate (see §3.4)

r radial coordinate direction in cylindrical polar system

$r(s)$ local radius ($=s\sin\lambda + n\cos\lambda$)

$r_e(s)$ radial location of end of source region

$r_0(s)$ radial location of rotor surface ($=s\sin\lambda$)

R_G perfect gas constant

Re Reynolds number used in finite difference program ($=\Omega b^2/\nu$)

Re^* Reynolds number used in order of magnitude analysis (equation (3.3.10))

Re_θ Reynolds number used in the integral method ($=\Omega b^2/(\nu\sin\lambda)$)

$Re_\ell(s)$ local Reynolds number (equation (5.3.48))

$R_T(s)$ thermal Reynolds number

s coordinate direction parallel to cone in 'tilted' cylindrical polar system

t time

T(s,n) Temperature

T_1 tolerance defined as $\max|F_i(\bar{V})|$ where F_i is given by equations (4.2.14) and (4.2.15)

T^* 'friction' temperature ($=q_0/(\rho Cpv^*)$)

u(s,n) s-velocity component

$\tilde{u}(s)$ s-dependent component of u(s,n)

$u_1(x)$ non-dimensional $\tilde{u}(s)$ ($=\tilde{u}/(\beta r_0)$)

$u_p(s,n)$ velocity component parallel to a surface in the s-n plane

U_m mean velocity of fluid in pipe ($=4Q/\pi D^2$)

U_{max} maximum velocity of fluid in a cross-section of the pipe

$\bar{U}(s)$ $=[\bar{u}^2 + (v_0-\bar{v})^2 + \bar{w}^2]^{1/2}$

v(s,n) tangential velocity component

$v^*(s)$ friction velocity ($=(|\tau_{\theta,0}|/\rho)^{1/2}$)

$\bar{V}(x)$ non-dimensional boundary layer edge tangential velocity ($=\bar{v}/(\beta r_0)$)

$V_0(x)$ non-dimensional surface tangential velocity ($=v_0/(\beta r_0)$)

w(s,n) n-velocity component

x non-dimensional distance ($=r_0/b$)

x_e non-dimensional radial location of end of source region ($=r_e/b$)

x_n normal distance from surface

x_n^+ non-dimensional normal distance from surface ($=x_n(\rho\tau_w)^{1/2}/\mu$)

YP non-dimensional near-wall grid spacing

z coordinate direction in cylindrical polar system

Greek letters

α_1 constant in new s-velocity profile (equation (7.3.3))

α_2 constant in new tangential velocity profile (equation (7.3.5))

α_G Gosman under-relaxation factor

β representative angular velocity

$\delta(s)$ momentum boundary layer thickness

$\delta_1(x)$ non-dimensional momentum boundary layer thickness

$\delta_T(s)$ thermal boundary layer thickness

Δx_e distance over which source region calculation is continued in core region calculation method 2 (see §4.2.4)

ϵ { x-a/b ; molecular diffusivity of heat ($=k/\rho Cp$)

$\epsilon_t(s,n)$ turbulent diffusivity of heat ($=k_t/\rho Cp$)

ζ non-dimensional distance from wall ($=nv^*/\nu$)

η non-dimensional distance in boundary layer ($=n/\delta$)

θ tangential coordinate in cylindrical and 'tilted' cylindrical polar systems

λ half cone angle

χ angle which a surface makes with the axis of rotation (equation (6.2.18))

Λ	coefficient of resistance in the 'law of friction' for turbulent pipe flows
μ	laminar dynamic viscosity
$\mu_e(s,n)$	effective dynamic viscosity ($=\mu+\mu_t$)
$\mu_t(s,n)$	turbulent dynamic viscosity
ν	laminar kinematic viscosity ($=\mu/\rho$)
$\nu_t(s,n)$	turbulent kinematic viscosity ($=\mu_t/\rho$)
ξ_1, ξ_2	constants used in asymptotic solutions (see §4.5)
$\rho(s,n)$	density
$\tau_{ij}(s,n)$	stresses components, where i and j represent s,θ or n
$\tau_w(s)$	resultant wall shear stress
φ	inlet swirl parameter ($=\bar{v}_{in}/(\Omega a)$)
$\chi(Pr,T_0)$	function expressing the dependence of the surface heat flux on the laminar Prandtl number and surface temperature distribution (equation (5.3.44))
ω	under-relaxation factor (equation (4.2.18))
Ω	angular velocity of rotor
Ω_b	angular velocity of outer-shroud

<u>Subscripts</u>

in	inlet value
0	value on rotor or stator surface
out	outlet value
t	turbulent value
e	effective value
ref	reference value

Superscripts

s stator variable

Overbars

values at the boundary layer edge

Appendix A - The Simple Iterative Method

The motivation for using equation (4.2.18) is from the general iterative method for finding the zero of a function f(x). The formula for the j^{th} iterate is

$$x^j = x^{j-1} + f(x^{j-1}) \quad . \tag{A1}$$

It may be shown that a condition for convergence of (A1) is that

$$-2 < f'(x^{j-1}) < 0 \quad . \tag{A2}$$

The above method has been extended to a system of N variables so that the j^{th} iterate is found from

$$x_i^{\,j} = x_i^{\,j-1} + f(x_i^{\,j-1}) \quad \text{for } i = 1,2,\ldots,N \quad . \tag{A3}$$

$f(x_i^{j-1})$ in equation (A3) is taken as $F_i(\bar{V})$ in equation (4.2.16) and an under-relaxation factor is used which appears multiplied by $F_i(\bar{V})$. It is not generally possible to check condition (A2) analytically in this case. The attractions of the method are its ease of application; derivatives of the function $F_i(\bar{V})$ are not required and only one initial guess is needed.

Appendix B - Analytical Solutions for a Free-Rotating Cone

Von Karman (1921) found analytical solutions to the integrated boundary layer equations governing the flow over a disc rotating in an infinite environment. His work has since been generalised to boundary layer flow over a cone rotating in an infinite environment by other authors, such as Kreith (1966) and Chew (1985). Their results are valid provided the inner hub-radius of the cone is zero (i.e. a = 0) and the case (i) boundary layer arguments of §3.3 are valid.

The relevant equations are (4.2.4) and (4.2.5) when the terms containing tanλ are omitted and $\bar{V}$ is set to zero. The equations then become

$$2Y_1Y_2\frac{dY_1}{dx} - I_{ff}\,Y_1^2\frac{dY_2}{dx} = -0.0225x^{7/4}\,Y_1\left[\left[\frac{Y_1}{x^2}\right]^2 + Y_2^2\right]^{3/8} + \frac{Y_1^2Y_2}{x}\,I_{ff} + x^3Y_2^3\,I_{gg}\,, \qquad \text{(B1)}$$

and

$$\frac{dY_1}{dx} = \frac{0.0225x^{7/4}}{I_{fg}\,Y_2}\left[\left[\frac{Y_1}{x^2}\right]^2 + Y_2^2\right]^{3/8} - \frac{2Y_1}{x}\,. \qquad \text{(B2)}$$

Re-writing $Y_1 = u_1\delta_1x^3$ and $Y_2 = \delta_1x$, equations (B1) and (B2) have analytical solutions of the form

$$u_1 = 0.162\,, \qquad \text{(B3)}$$

$$\delta_1 = 0.525x^{-0.4}\,. \qquad \text{(B4)}$$

As stated in §4.2.1, Y_2 is proportional to the boundary layer thickness and from equation (B4)

$$\frac{dY_2}{dx} = 0.315x^{-0.4} \quad . \tag{B5}$$

Y_1 is proportional to the mass flow rate in the boundary layer and may be written as $Y_1 = u_1 x^2 Y_2$, so that

$$\frac{dY_1}{dx} = 0.324x\ Y_2 + 0.162x^2\ \frac{dY_2}{dx} \quad . \tag{B6}$$

From equation (B5), the analytical results indicate that the boundary layer thickness (or Y_2) has an infinite gradient at $x = 0$ (i.e. at the inception of the boundary layer). It would seem reasonable to assume that for a cone where $a \neq 0$, the boundary layer grows in a similar way, so that

$$\frac{dY_2}{dx} \to \infty, \quad \text{at } x = a/b, \quad \forall\ a/b \quad . \tag{B7}$$

From equation (B6), for a free cone where $a \neq 0$, the above assumption then leads to

$$\frac{dY_1}{dx} \to \infty, \quad \text{at } x = a/b, \quad \forall\ a/b \neq 0 \quad . \tag{B8}$$

Appendix C - Derivation of the Boundary Layer Energy Equations in §5.3.2

It is consistent with the case (i) boundary layer assumptions of §3.3 to assume that for any function $\varphi(s,n)$ and integer m (where m=1 or m=2), within the boundary layer

$$\frac{\partial \varphi}{\partial n} \gg \frac{m}{r} \varphi \cos\lambda \ . \tag{C1}$$

Using the continuity equation (3.3.7), the boundary layer energy equation and the momentum equations (3.3.18) and (3.3.19) may then be written:

$$\text{Energy} \quad : \rho\left[u \frac{\partial H}{\partial s} + w \frac{\partial H}{\partial n}\right] = - \frac{\partial}{\partial n} (q - u\tau_s - v\tau_\theta) \ , \tag{C2}$$

$$\text{s-momentum:} \ \rho\left[u \frac{\partial u}{\partial s} + w \frac{\partial u}{\partial n} - \frac{v^2}{r} \sin\lambda\right] = - \frac{\partial p}{\partial s} + \frac{\partial \tau_s}{\partial n} \ , \tag{C3}$$

$$\theta\text{-momentum:} \ \rho\left[u \frac{\partial v}{\partial s} + w \frac{\partial v}{\partial n} + \frac{uv}{r} \sin\lambda\right] = \frac{\partial \tau_\theta}{\partial n} \ . \tag{C4}$$

where $\tau_s \equiv \tau_{sn}$ and $\tau_\theta \equiv \tau_{\theta n}$.

Writing the shear stress terms in equation (C2) in terms of the effective viscosity and velocity gradients and applying the boundary layer simplifications of §3.3, the shear stress terms may be approximated by

$$\tau_s \simeq \mu_e \frac{\partial u_s}{\partial n} \ , \qquad \tau_\theta \simeq \mu_e \frac{\partial v}{\partial n} \ . \tag{C5}$$

Equation (C2) may then be written as

$$\rho\left[u\,\frac{\partial H}{\partial s} + w\,\frac{\partial H}{\partial n}\right] = -\,\frac{\partial}{\partial n}\left[-k_e\,\frac{\partial T}{\partial n} - \mu_e u\,\frac{\partial u}{\partial n} - \mu_e v\,\frac{\partial v}{\partial n}\right] . \qquad (C6)$$

The following approximations are consistent with the boundary layer simplifcations of §3.3:

$$u\,\frac{\partial u}{\partial n} \gg w\,\frac{\partial w}{\partial n} , \quad v\,\frac{\partial v}{\partial n} \gg w\,\frac{\partial w}{\partial n} , \qquad (C7)$$

so that for an effective Prandtl number of unity, equation (C6) may be written as

$$\rho\left[u\,\frac{\partial H}{\partial s} + w\,\frac{\partial H}{\partial n}\right] = \frac{\partial}{\partial n}\left[\frac{k_e}{C_p}\,\frac{\partial H}{\partial n}\right] . \qquad (C8)$$

Substituting for $u\,\frac{\partial \tau_s}{\partial n}$ and $v\,\frac{\partial \tau_\theta}{\partial n}$ from equations (C3) and (C4) into equation (C2) and using the fact that $H = C_pT + \frac{1}{2}(u_s^2+v^2+u_n^2)$, the following boundary layer energy equation is obtained:

$$\rho C_p\left[u\,\frac{\partial T}{\partial s} + w\,\frac{\partial T}{\partial n}\right] = -\,\frac{\partial q}{\partial n} + \tau_s\,\frac{\partial u}{\partial n} + \tau_\theta\,\frac{\partial v}{\partial n} + u\,\frac{dp}{ds} . \qquad (C9)$$

If the effects of frictional heating and compressive work in the energy equation are neglected, then the stress terms and the compressibility term will be zero. Under such conditions, the energy equation (D9) may therefore be written as

$$\rho\left[u_s\,\frac{\partial T}{\partial s} + u_n\,\frac{\partial T}{\partial n}\right] = \frac{\partial}{\partial n}\left[\frac{k_e}{C_p}\,\frac{\partial T}{\partial n}\right] . \qquad (C10)$$

Appendix D - Derivation of the Relationship between F(ζ) and G(ζ) in §5.3.4

The assumed three layer scheme is

viscous sub-layer: $0 < \zeta < 5$, $\quad F(\zeta) = \zeta$ (D1)

transition layer : $5 < \zeta < 30$, $\quad F(\zeta) = 5\left[\ell n\left[\frac{\zeta}{5}\right] + 1\right]$ (D2)

and for $\zeta > 30$, molecular transport processes are negligible compared with turbulent transport processes. For the present purposes, an explicit formula for $F(\zeta)$ in the fully turbulent layer is not required.

The derived relationship between $F(\zeta)$ and $G(\zeta)$ (equation (5.3.35)) is

$$\frac{1}{G'(\zeta)} = \frac{1}{Pr} + \frac{1}{F'(\zeta)} - 1 \qquad \text{(D3)}$$

In the viscous sub-layer, the expression for $F'(\zeta)$ from equation (D1) may be substituted into equation (D3) to obtain

$$G'(\zeta) = Pr \ . \qquad \text{(D4)}$$

If equation (D4) is integrated and the condition that when $\zeta = 0$, $G(\zeta) = 0$ (provided $q_0 \neq 0$) is used, the following expression is obtained:

$$G(\zeta) = \zeta Pr \ . \qquad \text{(D5)}$$

In the transition layer, the expression for $F'(\zeta)$ from equation (D2) may be substituted into equation (D3) to obtain

$$G'(\zeta) = \frac{5Pr}{5+Pr-5Pr} \cdot \tag{D6}$$

Equation (D6) may be integrated and the boundary condition at $\zeta = 5$ from equation (D5) may be used to obtain

$$G(\zeta) = 5Pr + 5\ell n \left[\zeta \frac{Pr}{5} + 1 - Pr\right] . \tag{D7}$$

In the fully turbulent region of the boundary layer, neglect of molecular terms in equations (5.3.29) and (5.3.30) leads to

$$\left.\begin{aligned} \tau_\theta &= \nu_t \frac{\partial v}{\partial n} \\ \frac{q}{\rho C_p} &= -\nu_t \frac{\partial T}{\partial n} \end{aligned}\right\} \quad \zeta > 30 . \tag{D8}$$

A substitution of $\frac{\partial v}{\partial n}$ and $\frac{\partial T}{\partial n}$ from equations (5.3.26) and (5.3.34) into equations (D8) leads to

$$|\tau_\theta| = \rho \nu_t \frac{v^{*2}}{\nu} F'(\zeta) \quad \text{and} \quad \frac{q}{\rho C_p} = \frac{\nu_t}{\nu} T^* v^* G'(\zeta) . \tag{D9}$$

Now, v^* and T^* are defined in the laminar and transition layers where τ_θ and q may be considered constant (see assumption (ii) of §5.3.3) and may therefore take their values at $\zeta = 30$, denoted by $\tau_{\theta,30}$ and $q_{,30}$. Equations (D9) may then be written as

$$|\tau_\theta| = \frac{\nu_t}{\nu} |\tau_{\theta,30}| F'(\zeta) \quad \text{and} \quad q = \frac{\nu_t}{\nu} q_{,30} G'(\zeta) . \tag{D10}$$

These combine to give

$$\frac{F'(\zeta)}{G'(\zeta)} = \frac{\tau_\theta/q}{|\tau_{\theta,30}| / |q_{,30}|} . \tag{D11}$$

Dorfman (1963) assumes that the quantity τ_θ/q is independent of ζ in the fully turbulent layer. This result follows directly from the Reynolds analogy result of §5.3.2 as follows. If laminar effects are neglected compared with turbulent effects and P_{rt} is put equal to one, then the equations for Φ_T, Φ_V and Φ_H (defined in equations (5.3.11)) will still be identical. From the equality of Φ_V and Φ_T, the quantity $(\partial v/\partial n)/(\partial T/\partial n))$ will be independent of ζ, so from equations (D8) the desired result of τ_θ/q being independent of ζ may be obtained. Since τ_θ/q is independent of ζ in the fully turbulent layer it equals its value obtained at $\zeta = 30$, so that equation (D11) reduces to

$$F'(\zeta) = G'(\zeta) \tag{D12}$$

Integrating equation (D12) and applying the boundary conditions at $\zeta = 30$ from equations (D2) and (D7), the final form of the relationship between $F(\zeta)$ and $G(\zeta)$ valid in the turbulent region of the boundary layer becomes

$$F(\zeta) = G(\zeta) - \Sigma(Pr) , \tag{D13}$$

where

$$\Sigma(Pr) = 5(Pr-1) + 5\ell n \left[\frac{5Pr+1}{6}\right] . \tag{D14}$$

Appendix E- The Derivation of F(Pr) and β in §5.3.5

Substitution of equations (5.3.48) and (5.3.50) into equation (5.3.47) leads to

$$Nu = F(Pr)\left[\frac{\rho}{\mu}\right]^{\beta+1} r_0[u^2+(v_0-\bar{v})^2]^{\frac{(\beta+1)}{2}} [\delta|I_f-I_{fh}|]^{\beta} . \qquad (E1)$$

Comparing equation (5.3.22) or (5.3.23) with equation (5.3.44), it is clear that in this special case $\chi = Rc = 1$. The Nusselt number equation (5.3.45) for this case gives

$$Nu = -\frac{r_0\tau_{\theta,0}}{\mu(v_0-\bar{v})} . \qquad (E2)$$

It may also be deduced from the profile equations (5.2.9) and (3.4.15) that the equality of Φ_V and Φ_H in equations (5.3.11) gives the following value of I_{fh}, independent of s:

$$I_{fh} = I_f - I_{fg} . \qquad (E3)$$

If the Nusselt number in equation (E2) is equated with the general Nusselt number in equation (E1), then for consistency,

$$\beta = -\tfrac{1}{4} . \qquad (E4)$$

Comparing equation (5.3.38) with equation (5.3.44), it is clear that in this case, $Rc = 0$ and $\chi = \xi$, where

$$\xi = \left[1 + \frac{\Sigma(Pr)}{|v_0-\bar{v}|}\sqrt{\frac{|\tau_{\theta,0}|}{\rho}}\right]^{-1} \qquad (E5)$$

The Nusselt number equation (5.3.45) for this case gives

$$Nu = - \frac{\xi \ Pr \ r_0 \ \tau_{\theta,o}}{\mu(v_0-\bar{v})} \ . \qquad (E6)$$

If friction and compressive work are neglected, the boundary layer energy equation may be written as

$$\frac{\partial}{\partial s} (\rho r u_s H) + \frac{\partial}{\partial n} (\rho r u_n H) = - \frac{\partial q}{\partial n} \ . \qquad (E7)$$

Assuming the case (i) boundary layer arguments of §3.3 and using the enthalpy and velocity profiles given by equations (5.2.9) and (3.4.14), equation (E7) may be integrated across the boundary layer to give

$$\frac{d}{ds} [\rho u \delta s \ \sin\lambda (H_0-\bar{H})(I_f-I_{fh}] = s \sin\lambda \ q_0 \ . \qquad (E8)$$

Substitute for q_0 from equation (5.3.38) to obtain

$$\frac{d}{ds} \left[\rho u \delta s \ \sin\lambda (H_0-\bar{H}) \ \frac{(I_f-I_{fh})}{\xi}\right] = -s \sin\lambda \ C_p \tau_{\theta,o} \ \frac{(T_0-\bar{T})}{(v_0-\bar{v})} \ . \qquad (E9)$$

For a laminar Prandtl number of unity, equation (E3) will be valid and $\xi = 1$. Consideration of equation (E9) in which only $I_{fh}(s)$ and ξ depend on Pr shows that

$$I_f - I_{fh} = \xi \ I_{fg} \ . \qquad (E10)$$

Equating the Nusselt numbers given by (E1) and (E6), gives

$$F(Pr) = 0.0225 \ Pr \ \xi^{5/4} \ I_{fg}^{1/4} \ . \qquad (E11)$$

Appendix F - The Finite Difference Coefficients of Equation (6.2.22)

The coefficients of equation (6.2.22), where Φ can represent either u, v, w or H may be written:

$$A_P = A_N + A_S + A_E + A_W + A_\Phi$$

The coefficients A_N, A_S, A_E and A_W were calculated using the hybrid differencing of the convective terms described by Patanker (1980) and A_Φ is different for each variable.

Following Patanker (1980), A_N, A_S, A_E and A_W have the following forms:

$$A_N = \left[\left| \left|\frac{C_n}{2}\right| , D_n \right|\right] - \frac{C_n}{2} \qquad (F1)$$

$$A_S = \left[\left| \left|\frac{C_s}{2}\right| , D_s \right|\right] + \frac{C_s}{2} \qquad (F2)$$

$$A_E = \left[\left| \left|\frac{C_e}{2}\right| , D_e \right|\right] - \frac{C_e}{2} \qquad (F3)$$

$$A_W = \left[\left| \left|\frac{C_w}{2}\right| , D_w \right|\right] + \frac{C_w}{2} \qquad (F4)$$

where $C_n = \frac{\rho_n u_n r_n}{r_p Ds_p}$, $C_s = \frac{\rho_s u_s r_s}{r_p Ds_p}$, $C_e = \frac{\rho_e w_e r_e}{r_p Dn_p}$, $C_w = \frac{\rho_w w_w r_w}{r_p Dn_p}$

$$D_n = \frac{B_1 \Gamma_n r_n}{r_p Ds_n Ds_p} , \quad D_s = \frac{B_2 \Gamma_s r_s}{r_p Ds_s Ds_p} , \quad D_e = \frac{B_3 \Gamma_e r_e}{r_p Dn_e Dn_p} , \quad D_w = \frac{B_4 \Gamma_w r_w}{r_p Dn_w Dn_p}$$

and where $\Gamma = \mu_e$ (effective viscosity) when Φ = u, v or w and $\Gamma = k_e/c_p$ when Φ = H.

The constants B_1, B_2, B_3 and B_4 are different for each variable and will be given in the following sections where each variable will be considered separately.

<u>Φ = u</u>

$$A\Phi = \frac{2\Gamma_p \sin^2\lambda}{r_p^2} + \left[\left| \frac{2}{3} I_c \left[\frac{\Gamma_n}{r_n} - \frac{\Gamma_s}{r_s}\right] \frac{\sin\lambda}{Ds_p} , 0 \right|\right] + \left|\frac{\alpha_G \rho_p v_p \sin\lambda}{r_p}\right|$$

I_c is a constant which is set to zero or one when the flow is incompressible or compressible respectively. α_G is a constant and is an under-relaxation factor recommended by Gosman et al (1976) for fluid flows in rotating disc systems. The motivation is that there are strong links between the radial and tangential momentum equations and if u increases, a decrease in v is expected and so the centrifugal force term should be reduced. In the present program, the α_G term is added to both the s and the n momentum equations.

$$B_1 = 2 - \frac{2}{3} I_c , \quad B_2 = 2 - \frac{2}{3} I_c , \quad B_3 = 1 , \quad B_4 = 1$$

$$S_1 = \frac{(p_s - p_n)}{Ds_p} + \frac{\Gamma_e r_e (w_{ne} - w_{se}) - \Gamma_w r_w (w_{nw} - w_{sw})}{r_p Ds_p Dn_p}$$

$$+ 2\Gamma_p \frac{w_p}{r_p^2} \sin\lambda\cos\lambda + \rho_p v_p^2 \frac{\sin\lambda}{r_p}$$

$$- \frac{2}{3} I_c \frac{[\Gamma_n r_n (w_{ne} - w_{nw}) - \Gamma_s r_s (w_{se} - w_{sw})]}{r_p Ds_p Dn_p}$$

$$+ \frac{2}{3}\frac{I_c}{r_p}\left[\cos\lambda(\Gamma_n w_n - \Gamma_s w_s) + \Gamma_p \frac{\sin\lambda}{r_p}(r_e w_e - r_w w_w)\right]$$

$$S_2 = \left[\left| - \frac{2}{3} I_c \left[\frac{\Gamma_n}{r_n} - \frac{\Gamma_s}{r_s}\right] \frac{\sin\lambda}{DS_p} , 0 \right|\right] + \left|\frac{\rho_p \alpha_G v_p \sin\lambda}{r_p}\right|$$

<u>$\Phi = v$</u>

$$A\Phi = \left[\left|\frac{\rho_p u_p}{r_p} \sin\lambda, 0\right|\right] + \left[\left| - \frac{\rho_p w_p}{r_p} \cos\lambda, 0\right|\right] + \left[\left|\frac{(\Gamma_n - \Gamma_s)}{r_p Ds_p} \sin\lambda, 0\right|\right]$$

$$+ \left|\left[- \frac{(\Gamma_e - \Gamma_w)}{r_p Dn_p} \cos\lambda, 0\right|\right]$$

$$B_1 = B_2 = B_3 = B_4 = 1$$

$$S_1 = 0$$

$$S_2 = \left[\left| - \frac{\rho_p u_p}{r_p} \sin\lambda, 0\right|\right] + \left[\left|\frac{\rho_p w_p}{r_p} \cos\lambda, 0\right|\right] + \left[\left| - \frac{(\Gamma_n - \Gamma_s)}{r_p Ds_p} \sin\lambda, 0\right|\right]$$

$$+ \left[\left|\frac{(\Gamma_e - \Gamma_w)}{r_p Dn_p} \cos\lambda, 0\right|\right]$$

<u>$\Phi = w$</u>

$$A\Phi = \frac{2\Gamma_p \cos^2\lambda}{r_p^2} + \left[\left| - \frac{2}{3} I_c \left[\frac{\Gamma_e}{r_e} - \frac{\Gamma_w}{r_w}\right] \frac{\cos\lambda}{Dn_p} , 0 \right|\right] + \left|\frac{\alpha_G \rho_p v_p \cos\lambda}{r_p}\right|$$

$$B_1 = 1, \quad B_2 = 1, \quad B_3 = 2 - \frac{2}{3} I_c, \quad B_4 = 2 - \frac{2}{3} I_c$$

$$S_1 = \frac{(p_w - p_e)}{Dn_p} + \frac{\Gamma_n r_n (u_{ne} - u_{nw}) - \Gamma_s r_s (u_{se} - u_{sw})}{r_p Ds_p Dn_p}$$

$$+ 2\Gamma_p \frac{u_p}{r_p} \sin\lambda\cos\lambda - \rho_p \frac{v_p^2}{r_p} \cos\lambda$$

$$- \frac{2}{3} \frac{I_c}{r_p Ds_p Dn_p} \left[\Gamma_e r_e (u_{ne}-u_{se}) - \Gamma_w r_w (u_{nw}-u_{sw})\right]$$

$$- \frac{2}{3} \frac{I_c}{r_p} \left[\sin\lambda(\Gamma_e u_e - \Gamma_w u_w) + \Gamma_p \frac{\cos\lambda}{r_p} (r_n u_n - r_s u_s)\right]$$

$$S_2 = \left[\left| \frac{2}{3} I_c \left[\frac{\Gamma_e}{r_e} - \frac{\Gamma_w}{r_w}\right] \frac{\cos\lambda}{Dn_p} , 0 \right|\right] + \left|\frac{\alpha_G \rho_p v_p \cos\lambda}{r_p}\right|$$

<u>$\Phi = H$</u>

$$A\Phi = 0$$

$$B_1 = B_2 = B_3 = B_4 = 1$$

$$S_1 = \frac{1}{r_p Ds_p} \left[(\mu_n-\Gamma_n) \frac{r_n}{Ds_n} \{u_n(u_N-u_P)+v_n(v_N-v_P)-w_n(w_N-w_P)\}\right.$$

$$\left. - (\mu_s-\Gamma_s) \frac{r_s}{Ds_s} \{u_s(u_p-u_s)+v_s(v_p-v_s)+u_s(u_p-w_s)\}\right.$$

$$+ \frac{1}{r_p Dn_p} \left[(\mu_e-\Gamma_e) \frac{r_e}{Dn_e} \{u_e(u_E-u_P)+v_e(v_E-v_P)-w_e(w_E-w_P)\}\right.$$

$$\left. - (\mu_w-\Gamma_w) \frac{r_w}{Dn_w} \{u_w(u_p-u_w)+v_w(v_p-v_w)+w_w(w_p-w_w)\}\right.$$

$$- \frac{2}{3} \frac{I_c}{r_p Ds_p} \left[\mu_n u_n \left\{v_n \sin\lambda - u_n \cos\lambda + \frac{r_n}{Ds_n} (v_N-v_P) + \frac{r_n}{Dn_p} (u_{ne}-u_{nw})\right\}\right.$$

$$-\mu_s u_s\left\{v_s \sin\lambda - u_s \cos\lambda + \frac{r_s}{Ds_s}(v_p - v_s) + \frac{r_s}{Dn_p}(u_{se} - u_{sw})\right\}\Big]$$

$$-\frac{2}{3}\frac{I_c}{r_p Dn_p}\Big[\mu_e u_e\left\{v_e \sin\lambda - u_e \cos\lambda + \frac{r_e}{Ds_p}(v_{ne} - v_{se}) + \frac{r_e}{Dn_e}(u_E - u_p)\right\}$$

$$-\mu_w u_w\left\{v_w \sin\lambda - u_w \cos\lambda + \frac{r_w}{Ds_p}(v_{nw} - v_{sw}) + \frac{r_w}{Dn_w}(u_p - u_W)\right\}\Big]$$

$$+\frac{1}{r_p Ds_p}\Big[\mu_n r_n\left\{u_n \frac{(u_N - u_p)}{Ds_n} + w_n \frac{(w_{ne} - w_{nw})}{Dn_p} - \frac{v_n^2}{r_n}\sin\lambda\right\}$$

$$-\mu_s r_s\left\{u_s \frac{(u_p - u_S)}{Ds_s} + w_s \frac{(w_{se} - w_{sw})}{Dn_p} - \frac{v_s^2}{r_s}\sin\lambda\right\}\Big]$$

$$+\frac{1}{r_p Dn_p}\Big[\mu_e r_e\left\{w_e \frac{(w_E - w_p)}{Dn_e} + u_e \frac{(u_{ne} - u_{se})}{Ds_p} + \frac{v_e^2}{r_e}\cos\lambda\right\}$$

$$-\mu_w r_w\left\{w_w \frac{(w_p - w_W)}{Dn_w} + u_w \frac{(u_{nw} - u_{sw})}{Ds_p} + \frac{v_w^2}{r_w}\cos\lambda\right\}\Big]$$

$$S_2 = 0$$

where μ in the above equations is the effective viscosity (μ_e).

TABLES

(a) Effect of T_1 ($=\max|F_i|$); N = 10, x_1-x_e = 0.05

T_1	10^{-1}	10^{-2}	10^{-3}	10^{-4}
Iterations	9	23	34	44
Processing Time (sec)	17	30	40	50
Cm ($\times 10^3$)	3.89	3.84	3.84	3.84

(b) Effect of N; $T_1 = 10^{-2}$, x_1-x_e = 0.05

N	4	8	12	20	40
Iterations	23	23	35	101	152
Processing Time (sec)	23	28	45	153	264
Cm ($\times 10^3$)	3.82	3.84	3.84	3.84	3.84

(c) Effect of x_1-x_e; $T_1 = 10^{-2}$, N = 10

x_1-x_e	0.005	0.01	0.03	0.05	0.07	0.09	0.11
Iterations	53	34	15	16	19	17	17
Processing Time (sec)	75	50	26	27	29	26	26
Cm ($\times 10^3$)	3.84	3.84	3.84	3.84	3.85	3.85	3.85

Tables 4.1 The Effect of T_1, N and (x_1-x_e) on the method 1 solution

$\lambda = 60^{\circ}$, $C_q = 3000$, $a/b = 0.1$, $d/b = 0.1$,

$\varphi = 0$, $Re_\theta = 10^6$

(a) Effect of Δx_e; $T_2 = 10^{-3}$

Δx_e	0.1	0.05	0.01	0.005	0.002	0.0017
Iterations	16	28	33	45	48	51
Processing time (sec)	15	17	18	23	25	26
Cm ($x10^3$)	3.47	3.62	3.75	3.78	3.81	3.81

(b) Effect of T_2; $\Delta x_e = 0.005$

T_2	0.5	10^{-1}	10^{-2}	10^{-3}	10^{-4}	10^{-5}
Iterations	35	39	43	45	46	54
Processing Time (sec)	21	23	23	23	23	26
Cm ($x10^3$)	3.92	3.79	3.79	3.78	3.78	3.78

Tables 4.2 The effect of Δx_e and T_2 on the Method 2 solution

$\lambda = 60^{\circ}$, $Re_{\theta} = 10^6$, $C_q = 3000$, $a/b = 0.1$,
$d/b = 0.1$, $\varphi = 0$

λ / C_q	90°		60°		30°	
	Method 1	Method 2	Method 1	Method 2	Method 1	Method 2
0	2.52	2.53	2.53	2.53	2.55	2.53
500	2.78	2.78	2.79	2.78	2.80	2.79
3000	3.84	3.78	3.84	3.78	3.86	3.79
6000	4.47	4.36	4.48	4.36	4.49	4.37

Table 4.3 A Comparison of the Moment Coefficient ($\times 10^3$) predicted by the two Core Region Methods

$Re_\theta = 10^6$, $a/b = 0.1$, $d/b = 0.1$, $\varphi = 0$

	λ	a/b	C_q	Compressibility	T_0	T_0^s	T_{shroud}	T_{IN}
(a)	90°	0.001	0	Compressible	T_{ref} + 100	T_{ref}	T_{ref}	T_{ref}
(b)	90°	0.001	0	Compressible	T_{ref} + 1463x^2	T_{ref}	T_{ref}	T_{ref}
(c)	90°	0.2	0	Compressible	T_{ref}	T_{ref} + 1463x^2	T_{ref}	T_{ref}
(d)	90°	0.001	0	Compressible	T_{ref} + 500	T_{ref}	T_{ref}	T_{ref}
(e)	90°	0.001	0	Incompressible	T_{ref} + 500	T_{ref}	T_{ref}	T_{ref}
(f)	90°	0.2	3000	Incompressible	T_{ref} + 200	T_{ref}	T_{ref}	T_{ref}
(g)	90°	0.2	3000	Incompressible	T_{ref} + 200	T_{ref} + 200	T_{ref} + 200	T_{ref}
(h)	45°	0.001	0	Compressible	T_{ref} + 100	T_{ref}	T_{ref}	T_{ref}

Table 5.1 Table of Temperature Boundary Conditions
for the eight cases (a) - (h)

T_{ref} = 298°K, d/b = 0.12 and Re_θ = 1.7 x $10^6/\sin\lambda$,

Pr = 0.7 and Pr_t = 0.9

CASE	ROTOR			STATOR		
	Finite Difference	Integral Method	% Error	Finite Difference	Integral Method	% Error
(a)	641	668	4.21	-347	-442	27.4
(b)	864	798	7.64	-528	-542	2.65
(c)	-586	-635	8.40	658	718	9.12
(d)	434	454	4.61	-242	-329	35.6
(e)	746	748	0.268	-484	-474	2.07
(f)	1036	1062	2.51	-314	-290	7.64
(g)	808	742	7.92	-133	-22.0	83.5
(h)	605	598	1.12	-392	-440	12.2

Table 5.2 A comparison of the Predicted Average Nusselt numbers for rotor-stator systems with Boundary Conditions (a)-(h) of Table 4

$T_{ref} = 298^0K$, $d/b = 0.12$, $Re_\theta = 1.7 \times 10^6/\sin\lambda$, $Pr = 0.7$ and $Pr_t = 0.9$

MESH	MOMENT COEFFICIENT	
	Program	Yamada & Ito
25 x 25	0.0117	0.0119
33 x 33	0.0114	0.0119
41 x 41	0.0114	0.0119
49 x 49	0.0114	0.0119
57 x 57	0.0114	0.0119

Table 6.1 Laminar Flow: The Effect of Mesh Size on Moment Coefficient Predictions

$\lambda = 60^{\circ}$, $Re = 2 \times 10^4$, $C_q = 0$,

$a/b = 0$, $d/b = 0.16$

MESH	AXIAL EXP FACTOR	MOMENT COEFF (CM)	YP r_0/b = 0.2	YP r_0/b = 0.4	YP r_0/b = 0.6	YP r_0/b = 0.8
33 x 33	1.2	0.00292	3.81	5.58	9.48	14.8
41 x 41	1.2	0.00332	2.05	3.58	4.92	6.47
49 x 49	1.2	0.00310	0.97	1.63	2.20	2.94
57 x 57	1.2	0.00299	0.46	0.77	1.04	1.39
65 x 65	1.2	0.00294	0.22	0.37	0.50	0.66
73 x 73	1.2	0.00294	0.11	0.18	0.24	0.32

Table 6.2(a) Turbulent Flow: The Effect of Mesh Size on Moment Coefficient Predictions

$\lambda = 60^{\circ}$, $Re = 10^6$, $C_q = 0$, $a/b = 0$,

$d/b = 0.16$

MESH	AXIAL EXP FACTOR	MOMENT COEFF (CM)	YP r_0/b = 0.2	r_0/b = 0.4	r_0/b = 0.6	r_0/b = 0.8
49 x 49	1.0	0.00149	14.0	20.8	26.2	32.5
49 x 49	1.1	0.00292	5.00	7.40	10.5	12.6
49 x 49	1.2	0.00310	0.97	1.63	2.20	2.94
49 x 49	1.3	0.00294	0.17	0.35	0.47	0.62
49 x 49	1.4	0.00294	0.05	0.08	0.11	0.14

Table 6.2(b) Turbulent Flow: The Effect of the Axial Expansion Factor on Moment Coefficient Predictions

$\lambda = 60^{\circ}$, $Re = 10^6$, $C_q = 0$, $a/b = 0$,

$d/b = 0.16$

Re	C_m (incompressible)	C_m (compressible)	% Change
10^6	2.71 x 10-3	2.77 x 10^{-3}	2.21
2 x 10^6	2.25 x 10^{-3}	2.37 x 10^{-3}	5.33
4 x 10^6	1.88 x 10^{-3}	2.20 x 10^{-3}	17.0

Table 7.1 The effect of compressibility on Moment Coefficient Calculations. $P_{ref}=1.01\times10^5$ Pa, $T=298^0$K, $\mu=1.84\times10^{-5}$ kg m^{-1} s^{-1}, $\lambda=60^0$, a/b=0, d/b=0.08, Cq=0.

FIGURES

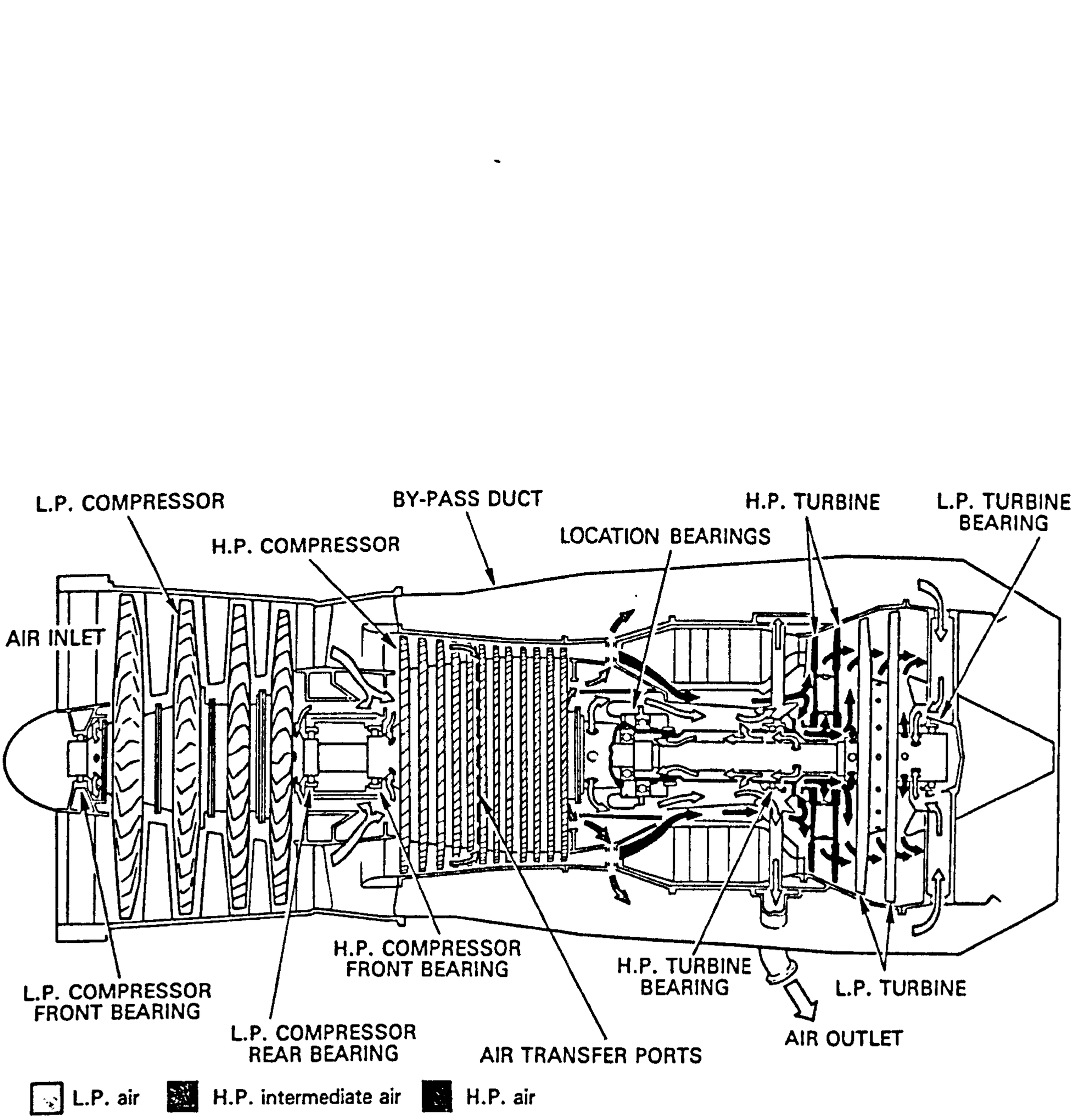

Figure 1.1 The Internal Air Flow in a typical Aero-engine.

(Taken from 'Rolls-Royce The Jet Engine', publication ref T.S.D.1302, July 1969)

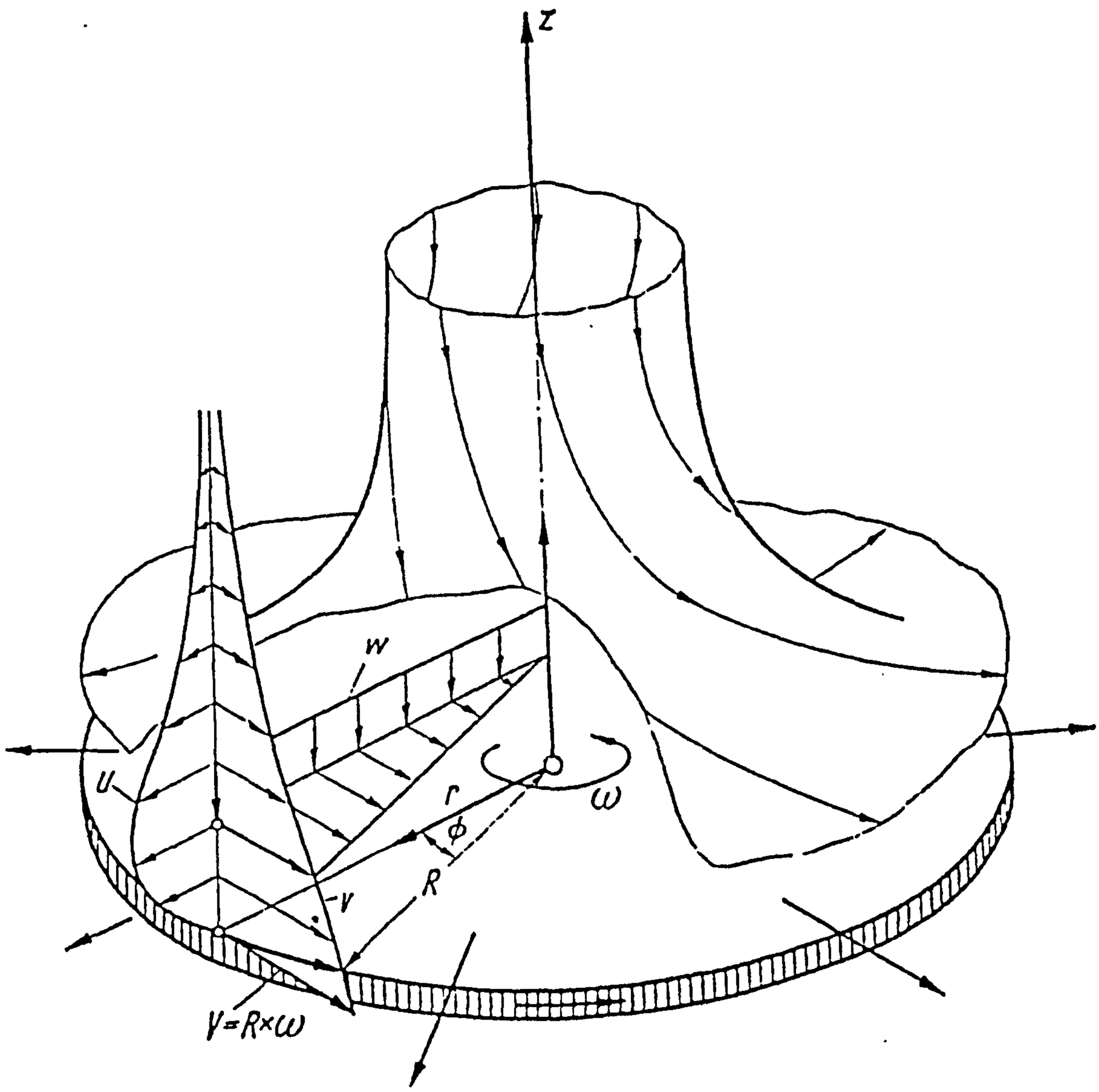

Figure 2.1(a) The Flow in the Neighbourhood of a Disc Rotating in a Fluid at rest. Velocity components: u-radial, v-tangential, w-axial. (Taken from Schlichting (1968)).

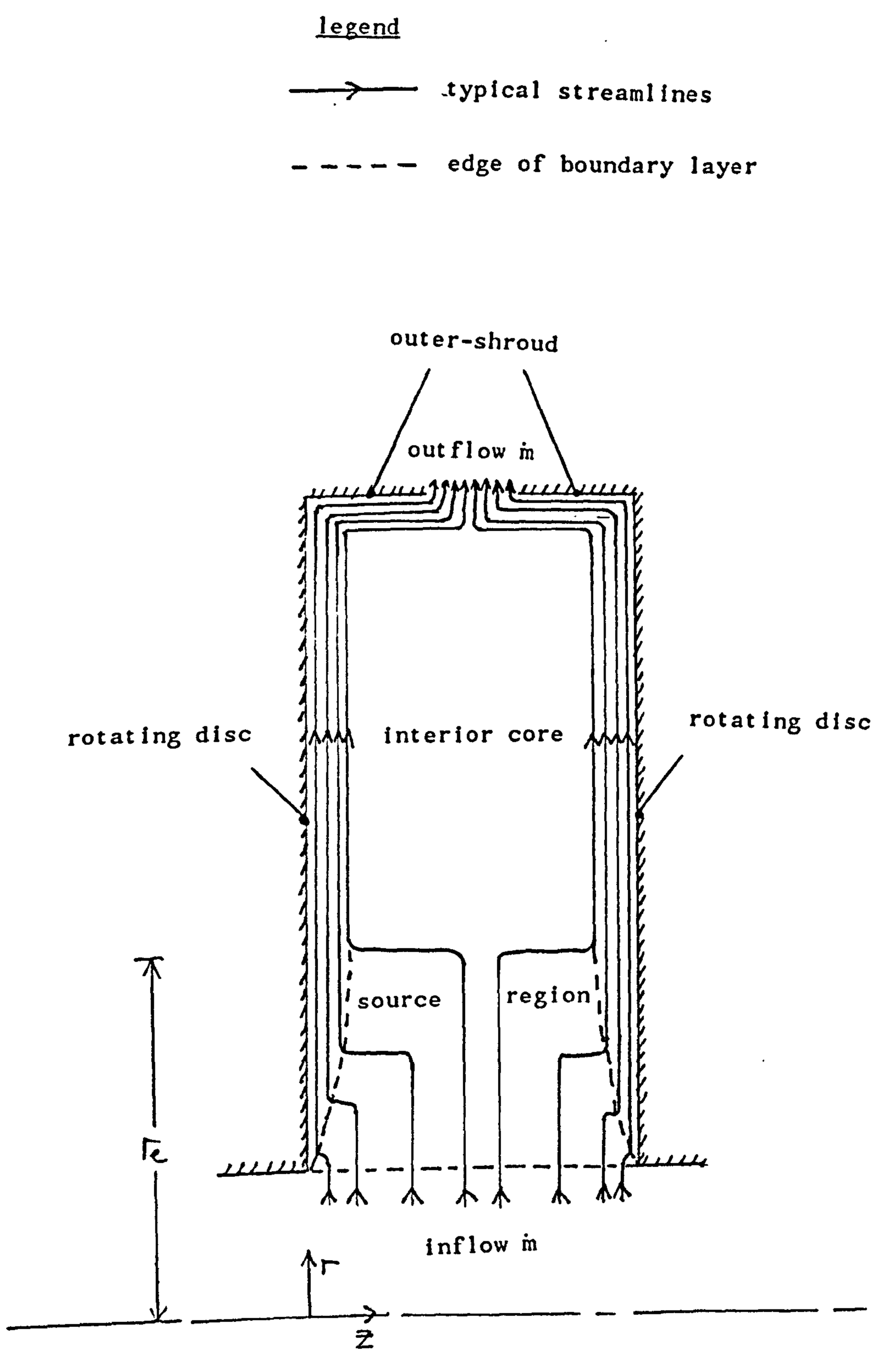

Figure 2.1(b) The Flow Pattern in a Co-Rotating Disc System

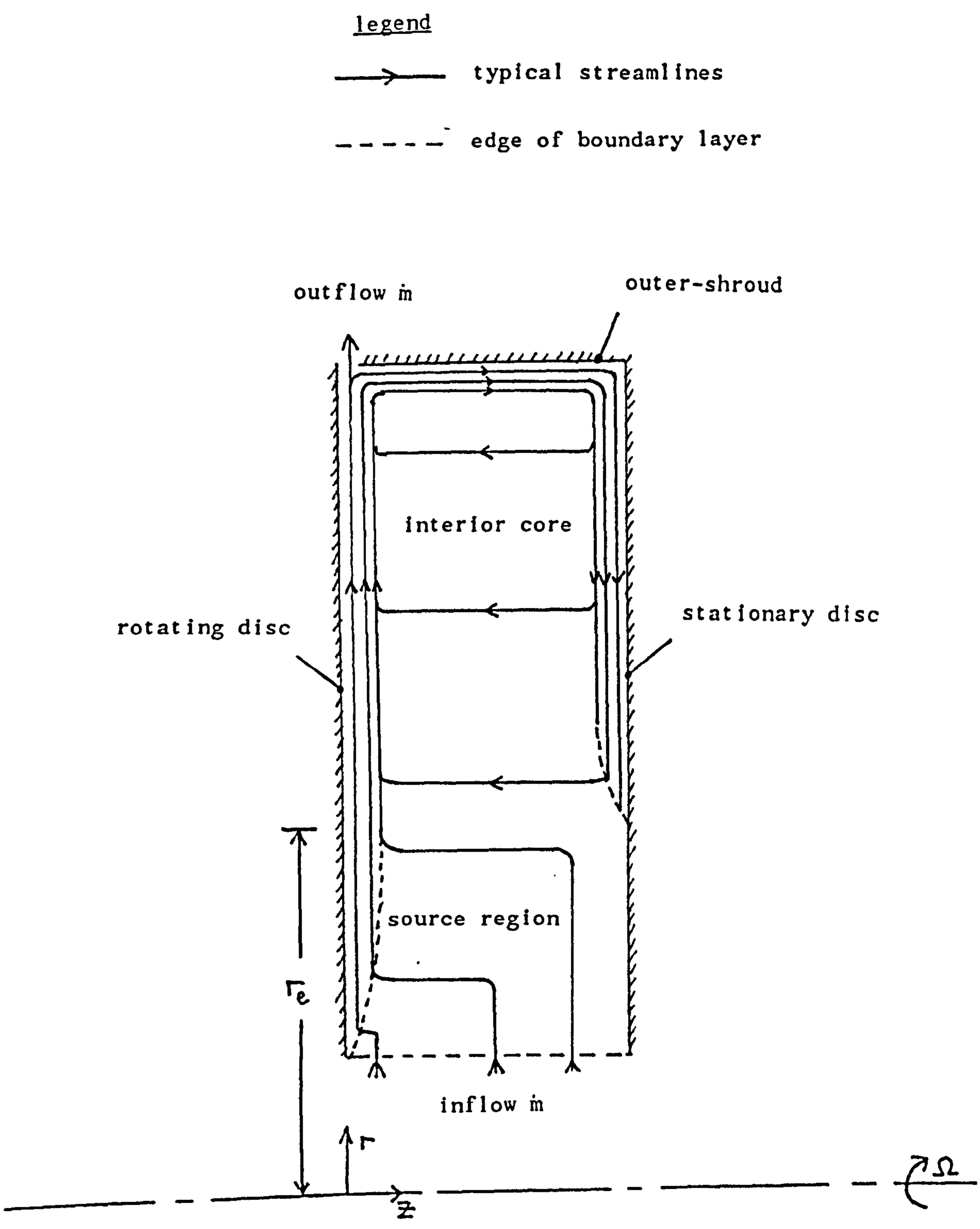

Figure 2.1(c) Flow Pattern in a Rotor-Stator Disc System

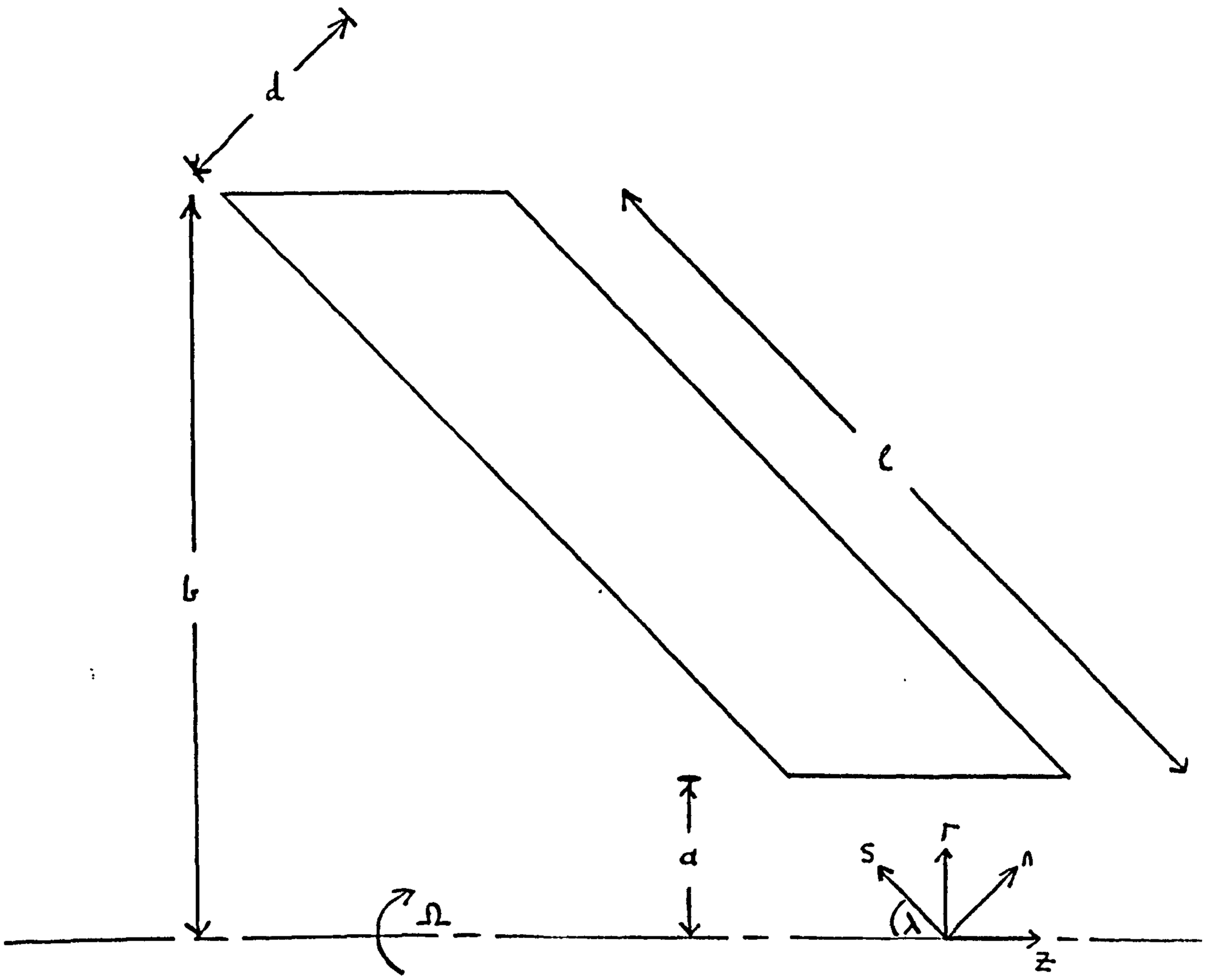

Figure 3.1 Geometry of the Rotor-Stator Cone System

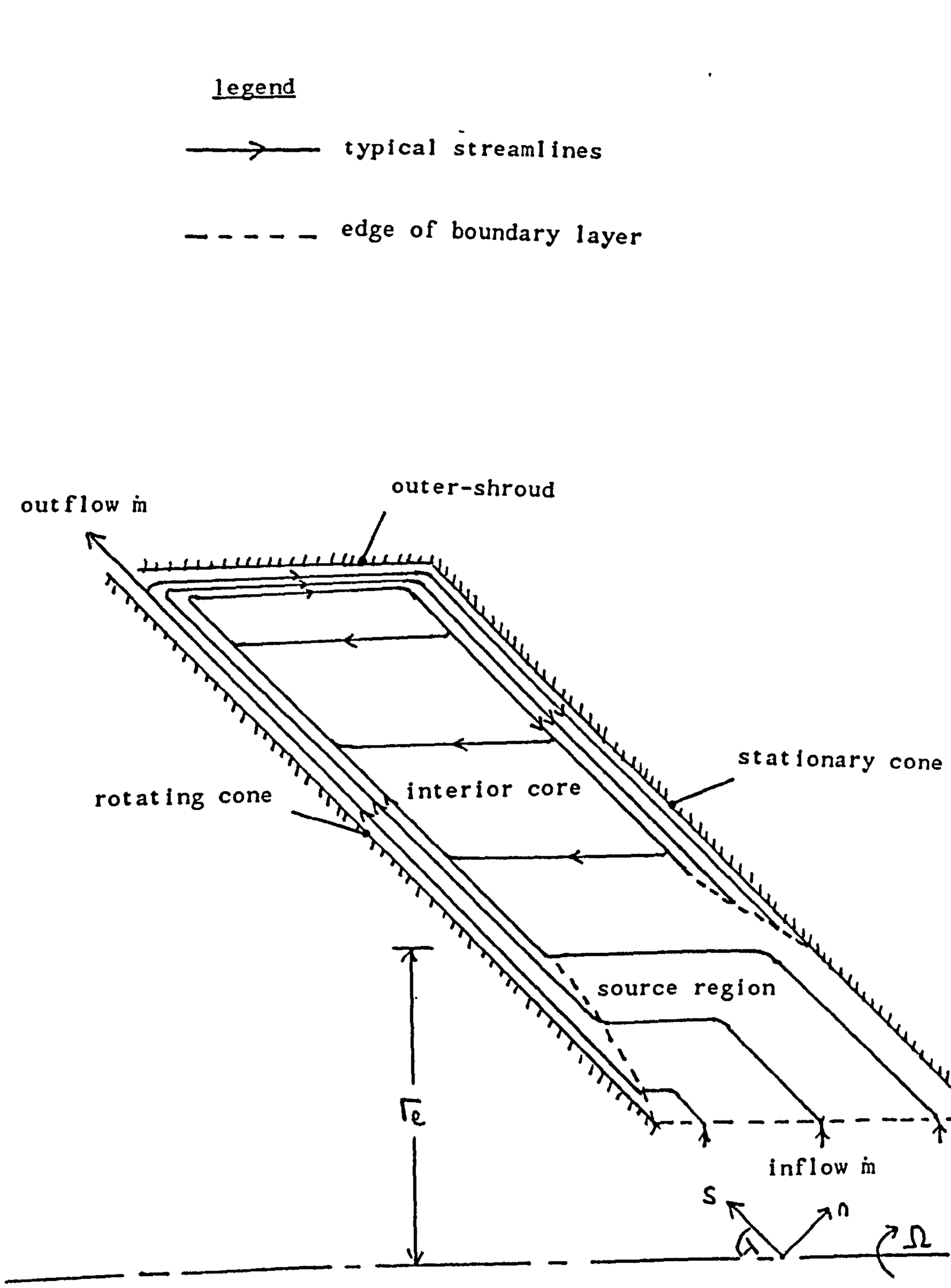

Figure 3.2 Postulated Flow Pattern in a Rotor-stator Cone System

Comparison of $\bar{V}(x)$ against x for various throughflow rates; $Re_\theta=10^6$, a/b=0.1, d/b=0.1, φ=0 and λ=90°

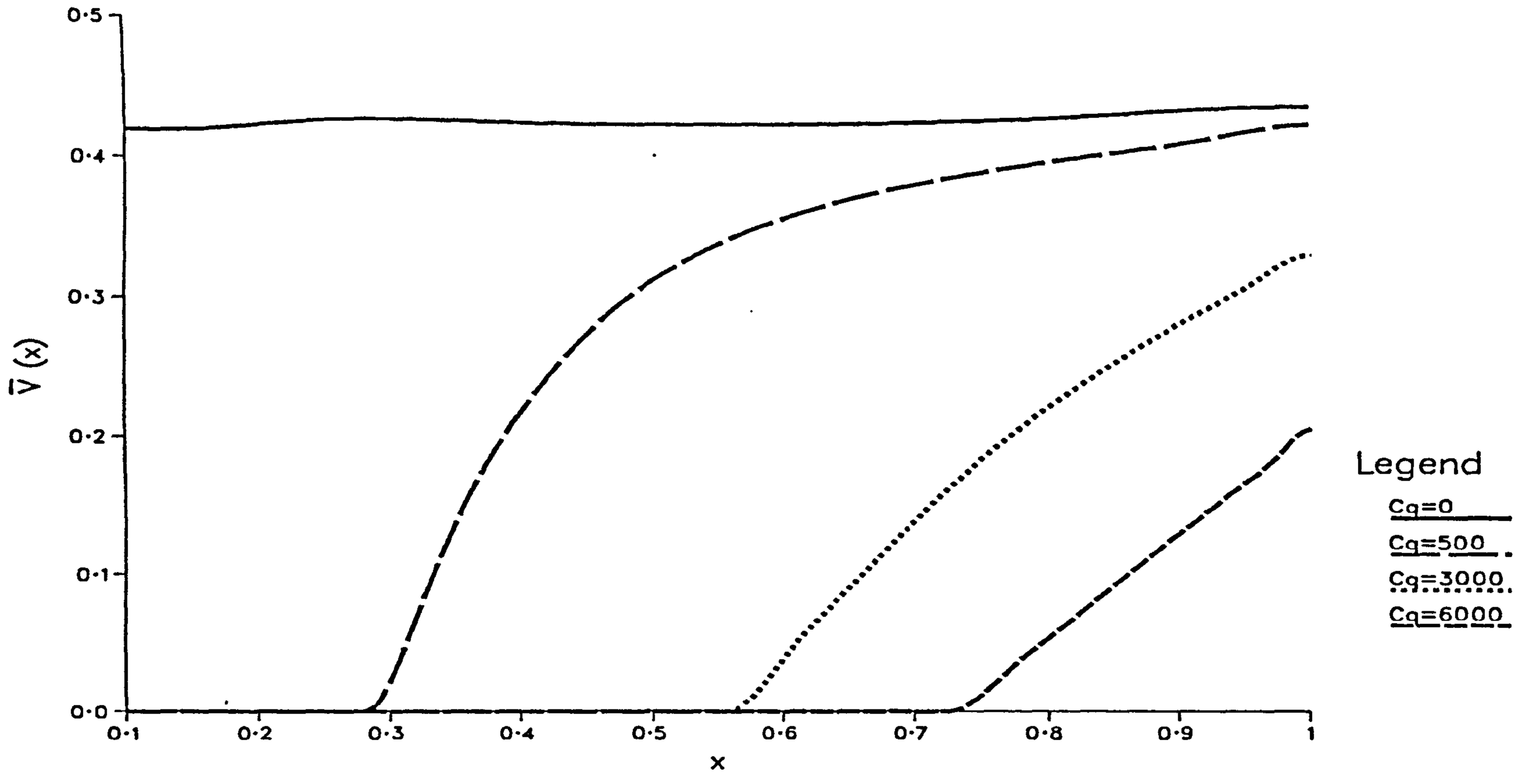

Figure 4.1

A comparison of $\bar{V}(x)$ predicted by method 1 and method 2; $a/b=0.1$, $d/b=0.1$, $\varphi=0$, $Re_\theta=10^6$ and $\lambda=60°$.

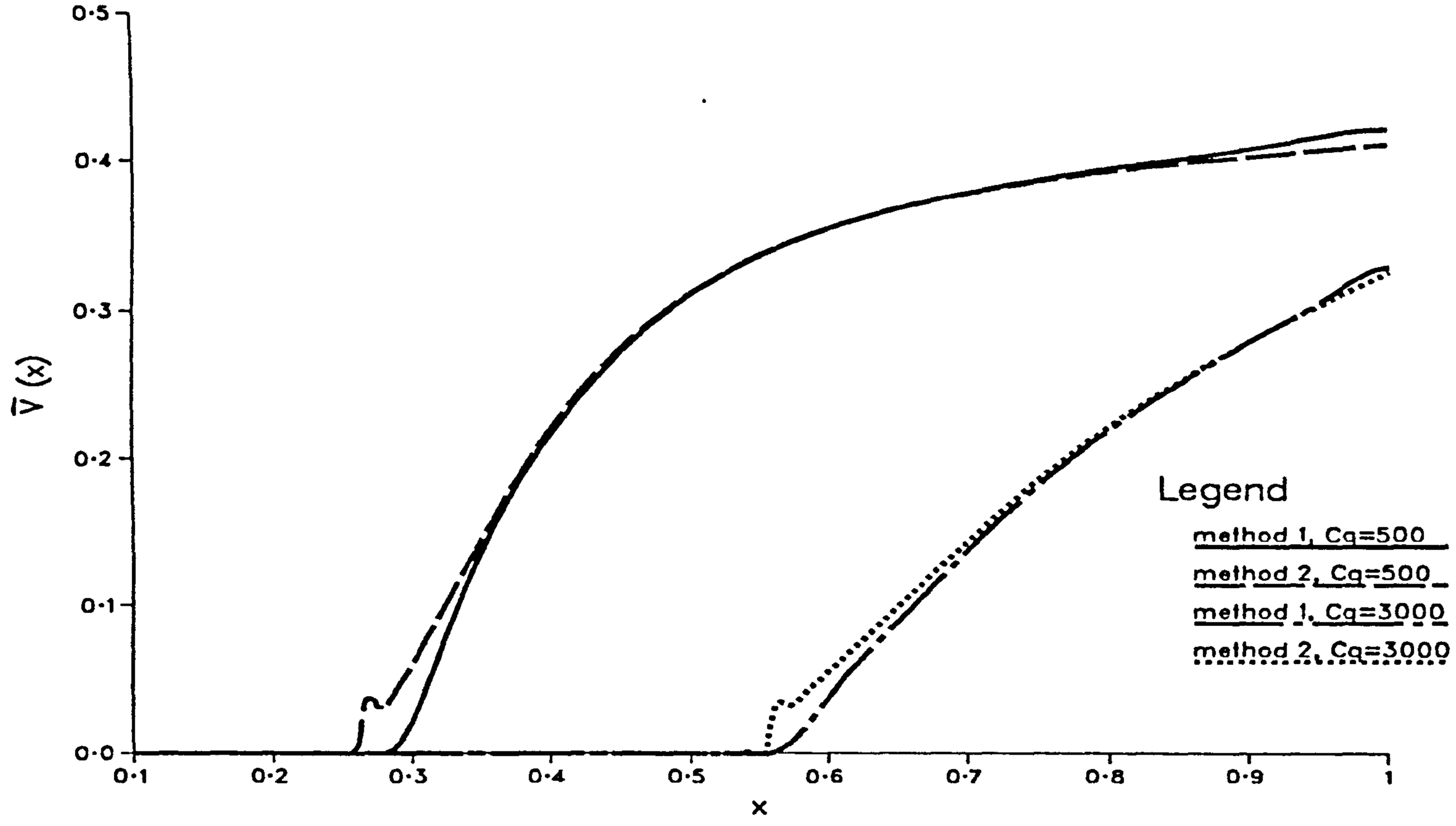

Figure 4.2

The effect of α on the solutons to the rotor equations; $Re_\theta=10^6$, a/b=0.001 and V=0

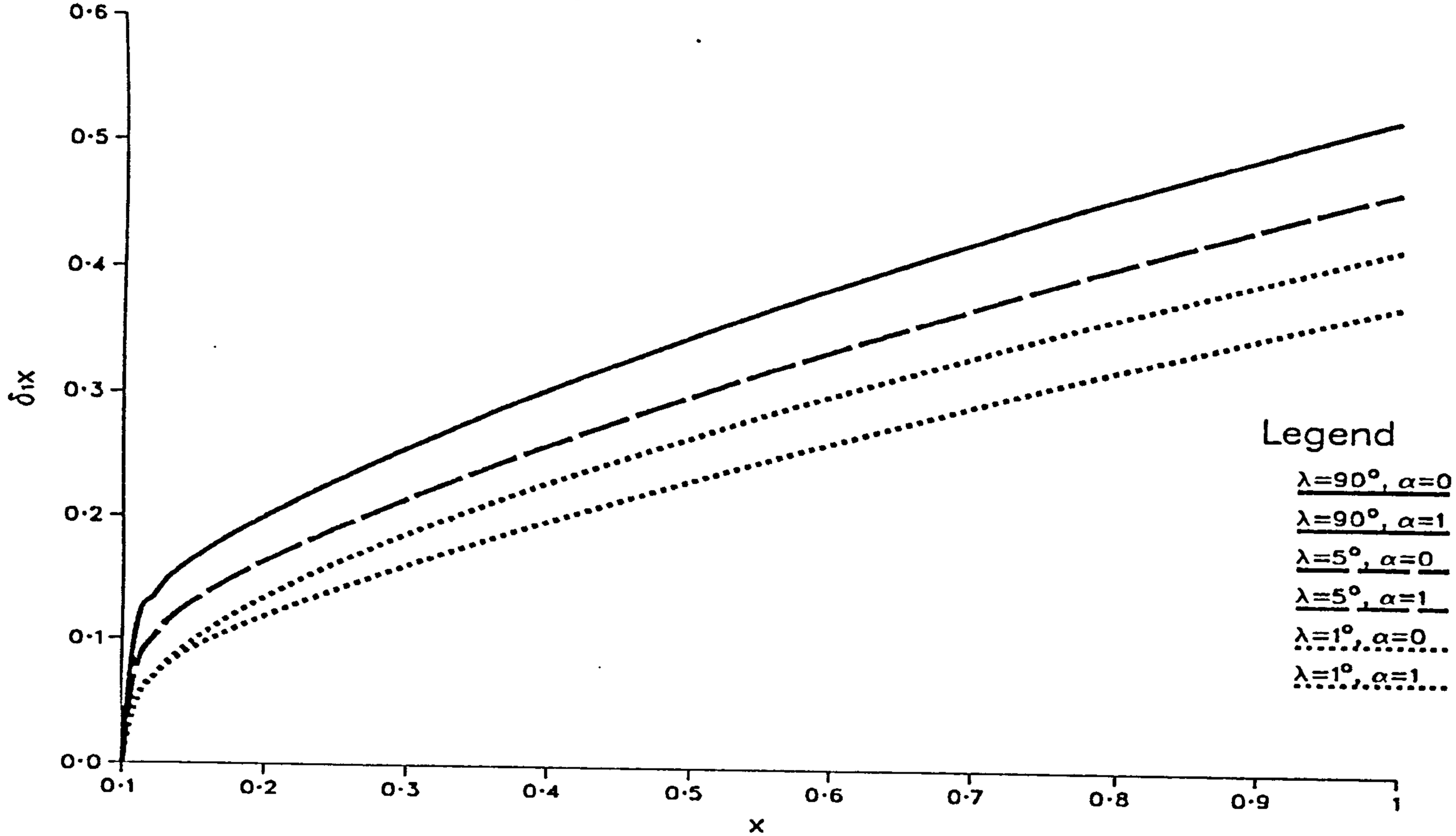

Figure 4.3

The effect of cone angle, λ, on the solutions to the rotor equations; $Re_{\delta}=10^6$, $a/b=0.001$, and $V=0$

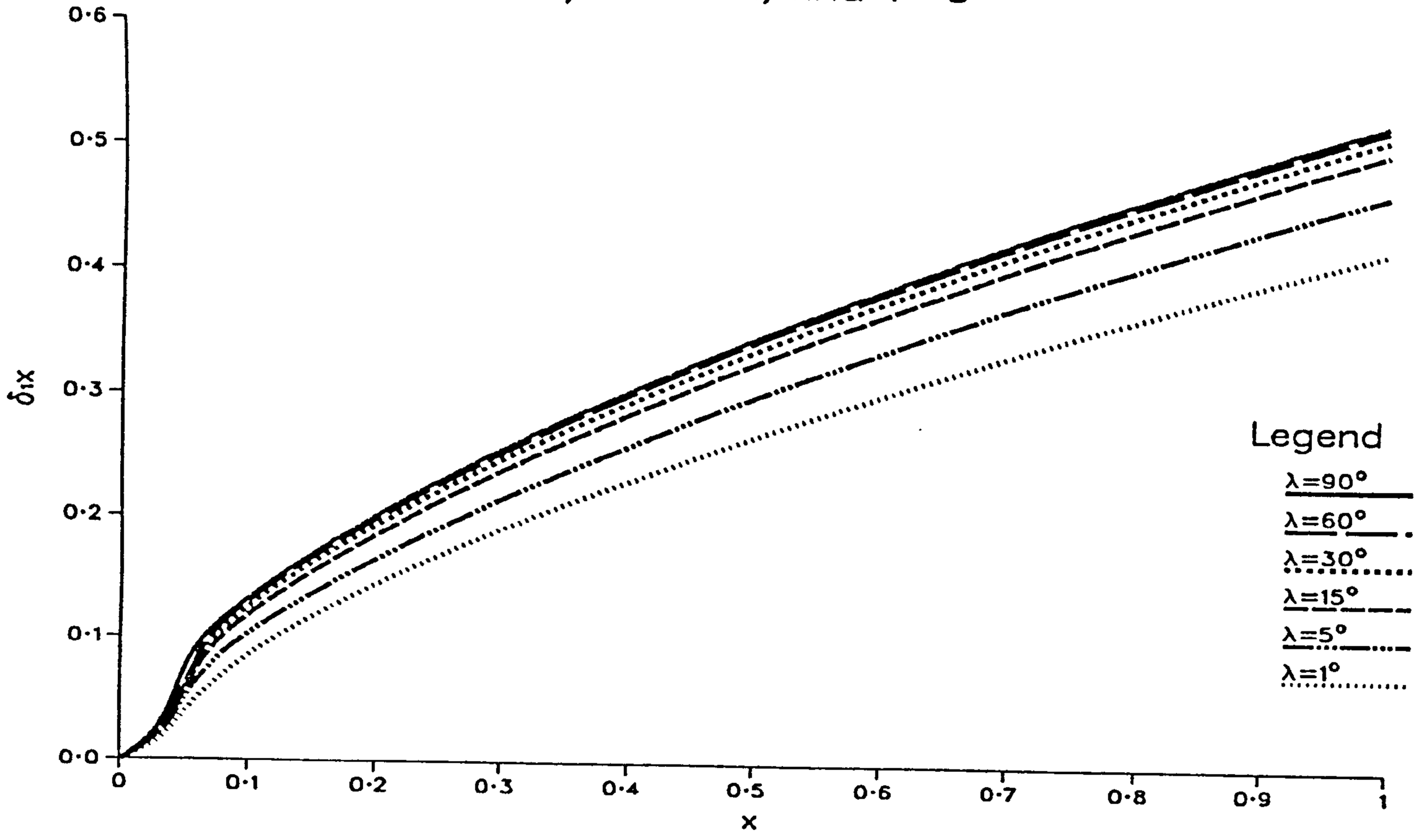

Figure 4.4(a)

The effect of cone angle, λ, on the solutions to the rotor equations; $Re_\theta = 10^6$, $a/b = 0.5$, and $\bar{V} = 0$

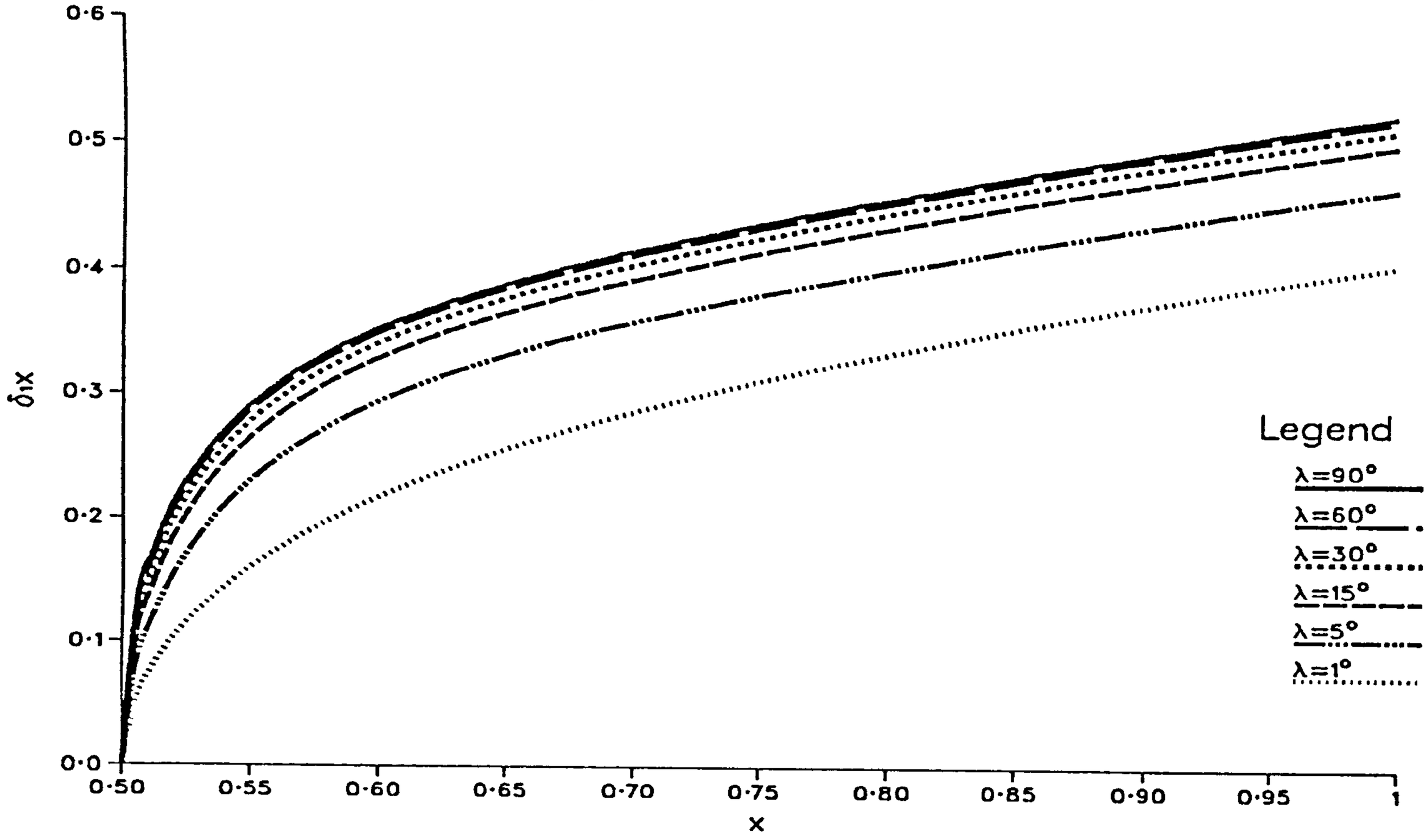

Figure 4.4(b)

The effect of cone angle, λ, on the solutions to the rotor equations; $Re_{\theta}=10^{6}$, $a/b=0.75$, and $V=0$

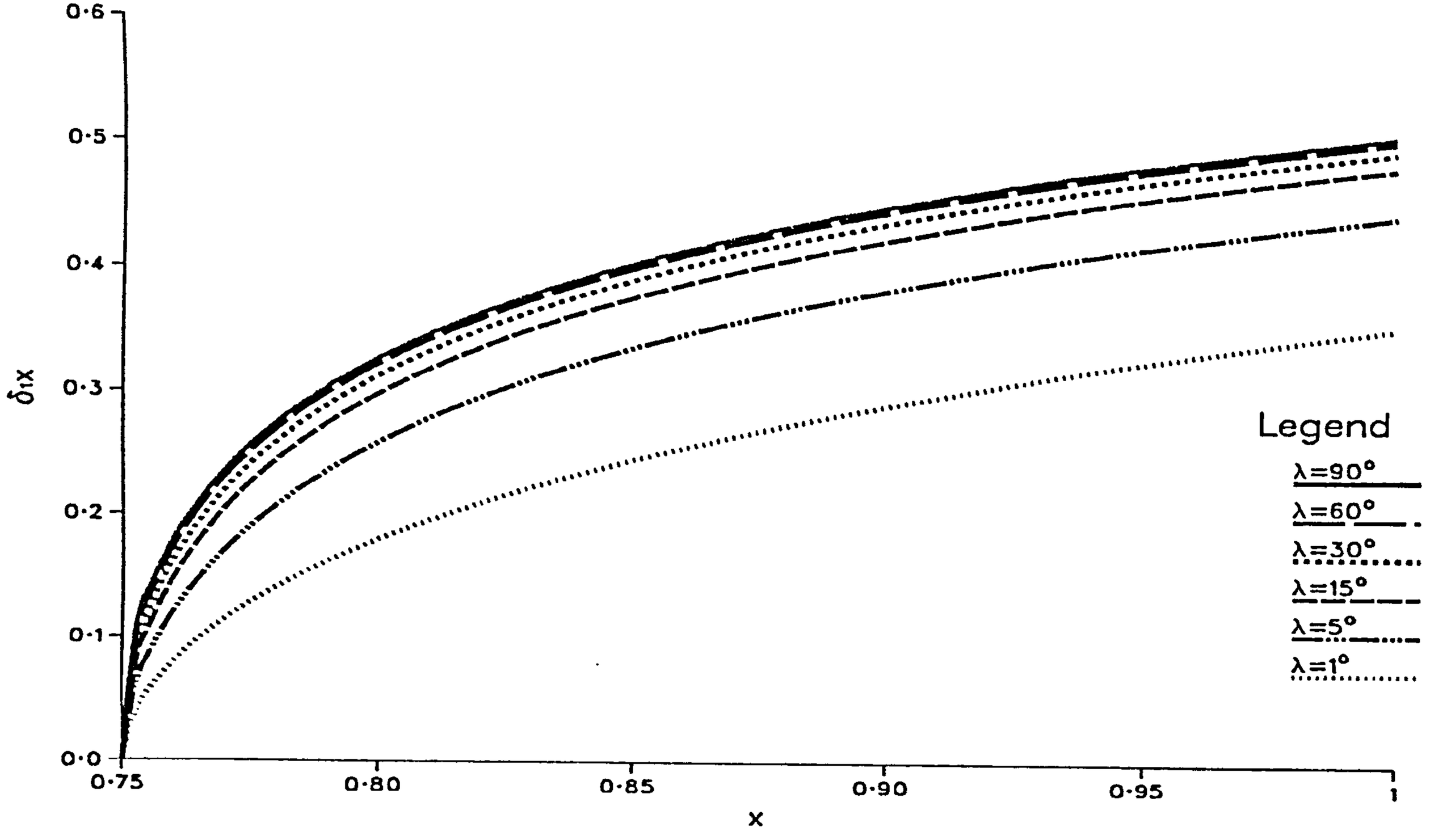

Figure 4.4(c)

The effect of cone angle, λ, on the solutions to the rotor equations; $Re_\theta = 10^6$, $a/b = 0.001$, and $\bar{V} = 0.42$

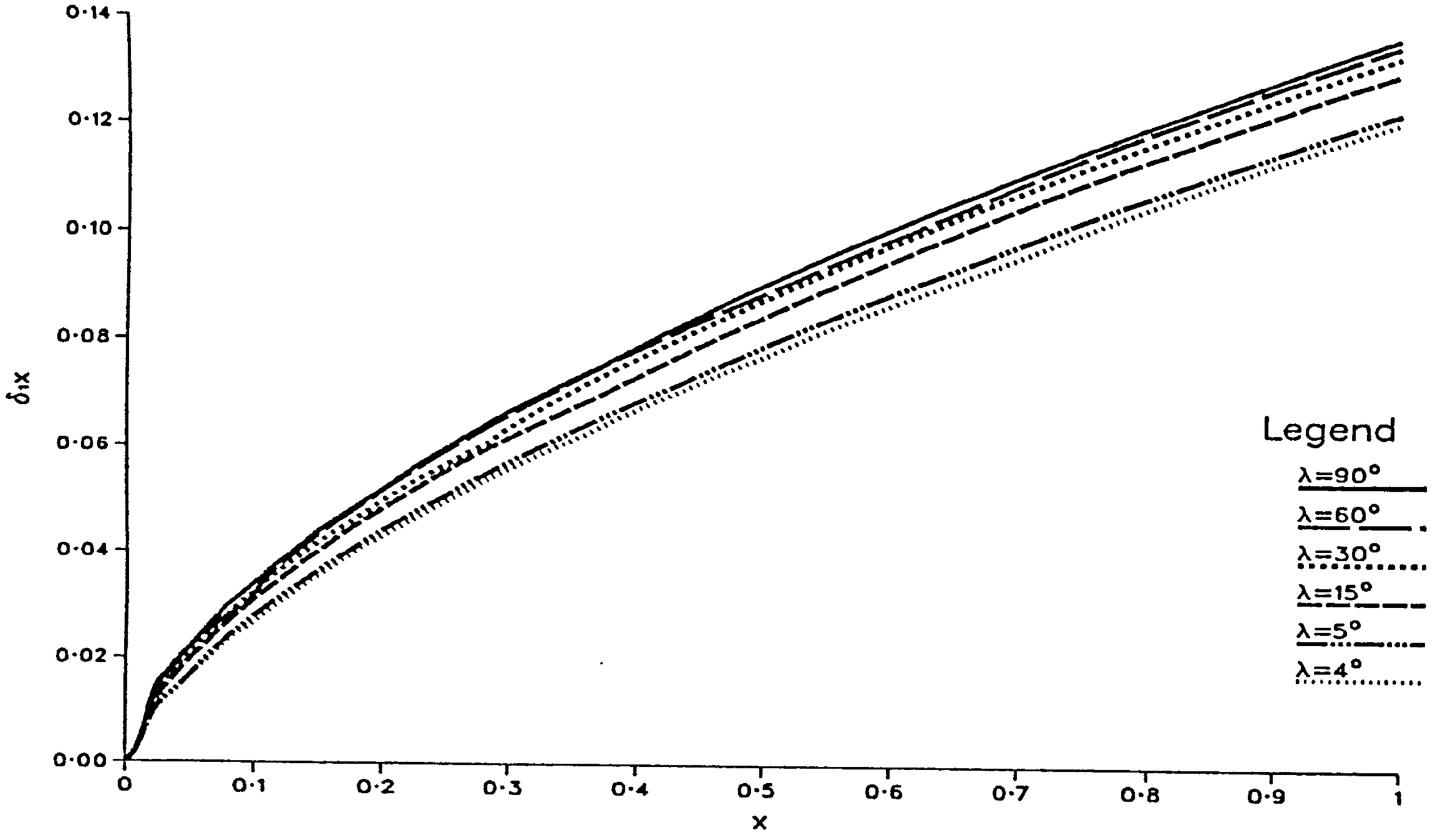

Figure 4.5

The effect of cone angle, λ, on the solutions to the stator equation; $Re_\theta = 10^6$, and $\bar{V} = 0.42$

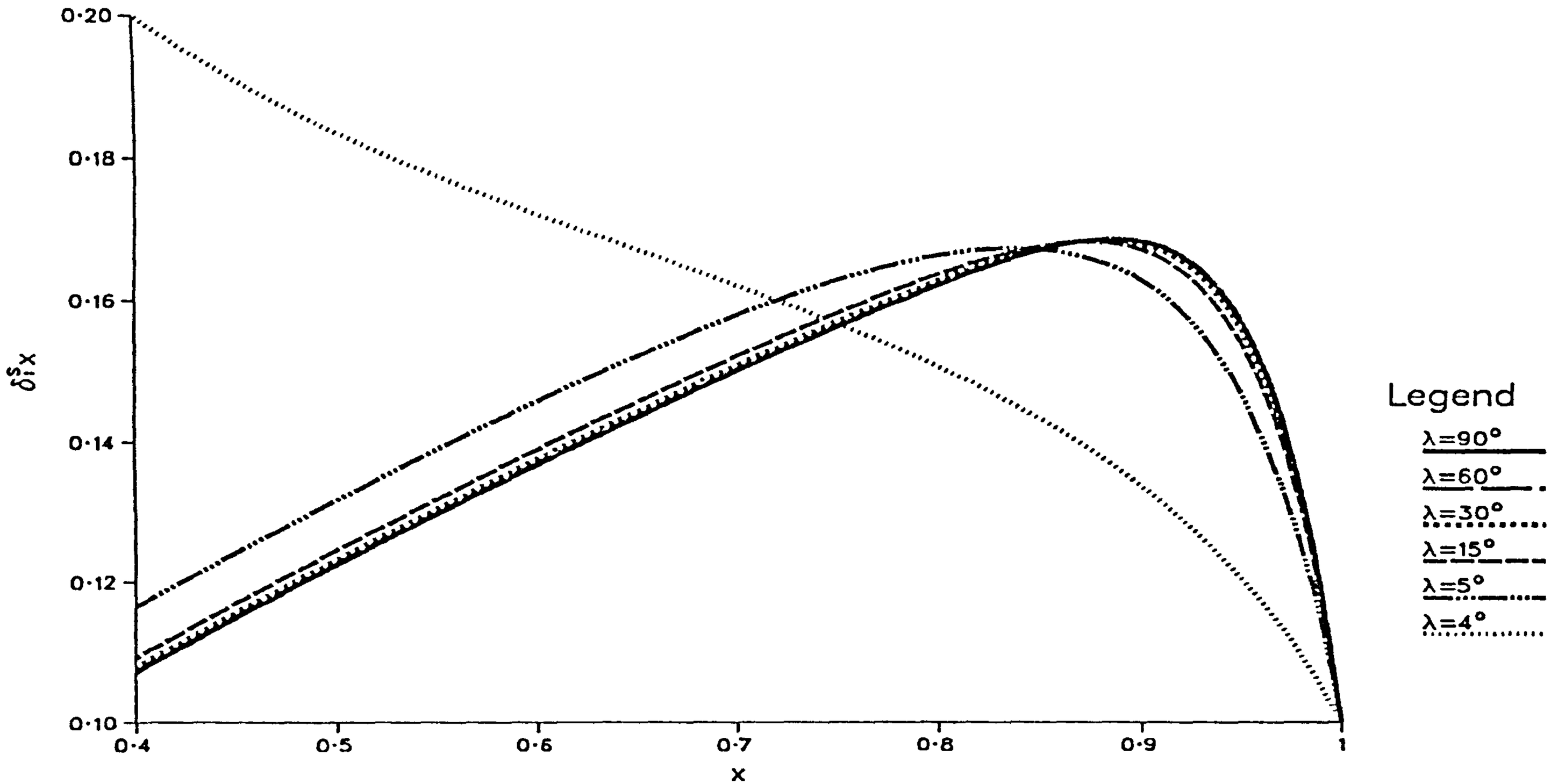

Figure 4.6(a)

The effect of cone angle, λ, on the solutions to the stator equation; $Re_\theta = 10^6$, and $\bar{V} = 0.42x$

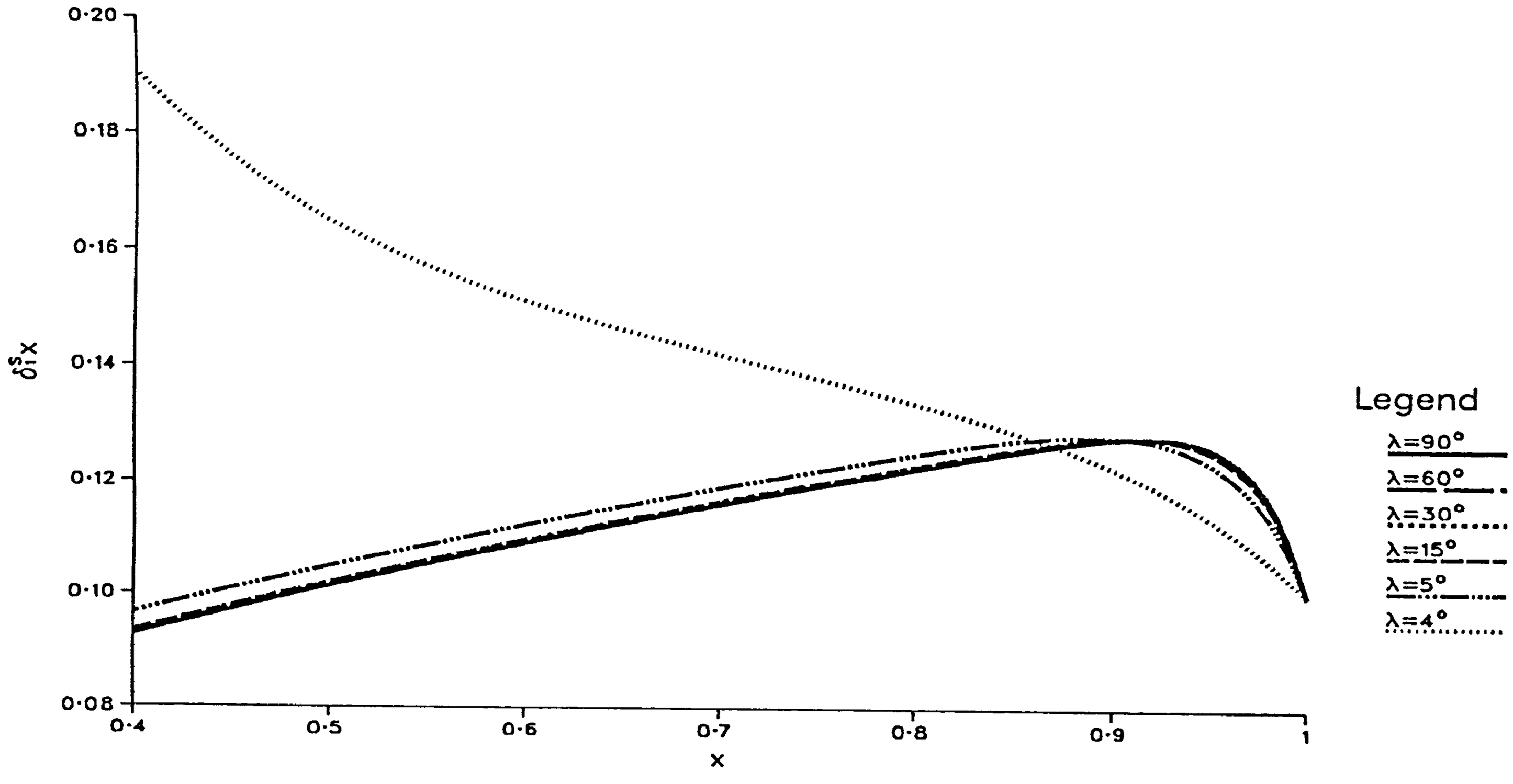

Figure 4.6(b)

The effect of the initial conditions on the solutions to the rotor equations; $Re_\theta=10^6$, $a/b=0.1$, $\lambda=90^\circ$ and $\bar{V}=0$

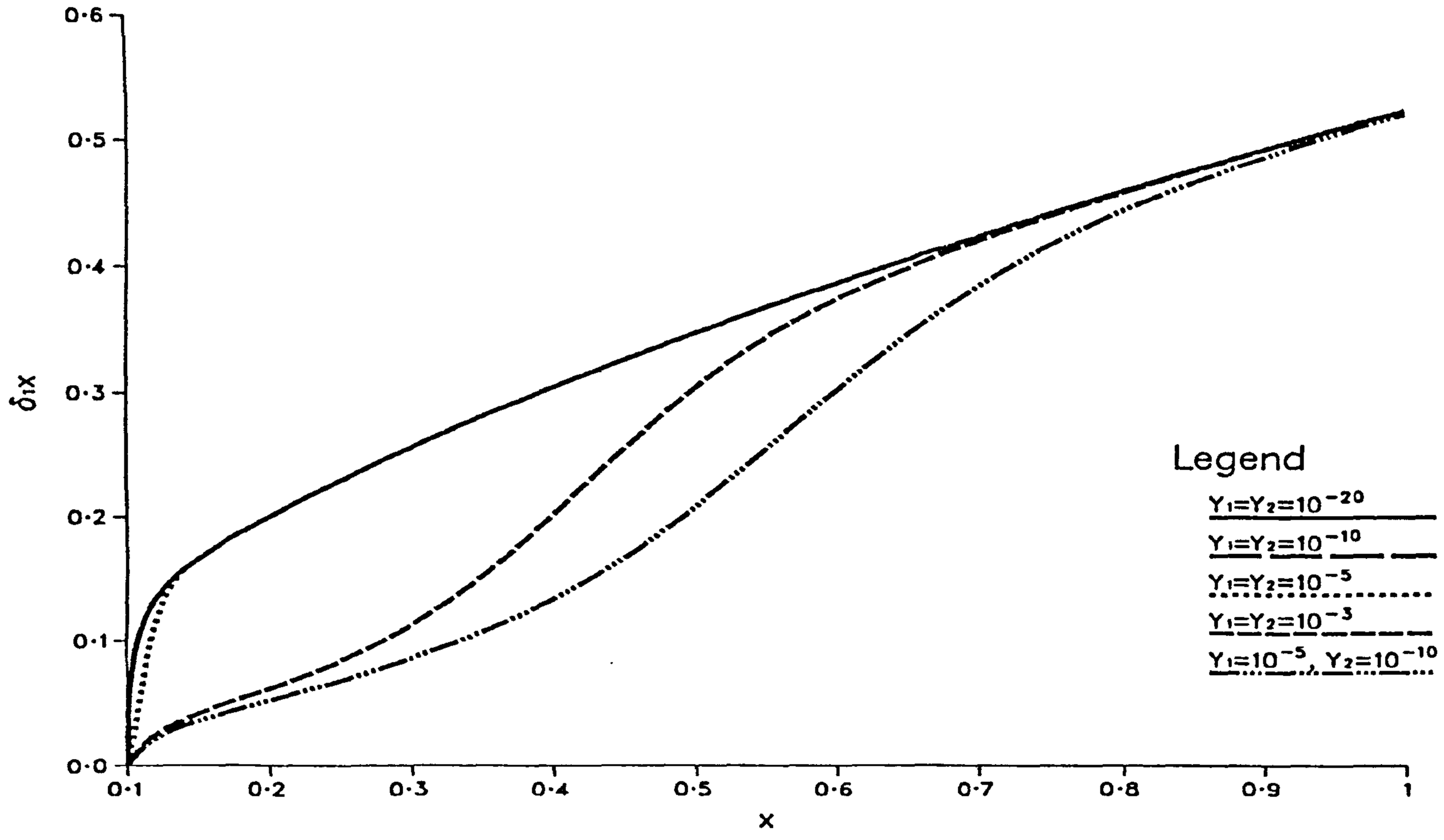

Figure 4.7

A comparison of the solutions to equations (4.2.4) and (4.2.5) with the solutions to equations (4.5.5) and (4.5.6), a/b=0.001, $\lambda=90^\circ$ and $V=0$

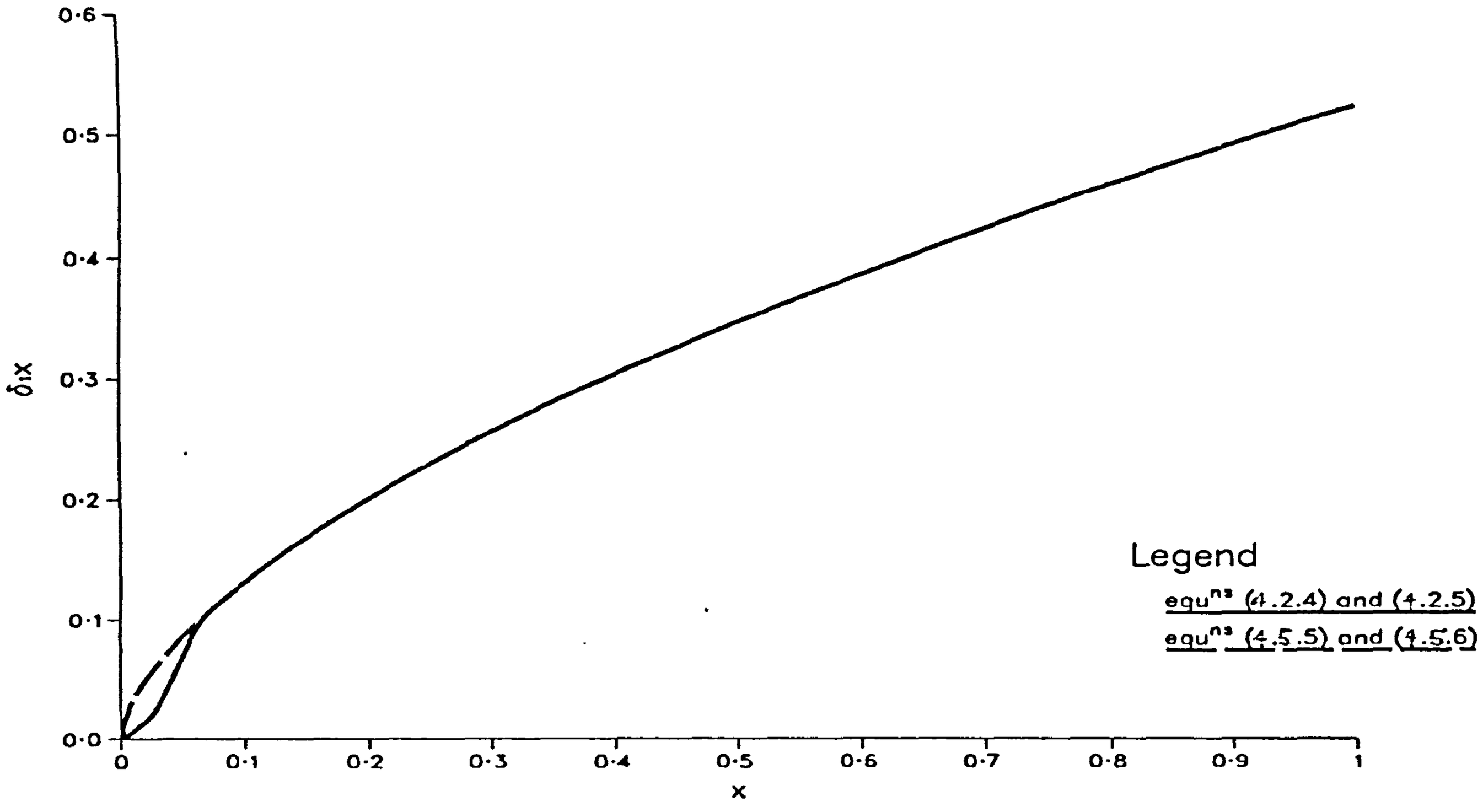

Figure 4.8

A comparison of the predicted moment coefficient with Daily and Nece (1960) and Chew (1988); Cq=0, a/b=0.1 and λ=90°.

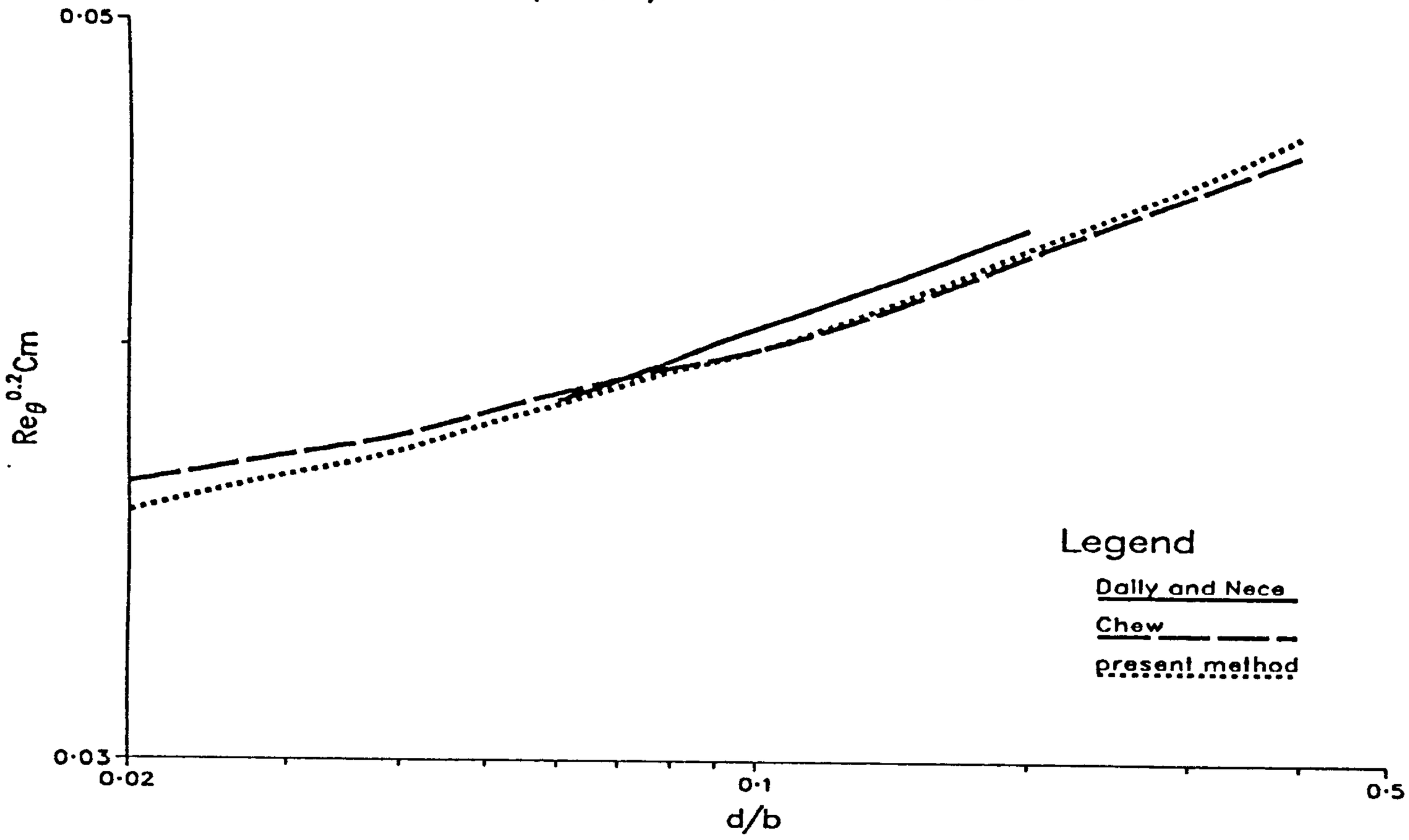

Figure 4.9(a)

A comparison of the predicted moment coefficient with Yamada and Ito (1975); Cq=0, a/b=0 and $\lambda=90^{\circ}$.

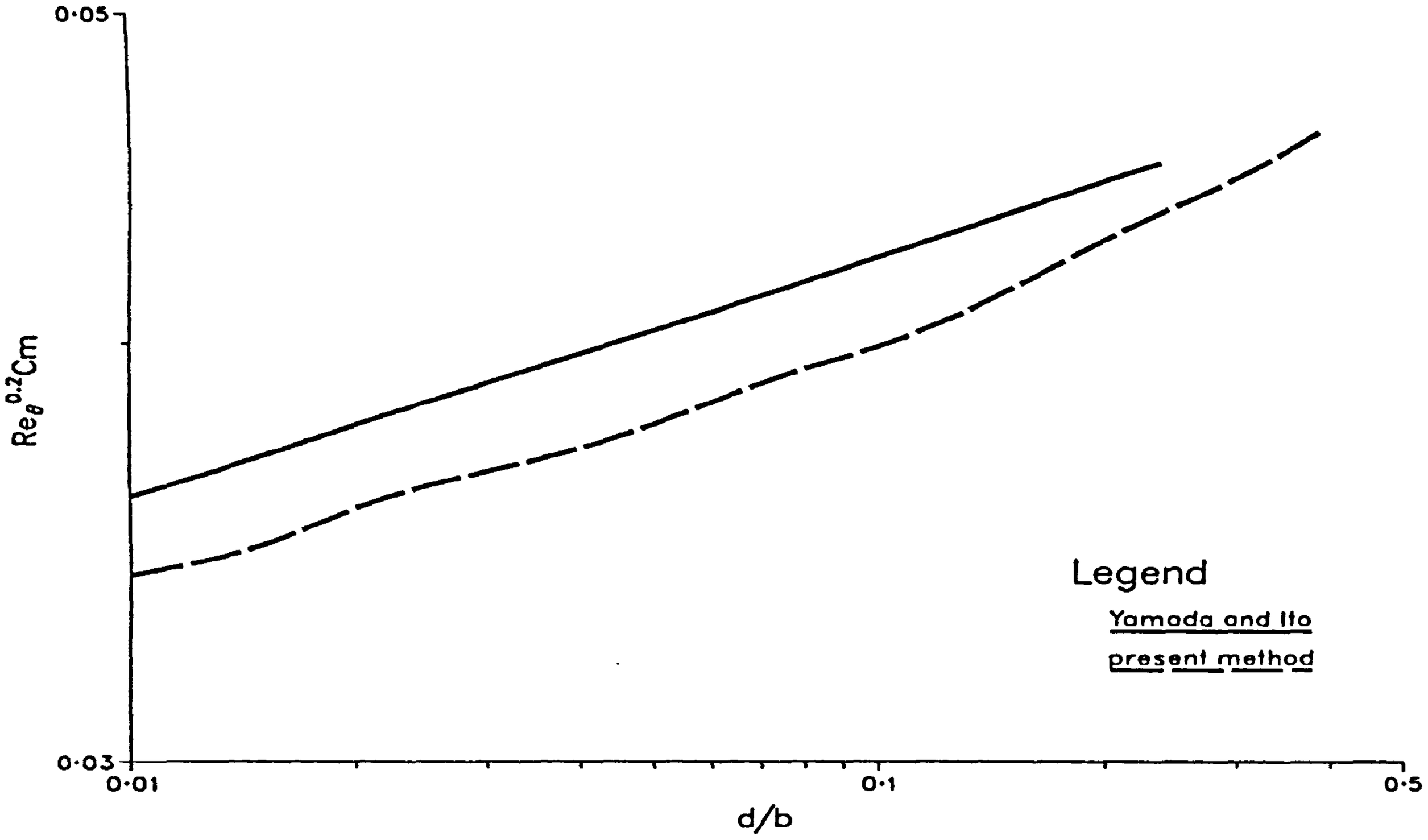

Figure 4.9(b)

A comparison of the predicted moment coefficient with Daily et al (1964); d/b=0.0685, a/b=0.11 and λ=90°.

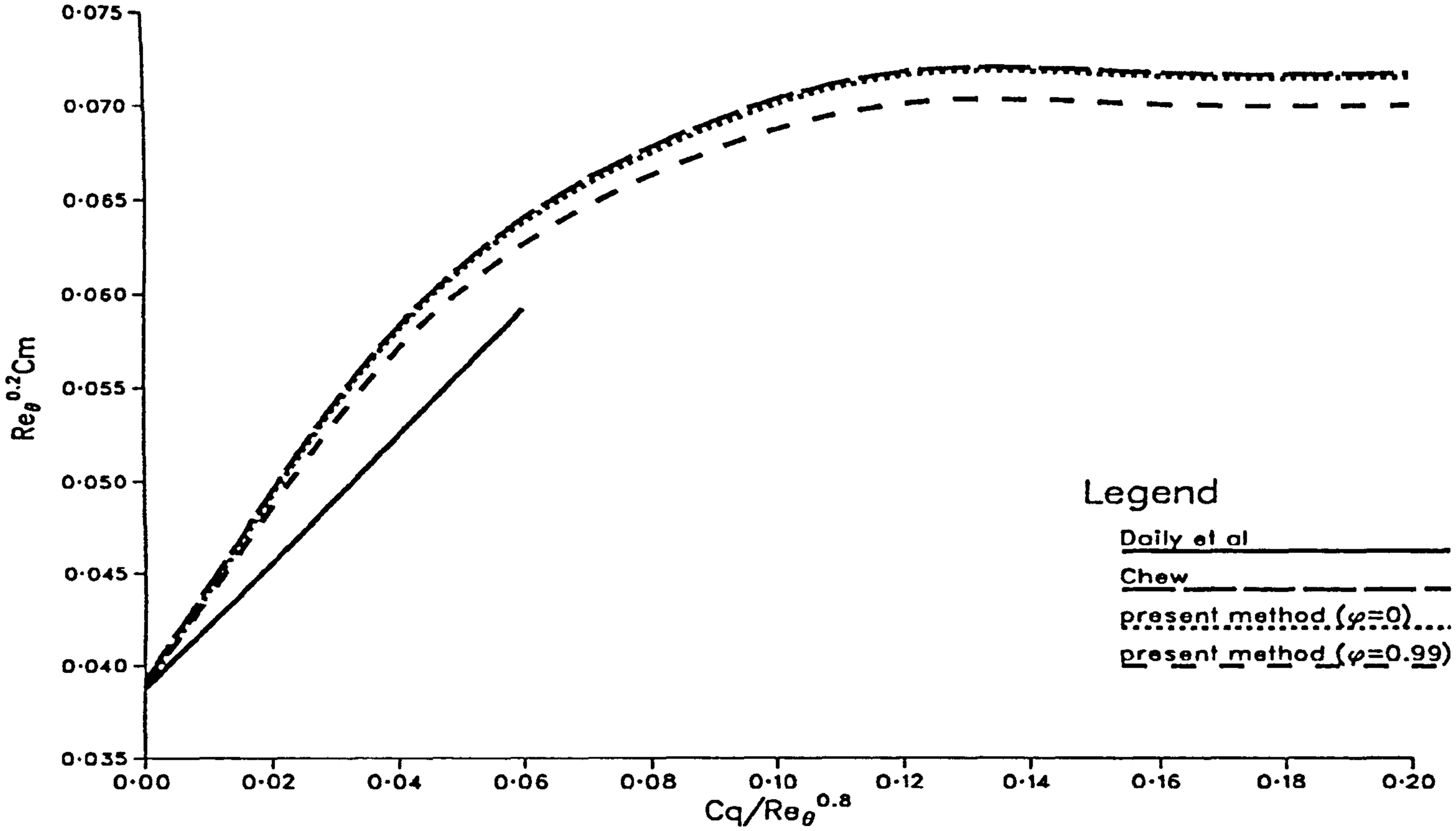

Figure 4.9(c)

A comparison of the predicted moment coefficient with Yamada and Ito (1975); Cq=0, a/b=0, d/b=0.24, Re=10^6

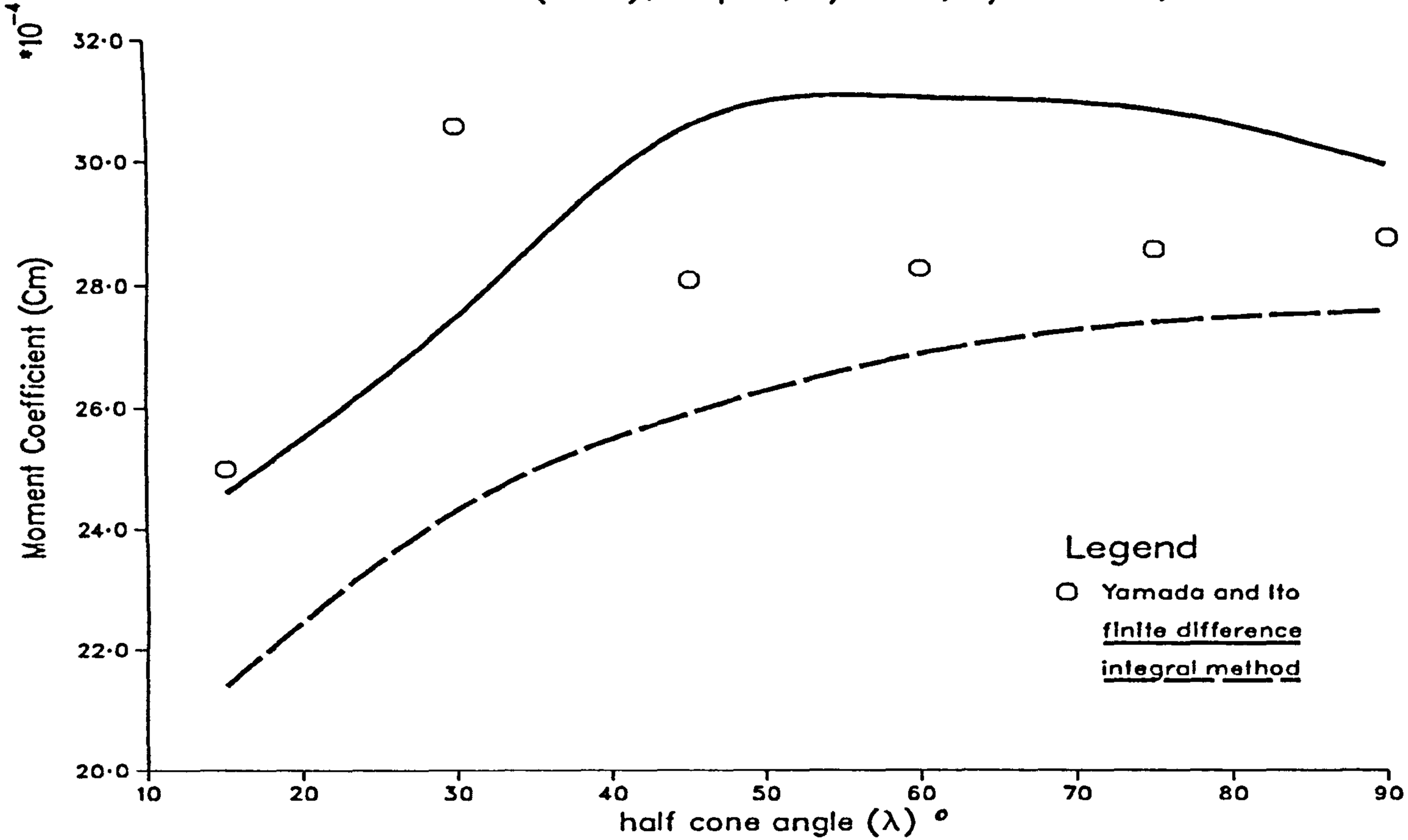

Figure 4.10(a)

A comparison of the predicted moment coefficient with Yamada and Ito (1975); Cq=0, a/b=0, d/b=0.16, Re=10^6

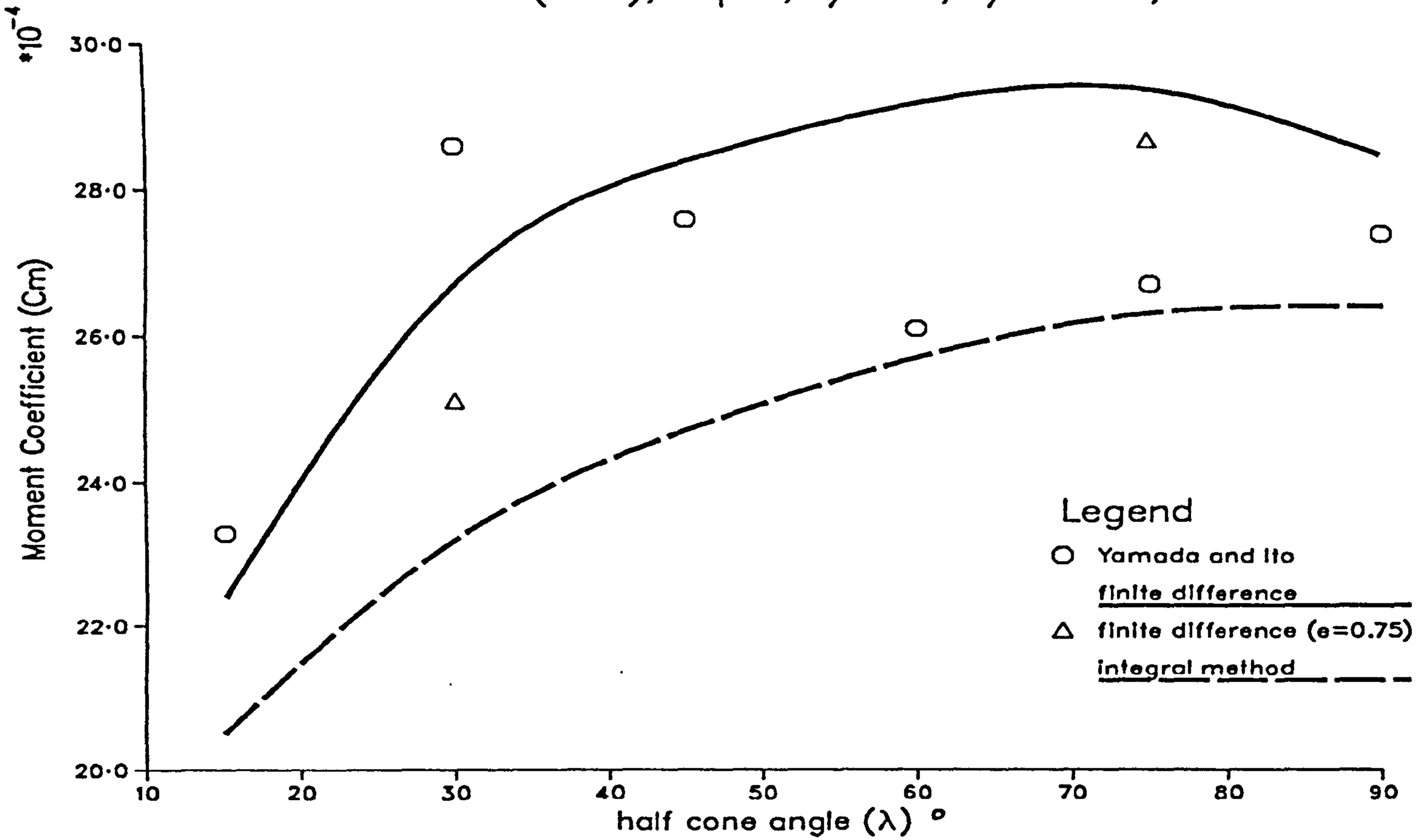

Figure 4.10(b)

A comparison of the predicted moment coefficient with Yamada and Ito (1975); Cq=0, a/b=0, d/b=0.08, Re=10^6

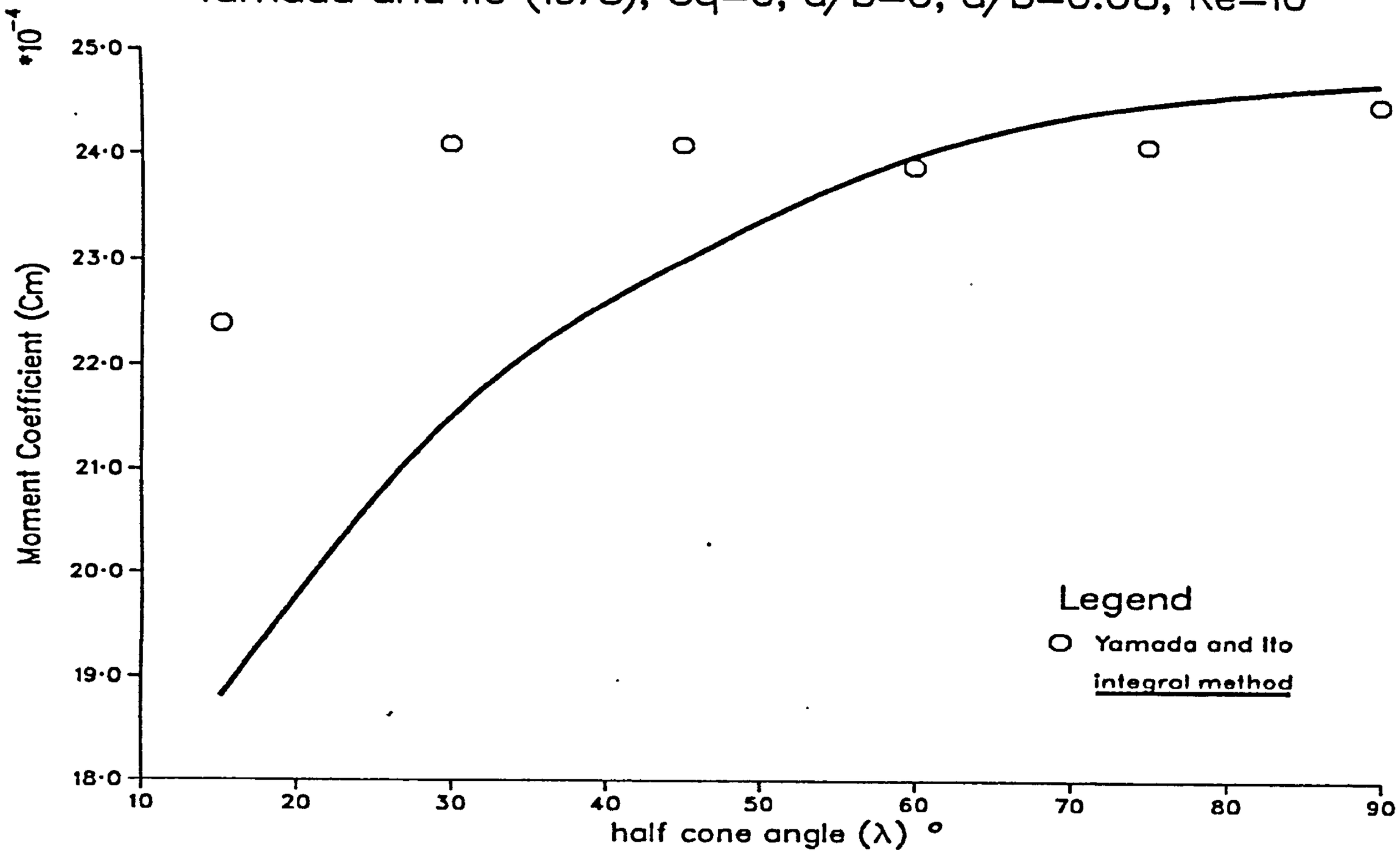

Figure 4.10(c)

A comparison of the predicted moment coefficient with Yamada and Ito (1975); Cq=0, a/b=0, d/b=0.024, Re=10^6

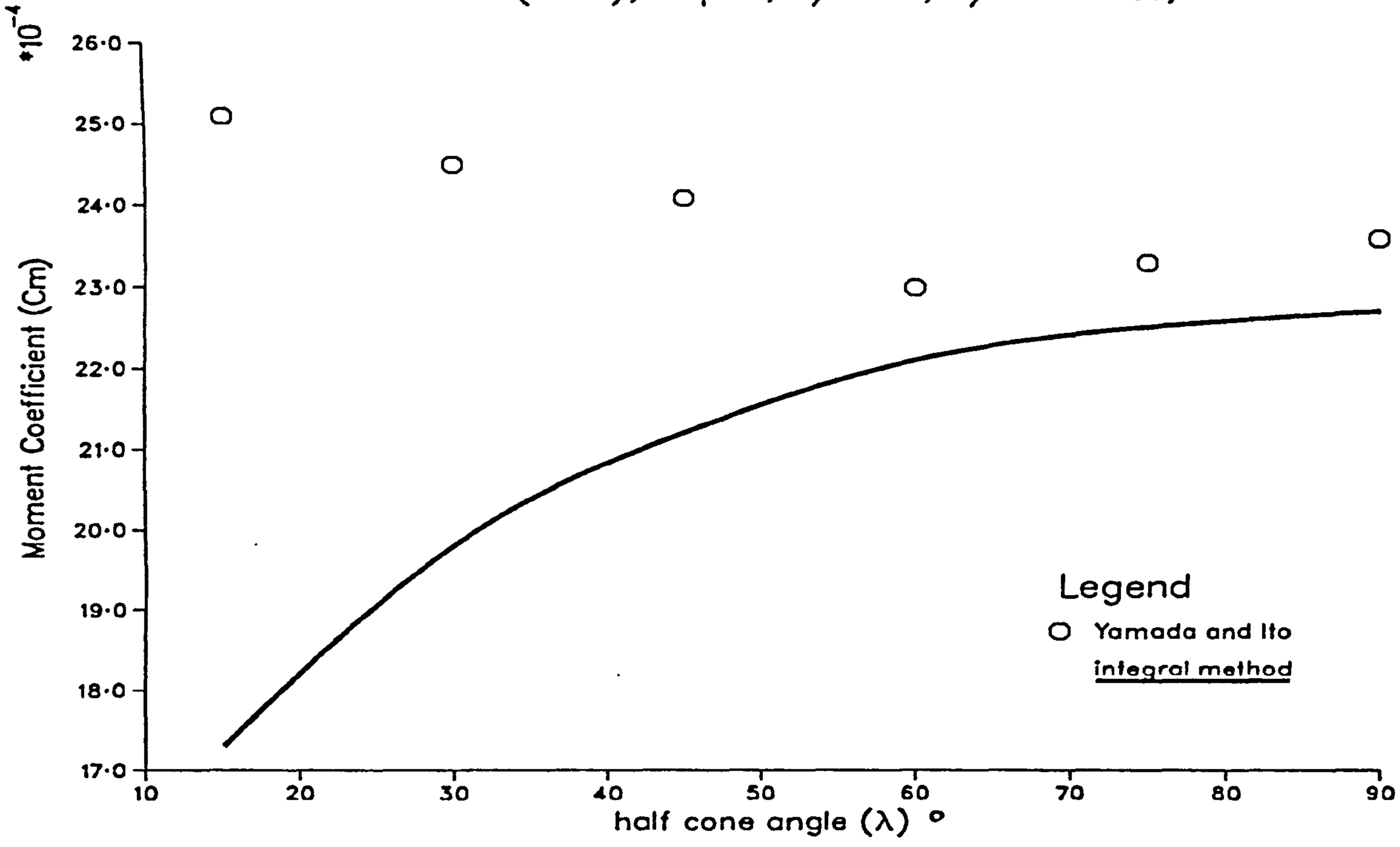

Figure 4.10(d)

A comparison of the predicted moment coefficient with Yamada and Ito (1975); Cq=0, a/b=0, d/b=0.016, Re=10^6

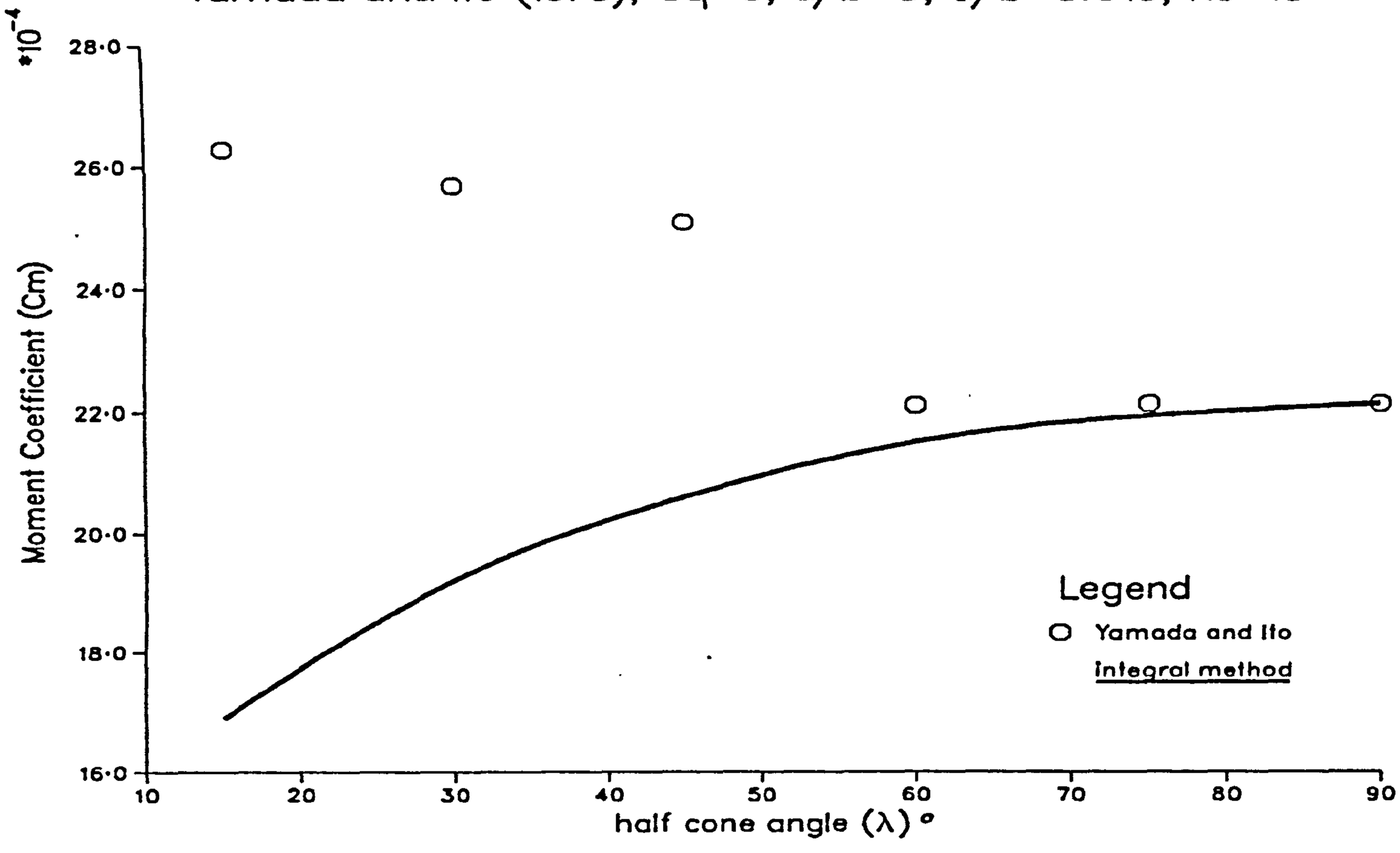

Figure 4.10(e)

A comparison of the predicted moment coefficient with Yamada and Ito (1975); Cq=0, a/b=0, d/b=0.008, Re=10^6

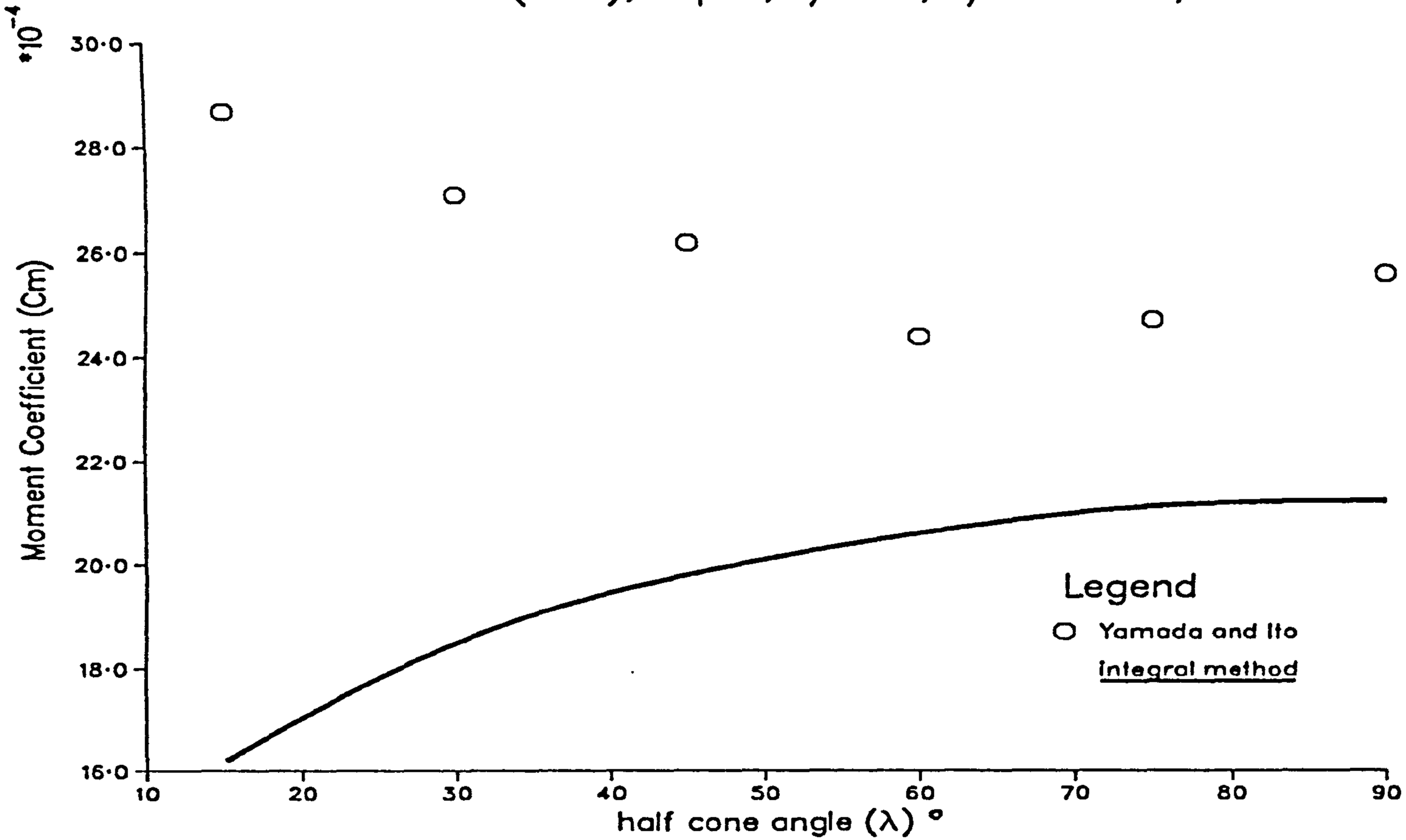

Figure 4.10(f)

A comparison of the predicted moment coefficient with Yamada and Ito (1975); Cq=0, a/b=0, d/b=0.08, λ=90°

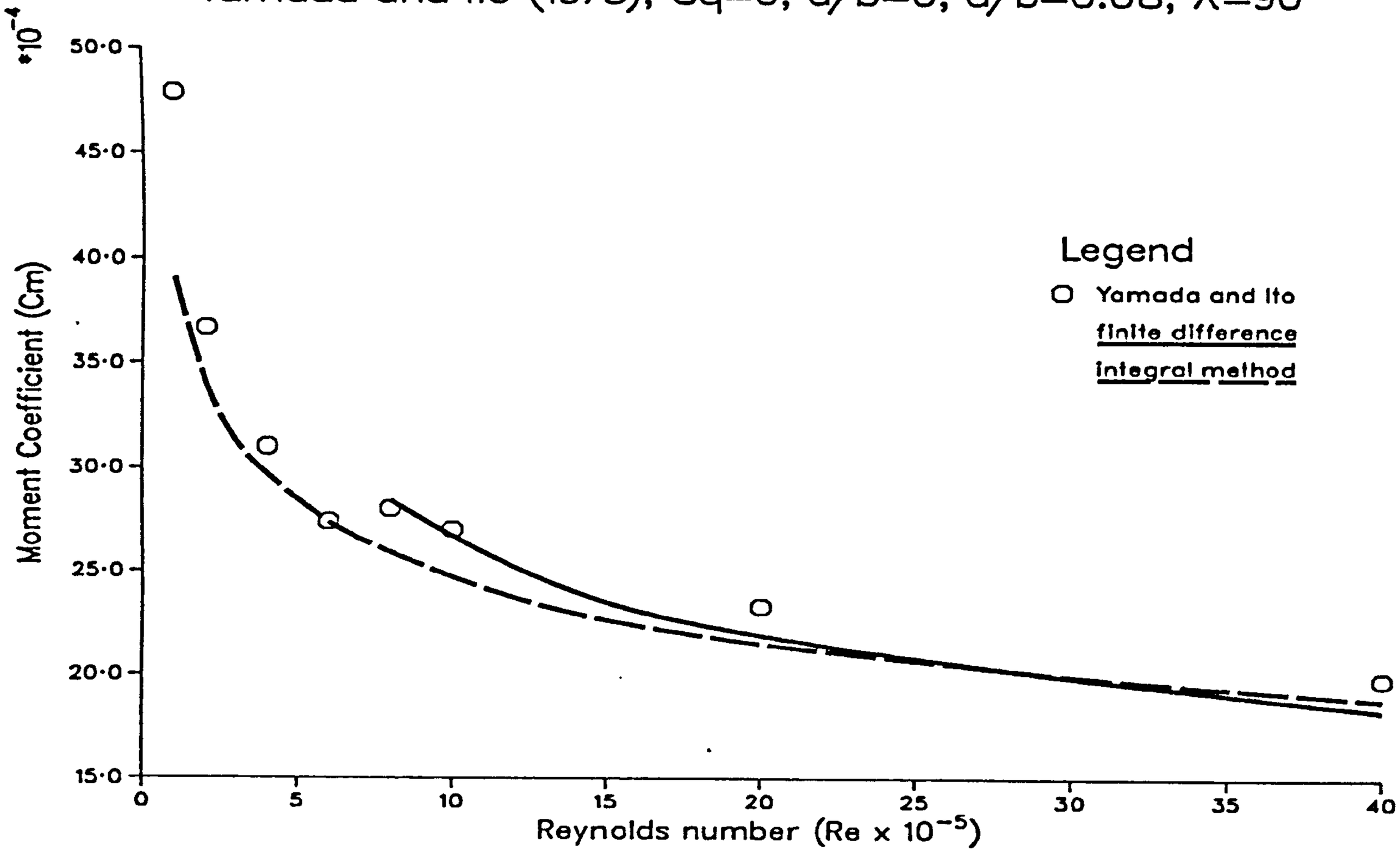

Figure 4.11(a)

A comparison of the predicted moment coefficient with Yamada and Ito (1975); Cq=0, a/b=0, d/b=0.08, λ=60°

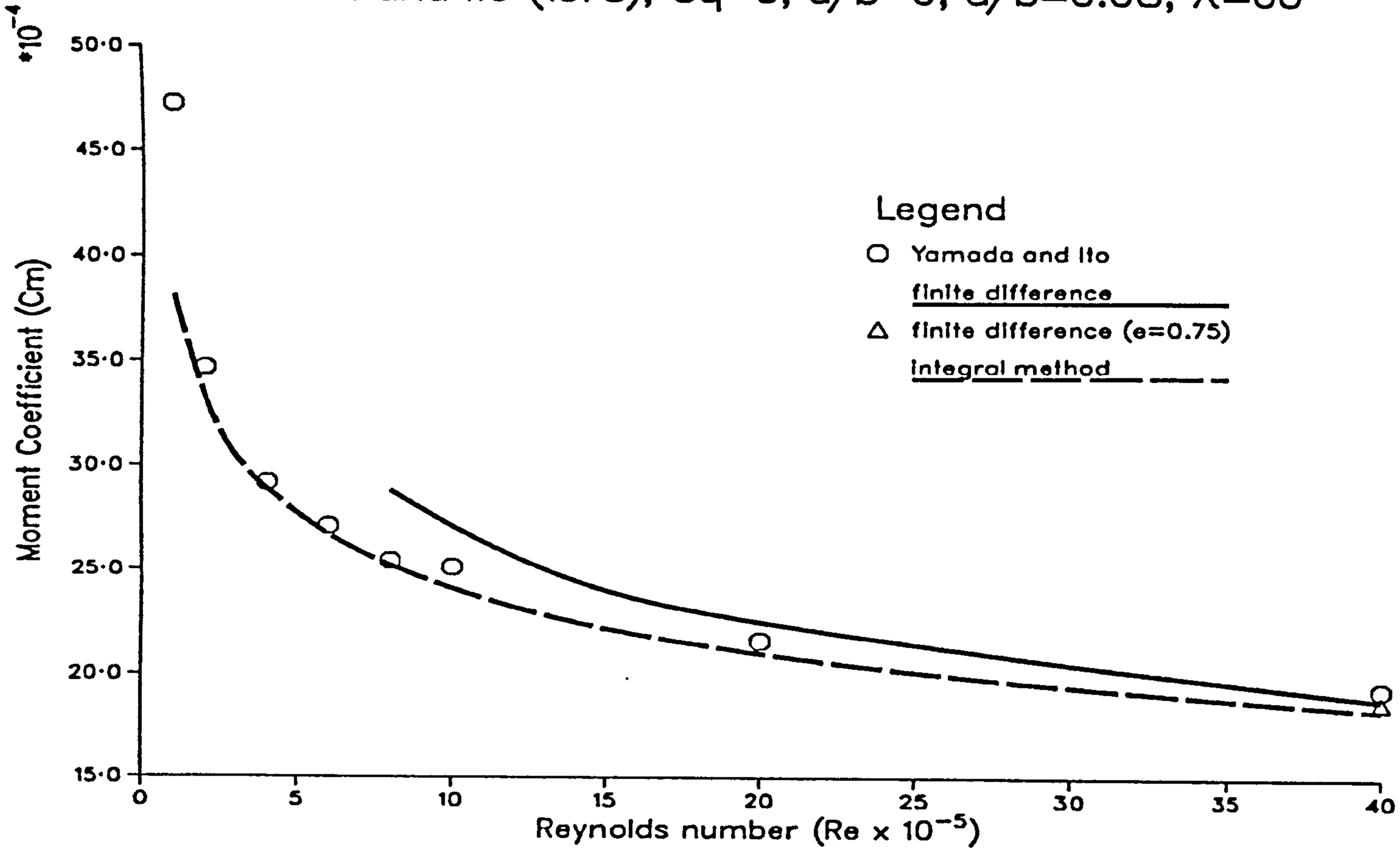

Figure 4.11(b)

A comparison of the predicted moment coefficient with Yamada and Ito (1975); Cq=0, a/b=0, d/b=0.08, λ=30°

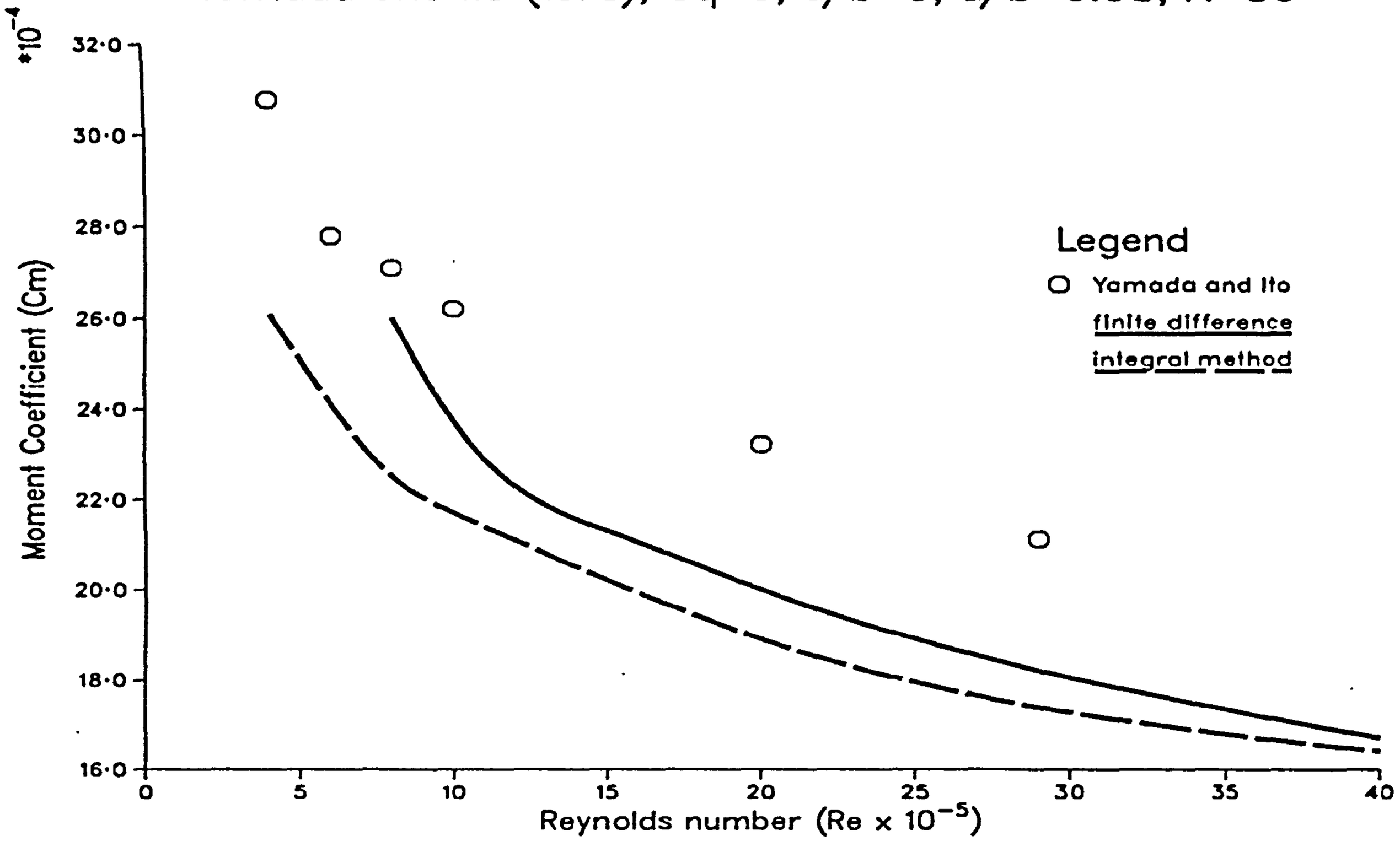

Figure 4.11(c)

A comparison of the predicted moment coefficient with Yamada and Ito (1975); a/b=0, d/b=0.16, Re=10^6, $\lambda=45^\circ$

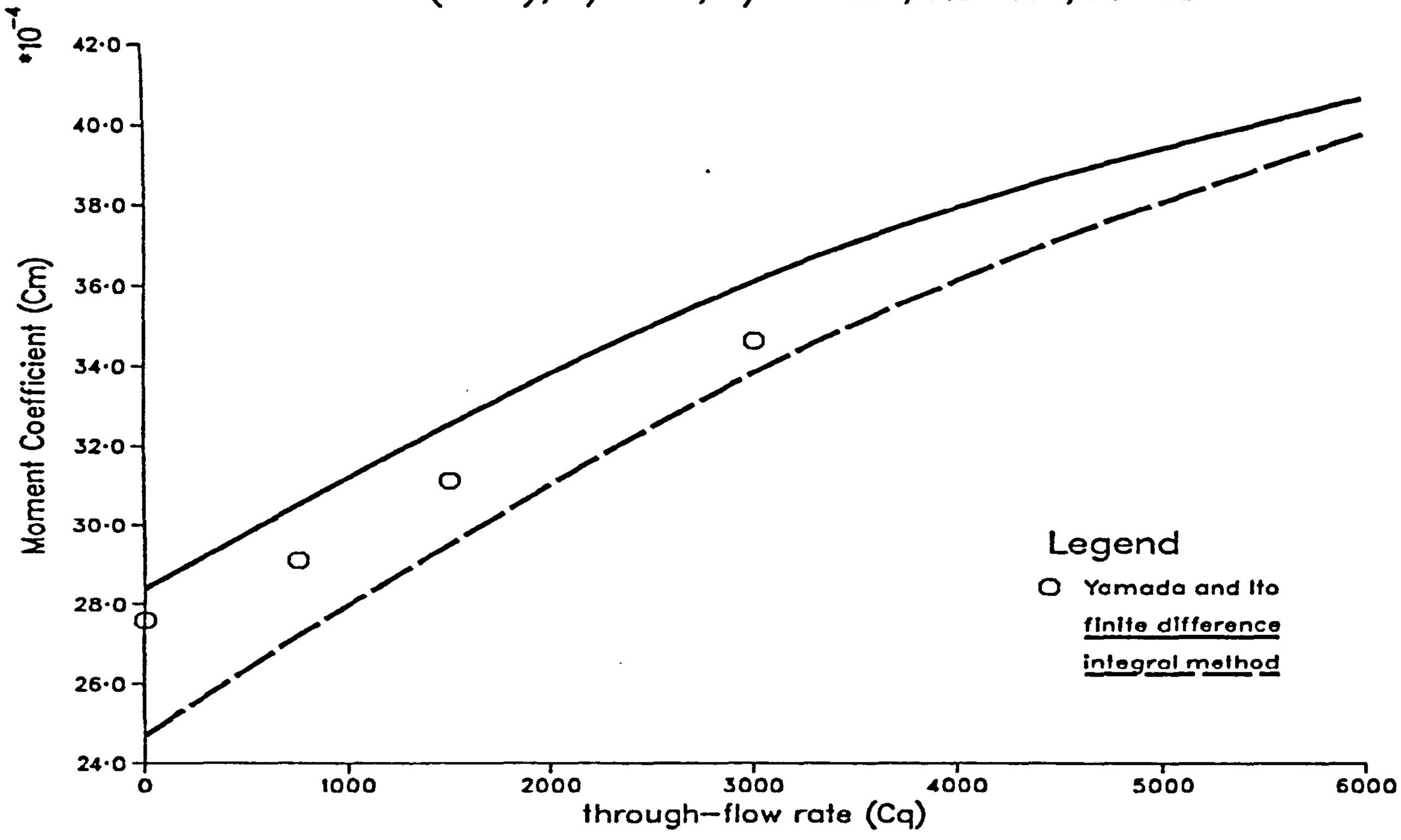

Figure 4.12(a)

A comparison of the predicted moment coefficient with Yamada and Ito (1975); a/b=0, d/b=0.16, Re=10^6, $\lambda=15^o$

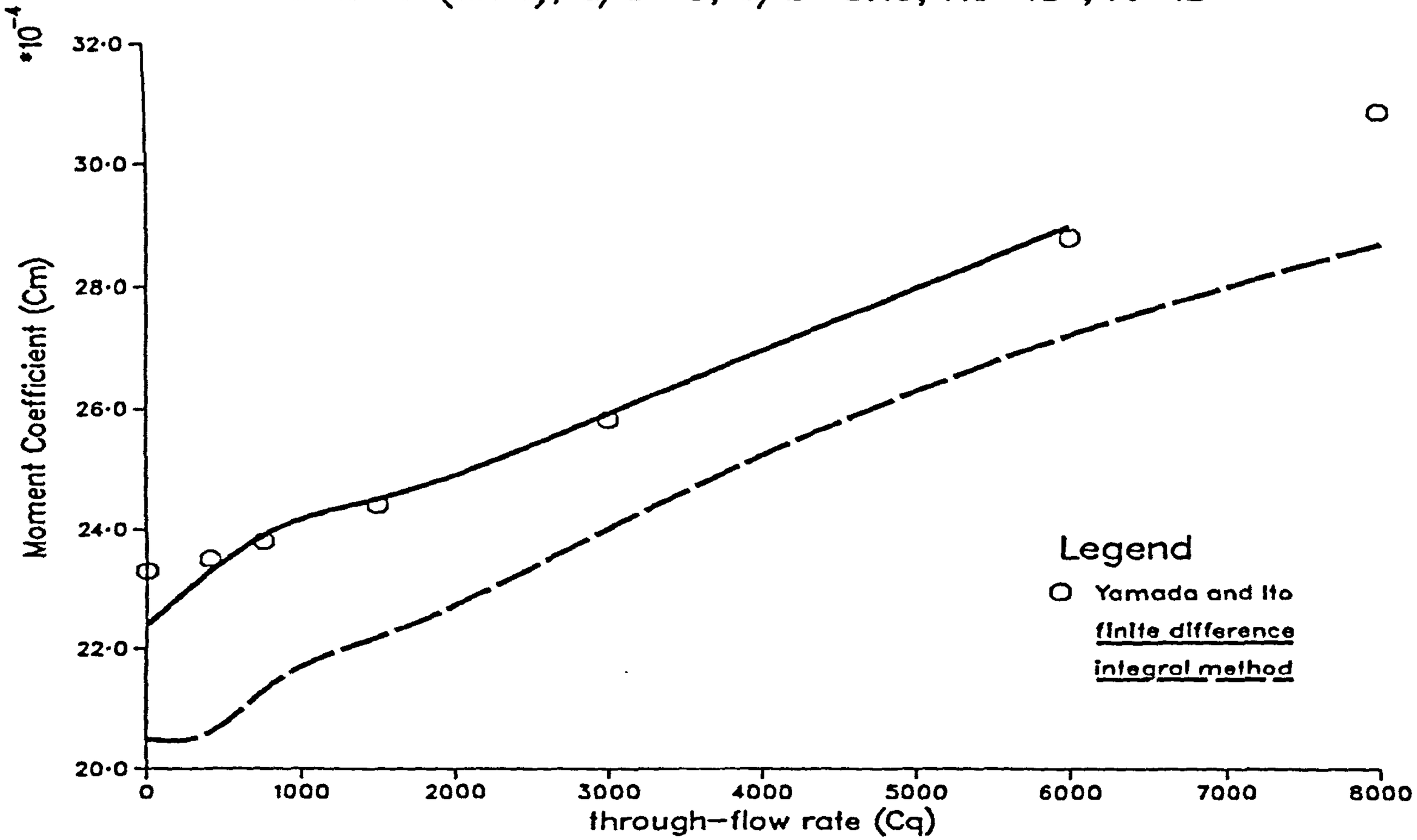

Figure 4.12(b)

A comparison of the predicted moment coefficient with Yamada and Ito (1975); a/b=0, d/b=0.08, Re=10^6, $\lambda=15^\circ$

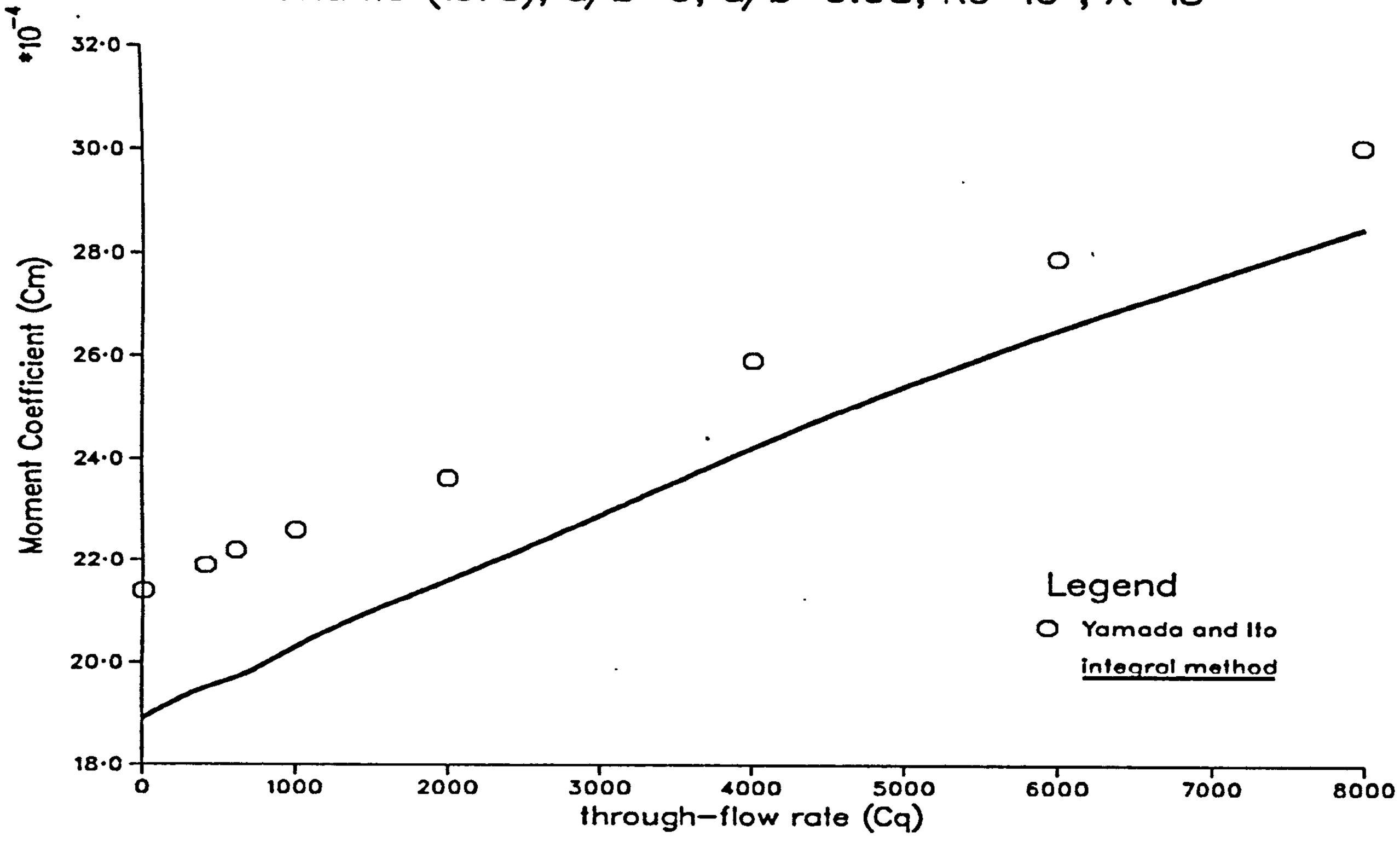

Figure 4.12(c)

A comparison of the predicted moment coefficient with Yamada and Ito (1975); a/b=0, d/b=0.04, Re=10^6, $\lambda=30^\circ$

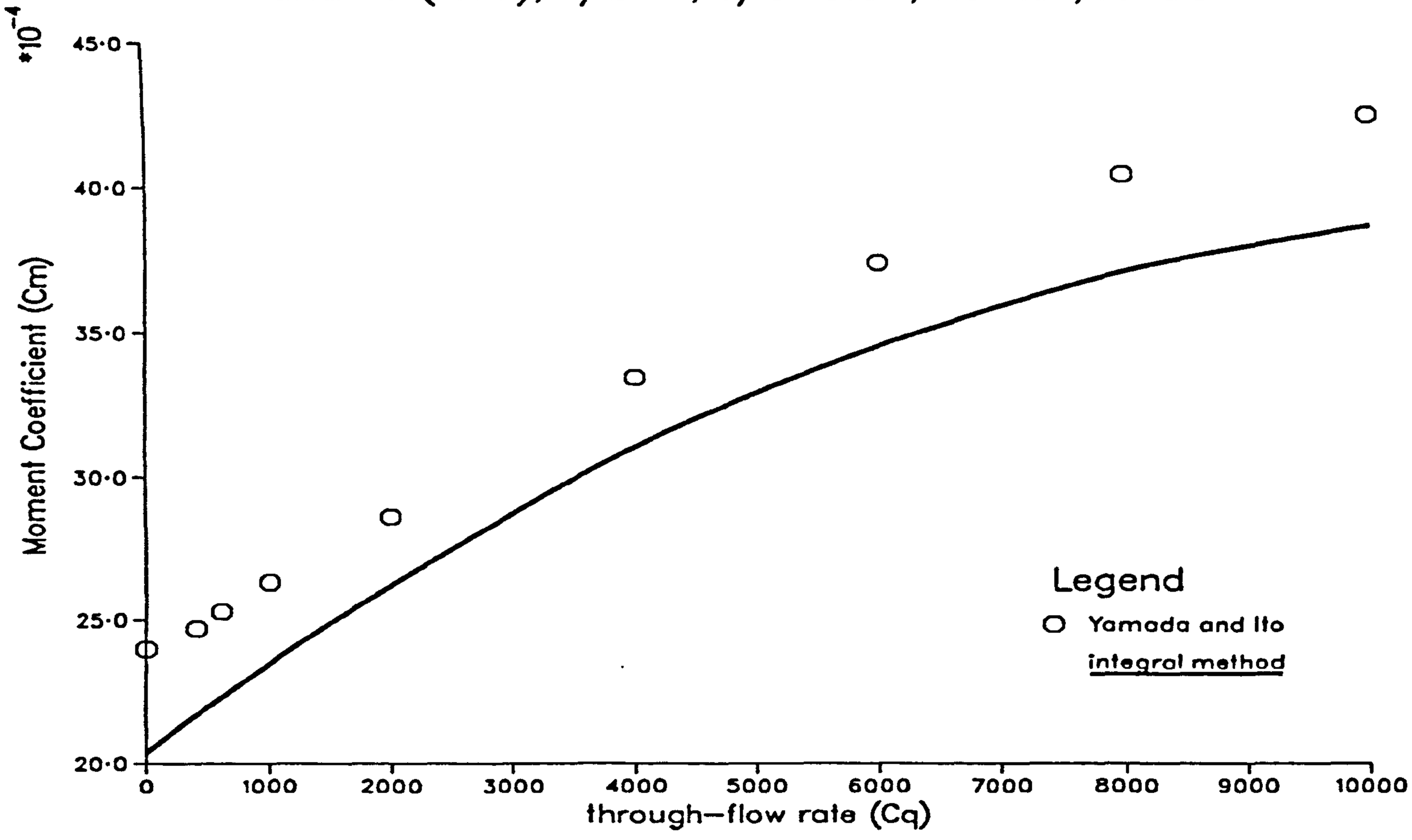

Figure 4.12(d)

A comparison of the predicted moment coefficient with Yamada and Ito (1975); a/b=0, d/b=0.04, Re=10^6, $\lambda=45°$

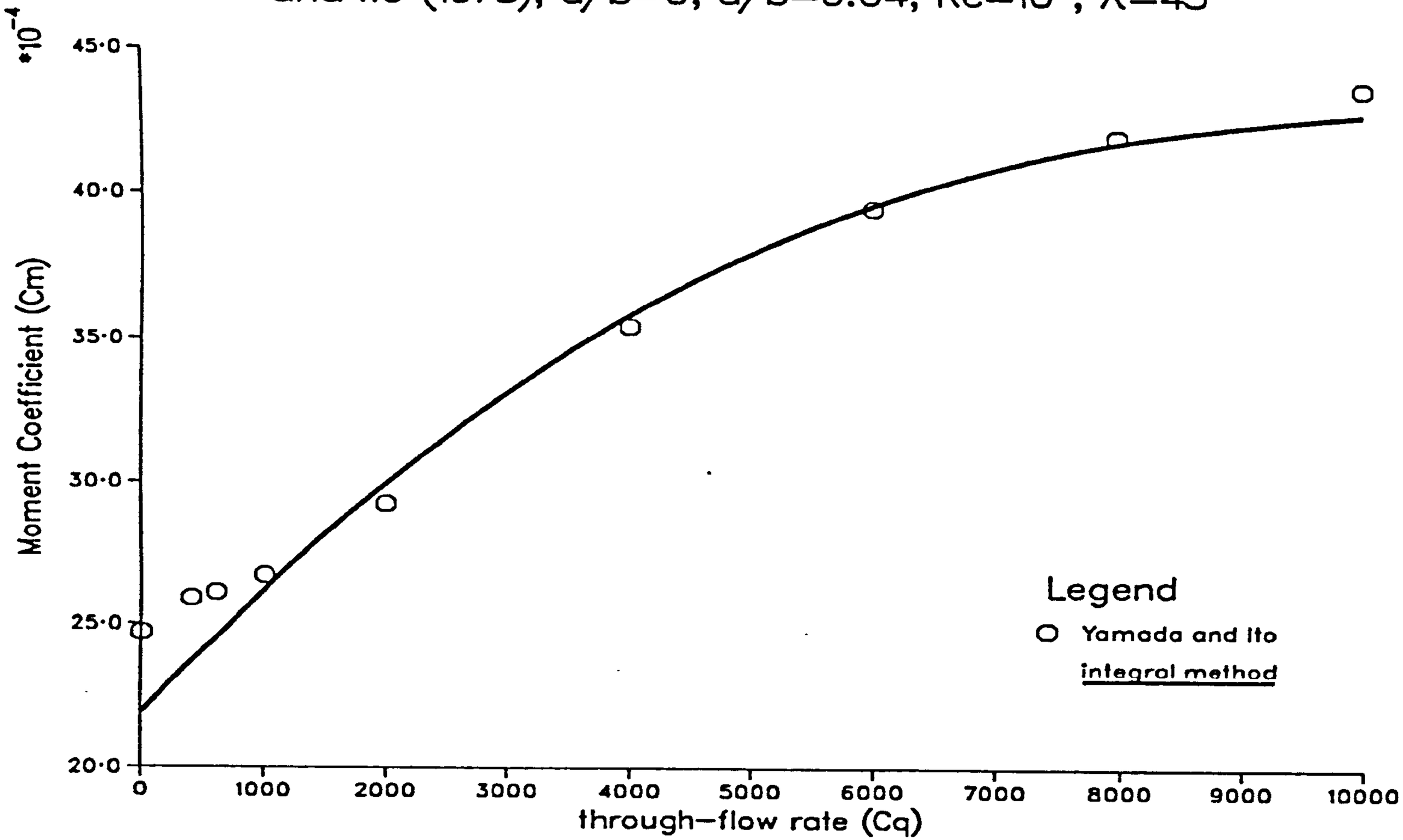

Figure 4.12(e)

Comparison of the average Nusselt number
for a free-rotating cone with the
data of Kreith(1966); a/b=0.001

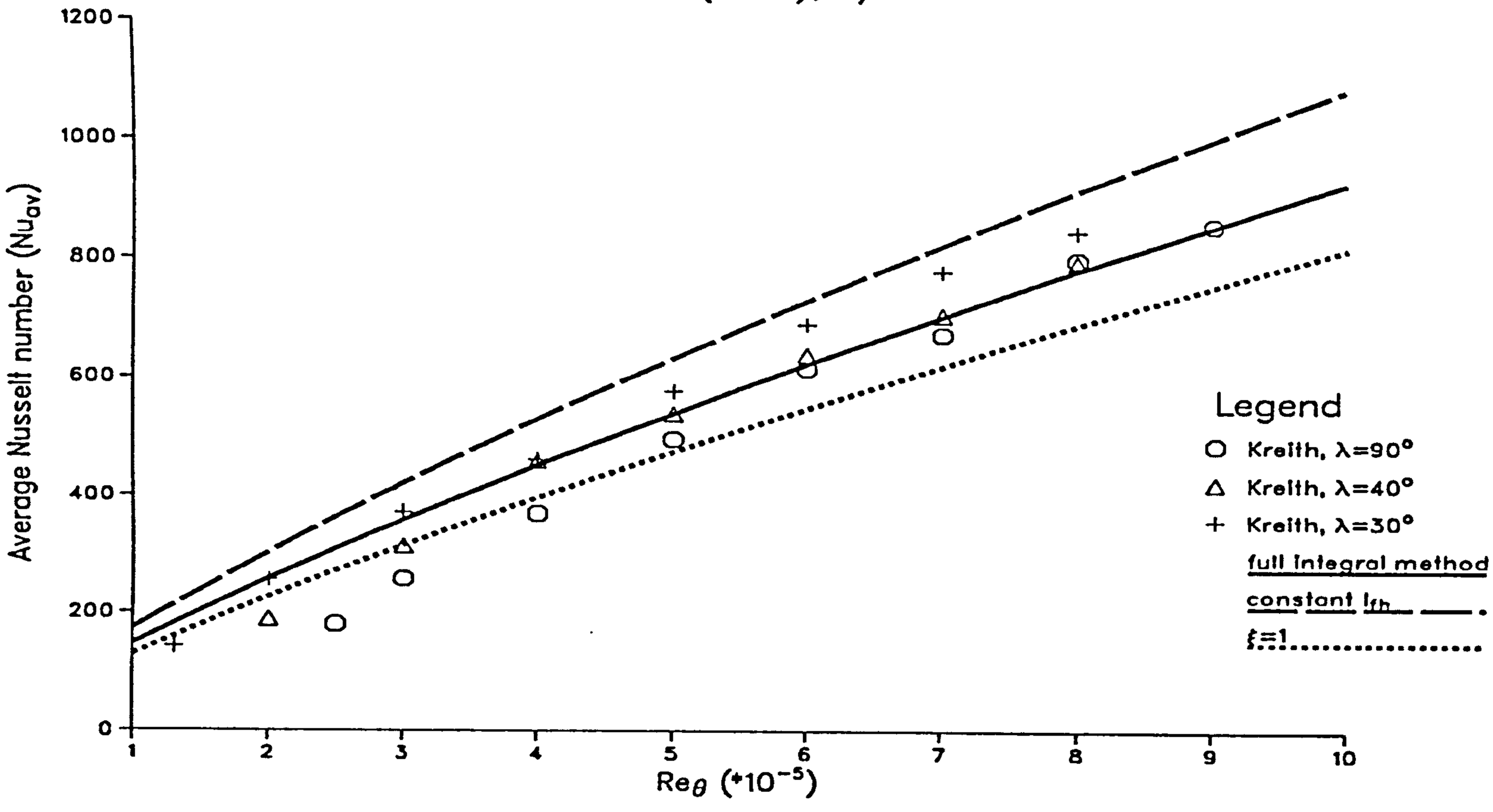

Figure 5.1(a)

Comparison of the average Nusselt number
for a free–rotating cone with the data
of Kreith(1966); a/b=0.001, λ=15°

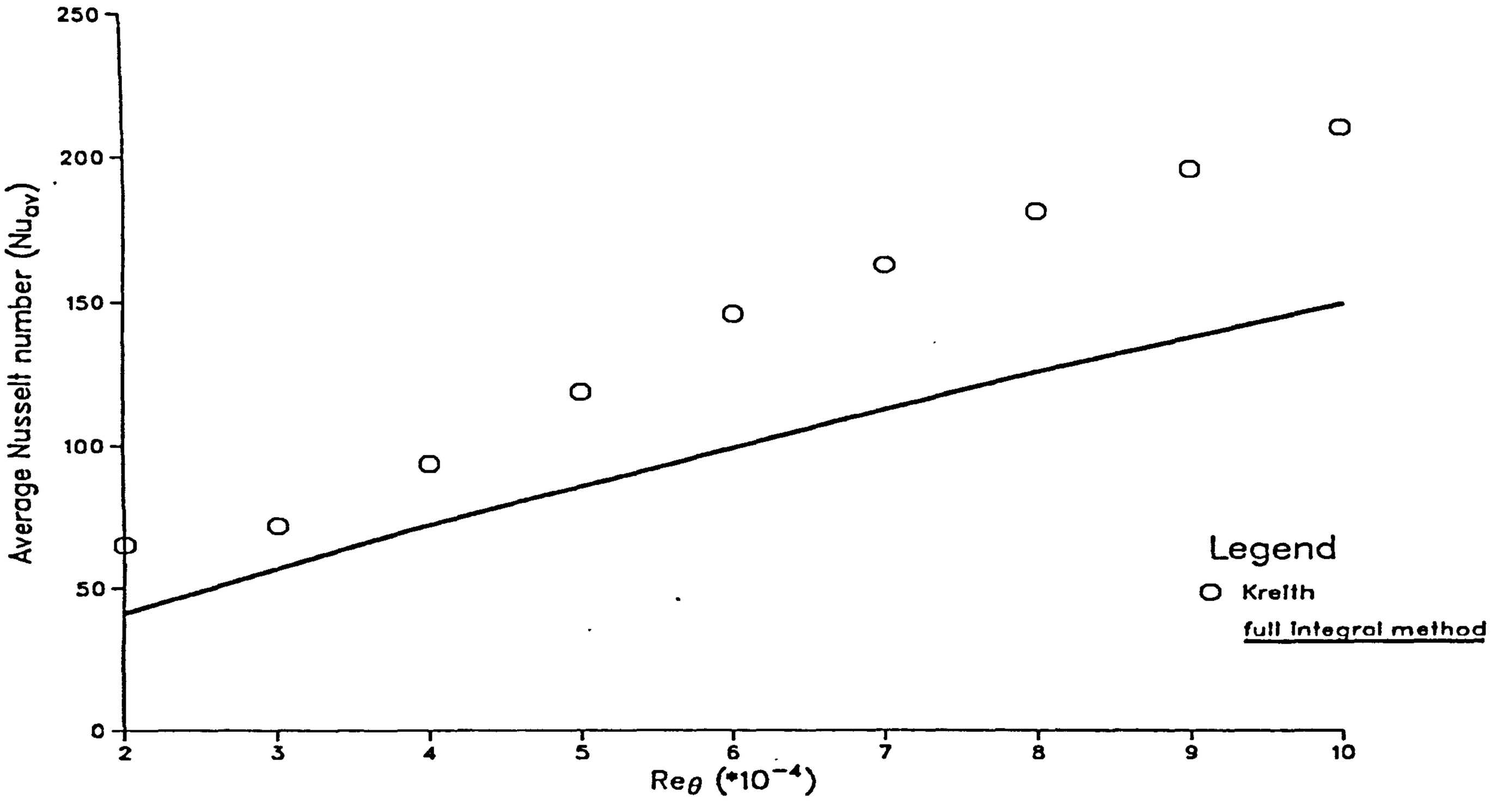

Figure 5.1(b)

Finite difference predictions for h_c;
$Re_\theta = 1.7 * 10^6$, $\lambda = 90°$,
$a/b = 0.2$, $d/b = 0.12$ and $Cq = 3000$

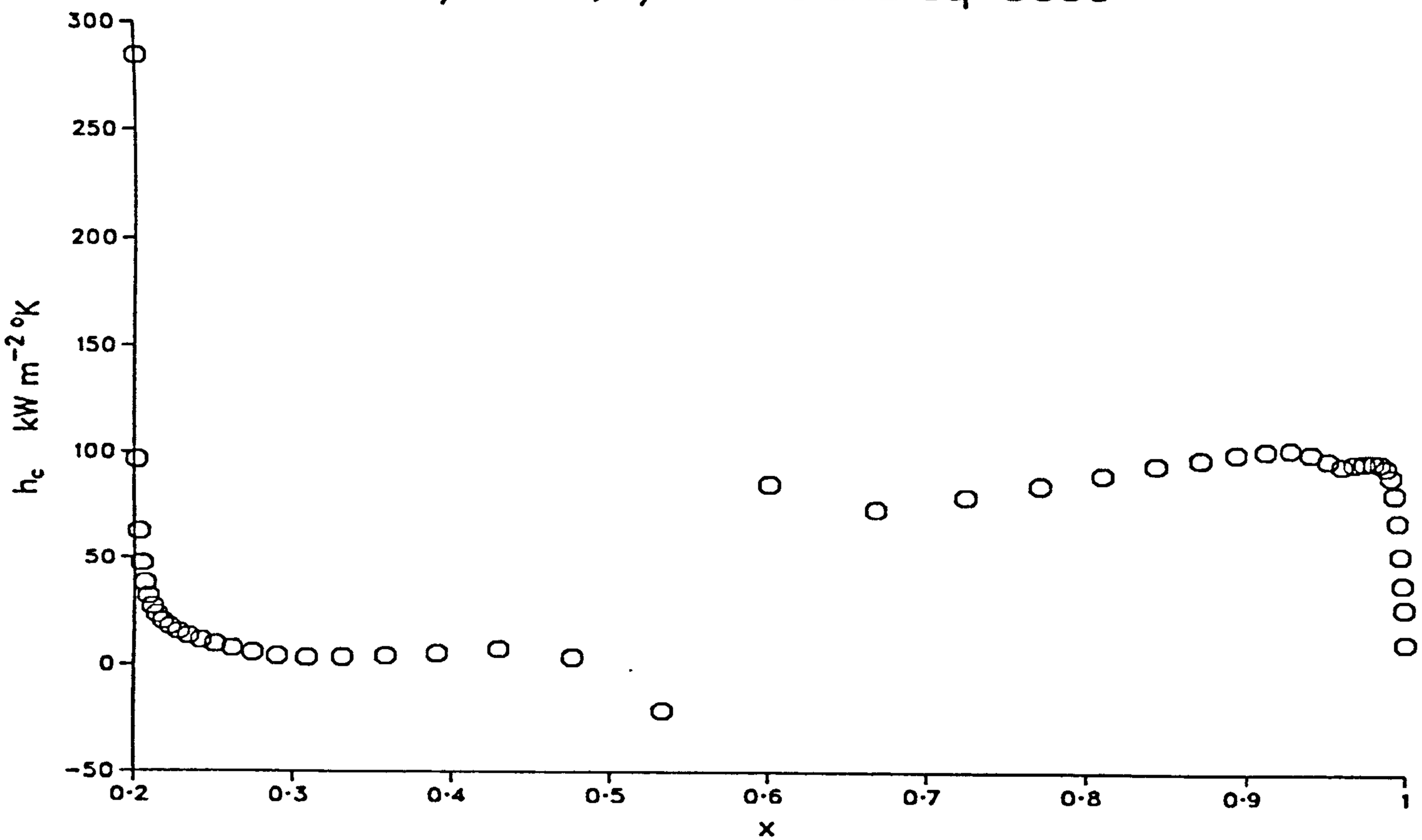

Figure 5.2

A comparison of the Predicted mid-axial temperature;
$Re_\theta = 1.7*10^6$, $\lambda = 90^\circ$,
a/b=0.001 ,d/b=0.12 and Cq=0

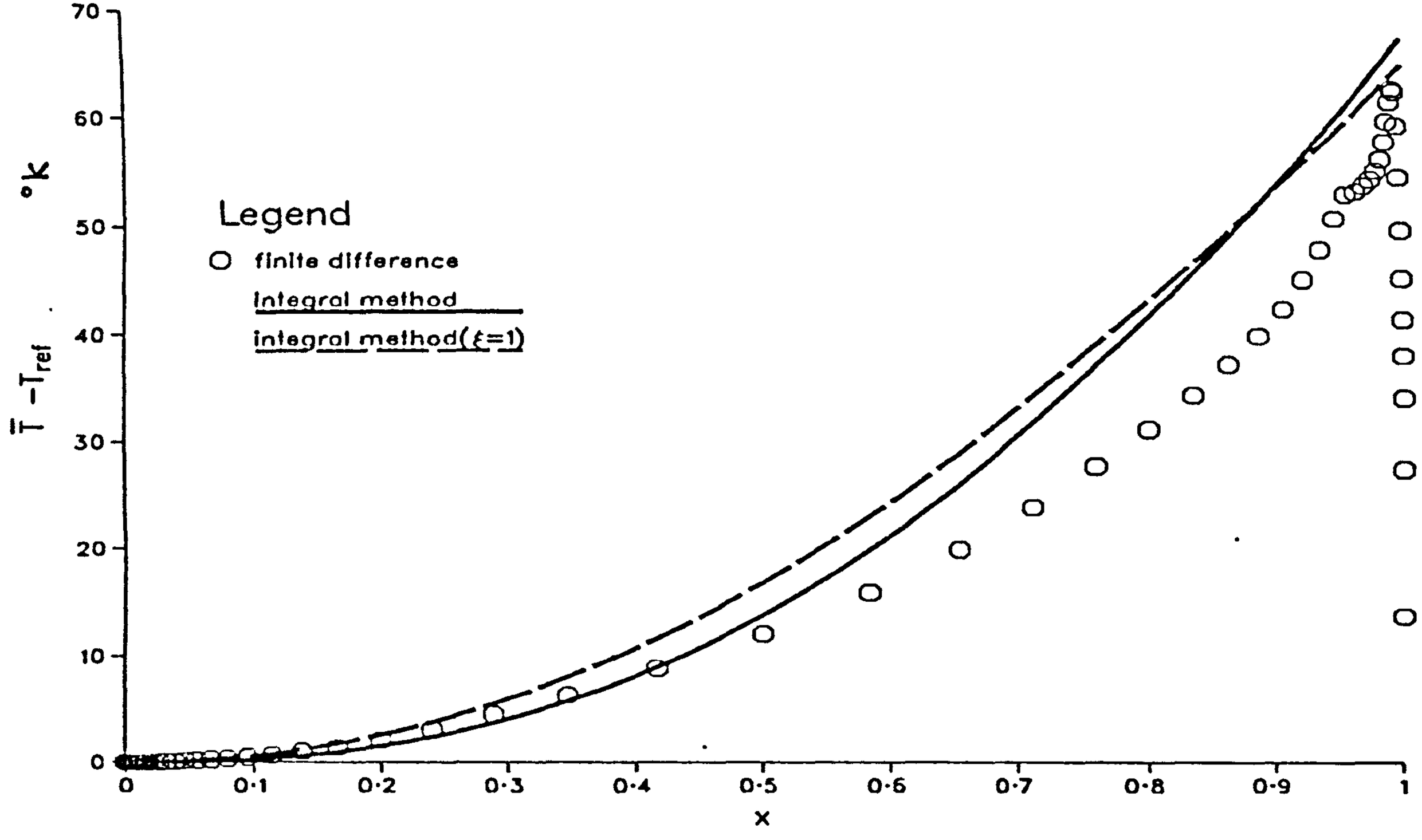

Figure 5.3(a)

A comparison of the Predicted local Nusselt numbers;
$Re_\theta = 1.7*10^6$, $\lambda = 90^\circ$,
a/b=0.001 ,d/b=0.12 and Cq=0

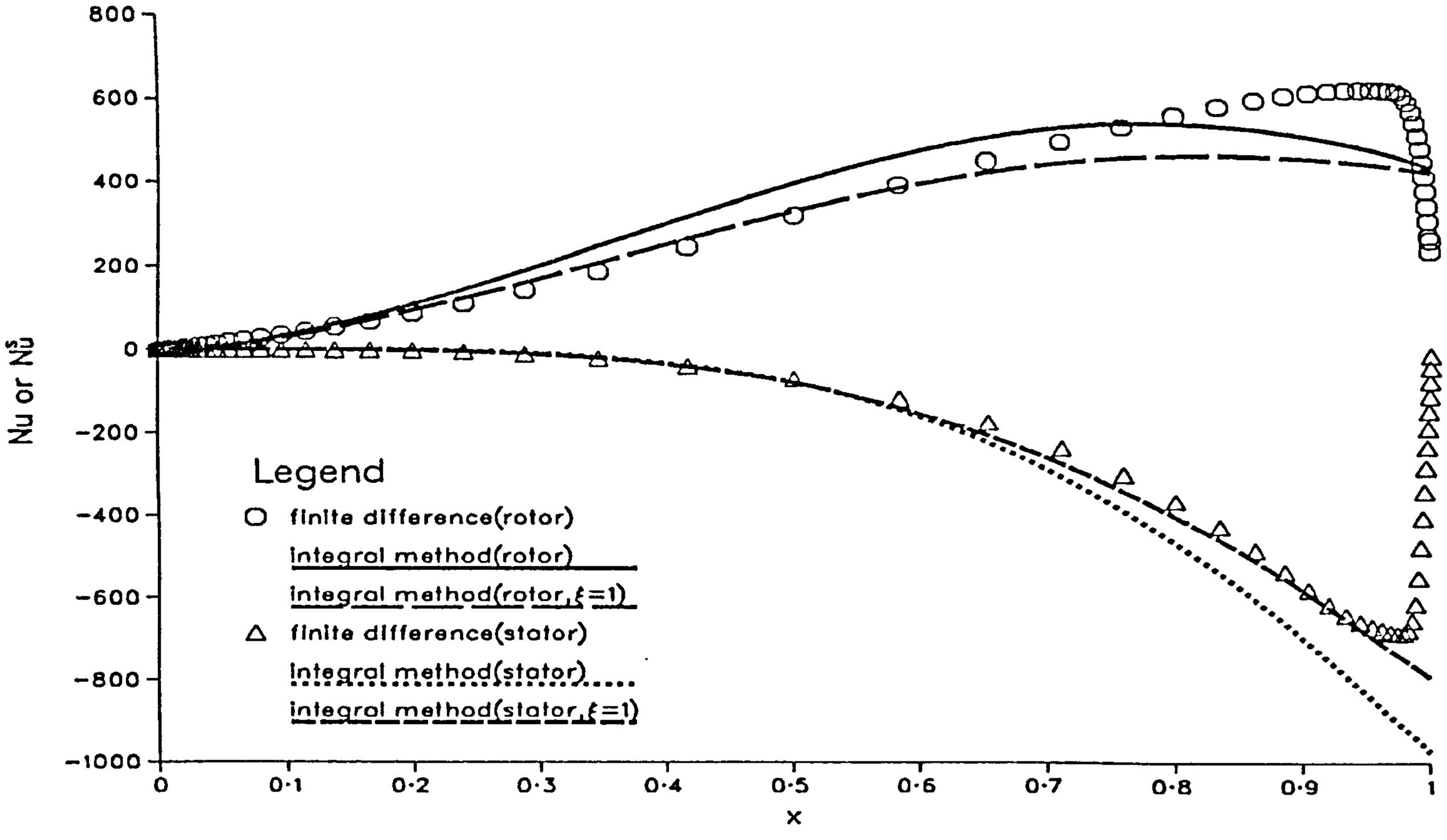

Figure 5.3(b)

A comparison of the Predicted mid-axial temperature;
$Re_\theta = 1.7*10^6$, $\lambda = 90°$,
a/b=0.001 ,d/b=0.12 and Cq=0

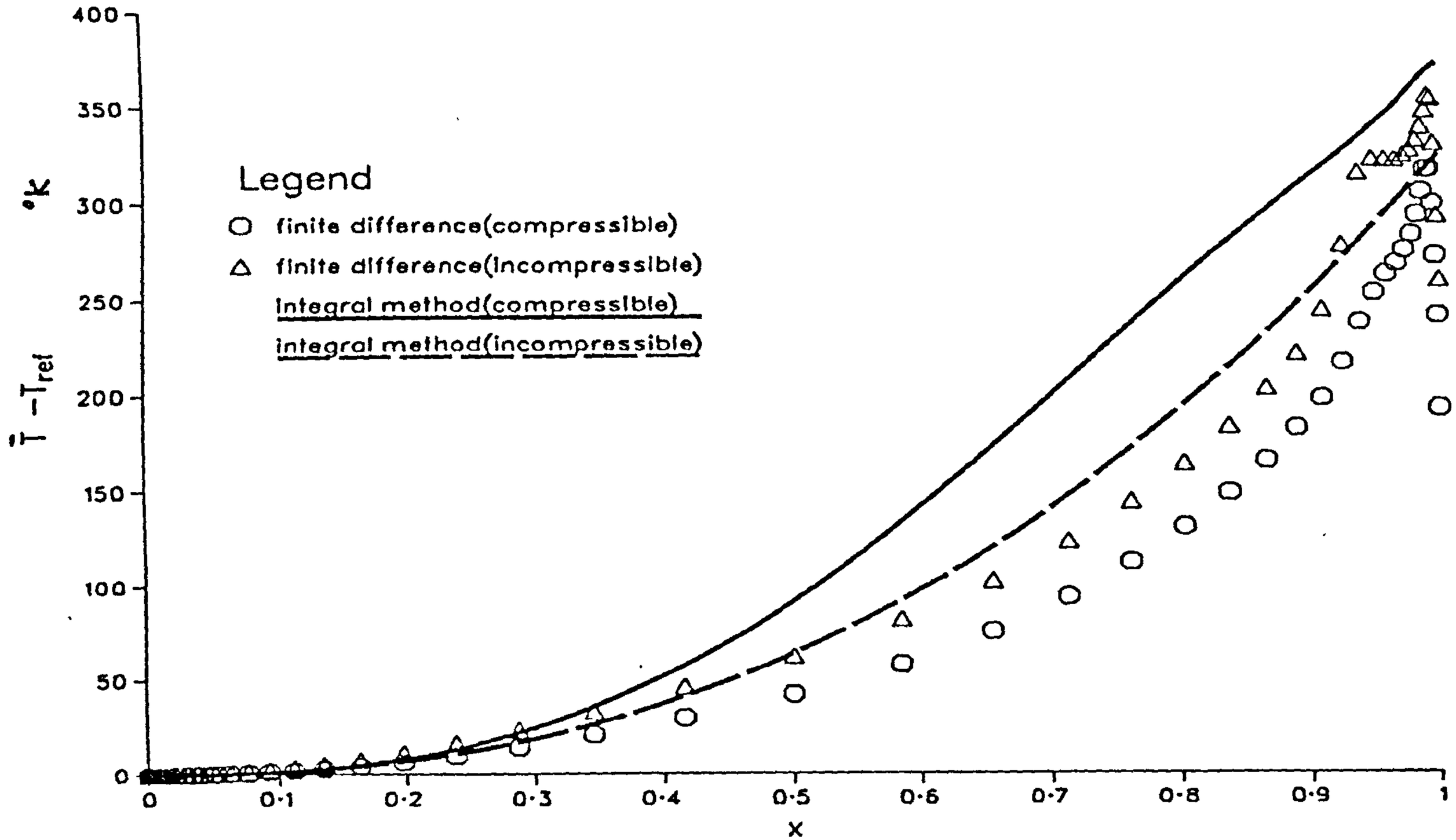

Figure 5.4(a)

A comparison of the Predicted local Nusselt number;
$Re_\theta = 1.7 * 10^6$, $\lambda = 90^\circ$,
a/b=0.001 ,d/b=0.12 and Cq=0

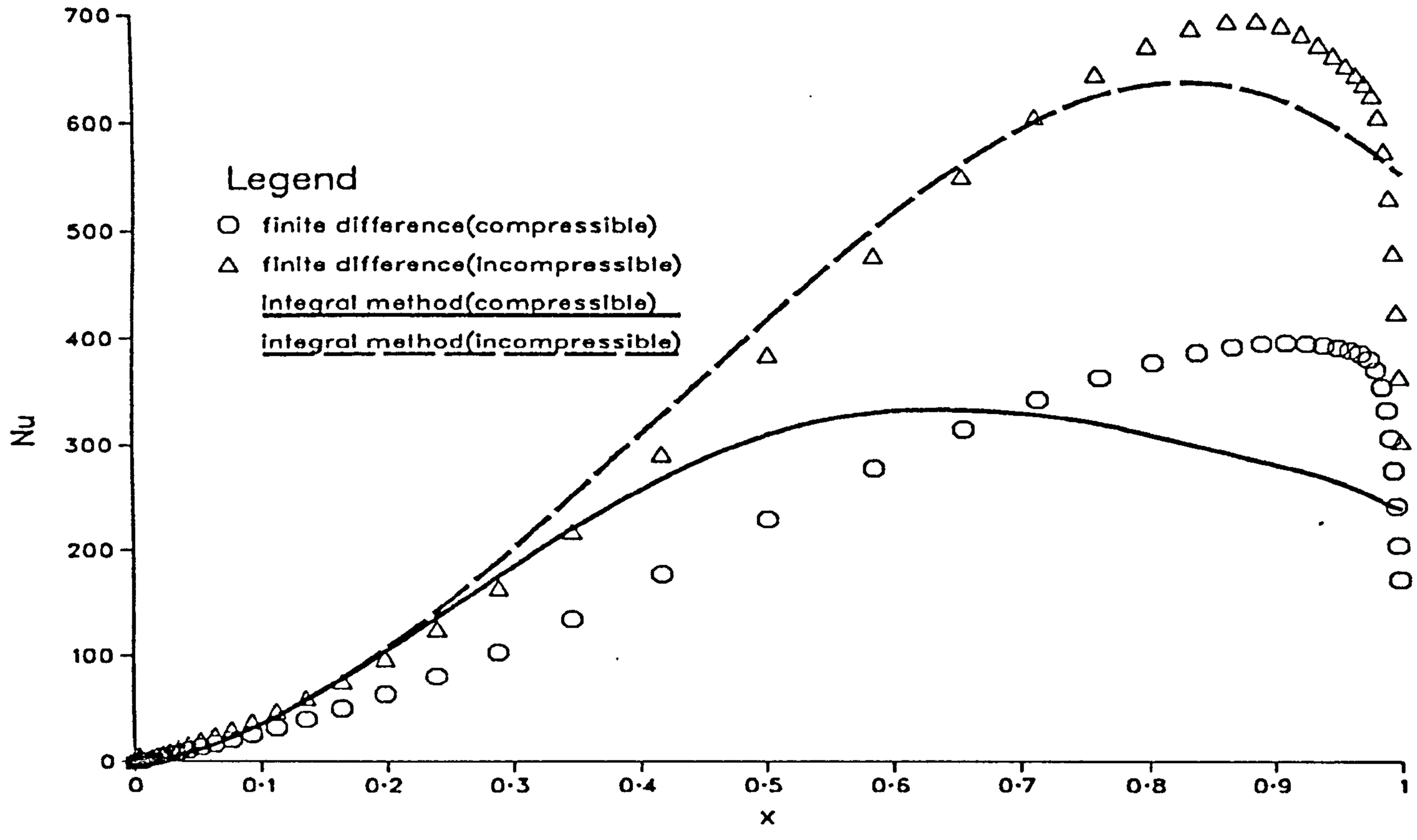

Figure 5.4(b)

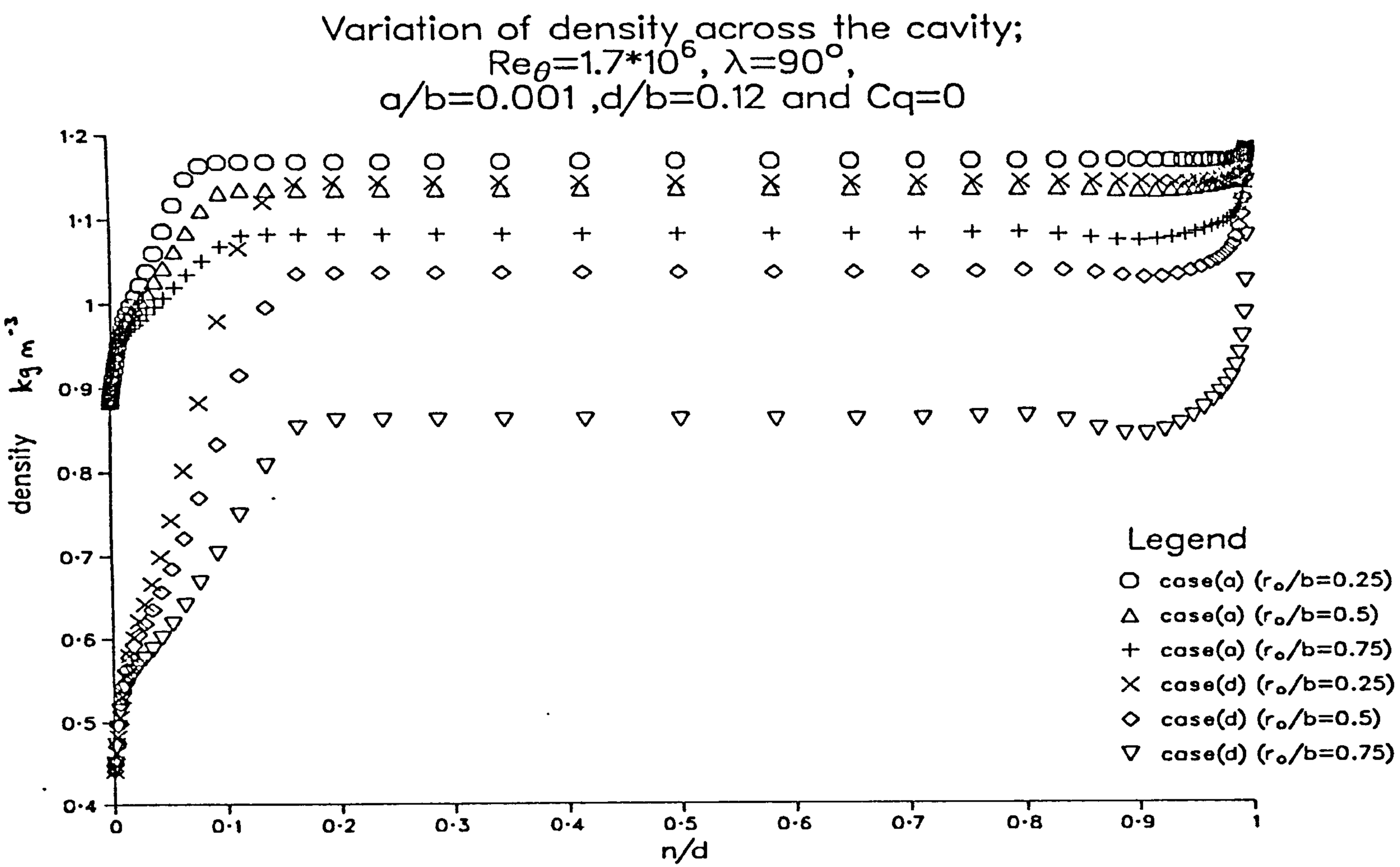
Variation of density across the cavity;
Reθ=1.7*10^6, λ=90°,
a/b=0.001 ,d/b=0.12 and Cq=0
density kg m^-3
1·2
1·1
1
0·9
0·8
0·7
0·6
0·5
0·4
0
0·1
0·2
0·3
0·4
0·5
0·6
0·7
0·8
0·9
1
n/d
Legend
case(a) (r_o/b=0.25)
case(a) (r_o/b=0.5)
case(a) (r_o/b=0.75)
case(d) (r_o/b=0.25)
case(d) (r_o/b=0.5)
case(d) (r_o/b=0.75)

Figure 5.5

A comparison of the tangential velocity profile with the enthalpy profile; a/b=0.001, d/b=0.12, Cq=0, $Re_\theta=1.7*10^6$ and $\lambda=90°$

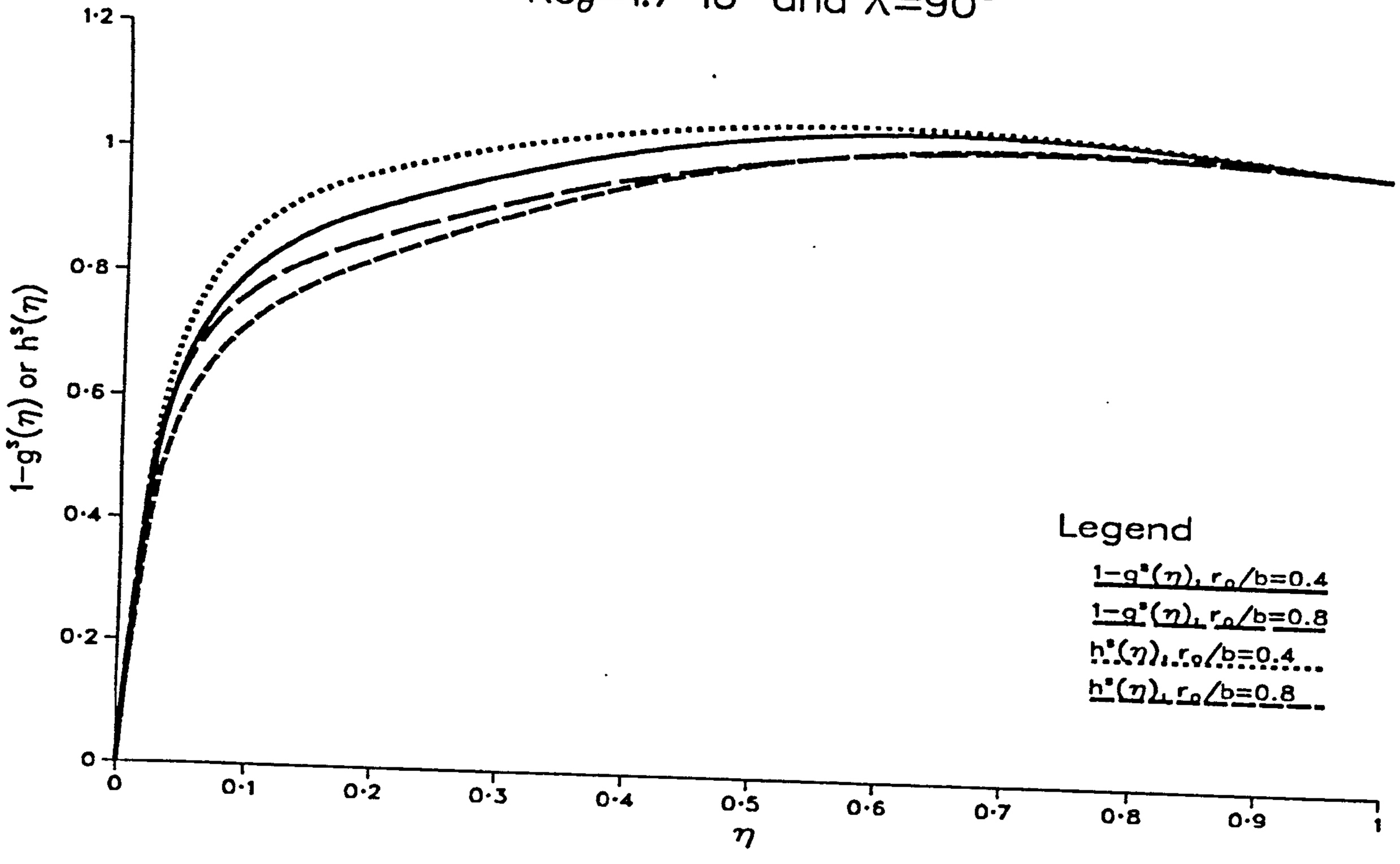

Figure 5.6(a)

A comparison of the tangential velocity profile with the enthalpy profile; a/b=0.001, d/b=0.12, Cq=0, $Re_\theta=1.7*10^6$ and $\lambda=90^\circ$

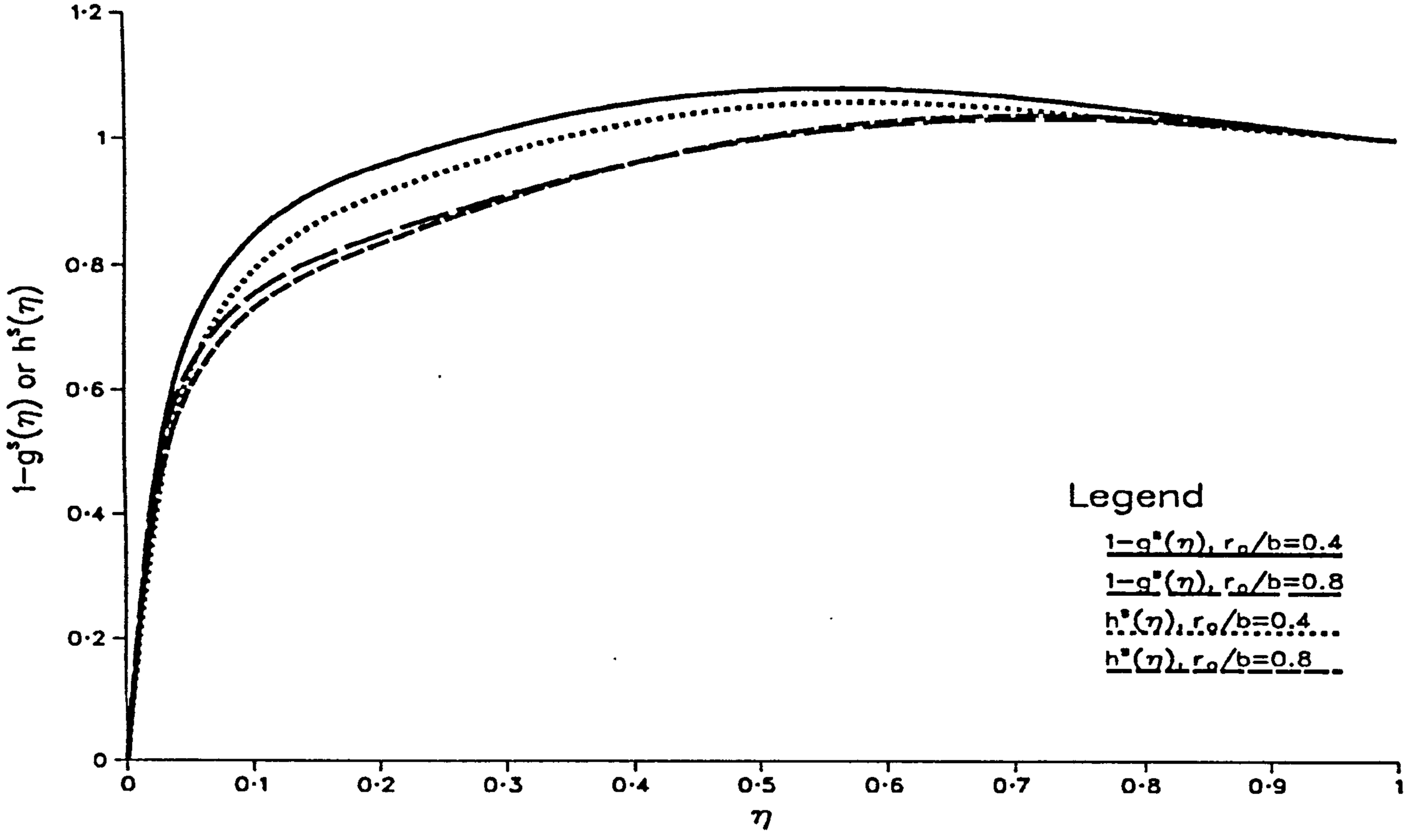

Figure 5.6(b)

A comparison of the mid-axial temperature;
$Re_\theta = 1.7*10^6$, $\lambda = 90^\circ$.
a/b=0.2, d/b=0.12 and Cq=3000

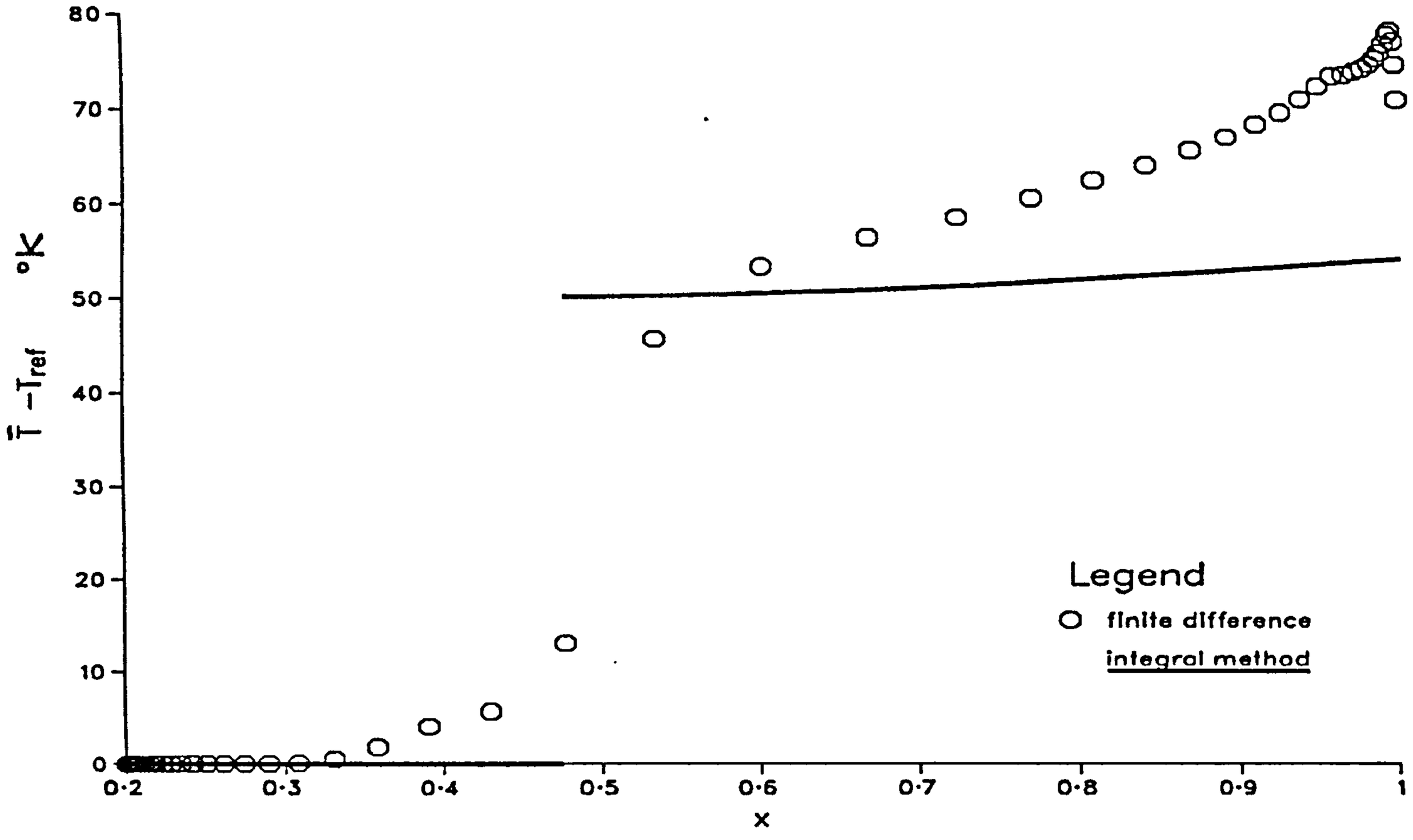

Figure 5.7

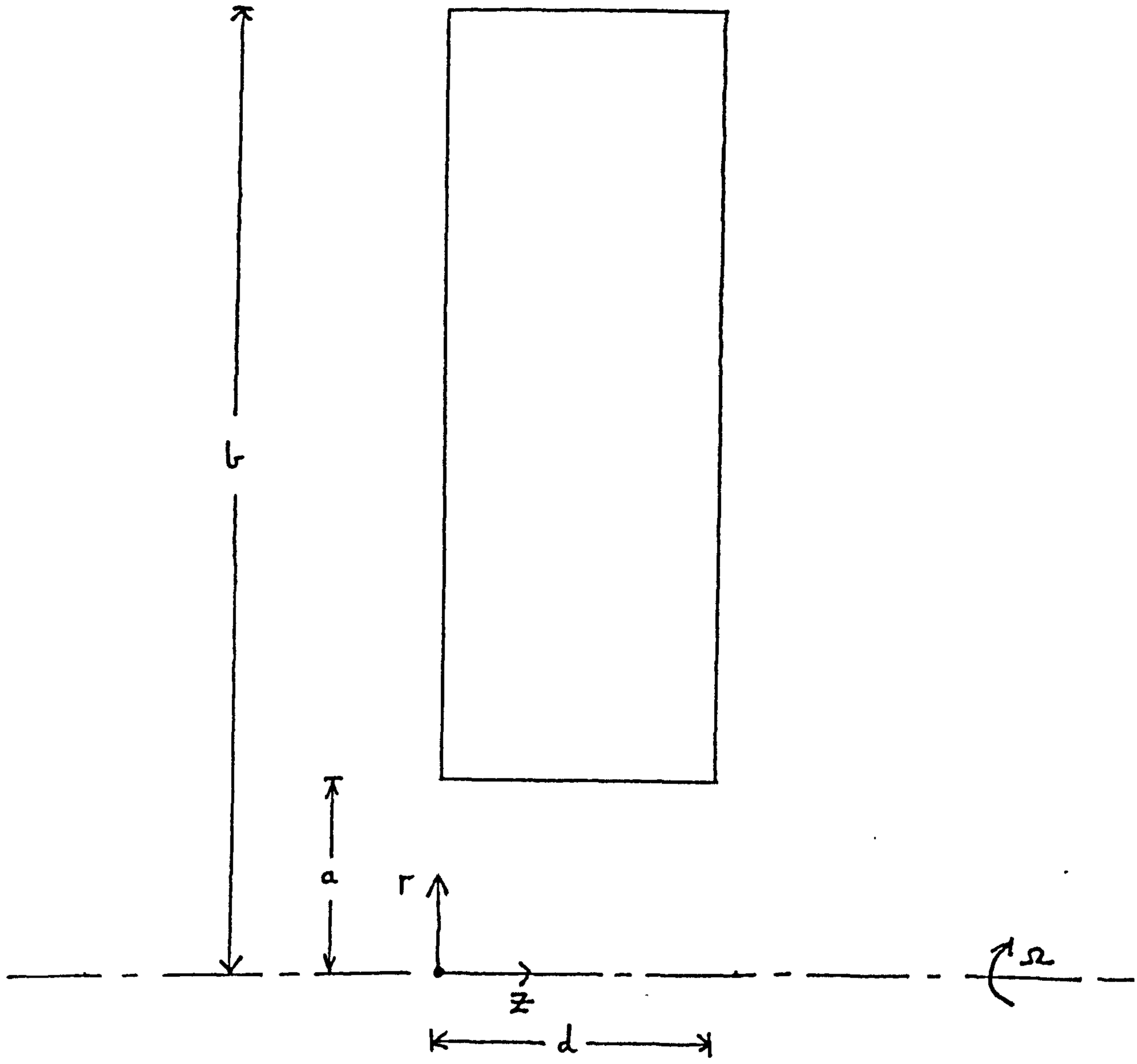

Figure 6.1(a) The Solution Domain for the Original Rotating Cavity

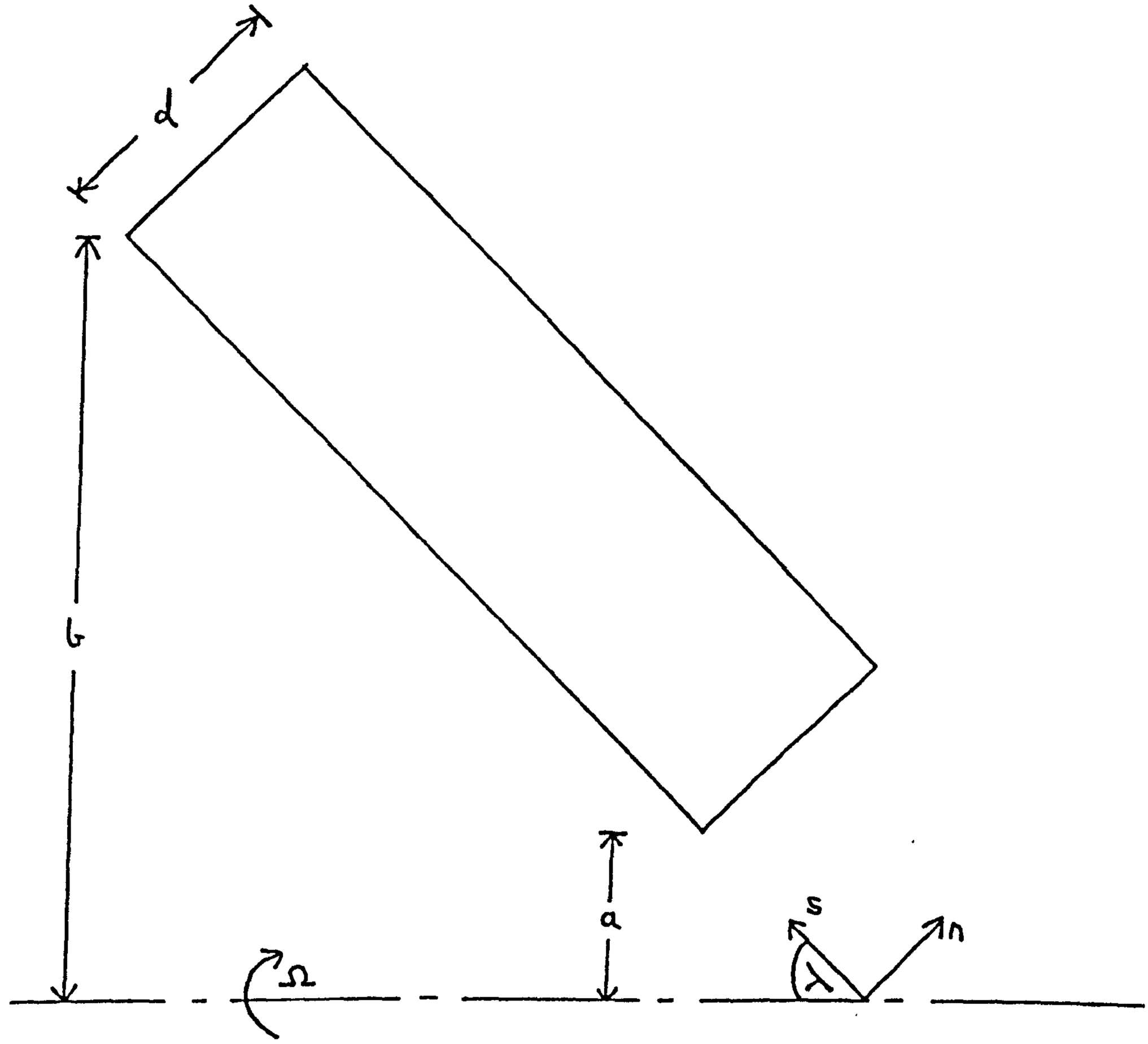

Figure 6.1(b) The Solution Domain for the Present 'Tilted' Rotating Cavity

<u>legend</u>

control volume for u

control volume for w

control volume for other variables

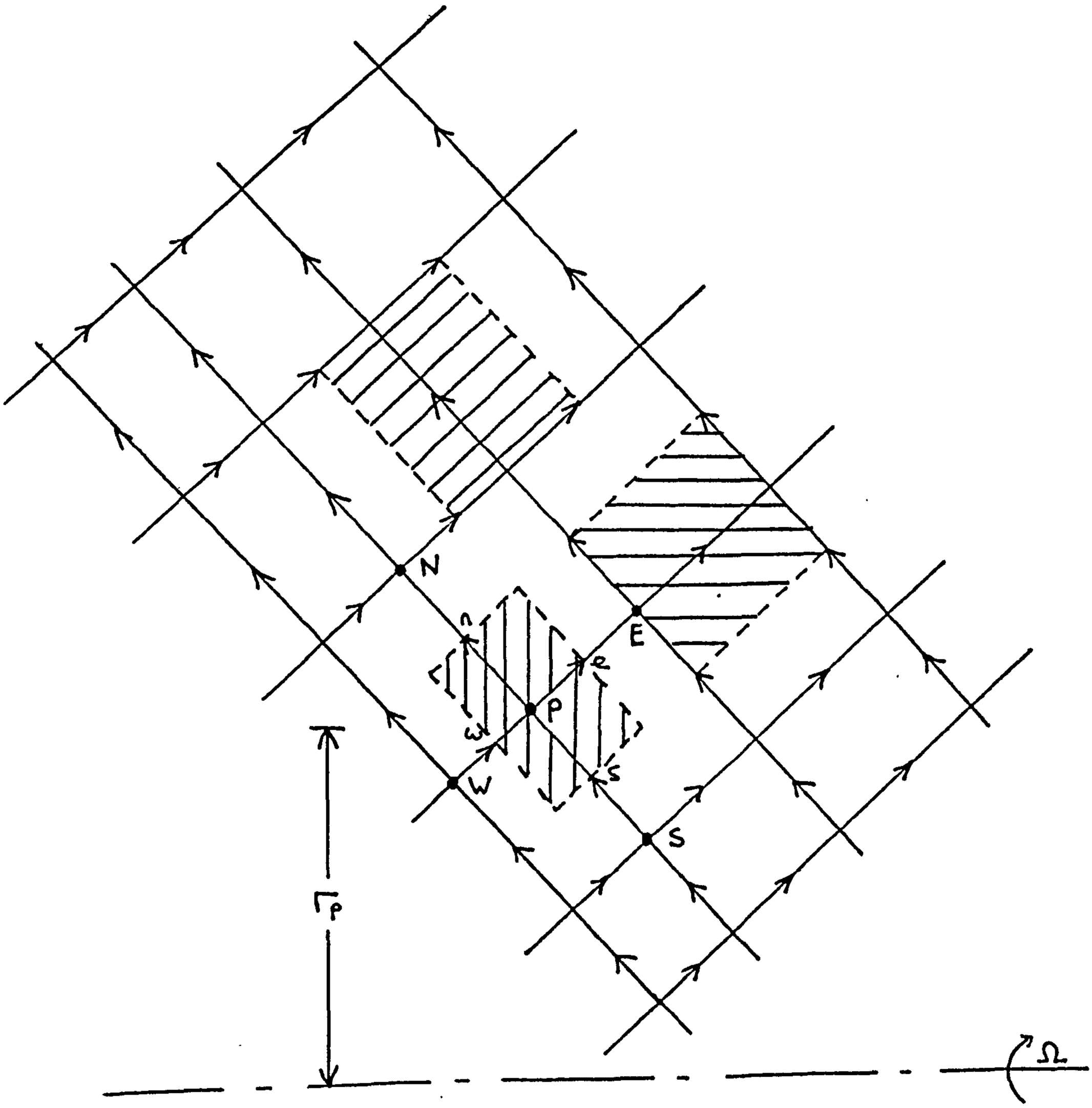

Figure 6.2 Control Volumes for the Flow Variables

Figure 6.3 Comparison of Velocity Profiles across the cavity on a 17 x 17 Grid.

Turbulent Flow:- $a/b = 0$, $d/b = 0.16$, $C_q = 0$, $Re = 10^4$

(a) u-velocity component

(b) v-velocity component

(c) w-velocity component

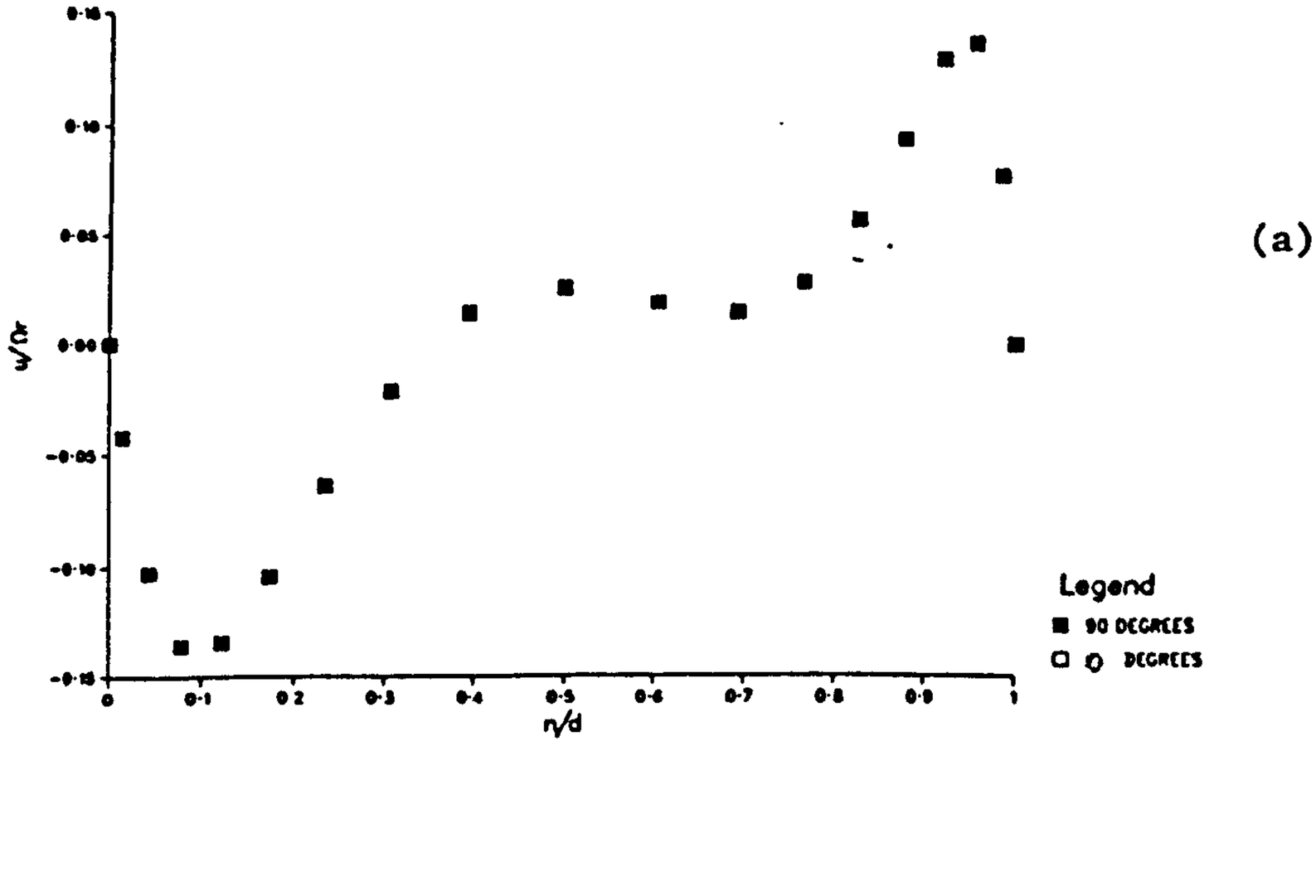
ψ/Ωr
n/d
Legend
90 DEGREES
0 DEGREES

(a)

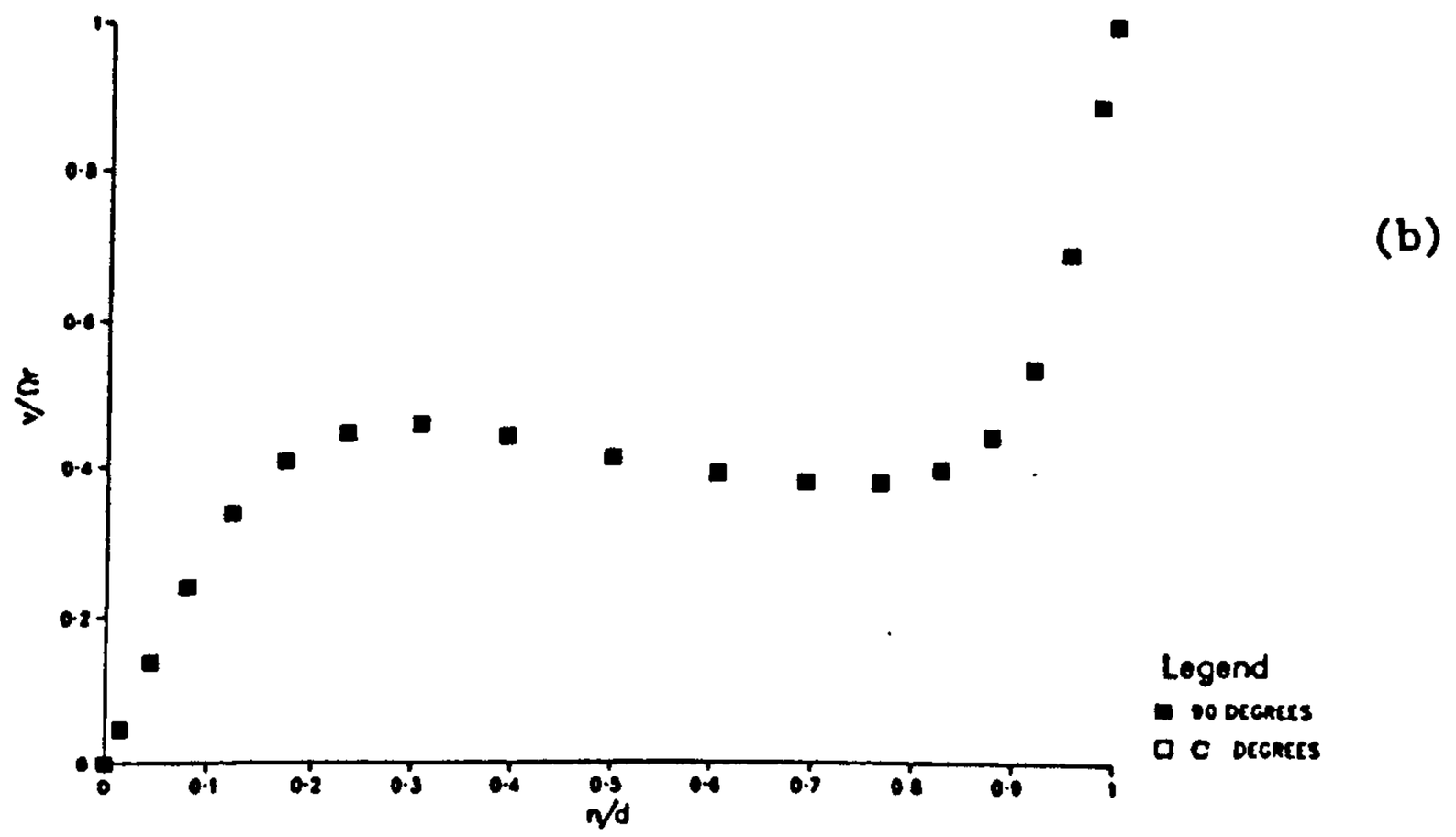
v/Ωr
n/d
Legend
90 DEGREES
0 DEGREES

(b)

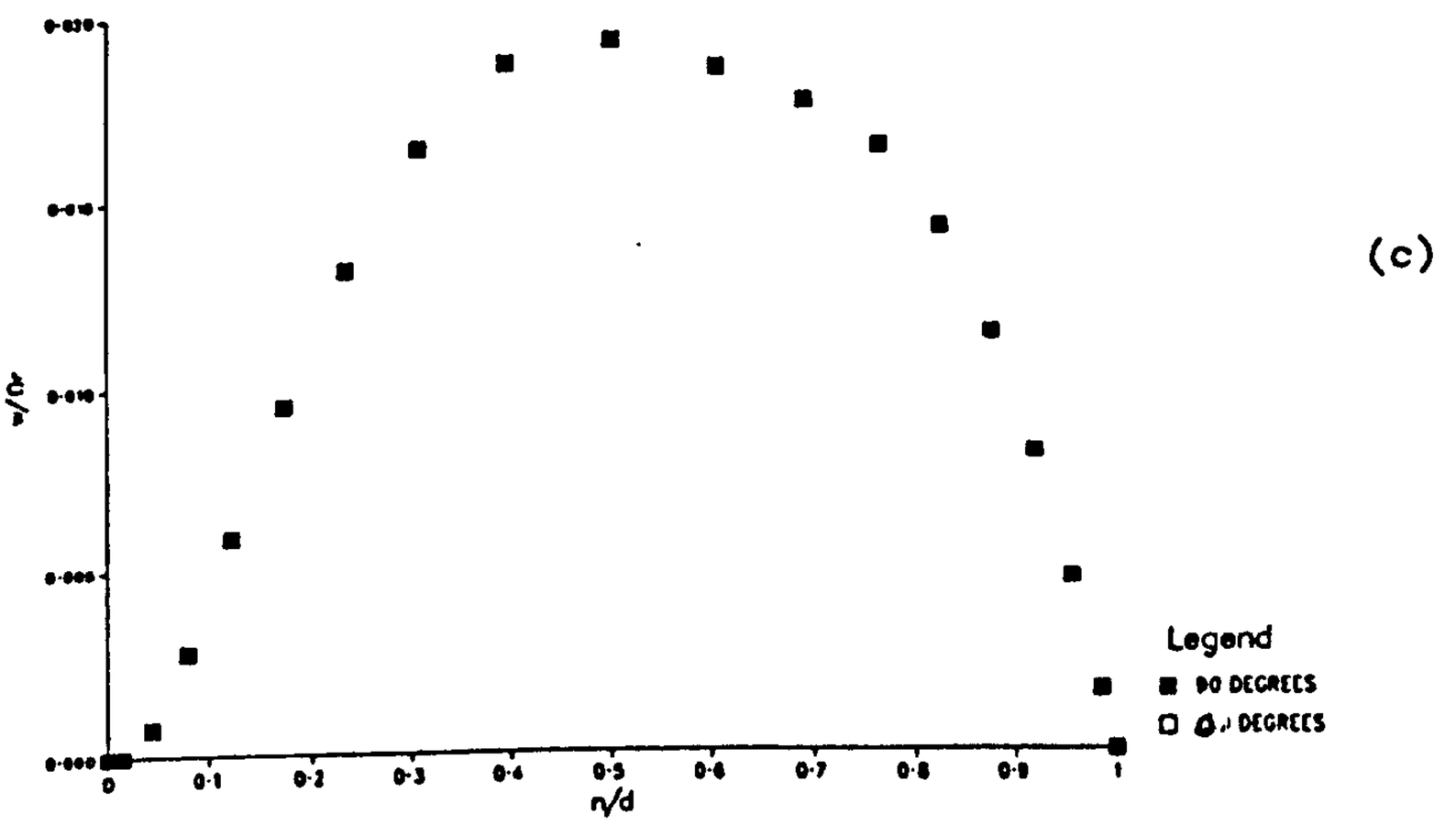
u/Ωr
n/d
Legend
90 DEGREES
0 DEGREES

(c)

Figure 6.4 Comparison of Velocity Profiles across the Cavity on a 17 x 17 Grid.

Turbulent Flow:- $a/b = 0$, $d/b = 0.16$, $Re = 10^6$, $C_q = 0$

(a) u-velocity component

(b) v-velocity component

(c) w-velocity component

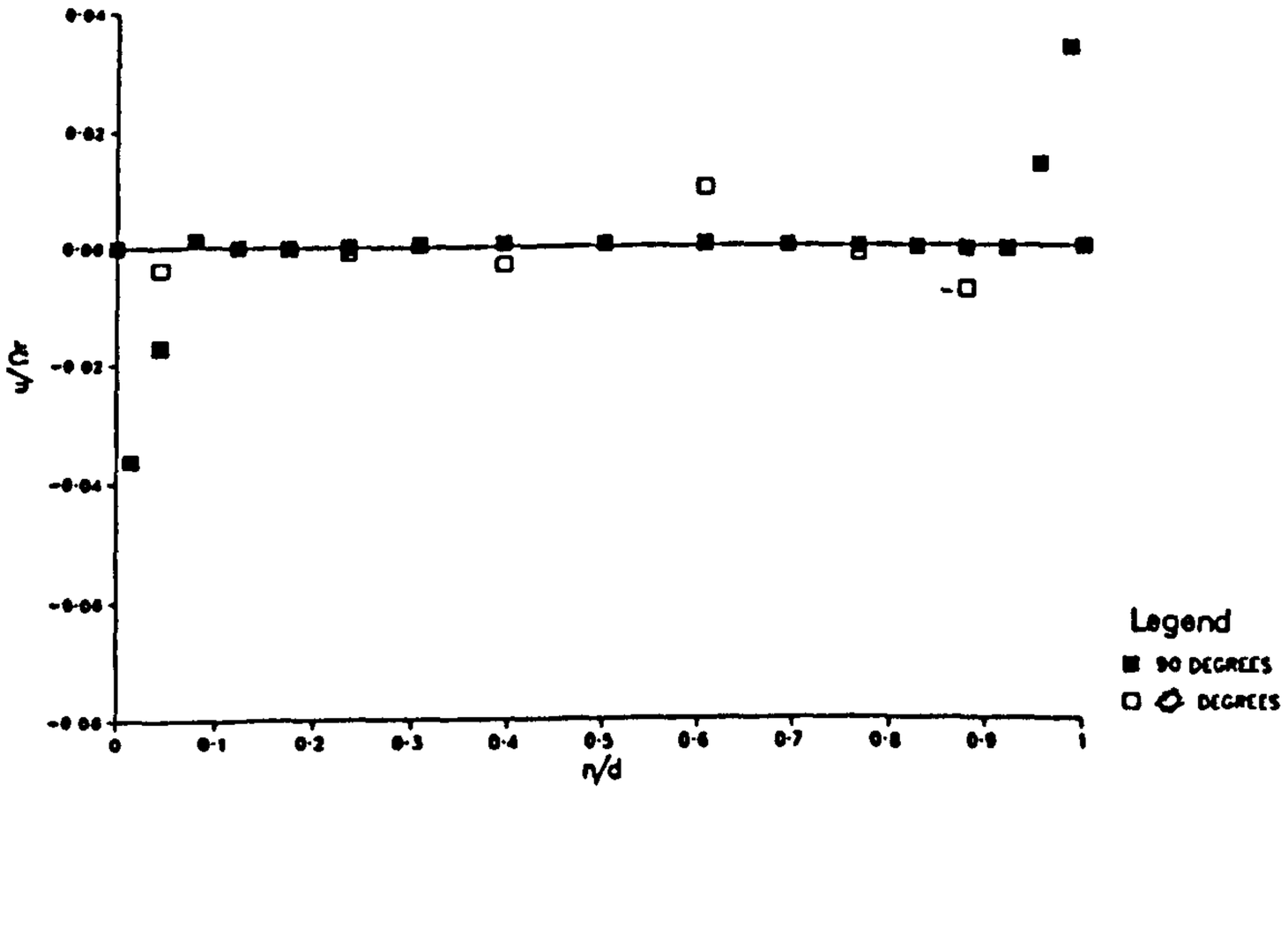
0·04
0·02
0·00
-0·02
-0·04
-0·06
-0·08
ψ/Ωr
0
0·1
0·2
0·3
0·4
0·5
0·6
0·7
0·8
0·9
1
r/d
Legend
90 DEGREES
DEGREES

(a)

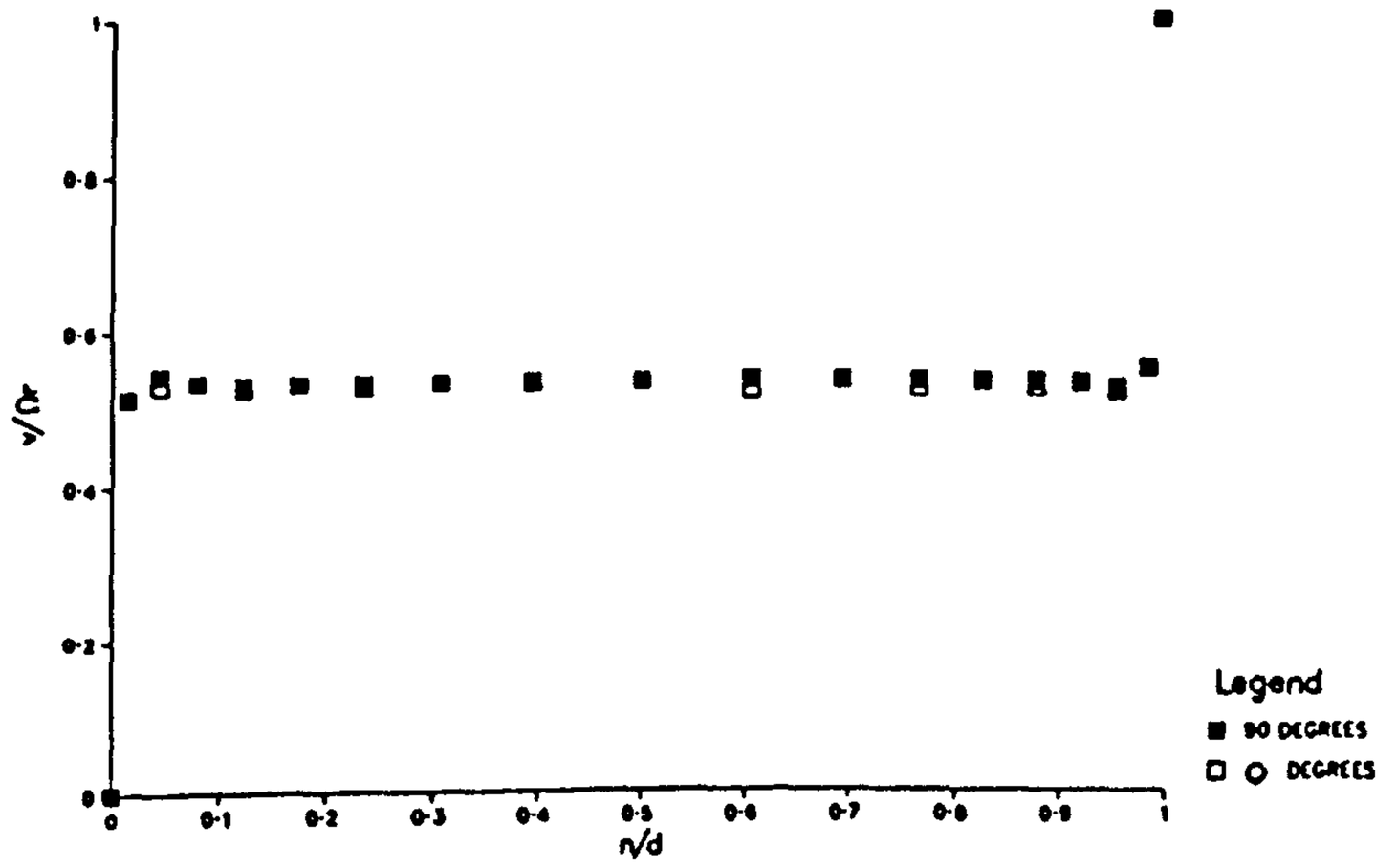
1
0·8
0·6
0·4
0·2
0
v/Ωr
0
0·1
0·2
0·3
0·4
0·5
0·6
0·7
0·8
0·9
1
r/d
Legend
90 DEGREES
O DEGREES

(b)

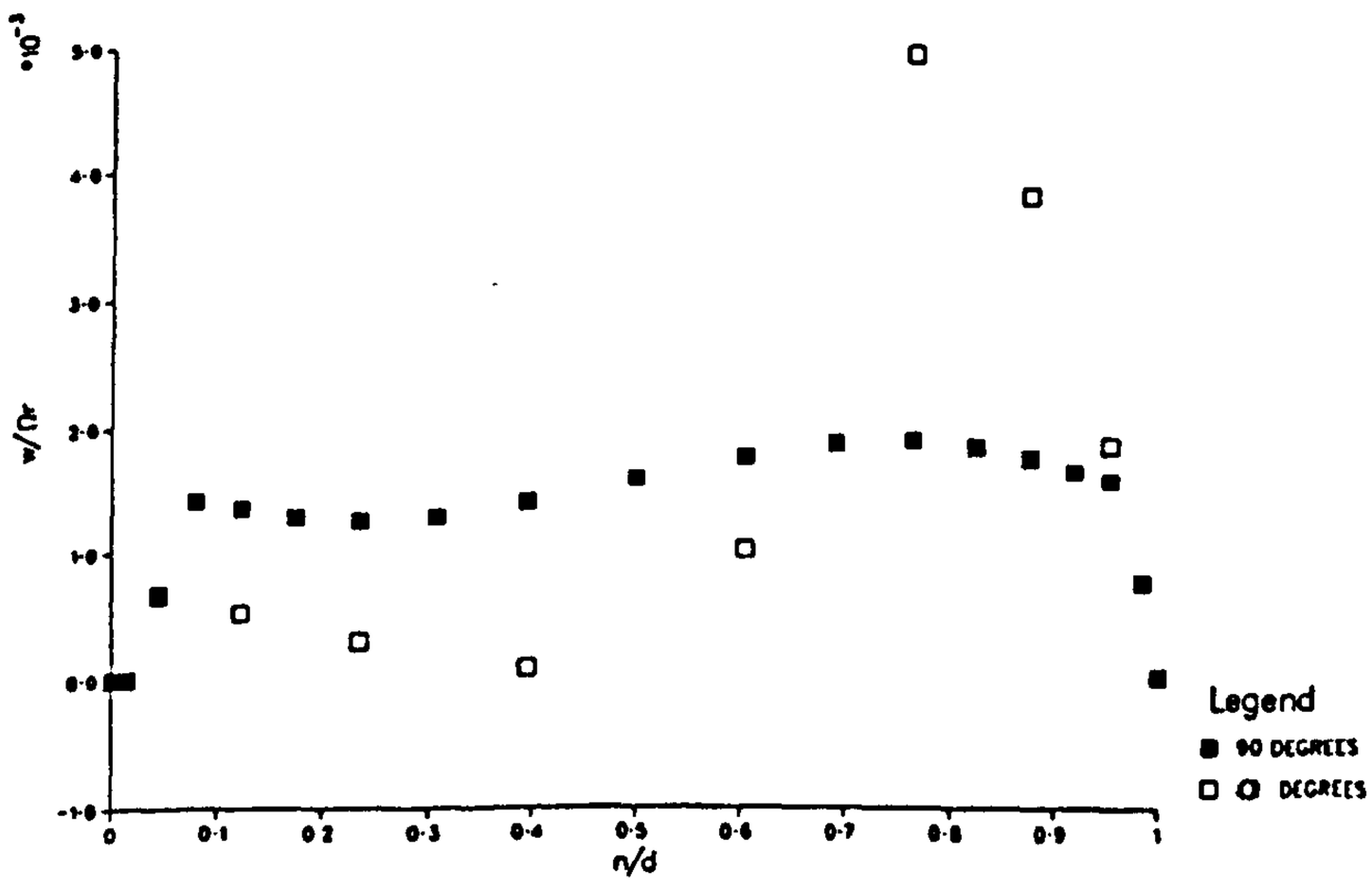
5·0
4·0
3·0
2·0
1·0
0·0
-1·0
v/Ωr
0
0·1
0·2
0·3
0·4
0·5
0·6
0·7
0·8
0·9
1
r/d
Legend
90 DEGREES
DEGREES

(c)

Figure 6.5 Comparison of Velocity Profile across the Cavity on a 41 x 41 Grid.

Turbulent Flow:- $a/b = 0$, $d/b = 0.16$, $Re = 10^6$, $C_q = 0$

(a) u-velocity component

(b) v-velocity component

(c) w-velocity component

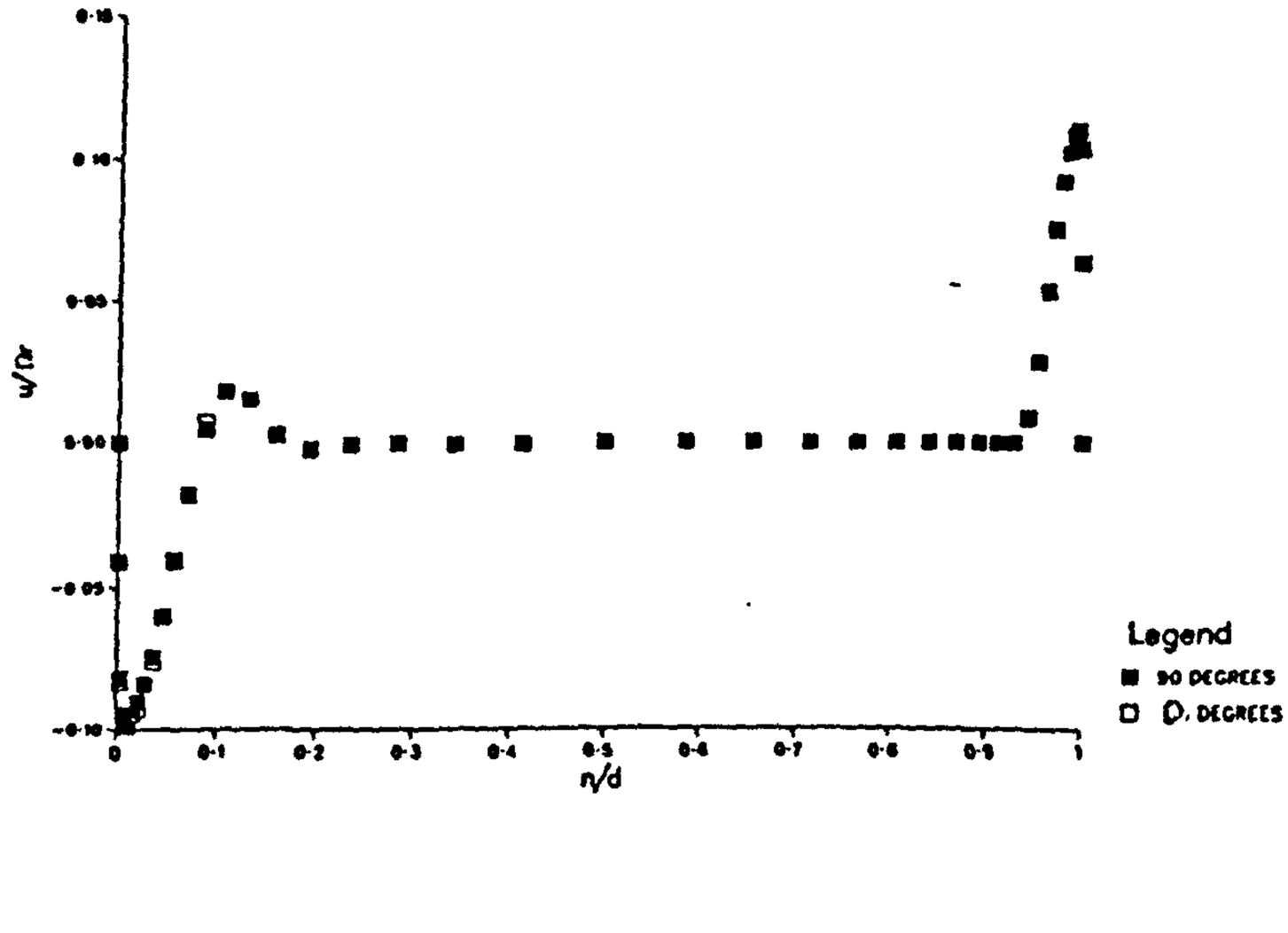
w/Ωr
r/d
Legend
90 DEGREES
0 DEGREES

(a)

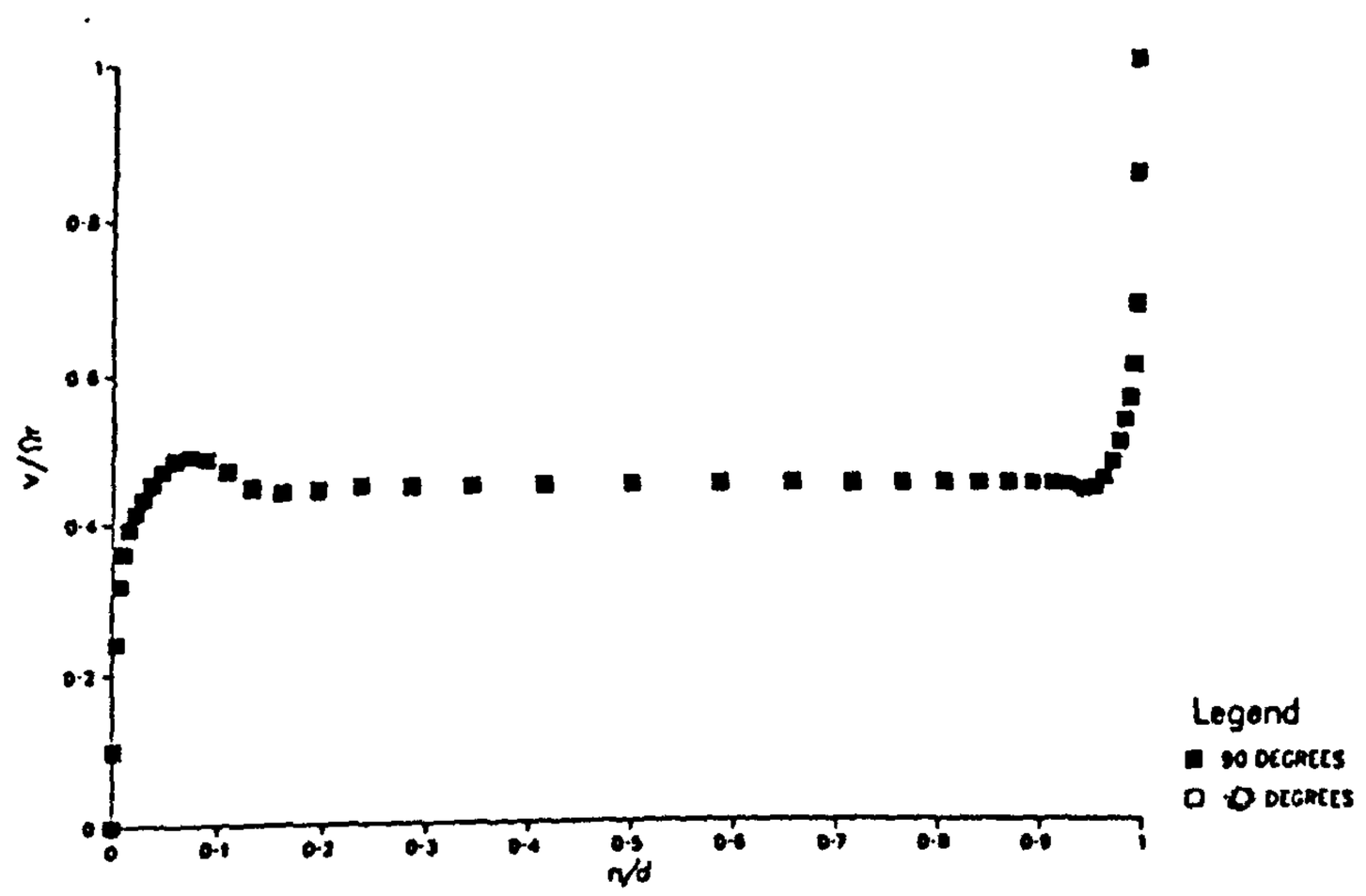
v/Ωr
r/d
Legend
90 DEGREES
0 DEGREES

(b)

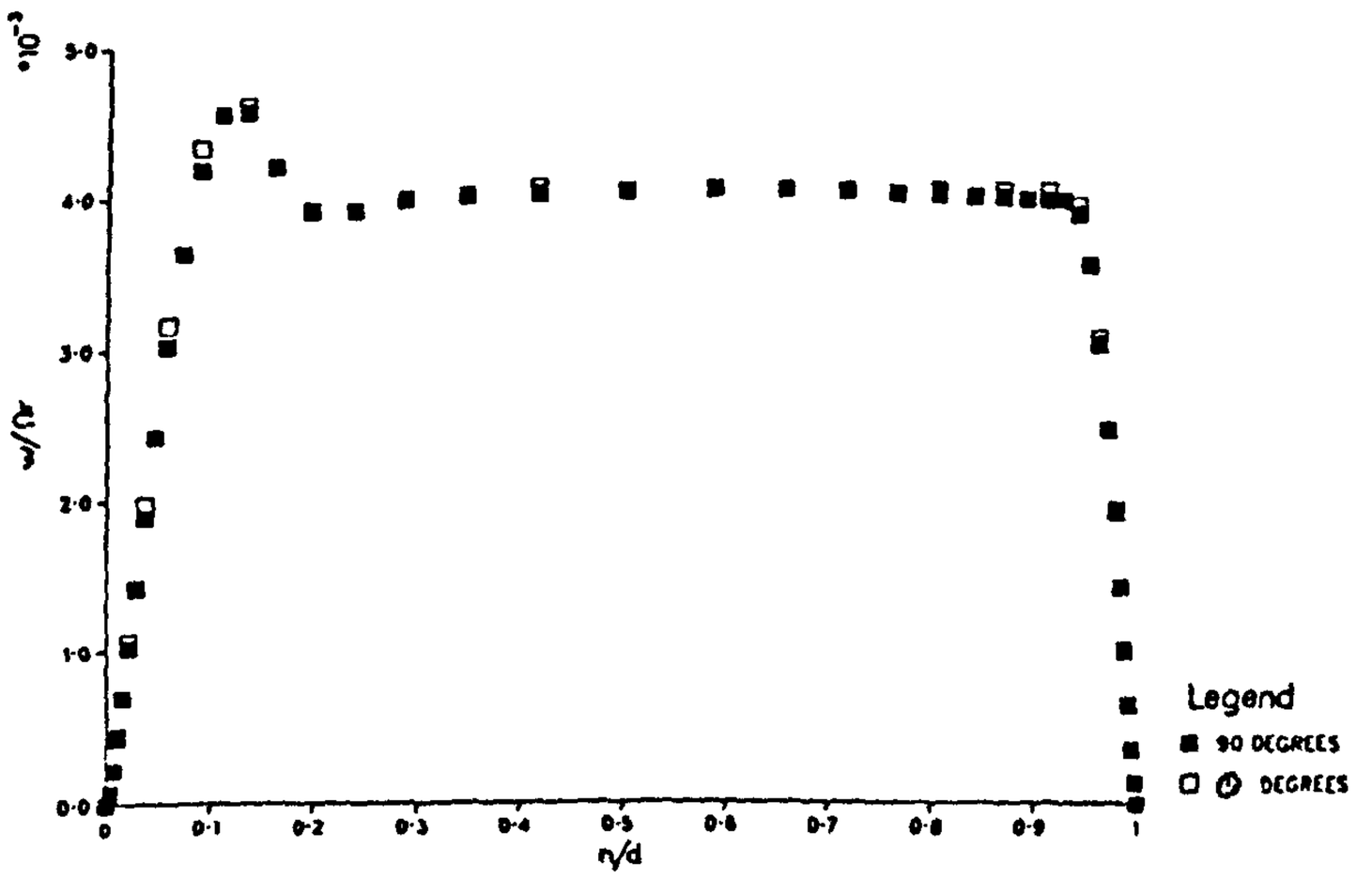
•10⁻³
u/Ωr
r/d
Legend
90 DEGREES
0 DEGREES

(c)

Figure 6.6 Comparison of Velocity Profiles across the Cavity.

Turbulent Flow:- $a/b = 0$, $d/b = 0.16$, $Re = 10^6$, $C_q = 0$

(a) u-velocity component

(b) v-velocity component

(c) w-velocity component

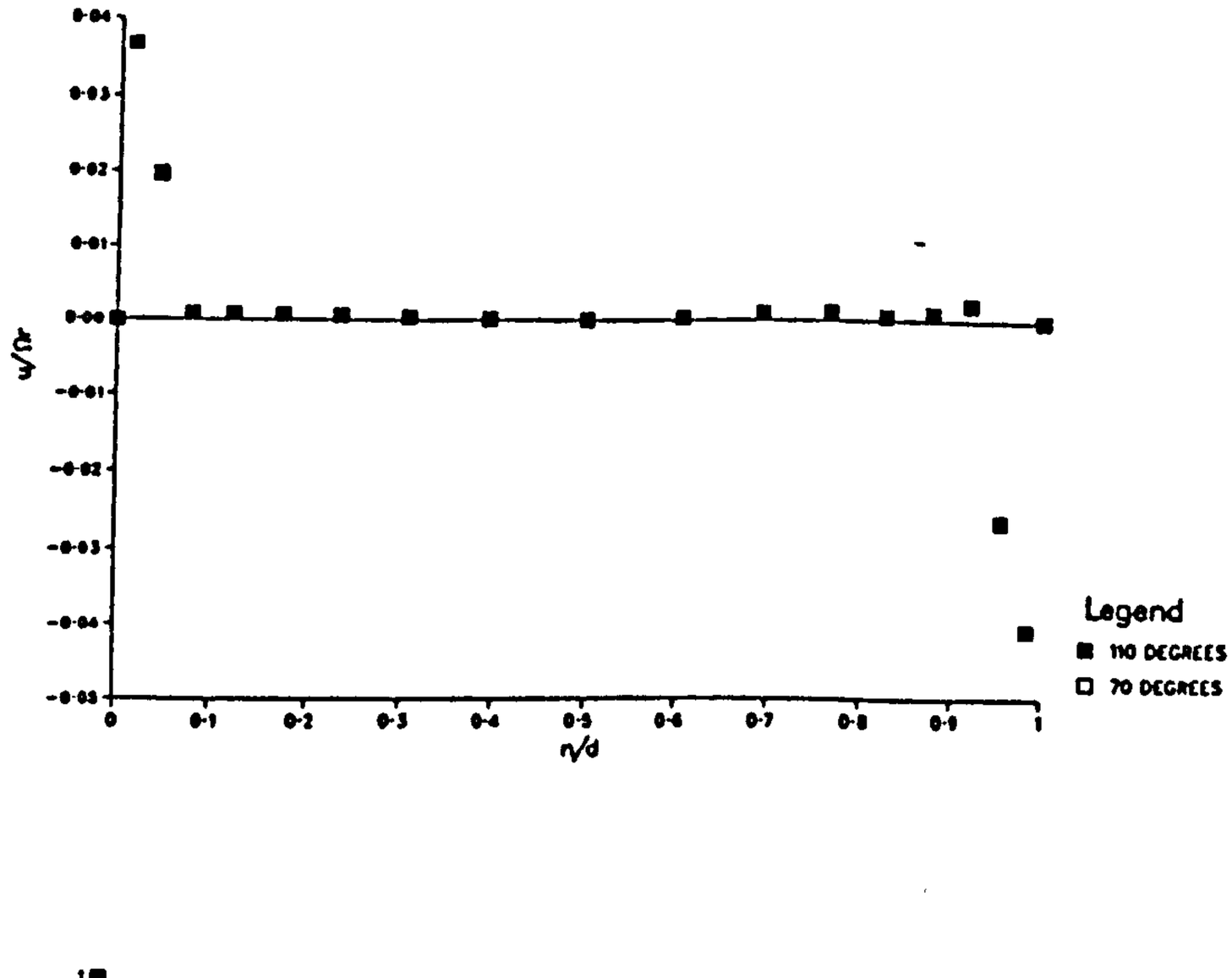
0·04
0·03
0·02
0·01
0·00
-0·01
-0·02
-0·03
-0·04
-0·05
ψ/Ωr
0
0·1
0·2
0·3
0·4
0·5
0·6
0·7
0·8
0·9
1
r/d
Legend
110 DEGREES
70 DEGREES

(a)

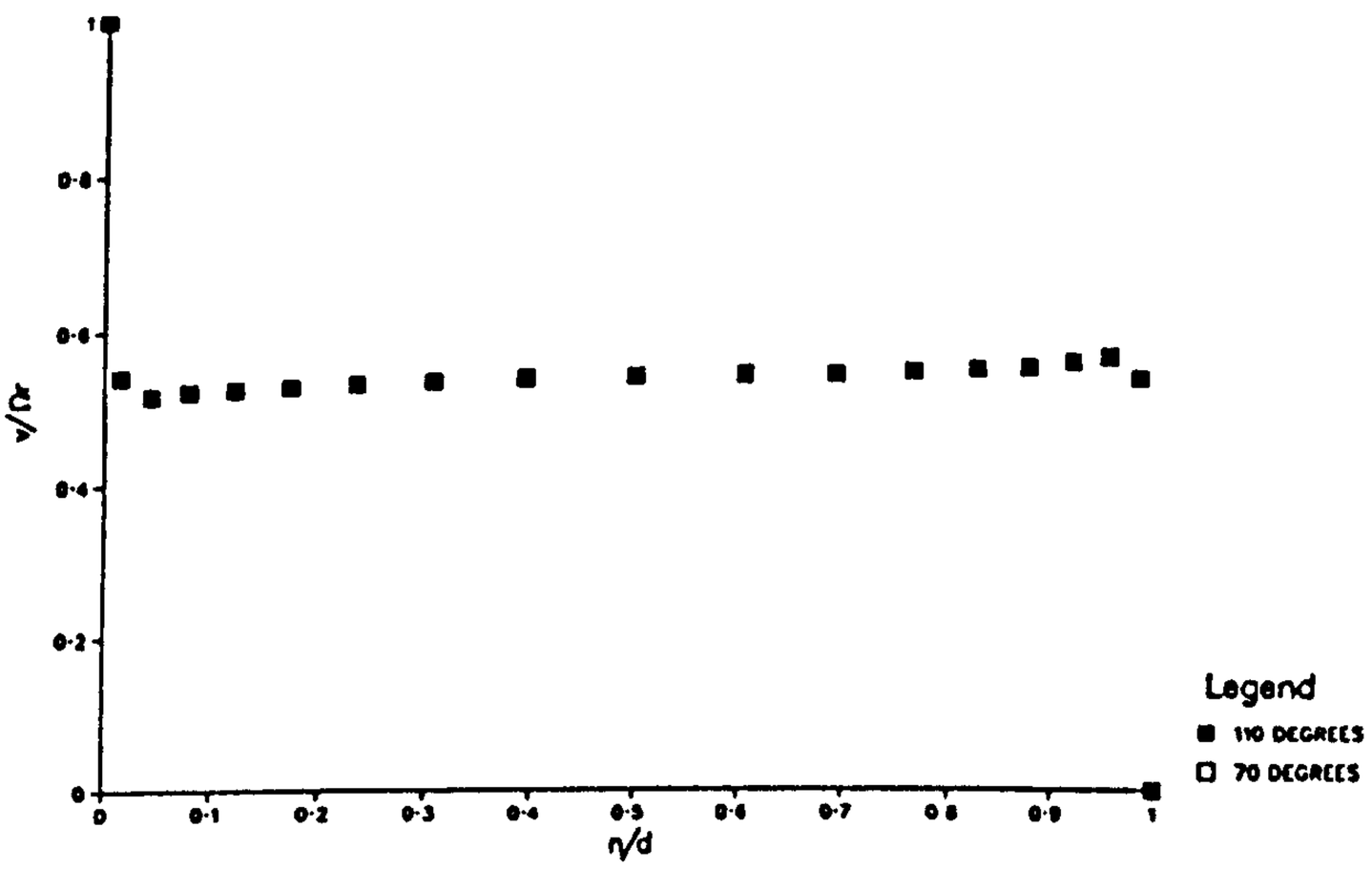
1
0·8
0·6
0·4
0·2
0
v/Ωr
0
0·1
0·2
0·3
0·4
0·5
0·6
0·7
0·8
0·9
1
r/d
Legend
110 DEGREES
70 DEGREES

(b)

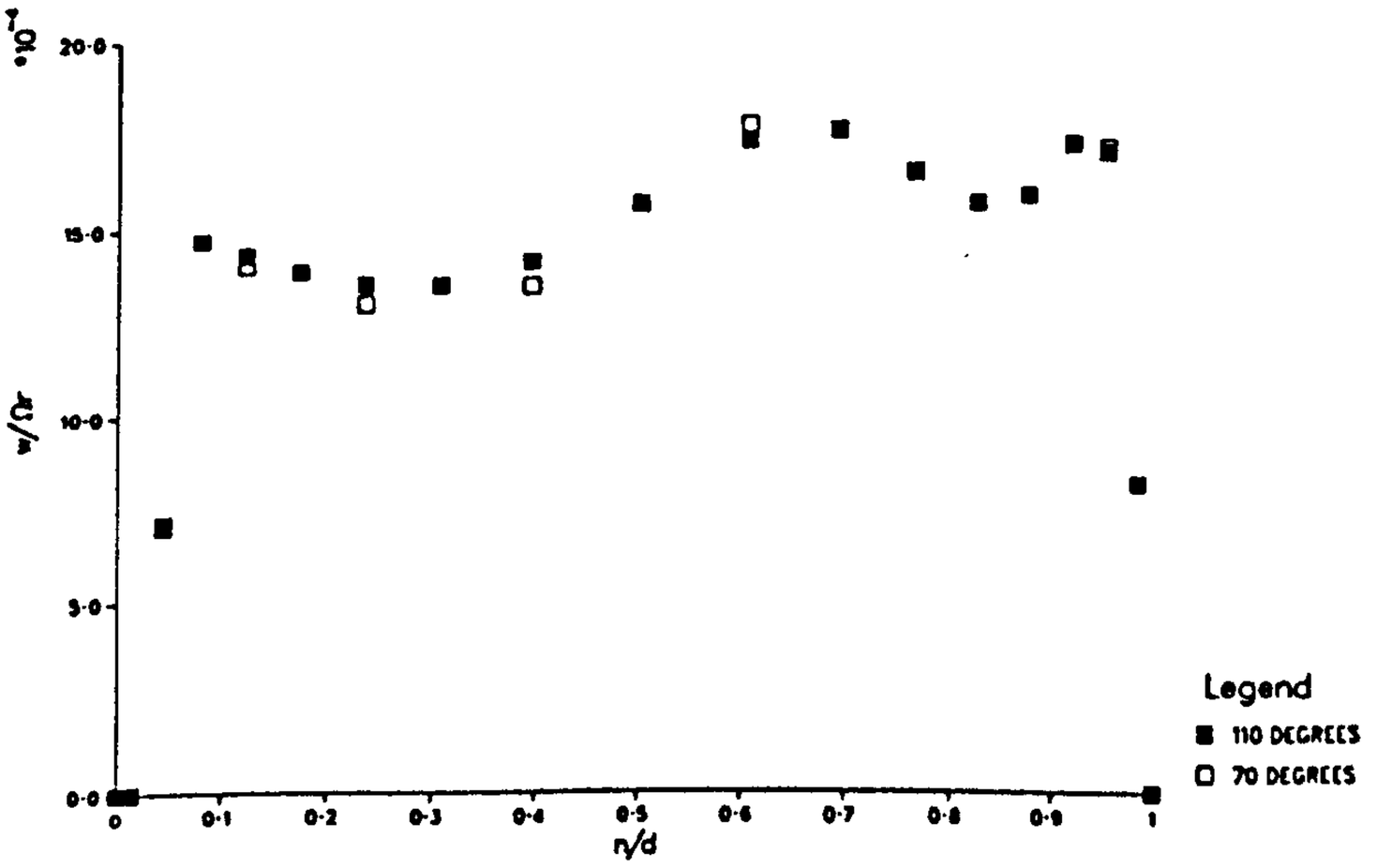
20·0
15·0
10·0
5·0
0·0
w/Ωr²
0
0·1
0·2
0·3
0·4
0·5
0·6
0·7
0·8
0·9
1
r/d
Legend
110 DEGREES
70 DEGREES

(c)

Figure 6.7 Comparison of Velocity Profiles across the Cavity.

Turbulent Flow:- $a/b = 0$, $d/b = 0.16$, $Re = 10^6$, $C_q = 3000$

(a) u-velocity component

(b) v-velocity component

(c) w-velocity component

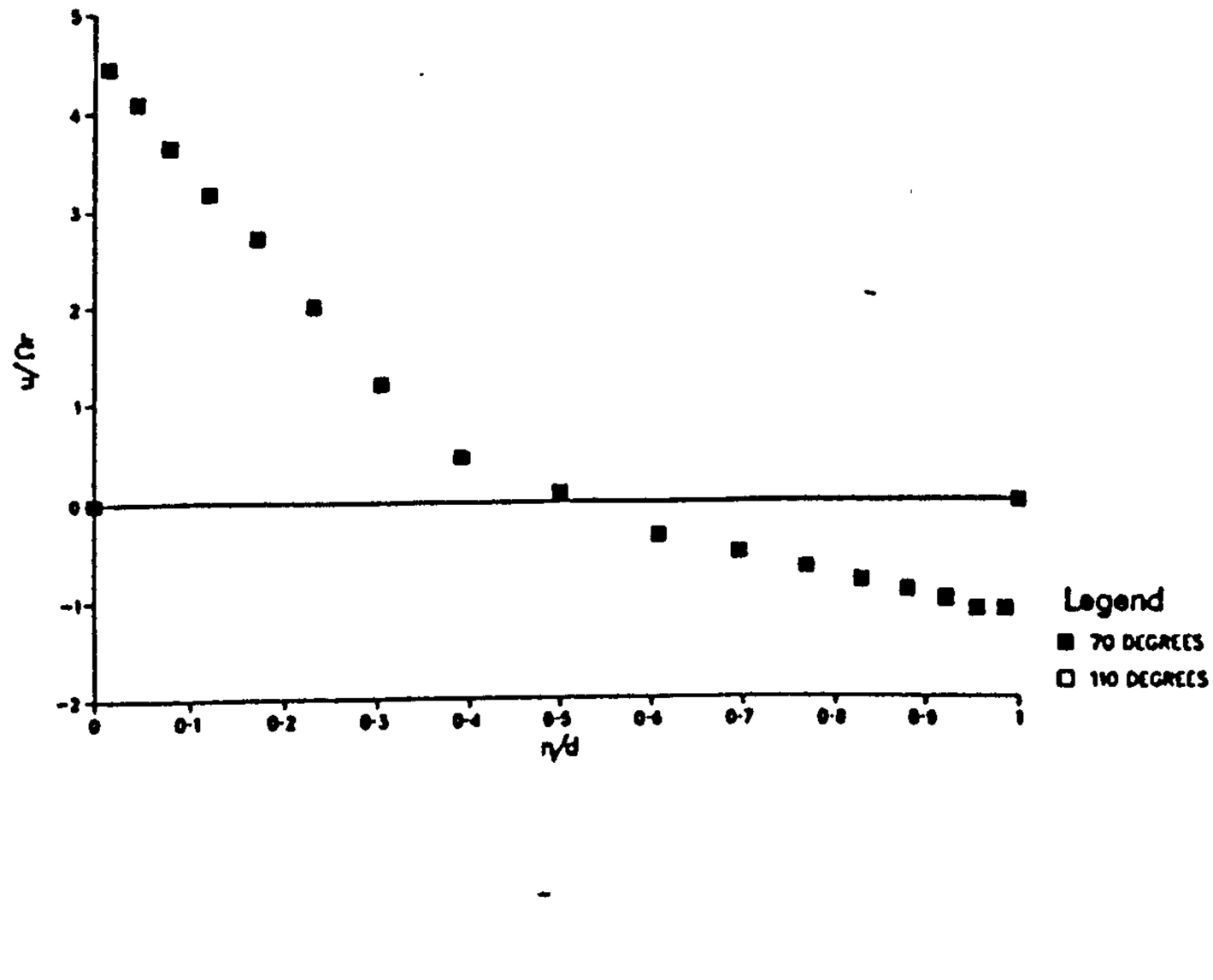
v/Ωr
r/d
0
0·1
0·2
0·3
0·4
0·5
0·6
0·7
0·8
0·9
1
-2
-1
1
2
3
4
5
Legend
70 DEGREES
110 DEGREES

(a)

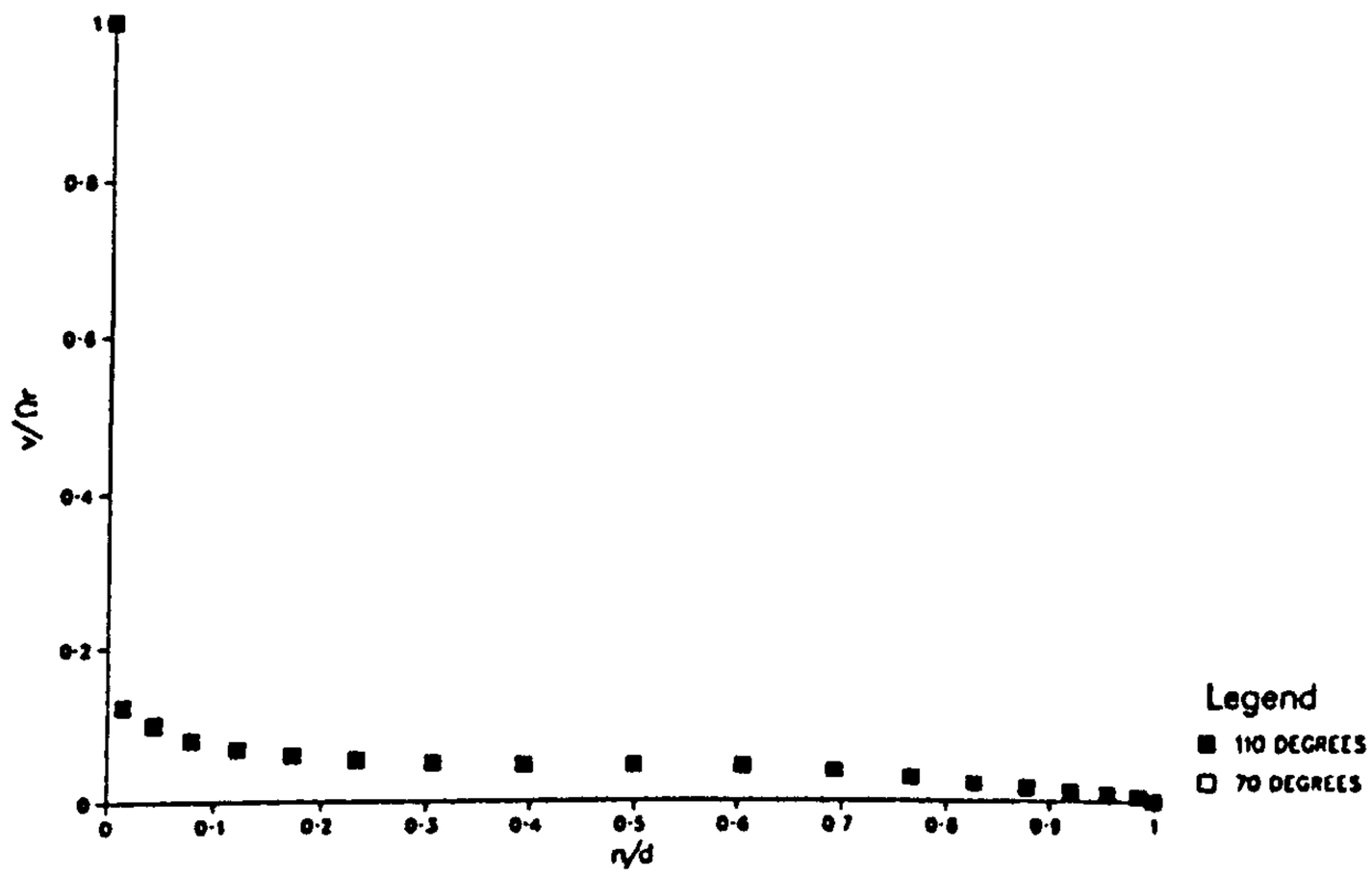
v/Ωr
r/d
0
0·1
0·2
0·3
0·4
0·5
0·6
0·7
0·8
0·9
1
0·2
0·4
0·6
0·8
1
Legend
110 DEGREES
70 DEGREES

(b)

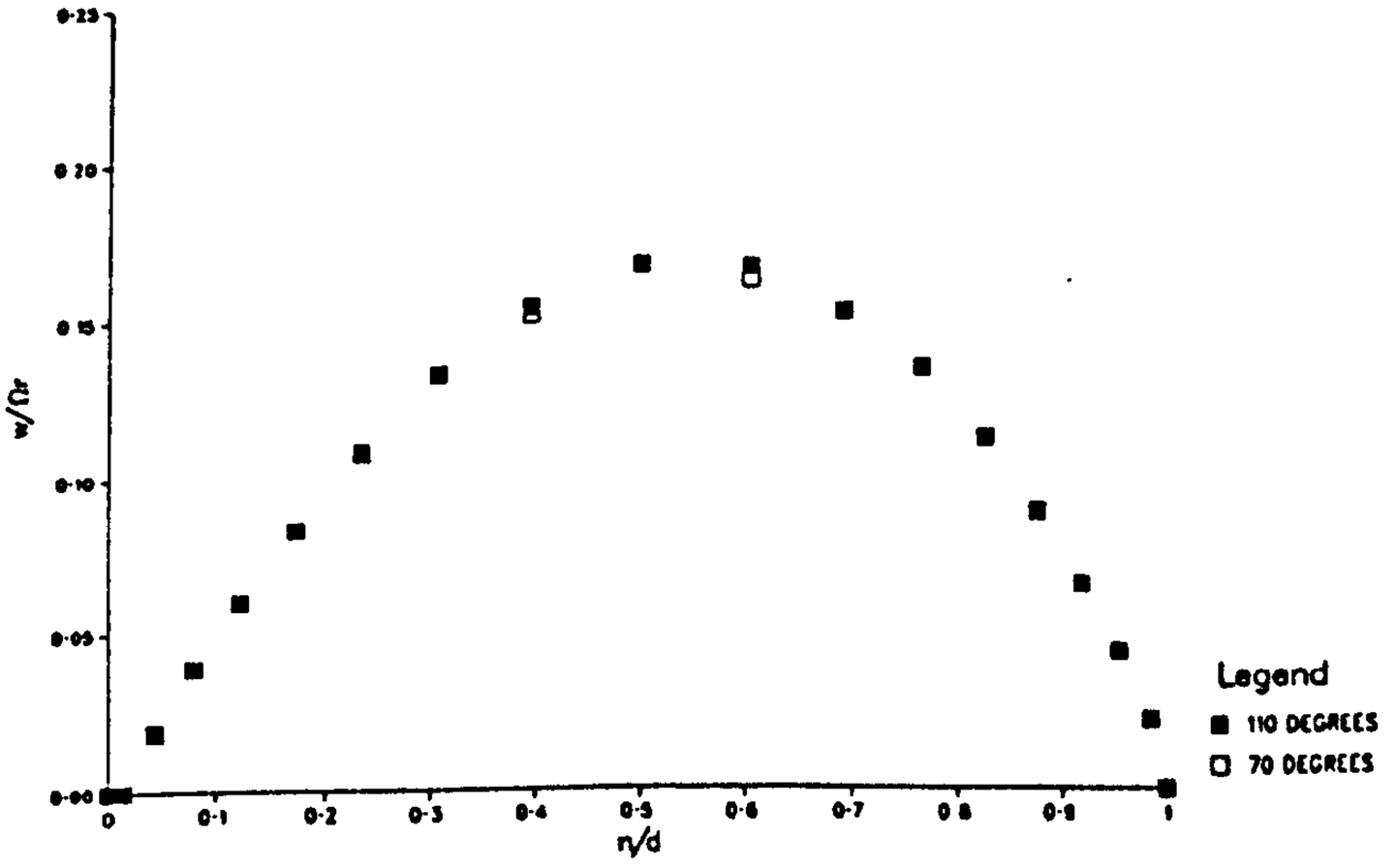
v/Ωr
r/d
0
0·1
0·2
0·3
0·4
0·5
0·6
0·7
0·8
0·9
1
0·05
0·10
0·15
0·20
0·25
Legend
110 DEGREES
70 DEGREES

(c)

A comparison of the predicted moment coefficient with Yamada and Ito (1975); Cq=0, a/b=0, d/b=0.16, Re=2*10^4

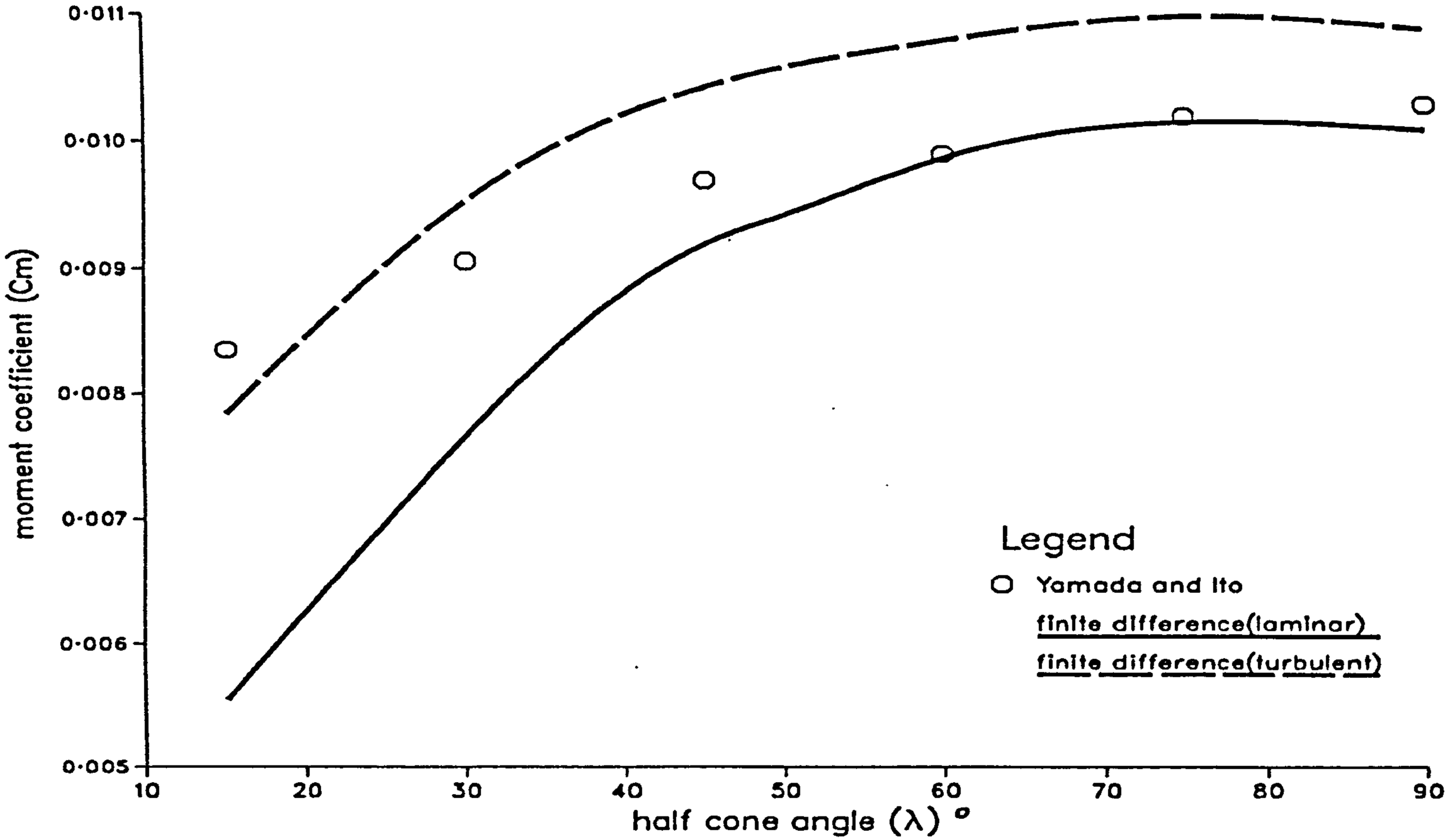

Figure 6.8(a)

A comparison of the predicted moment coefficient with Yamada and Ito (1975); Cq=0, a/b=0, d/b=0.024, Re=$2*10^4$

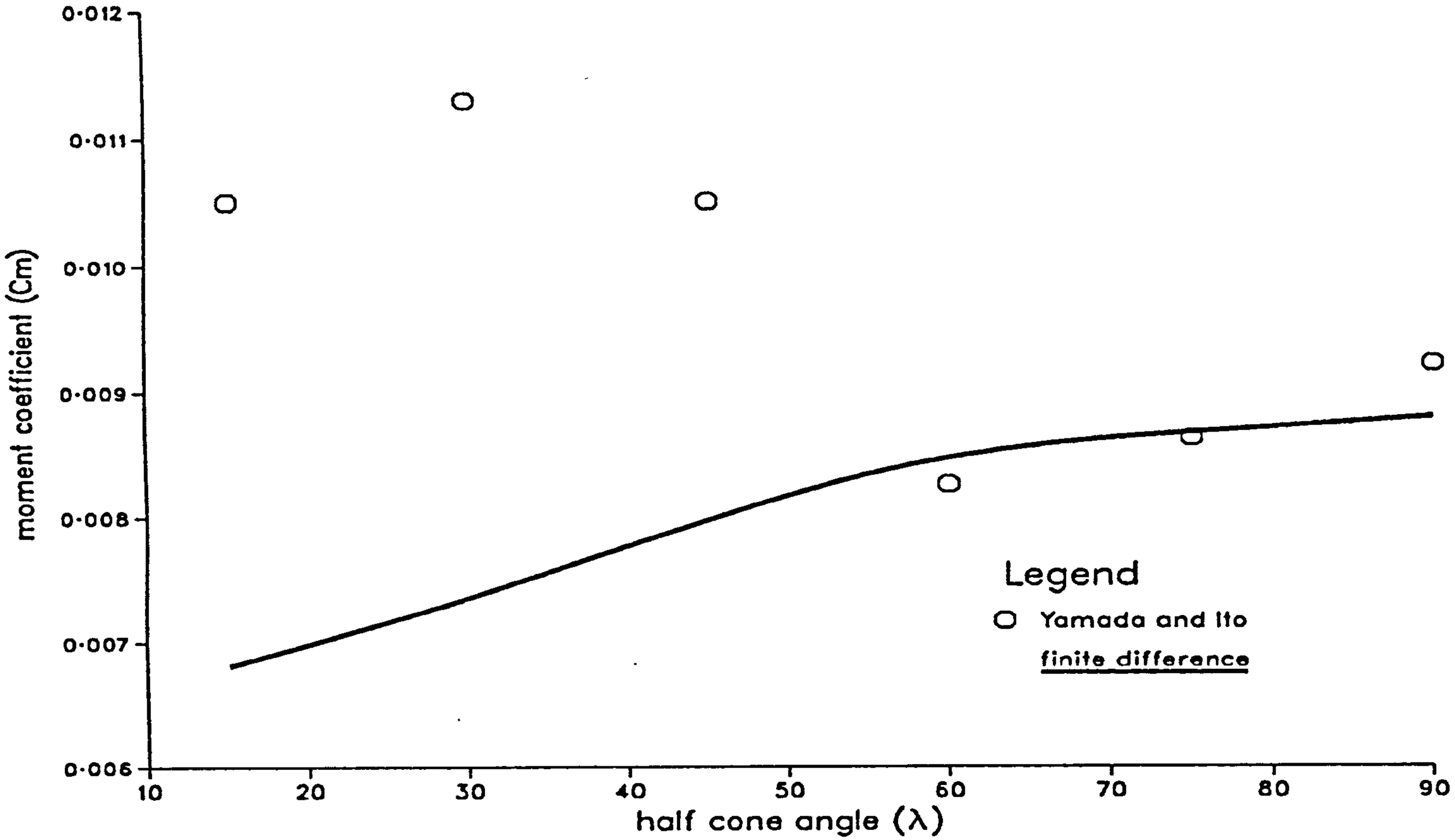

Figure 6.8(b)

A comparison of the predicted moment coefficient with Yamada and Ito (1975); Cq=0, a/b=0, d/b=0.016, λ=15°

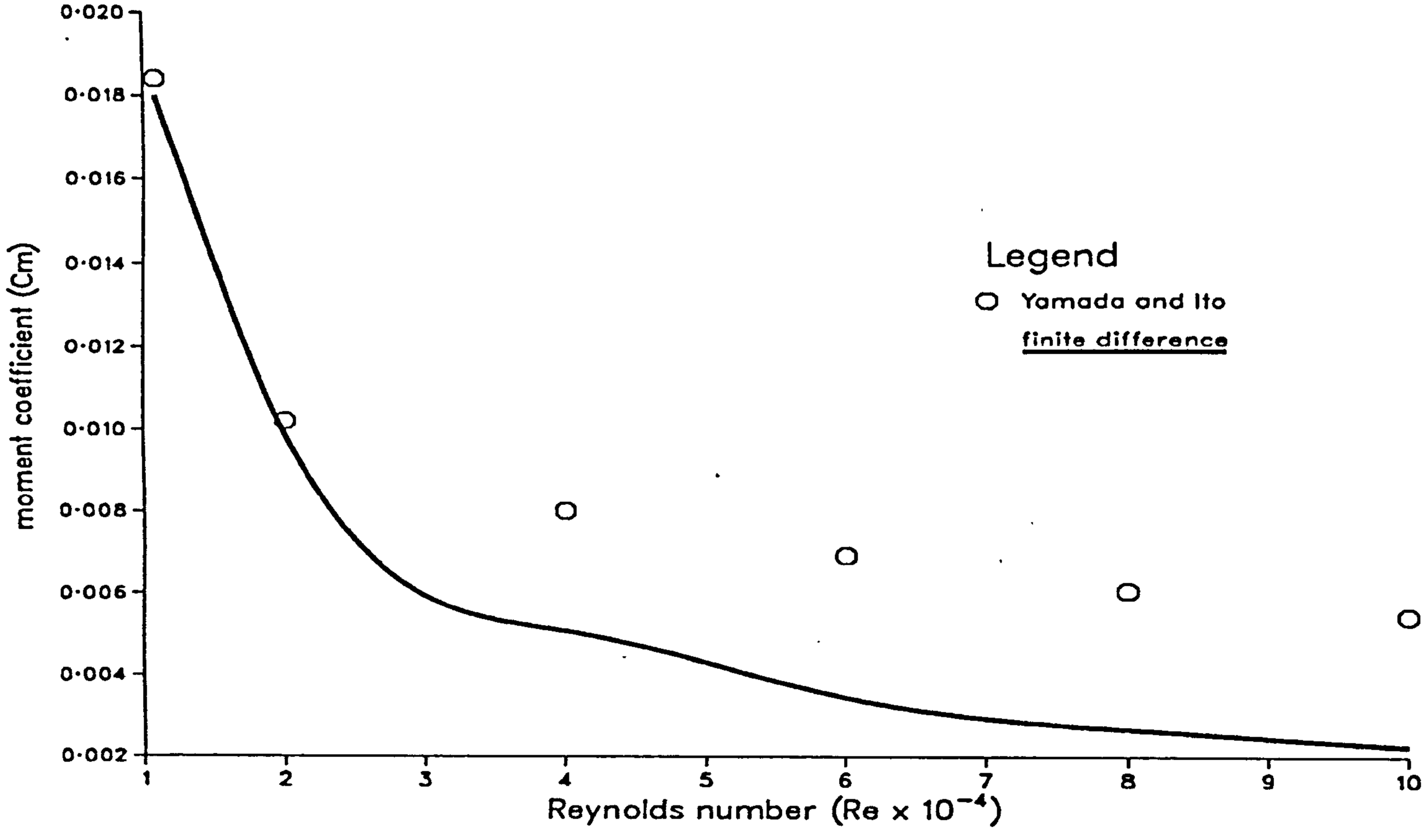

Figure 6.8(c)

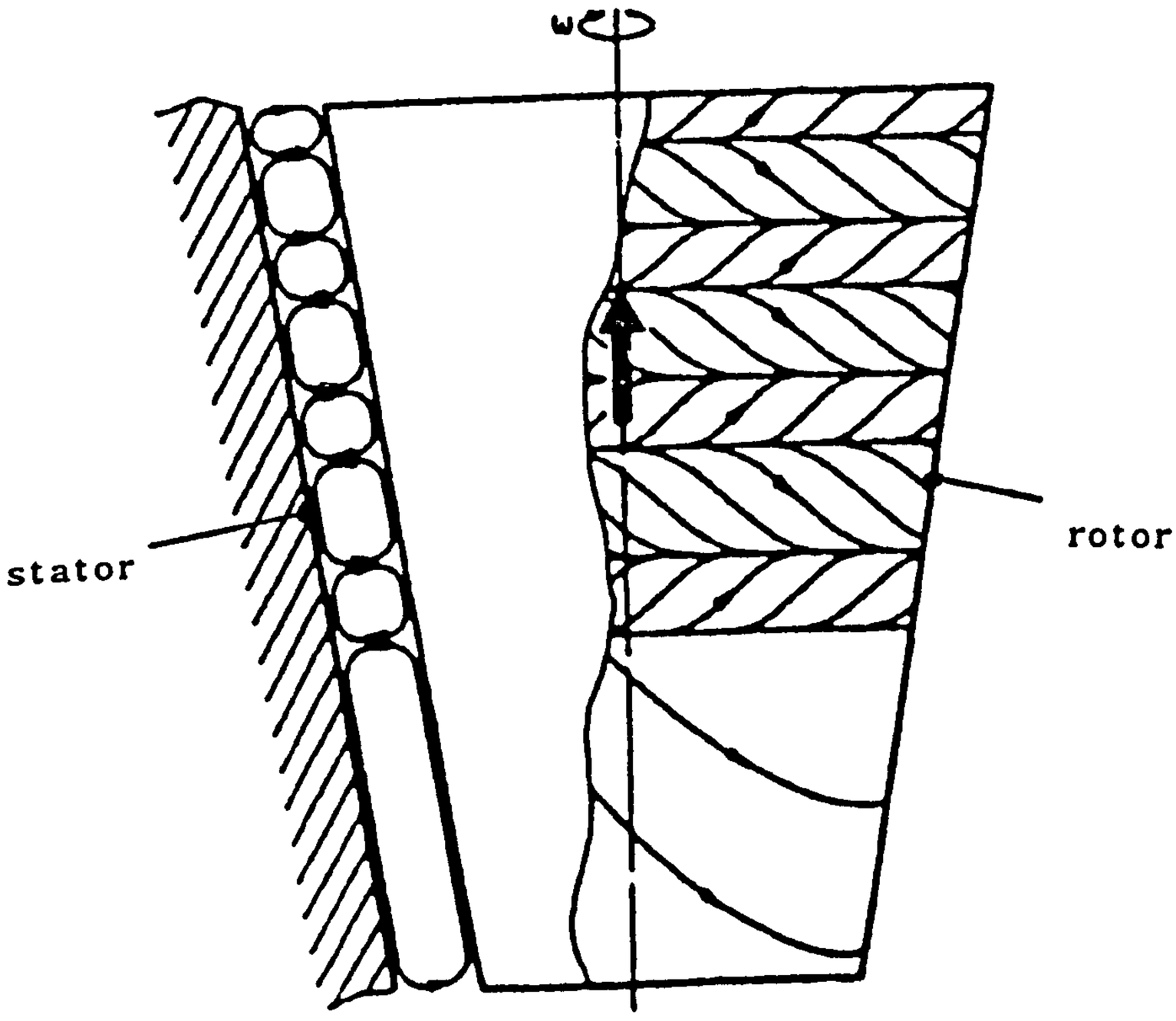

Figure 6.9 'Taylor-type' vortices in a Rotor-Stator Cone System.

(Taken from Wimmer (1983))

Figure 6.10 Steamline Plots; $C_q = 0$, $a/b = 0$, $\lambda = 15^0$

(a) Laminar, $d/b = 0.16$, $Re = 2 \times 10^4$

(b) Turbulent, $d/b = 0.16$, $Re = 2 \times 10^4$

(c) Laminar, $d/b = 0.016$, $Re = 4 \times 10^4$

(d) Laminar, $d/b = 0.024$, $Re = 10^4$

(a)

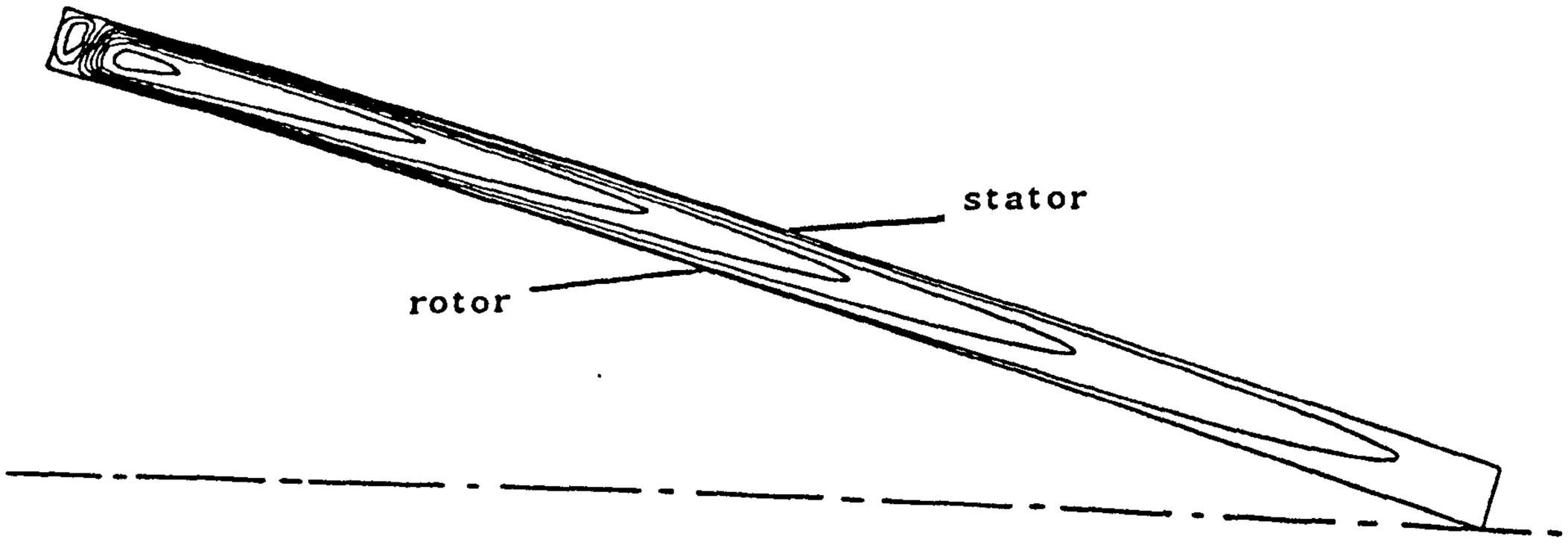

(b)

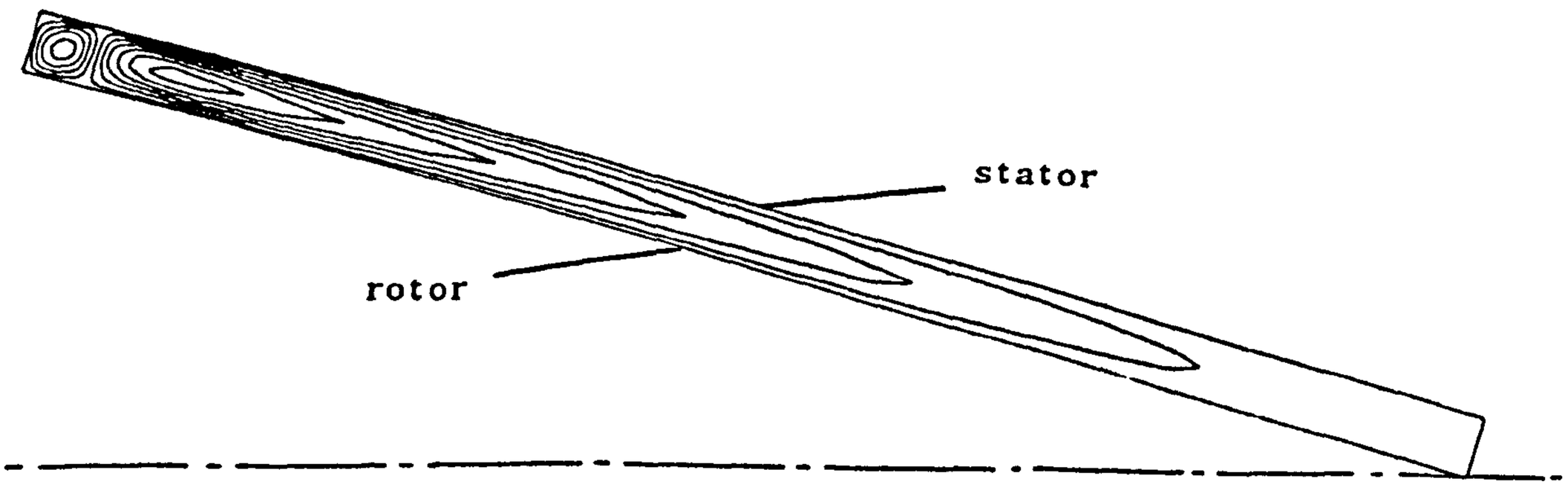

(c)

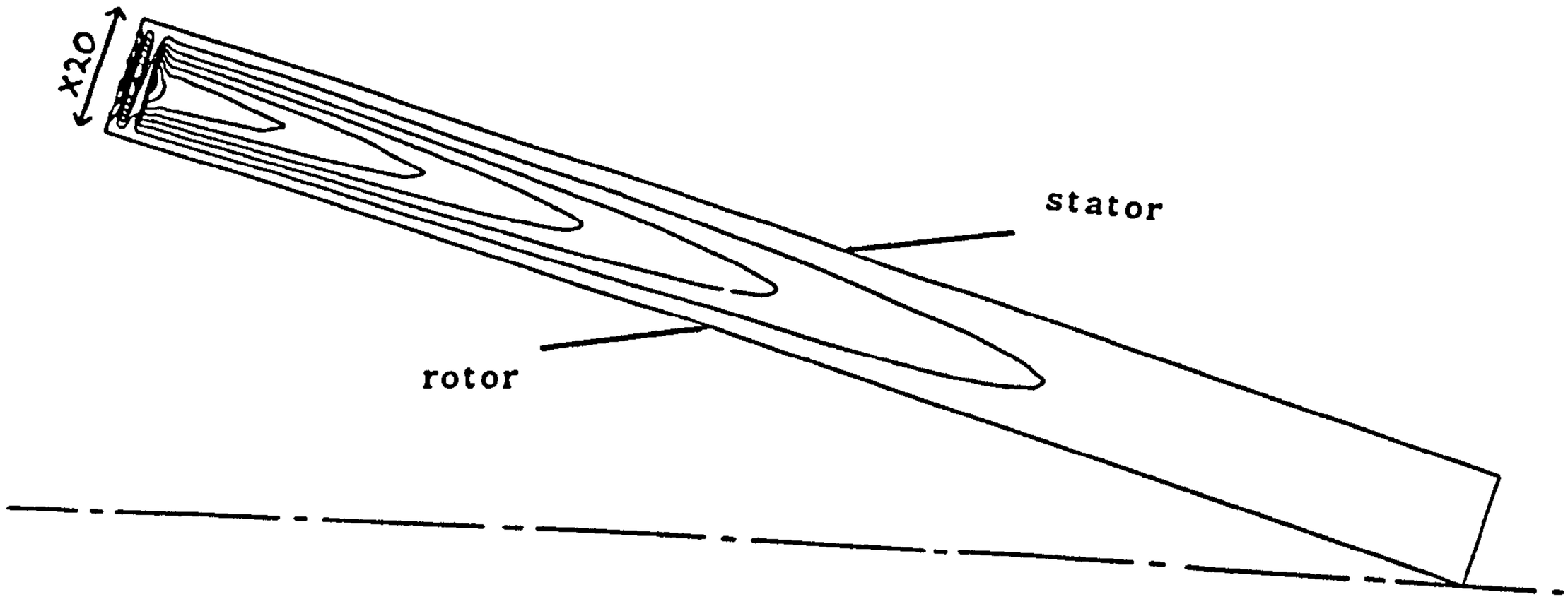

(d)

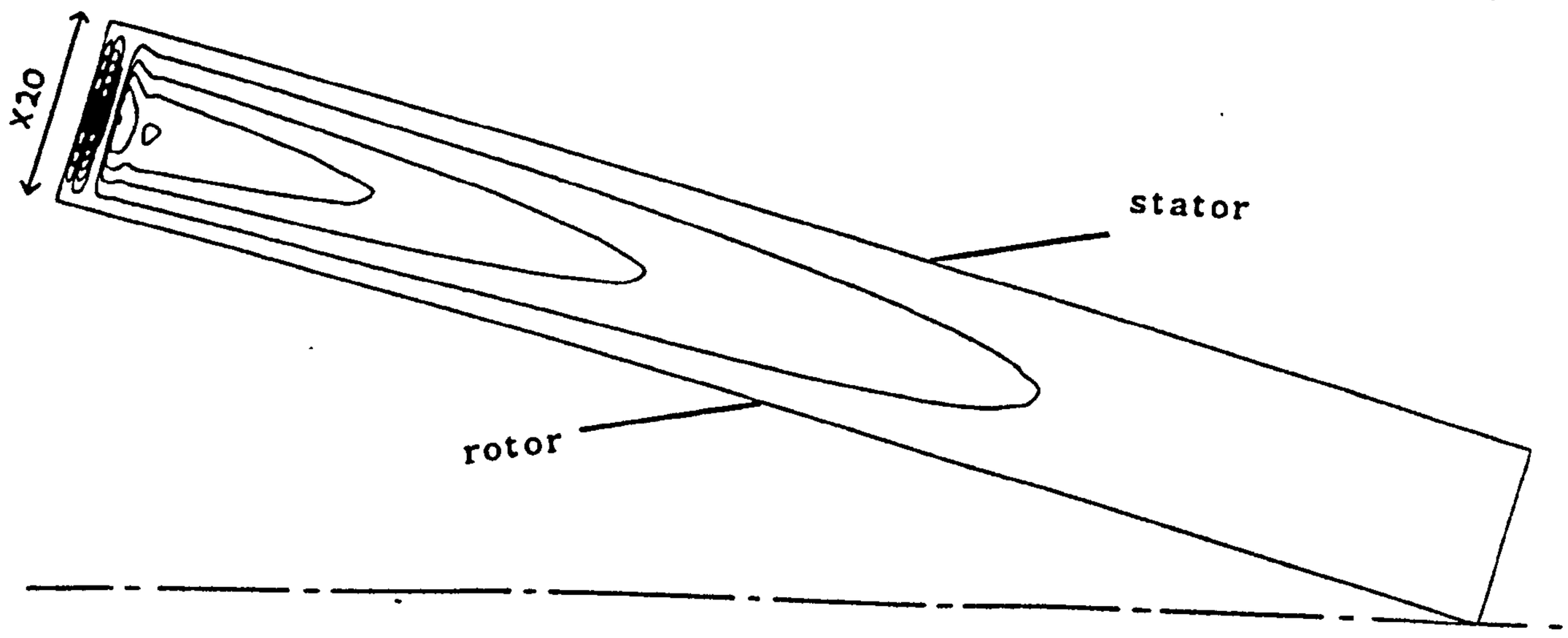

The effect of grid spacing on the radial velocity at r/b=0.8;
$\lambda=120^{\circ}$, Cq=0, a/b=0, d/b=0.16,and $Re=10^{6}$

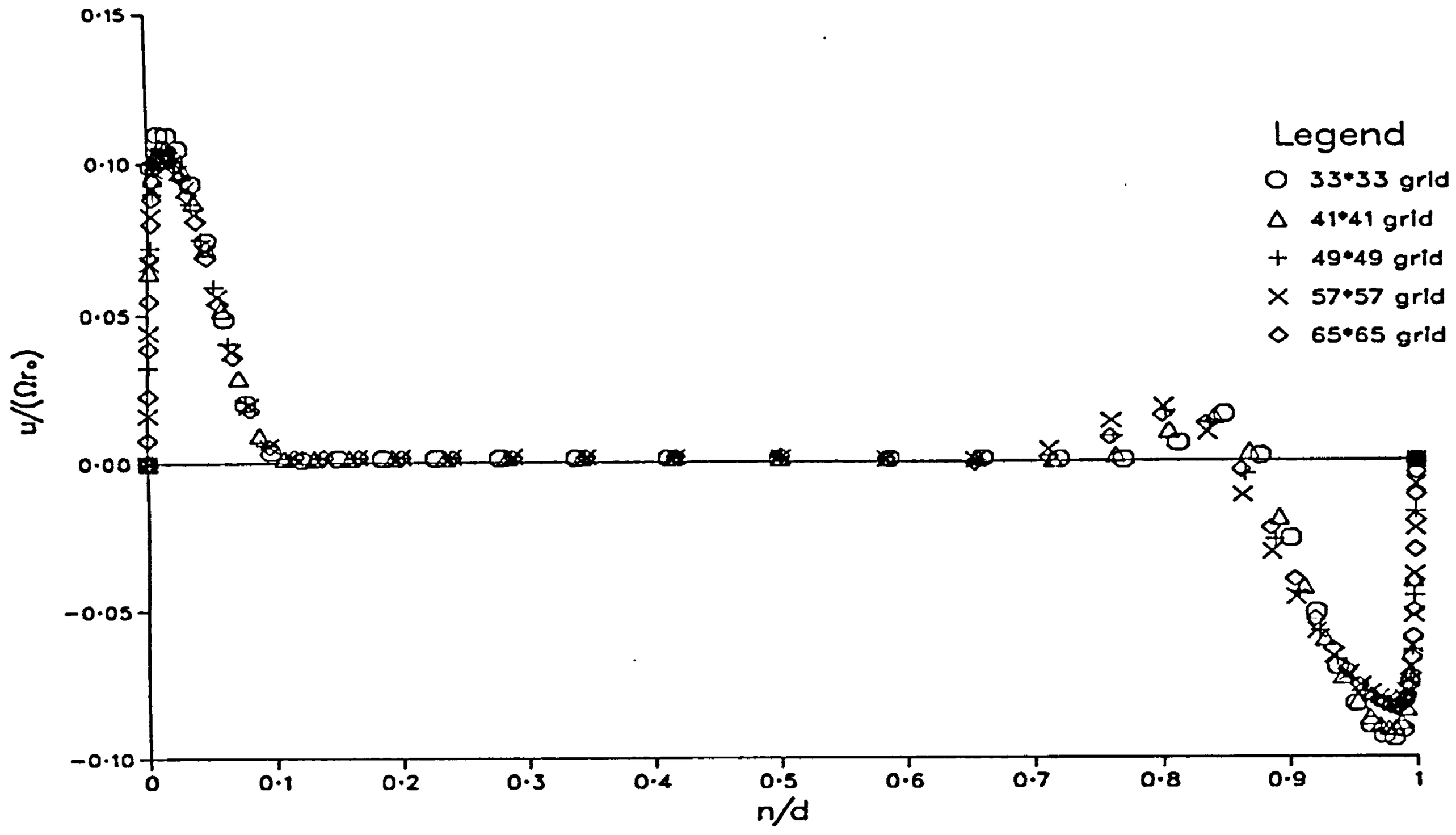

Figure 6.11

Figure 6.12 Turbulent Streamline Plots;

$d/b = 0.16$, $a/b = 0$, $C_q = 0$, $Re = 10^6$

(a) $\lambda = 90^0$

(b) $\lambda = 75^0$

(c) $\lambda = 60^0$

(d) $\lambda = 45^0$

(e) $\lambda = 30^0$

(f) $\lambda = 15^0$

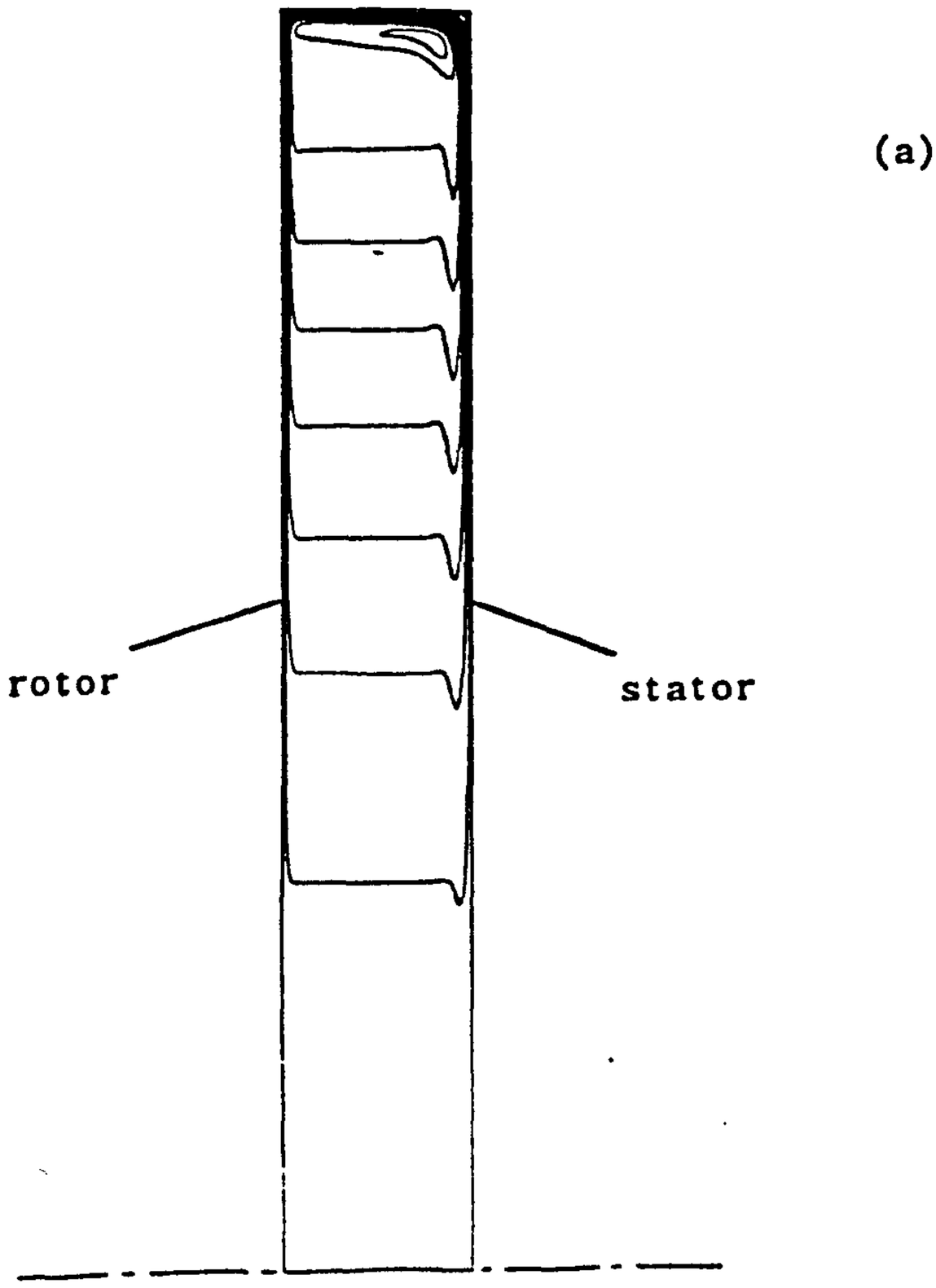

(a)

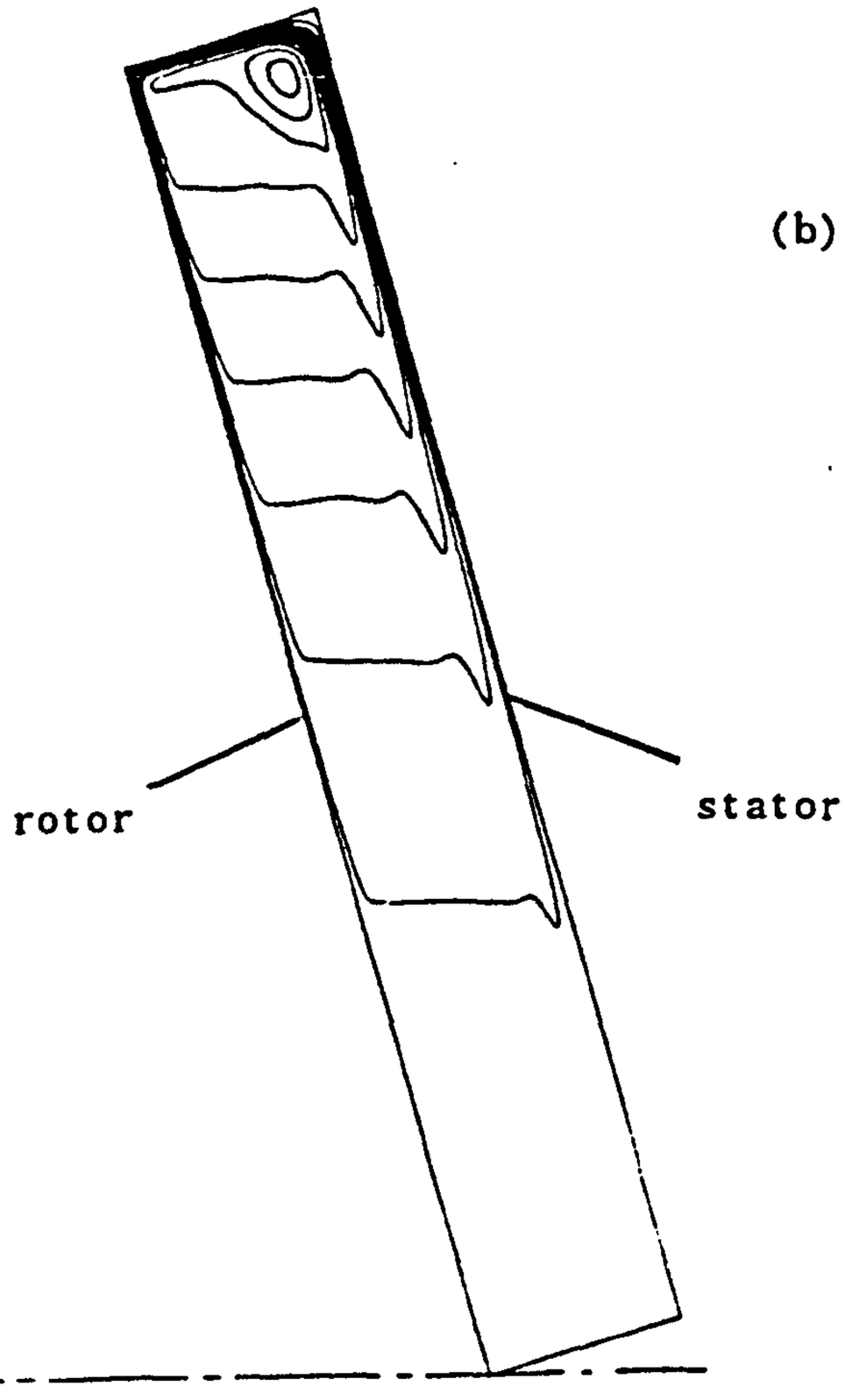

(b)

(c)

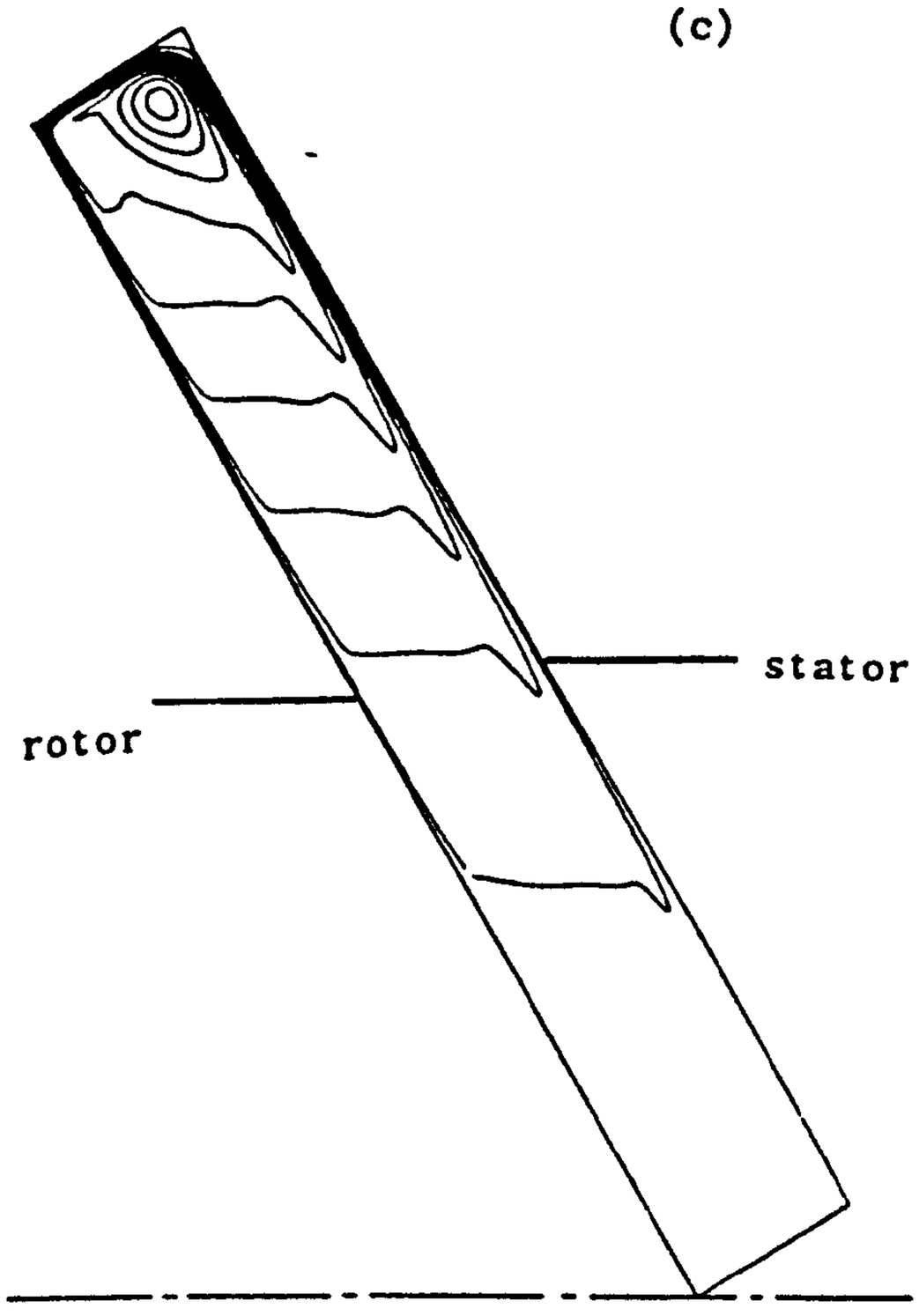

(d)

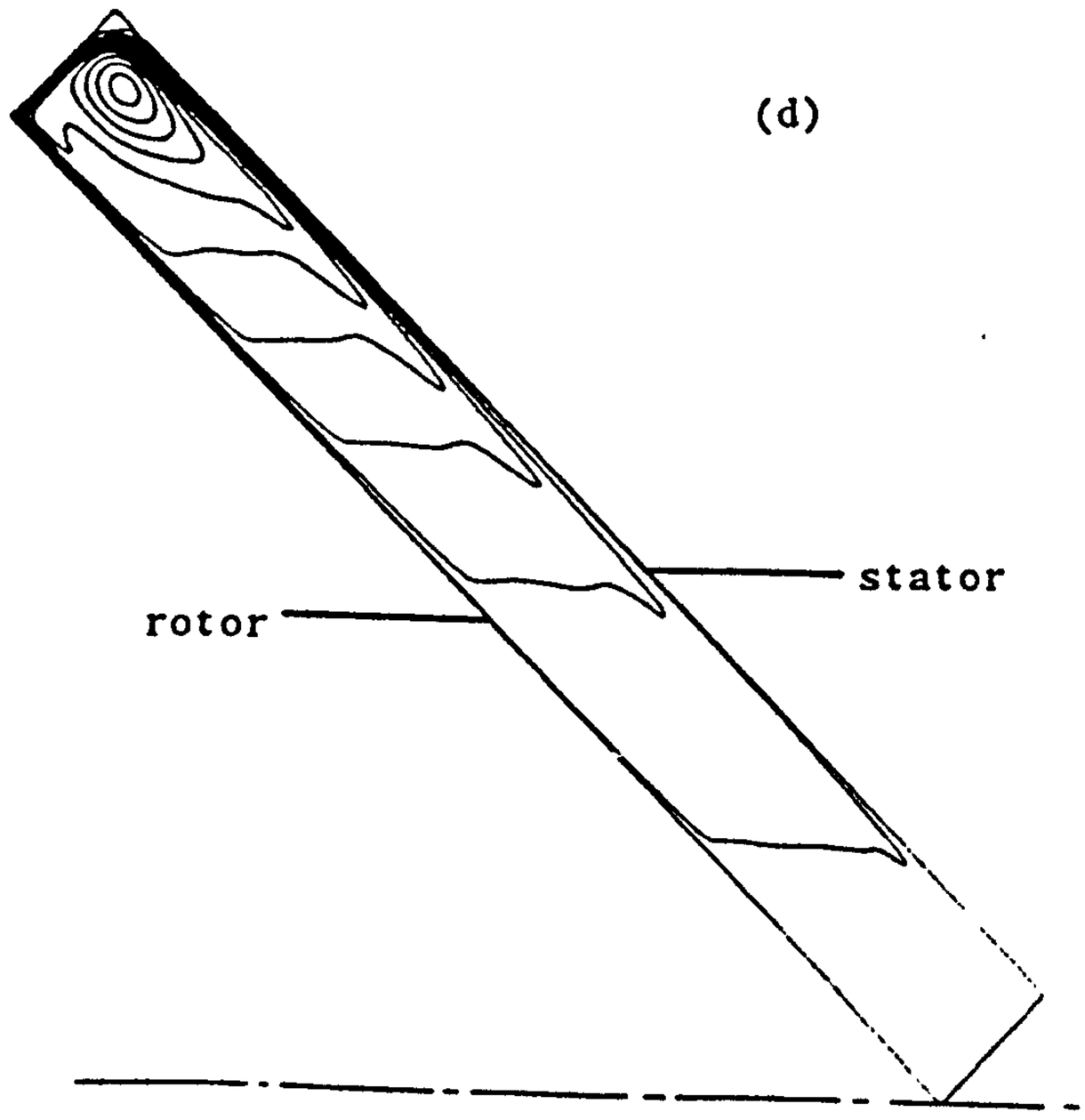

(e)

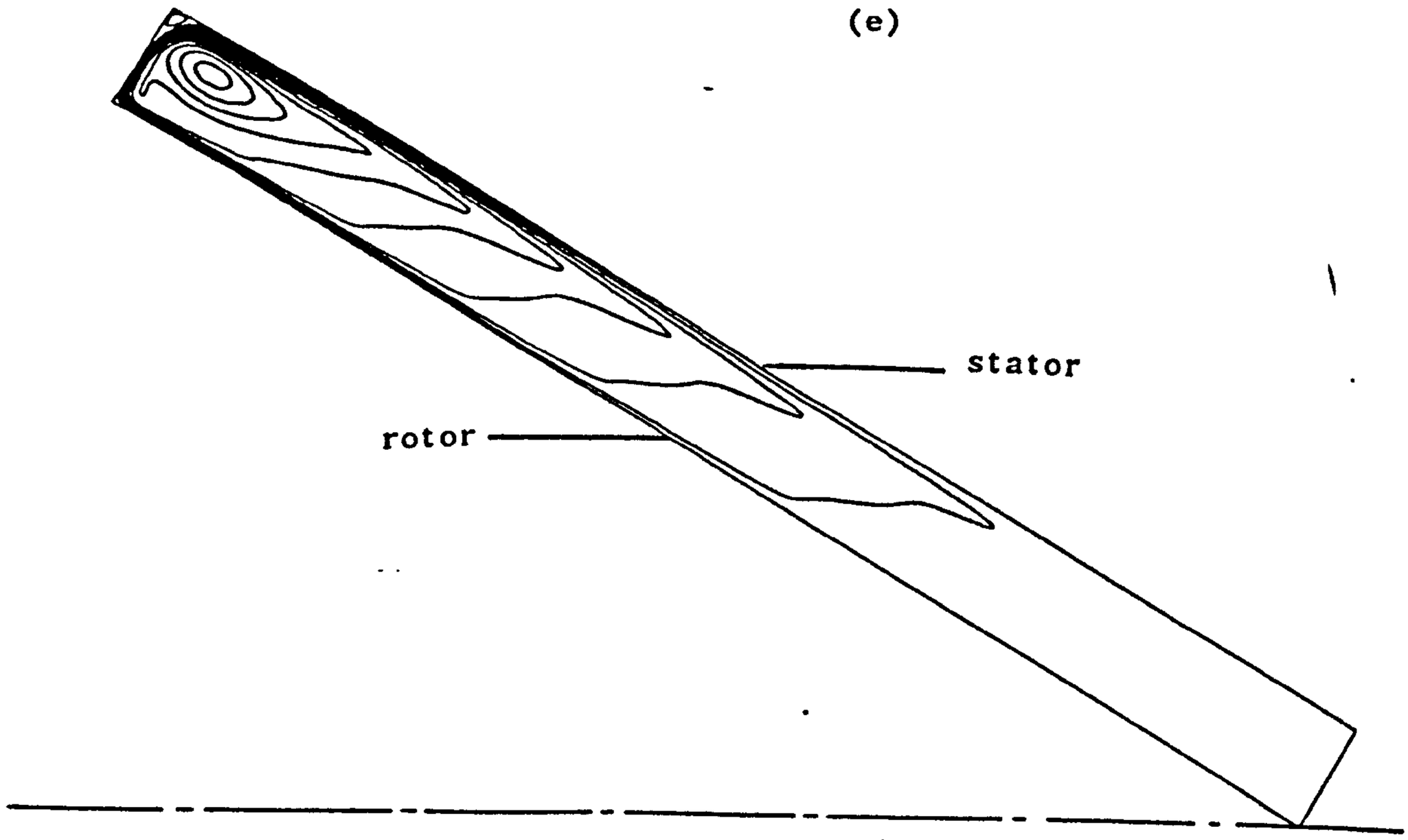

(f)

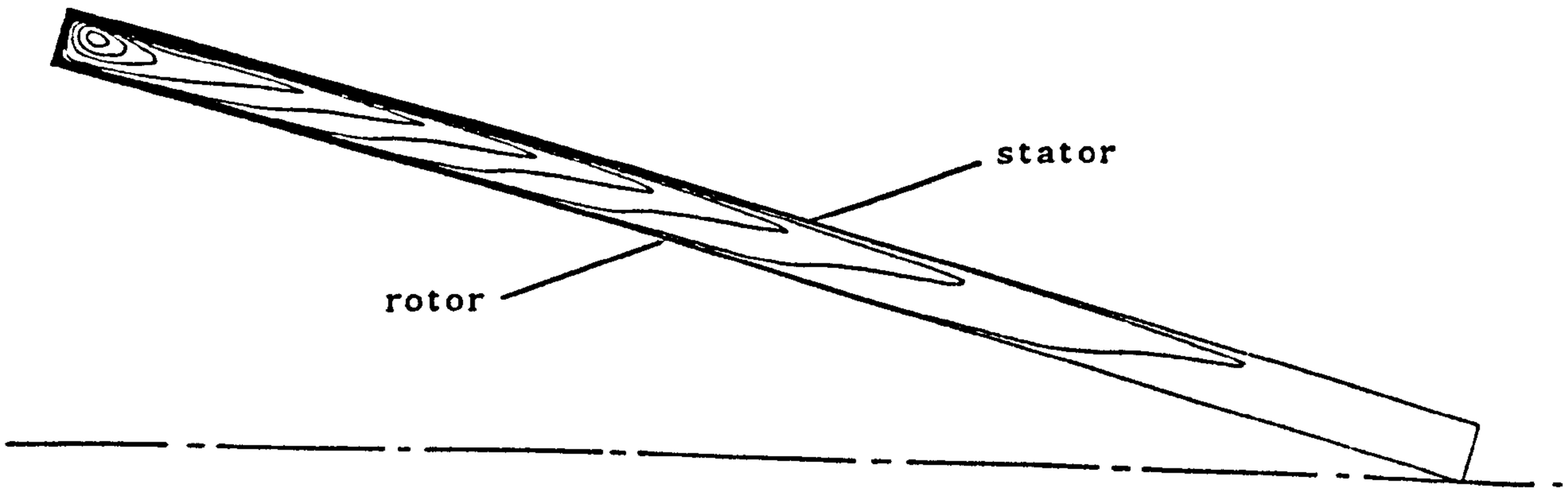

Figure 6.13 Turbulent Streamline Plots;

$d/b = 0.16$, $Re = 10^6$

(a) $\lambda = 75^0$, $a/b = 0.2$, $C_q = 6000$

(b) $\lambda = 45^0$, $a/b = 0$, $C_q = 1500$

(a)

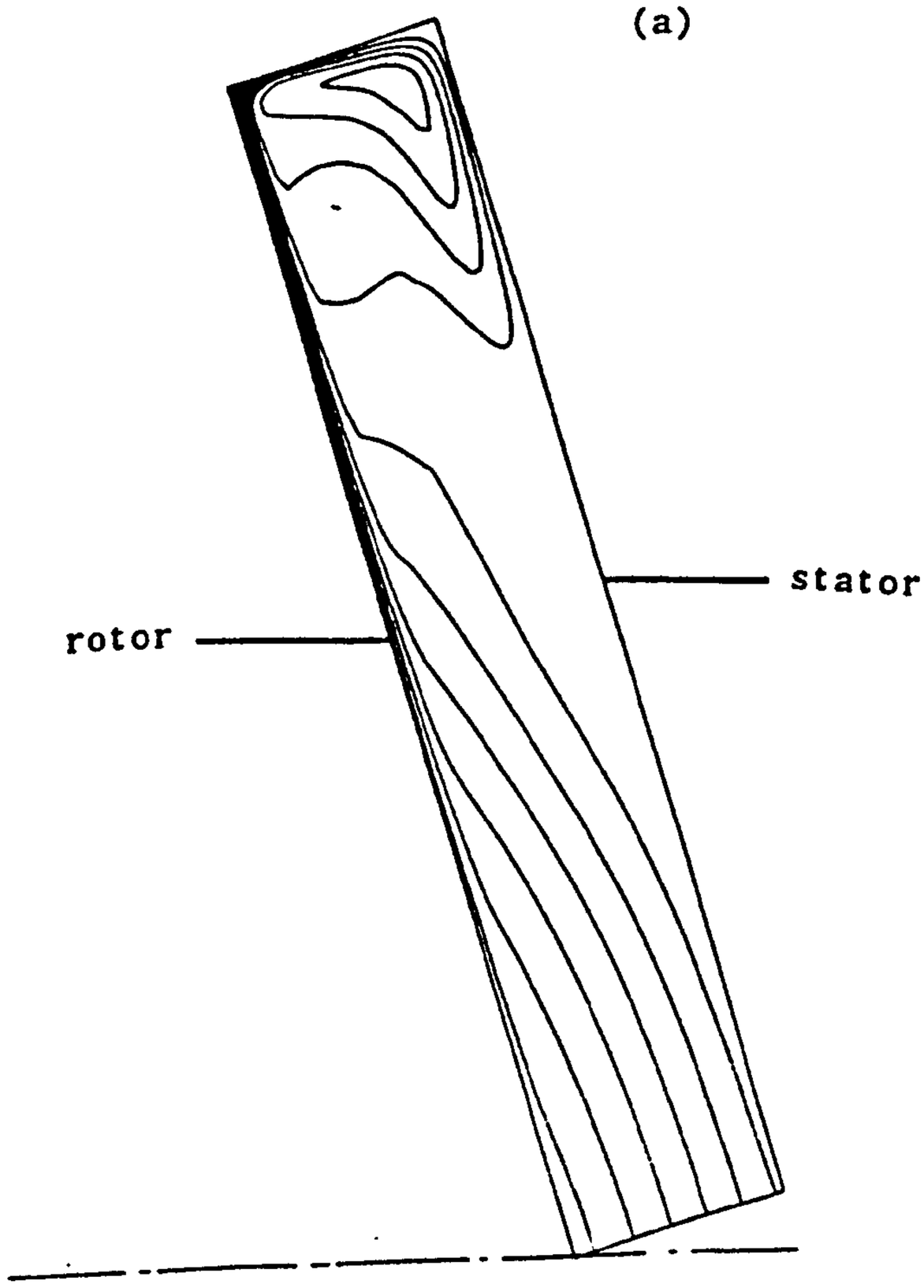

(b)

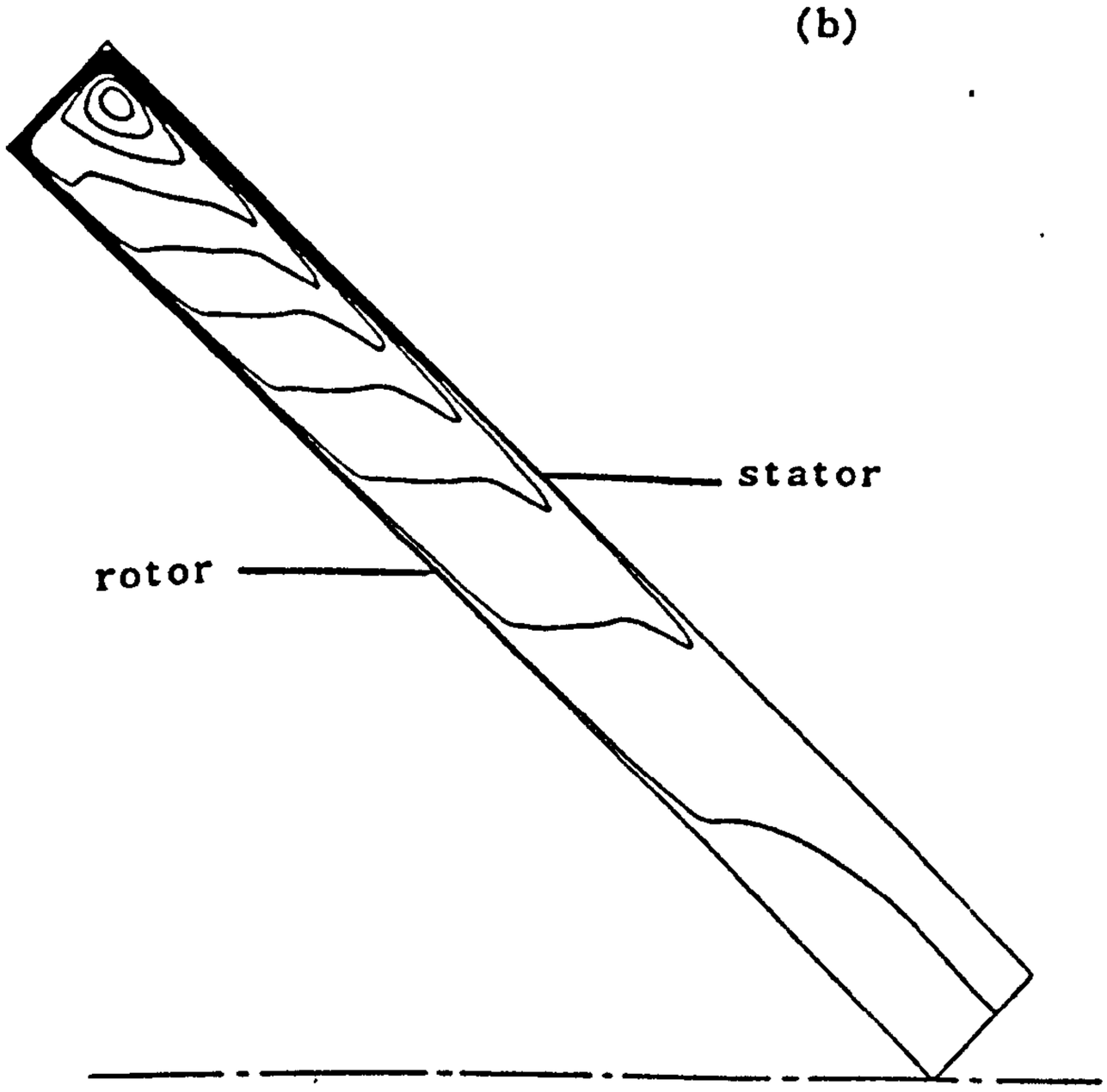

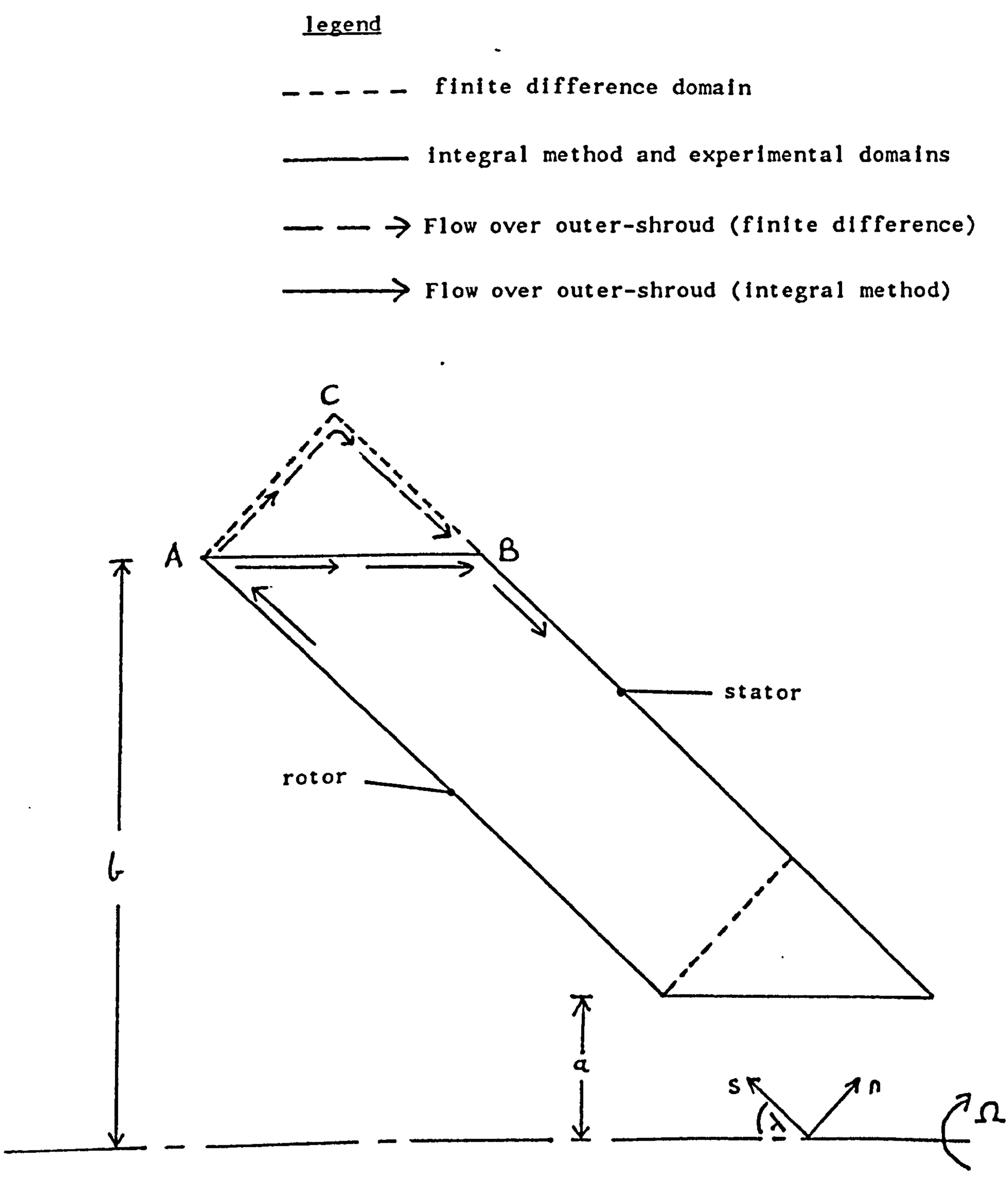

Figure 6.14 Finite Difference Solution Domain Super-imposed over the Integral Method and Experimental Domains

Radial velocity profiles across the cavity at $r_o/b=0.5$;
$Cq=0$, $a/b=0$, $d/b=0.16$, $Re=10^6$

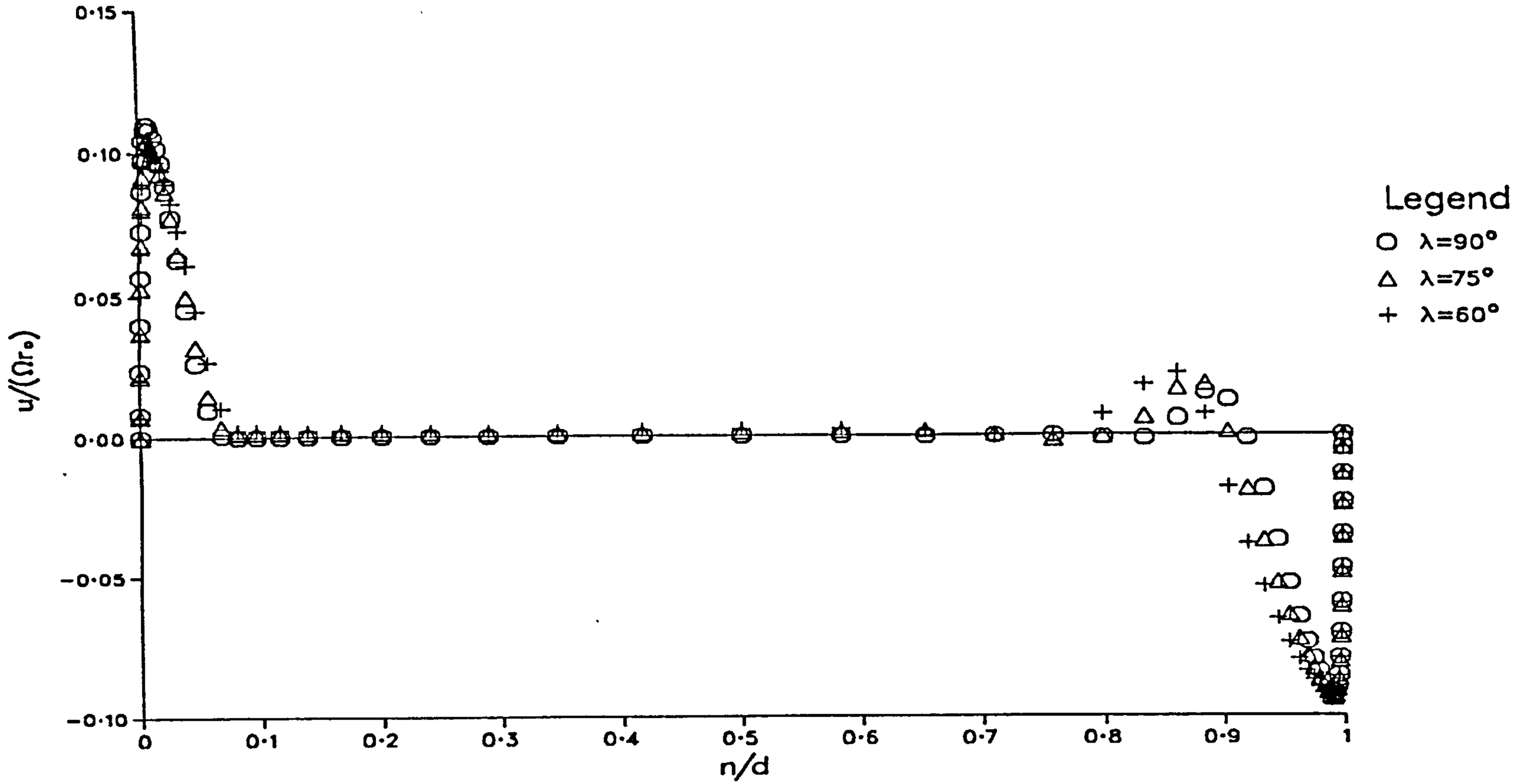

Figure 7.1(a)

Radial velocity profiles across the cavity at $r_o/b=0.5$;
$Cq=0$, $a/b=0$, $d/b=0.16$, $Re=10^6$

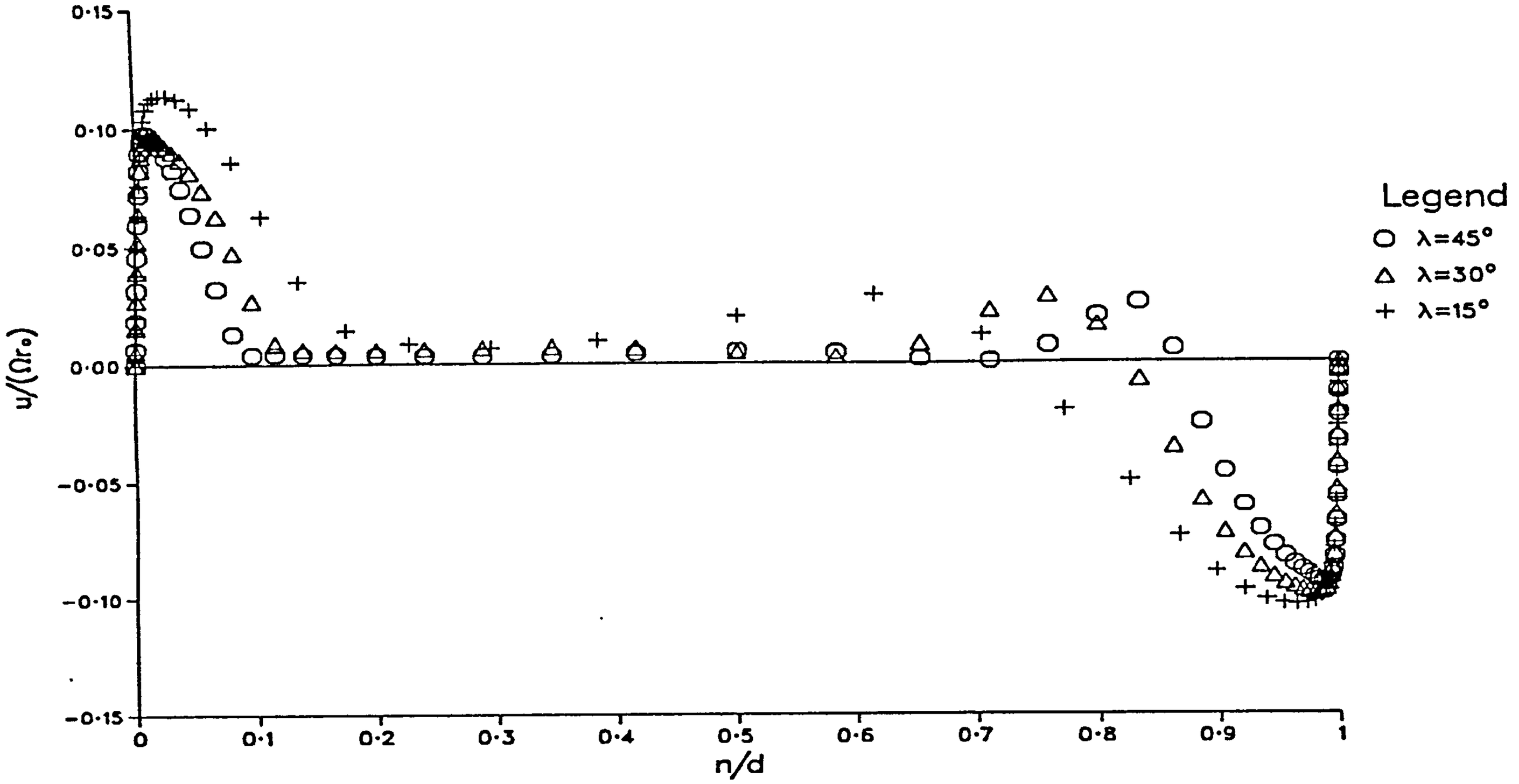

Figure 7.1(b)

Tangential velocity profiles across the cavity at $r_o/b=0.5$;
$Cq=0$, $a/b=0$, $d/b=0.16$ and $Re=10^6$

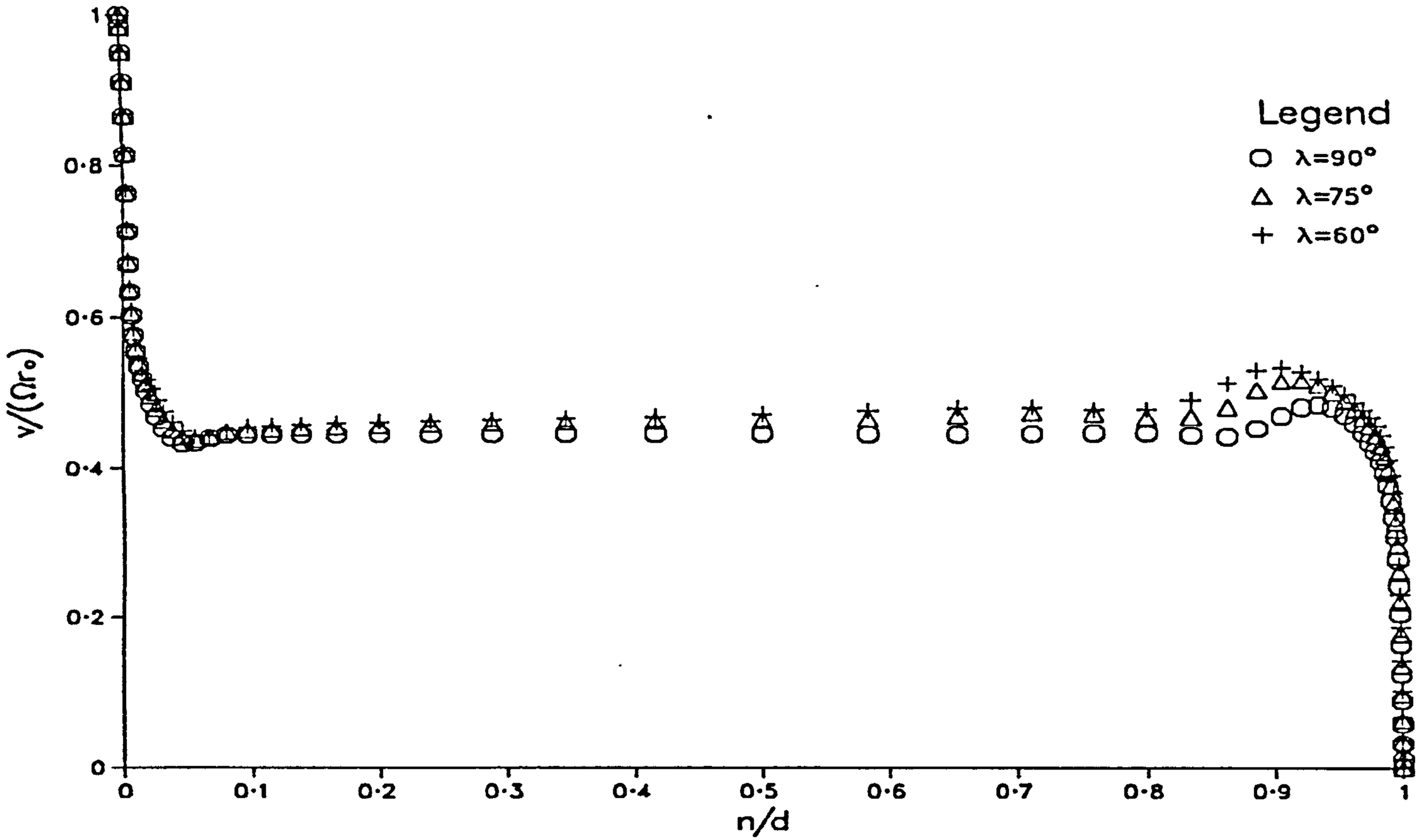

Figure 7.2(a)

Tangential velocity profiles across the cavity at $r_o/b=0.5$;
$Cq=0$, $a/b=0$, $d/b=0.16$ and $Re=10^6$

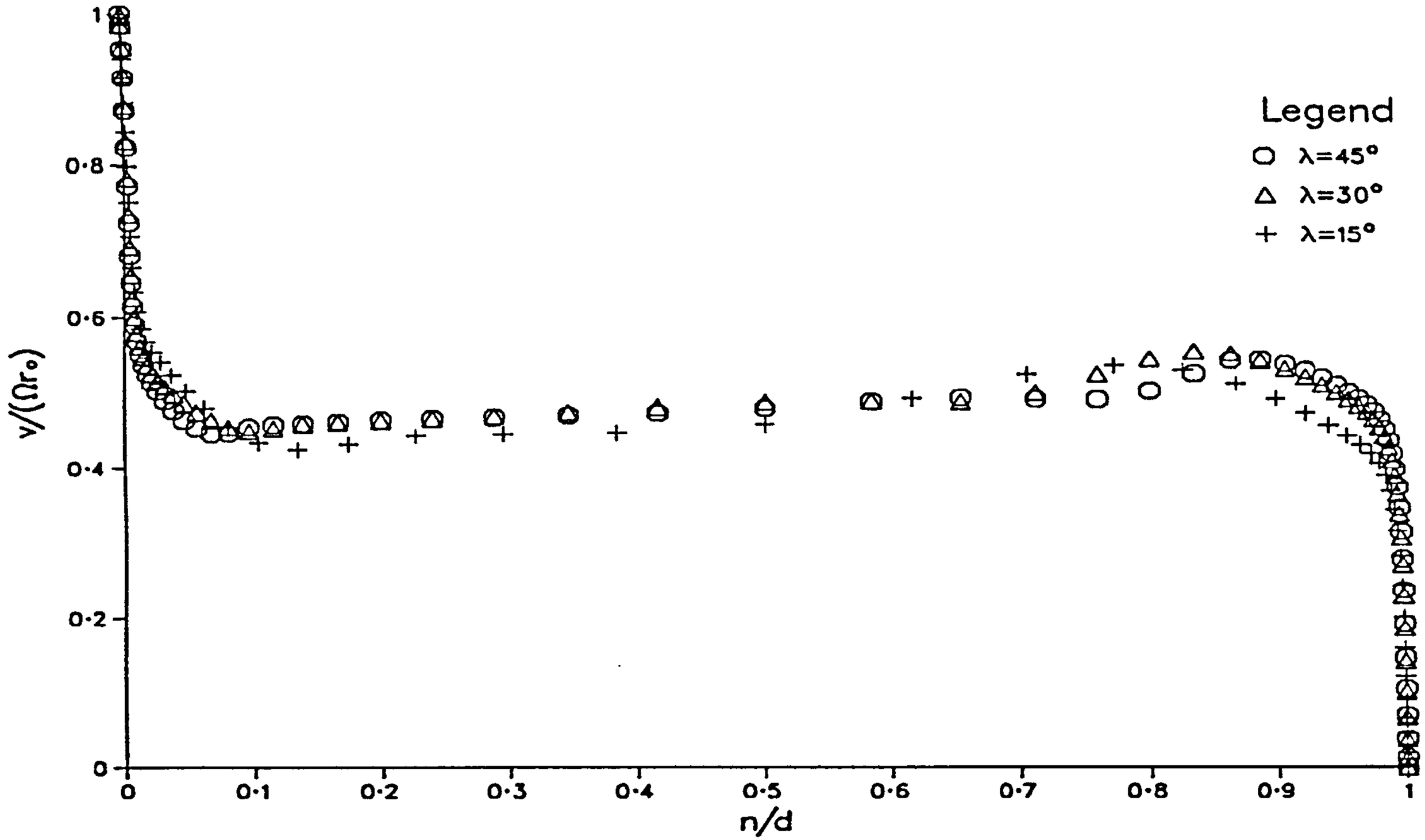

Figure 7.2(b)

Tangential velocity profiles across the cavity at constant r (=s sinλ+n cosλ); r/b=0.8, Cq=0, a/b=0, d/b=0.16 and Re=10^6.

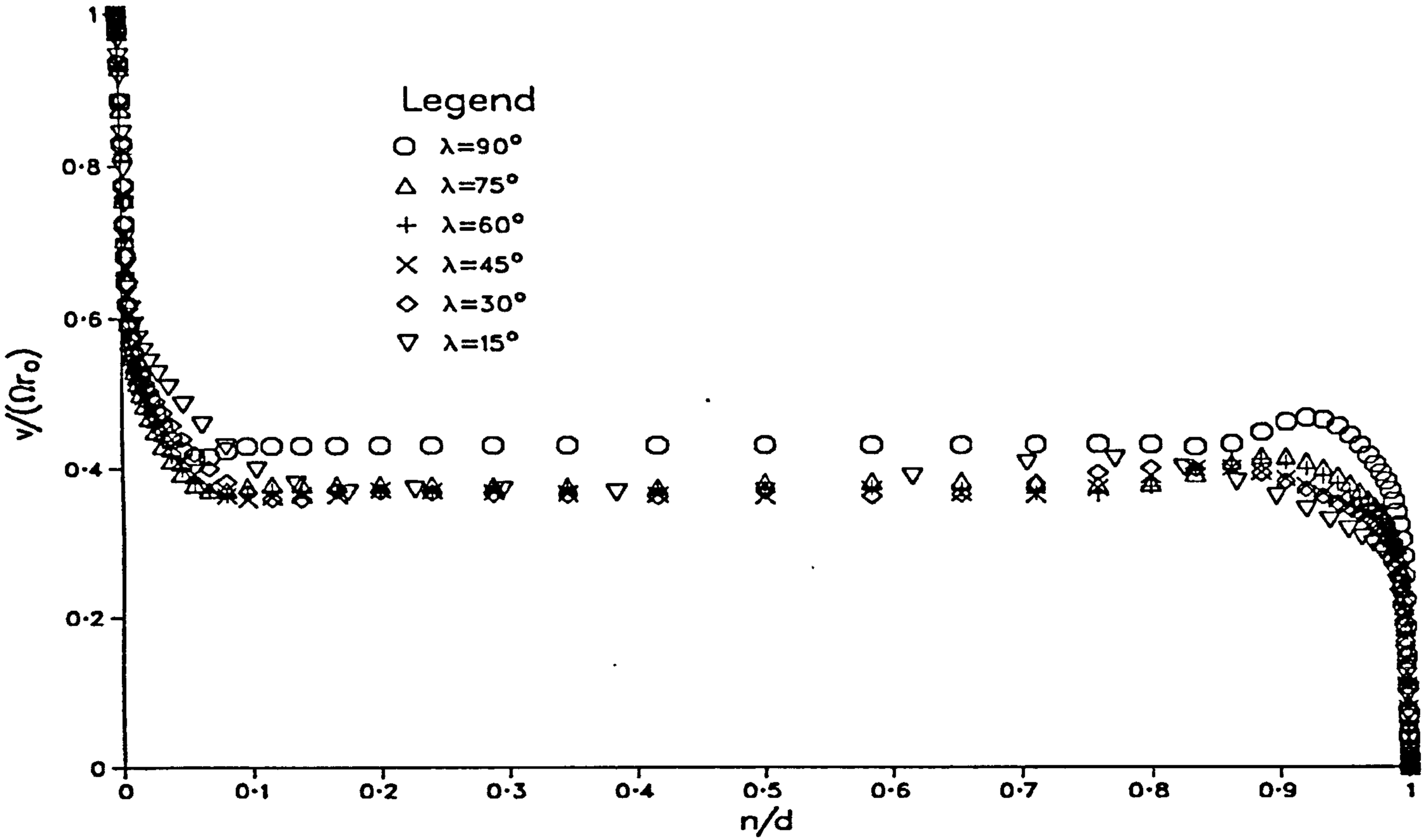

Figure 7.3

Density profiles across the cavity for an isothermal case; a/b=0, d/b=0.08, $Re_\theta=4*10^6$ and $\lambda=60^\circ$.

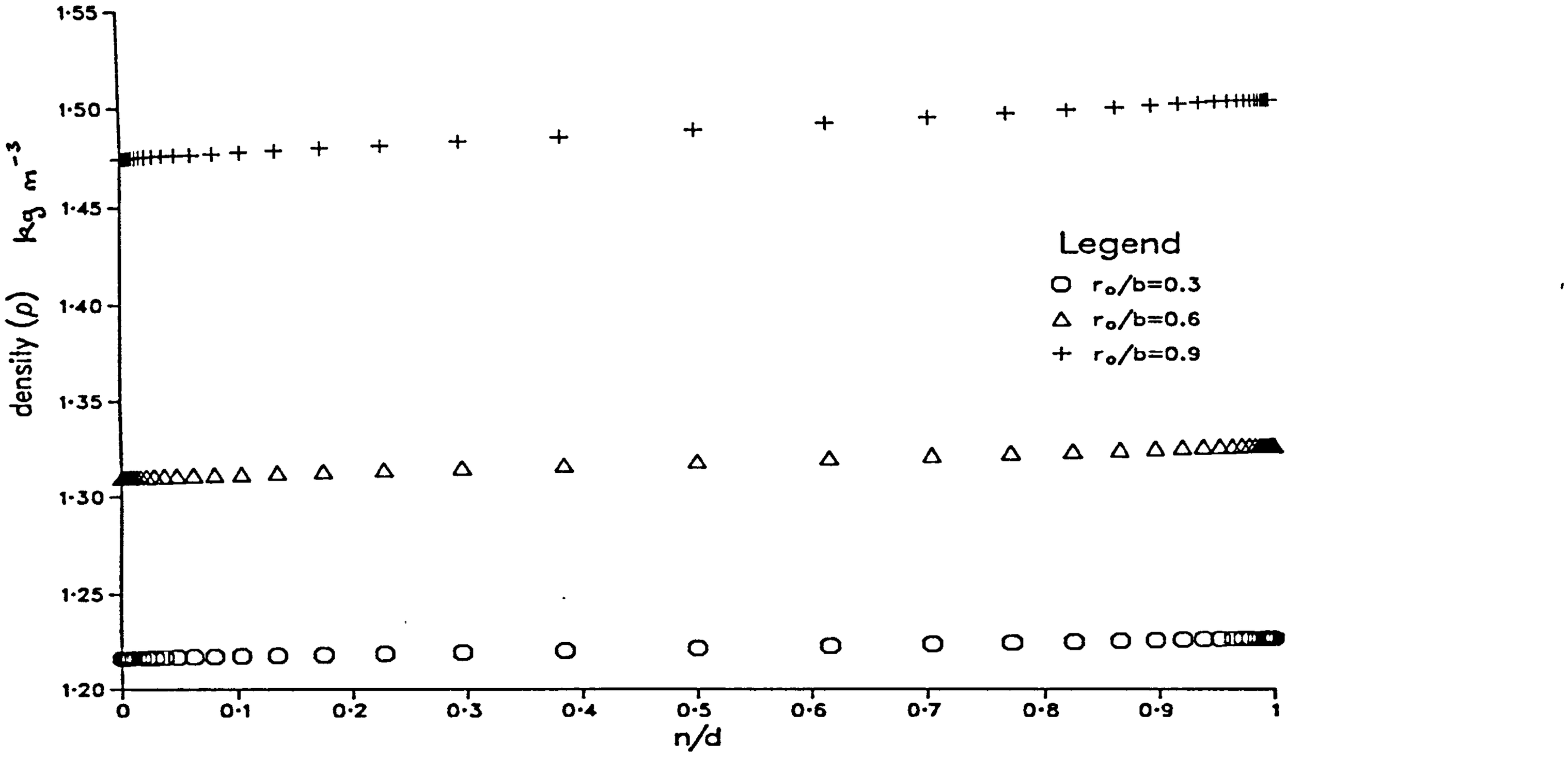

Figure 7.4(a)

Density profiles longitudinally through the rotor boundary layer for an isothermal case; a/b=0, d/b=0.08, $Re_\theta=4*10^6$ and $\lambda=60^\circ$.

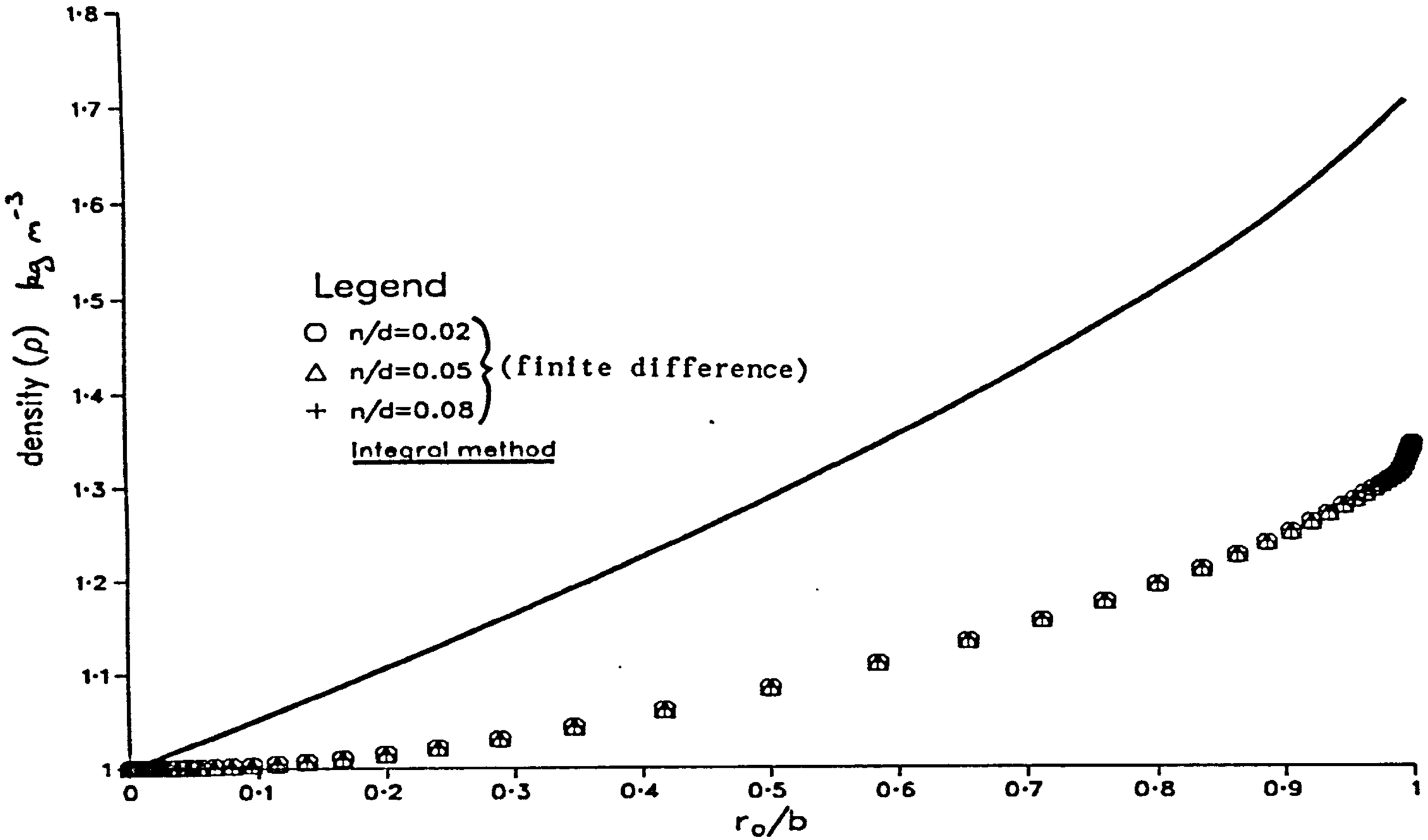

Figure 7.4(b)

Comparison of the predicted surface shear stress on the rotor
$\lambda=60^{\circ}$, Cq=0, a/b=0, d/b=0.08, $Re=4*10^{6}$

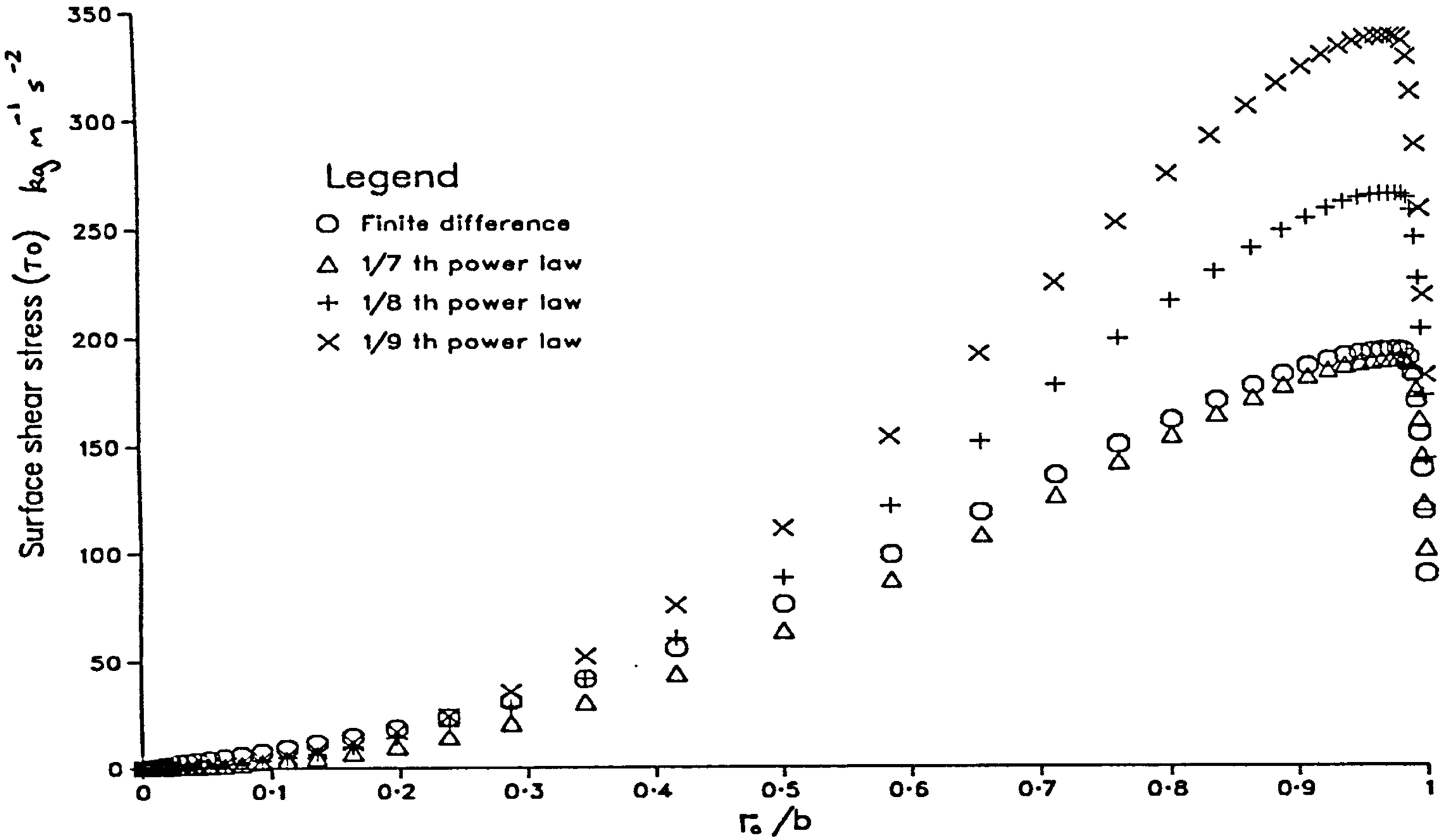

Figure 7.5(a)

Comparison of the predicted surface shear stress on the rotor
$\lambda=15^{\circ}$, Cq=750, a/b=0, d/b=0.16, $Re=10^{6}$

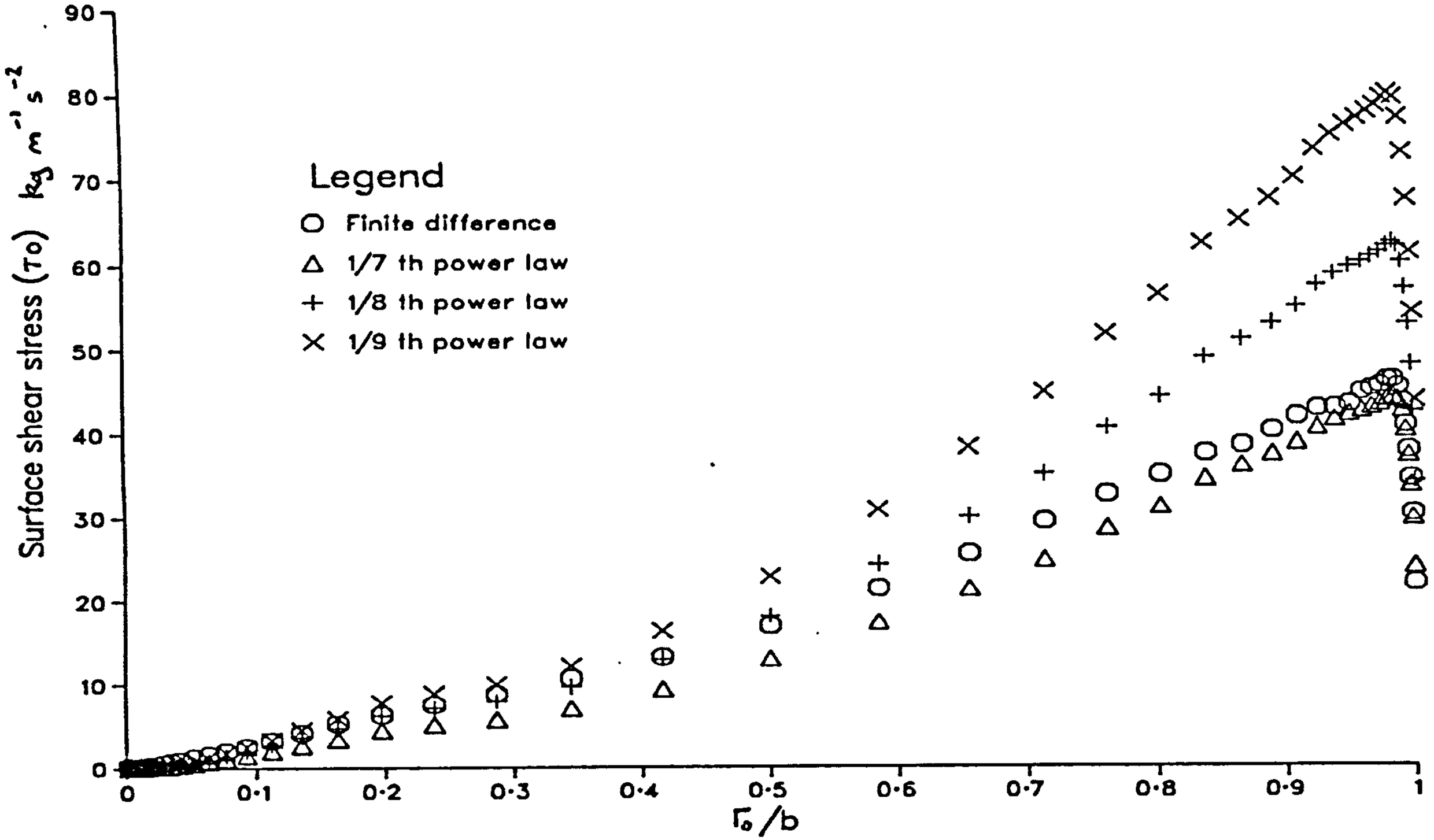

Figure 7.5(b)

Comparison of the surface shear stress on the stator
$Re=4*10^6$, $\lambda=90^\circ$, $Cq=0$, $a/b=0$, $d/b=0.08$

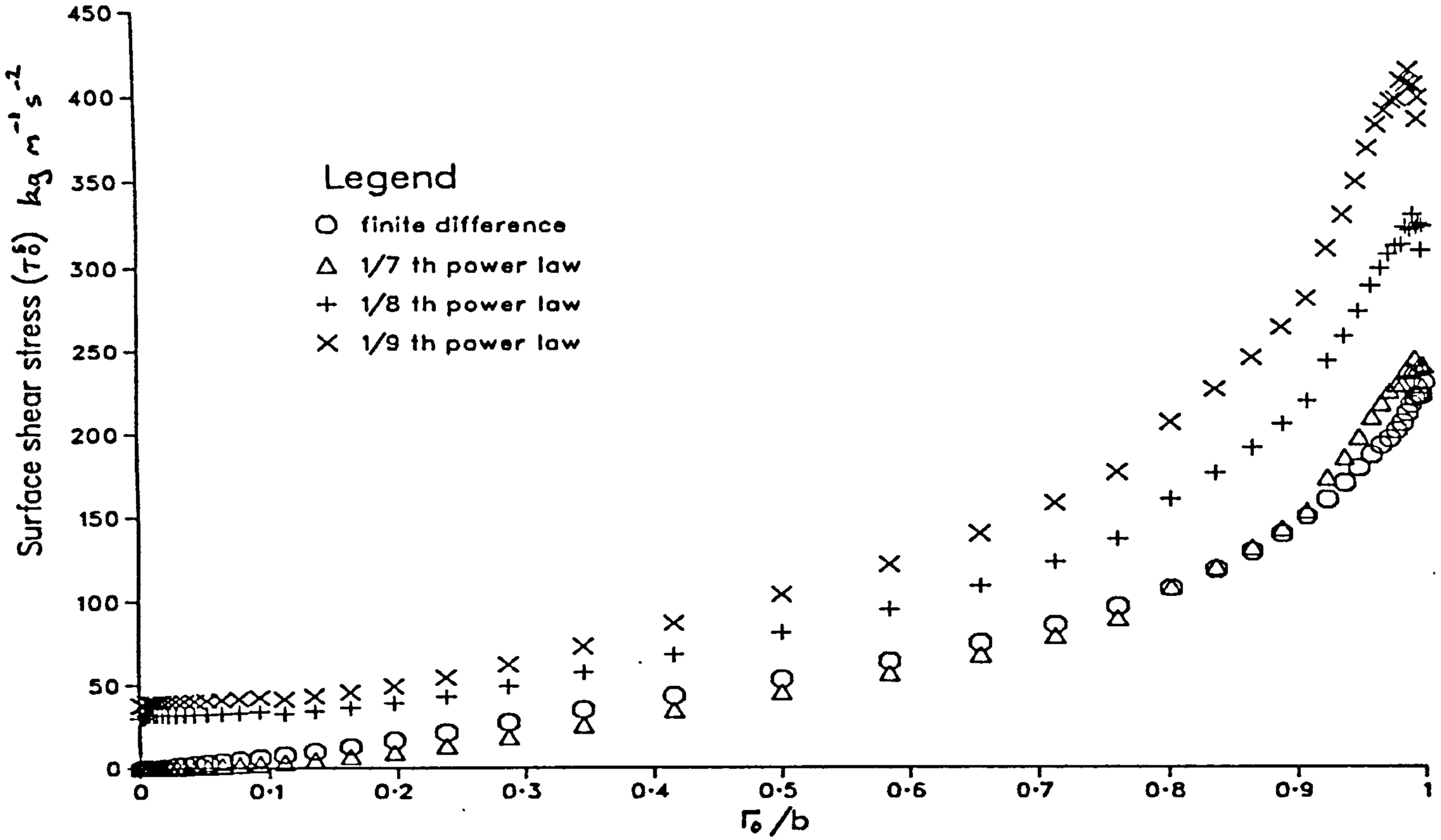

Figure 7.6(a)

Comparison of the surface shear stress on the stator
$Re=10^6$, $\lambda=15^\circ$, $Cq=3000$, $a/b=0$, $d/b=0.16$

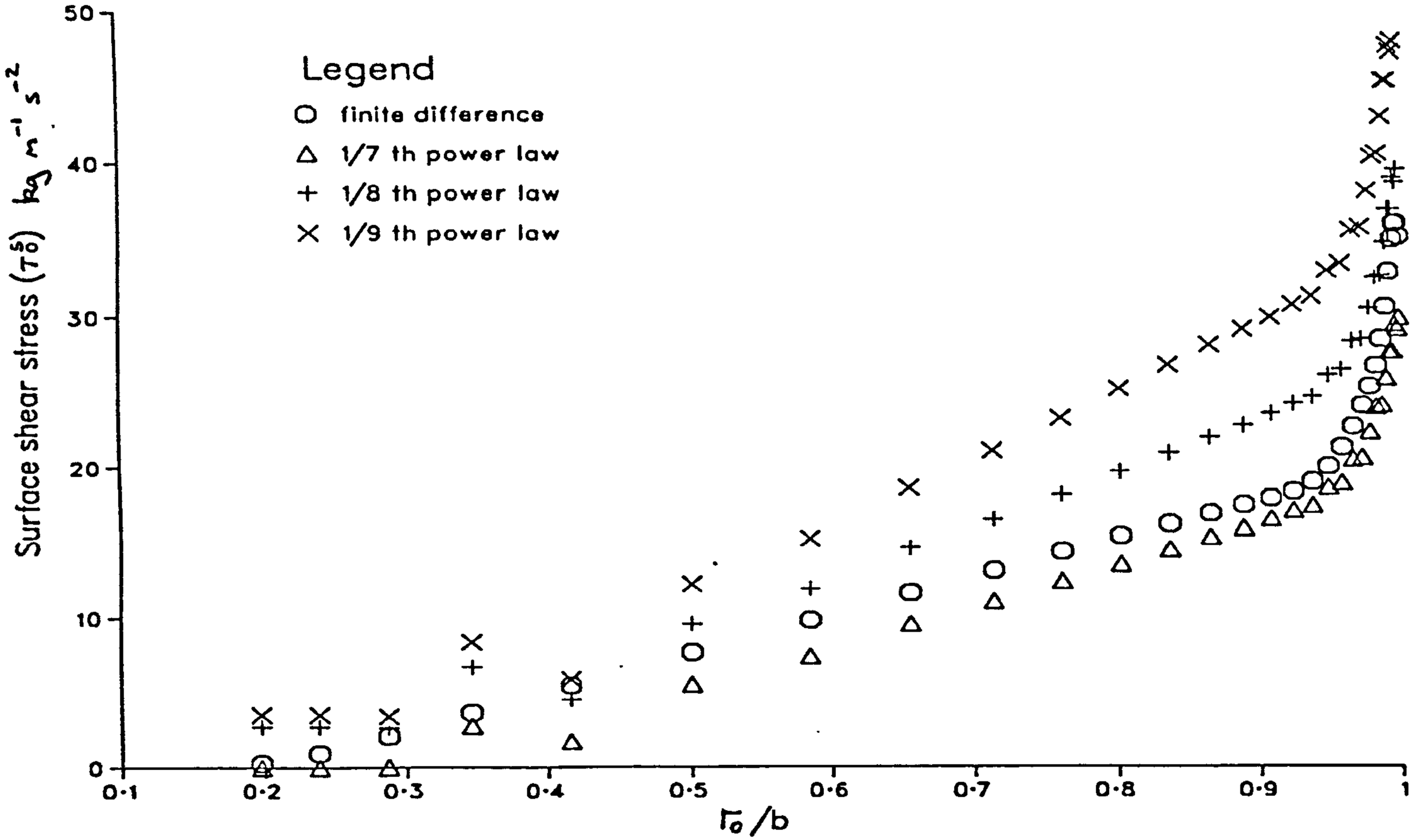

Figure 7.6(b)

Comparison of the predicted finite difference tangential velocity profiles with the 1/7th power law profiles; Cq=0, a/b=0, d/b=0.16, Re=$4*10^6$ and $\lambda=90°$.

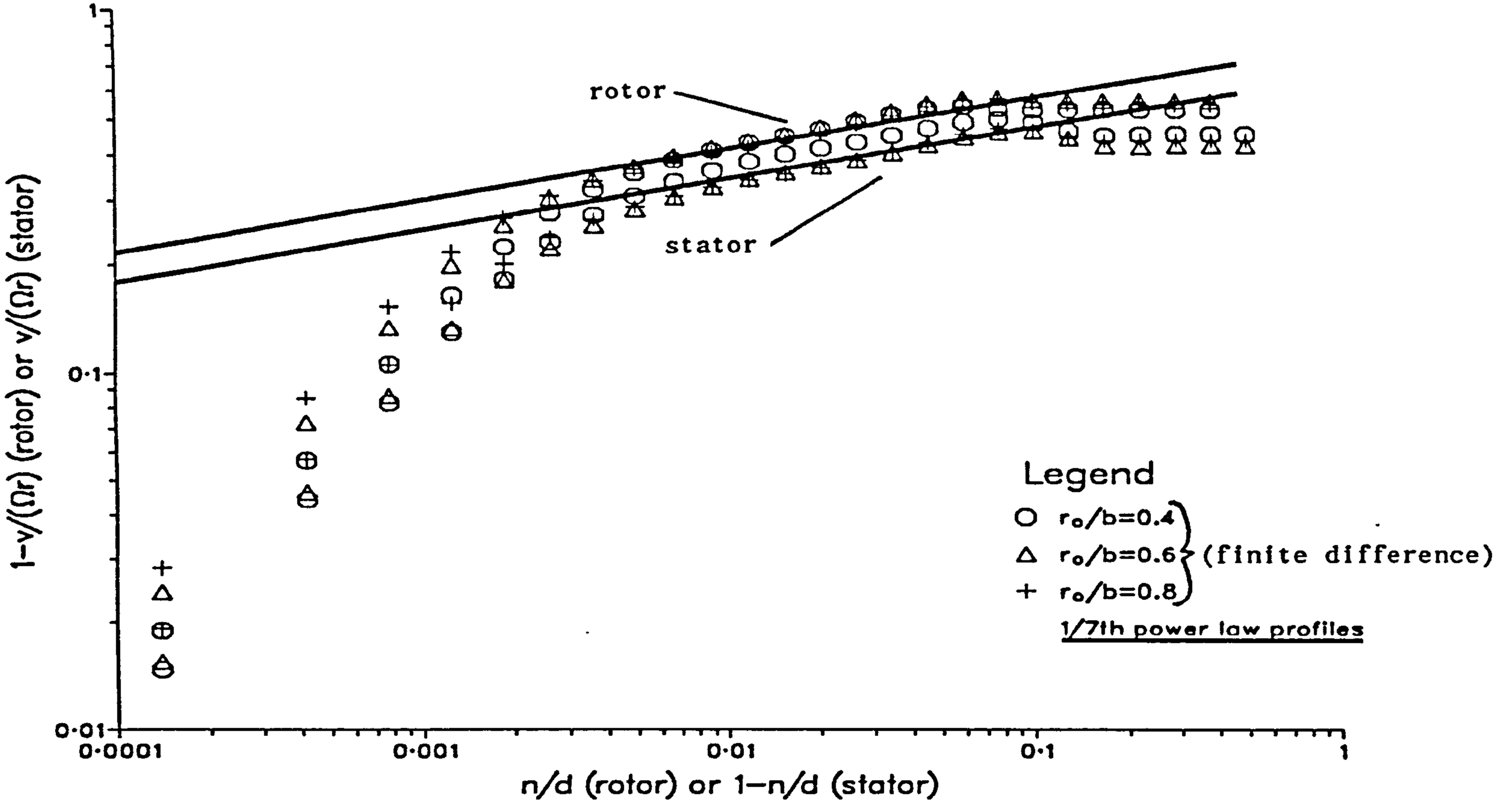

Figure 7.7(a)

Comparison of the predicted finite difference tangential velocity profiles with the 1/7th power law profiles; Cq=0, a/b=0, d/b=0.16, Re=4*10^6 and λ=60°.

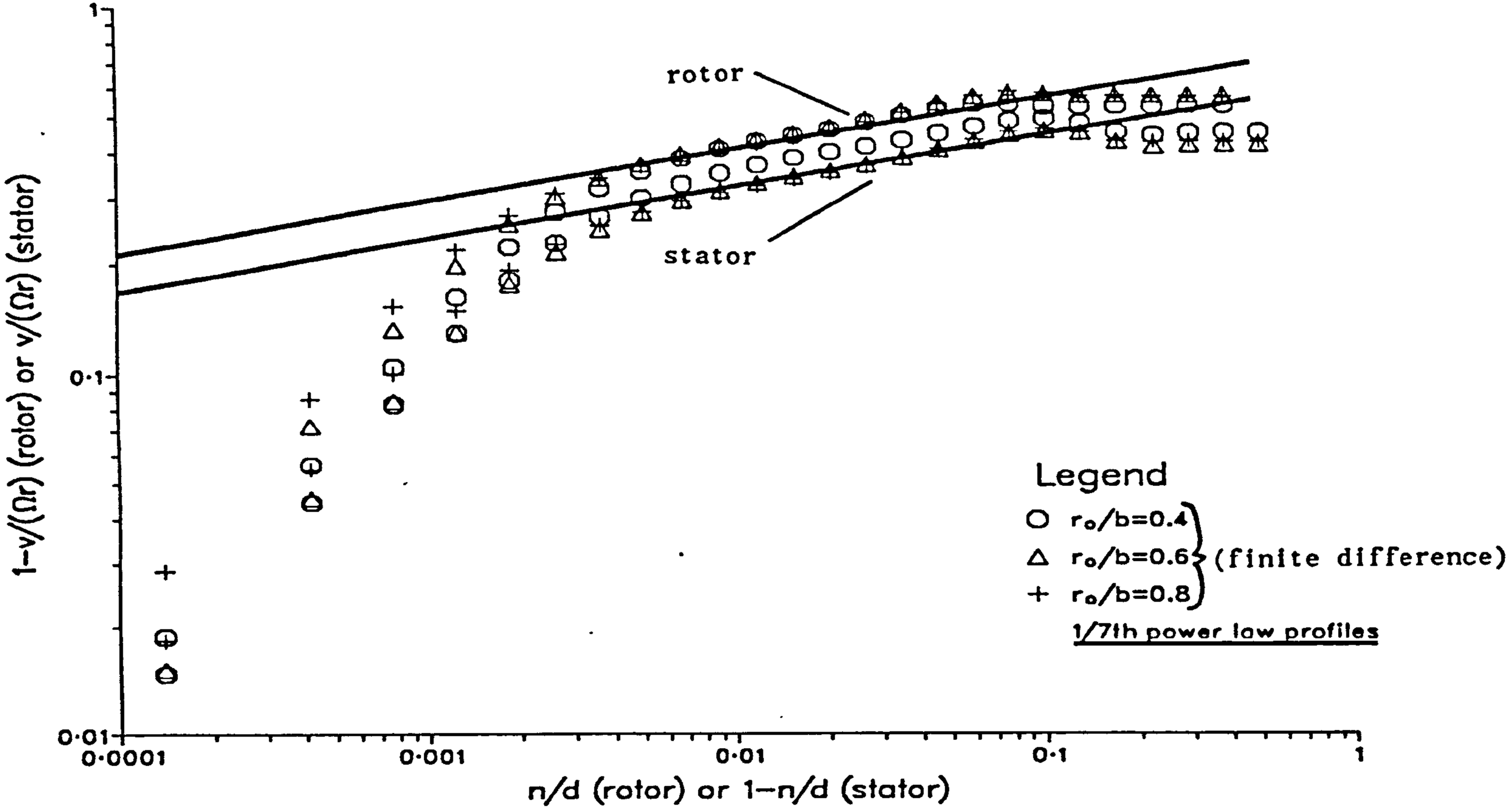

Figure 7.7(b)

Comparison of the predicted finite difference tangential velocity profiles with the 1/7th power law profiles; Cq=0, a/b=0, d/b=0.16, Re=$4*10^6$ and $\lambda=30°$.

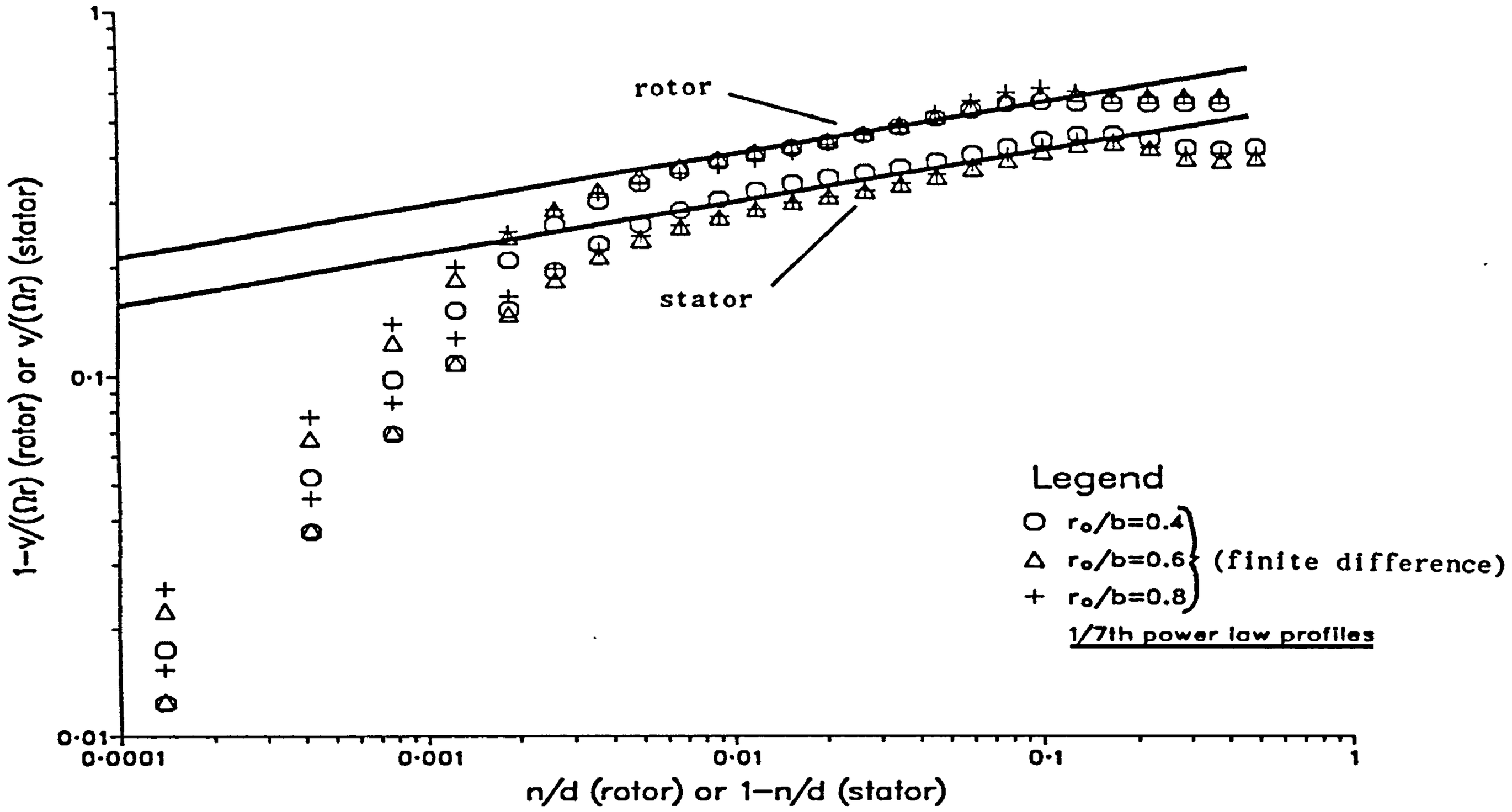

Figure 7.7(c)

Comparison of the predicted finite difference tangential velocity profiles with the 1/7th power law profiles; Cq=0, a/b=0, d/b=0.16, Re=10^6 and $\lambda=15°$.

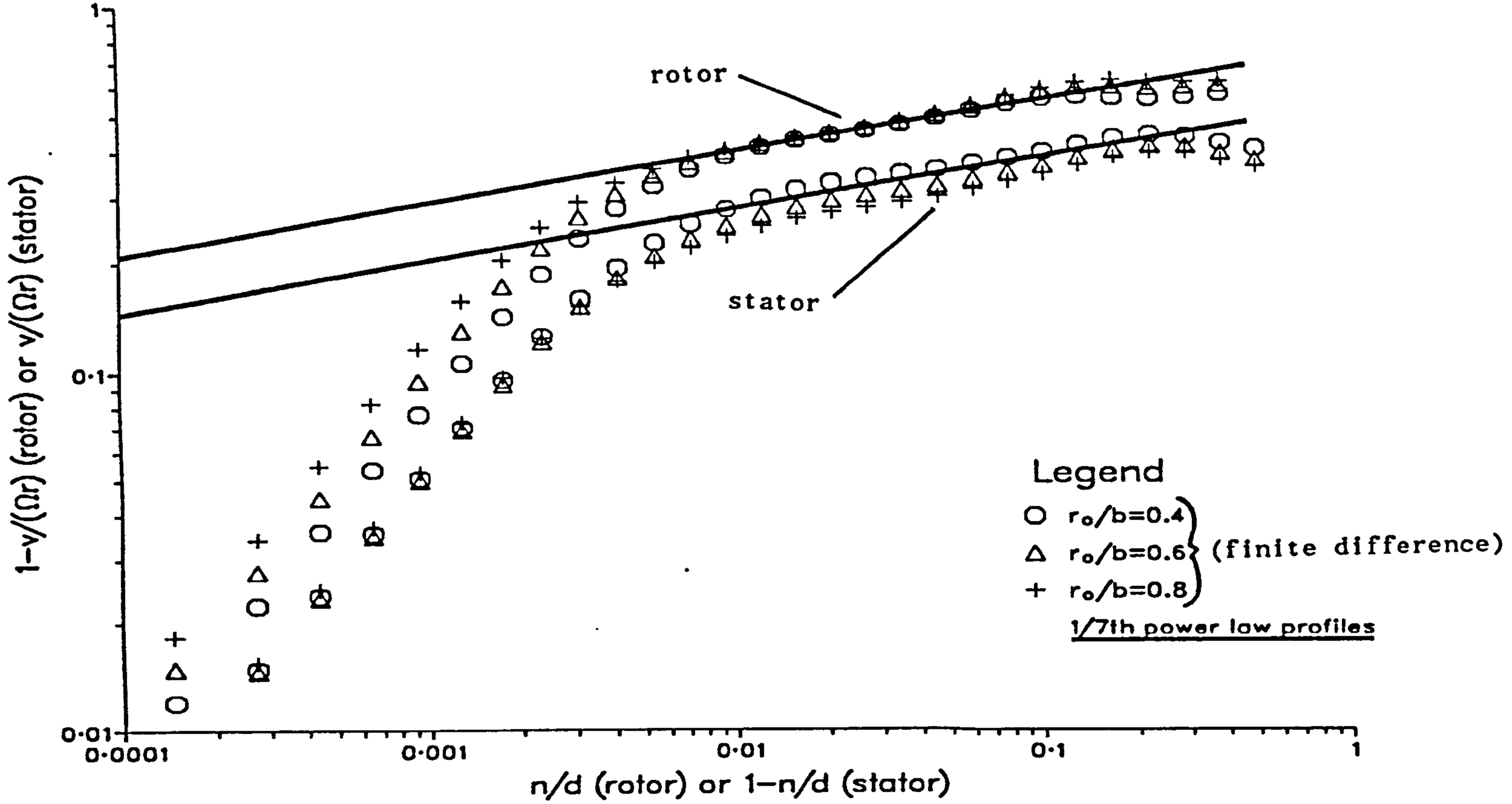

Figure 7.7(d)

Radial velocity profiles across the rotor boundary layer;
$\lambda=90°$, $Cq=0$, $a/b=0$, $d/b=0.16$, and $Re=10^6$

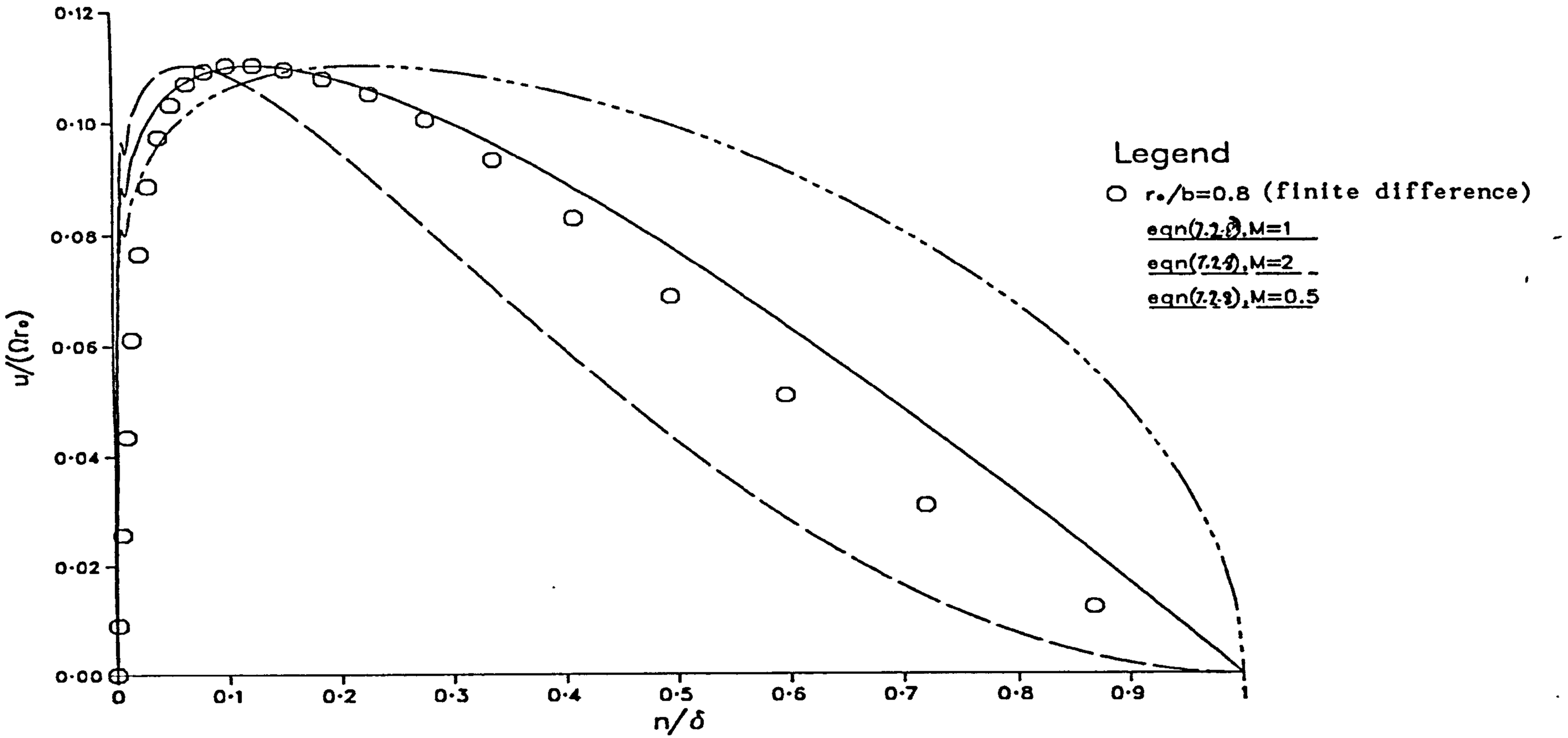

Figure 7.8(a)

Radial velocity profiles across the rotor boundary layer;
$\lambda=60°$, $Cq=0$, $a/b=0$, $d/b=0.16$, and $Re=10^6$

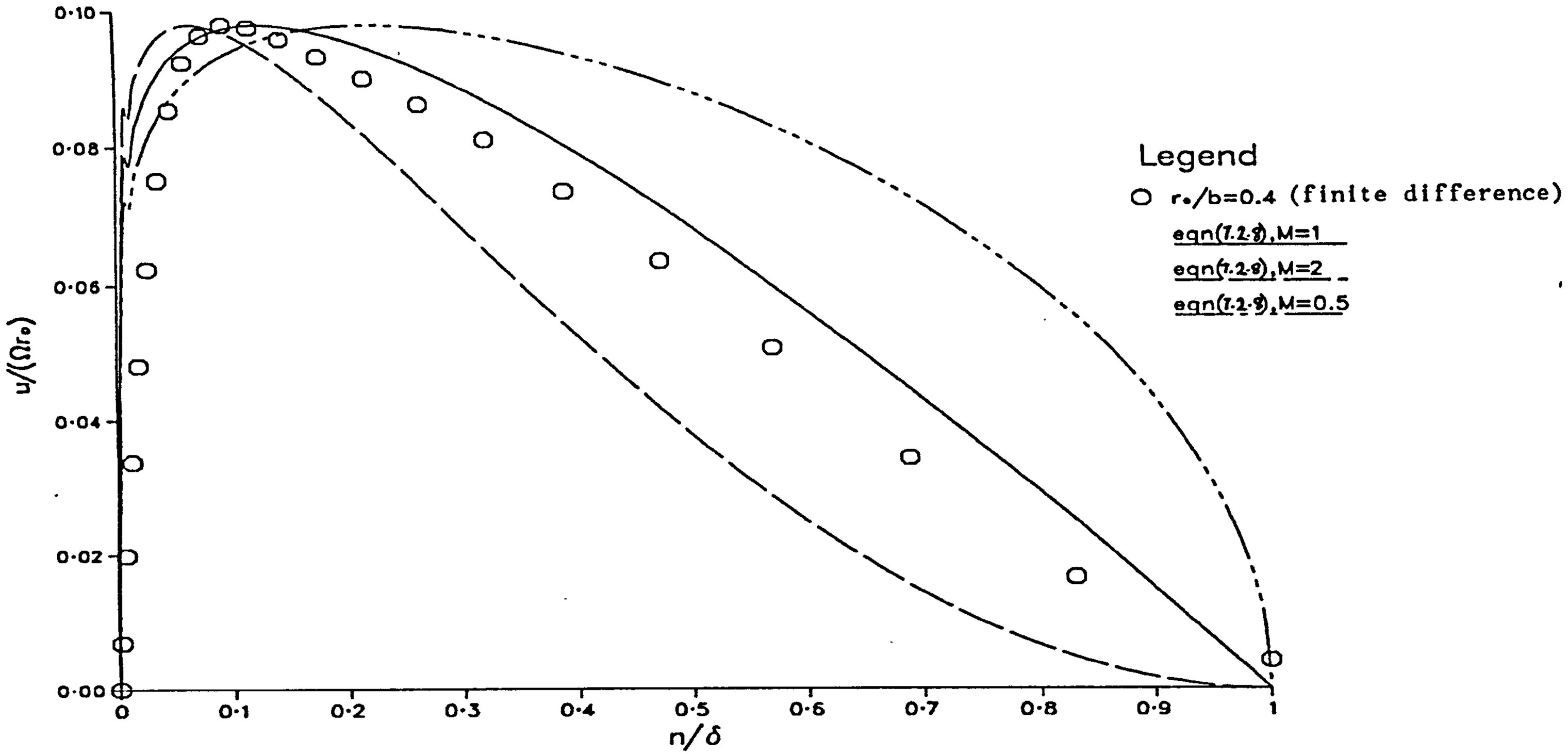

Figure 7.8(b)

Radial velocity profiles across the rotor boundary layer;
$\lambda=30°$, $Cq=0$, $a/b=0$, $d/b=0.16$, and $Re=10^6$

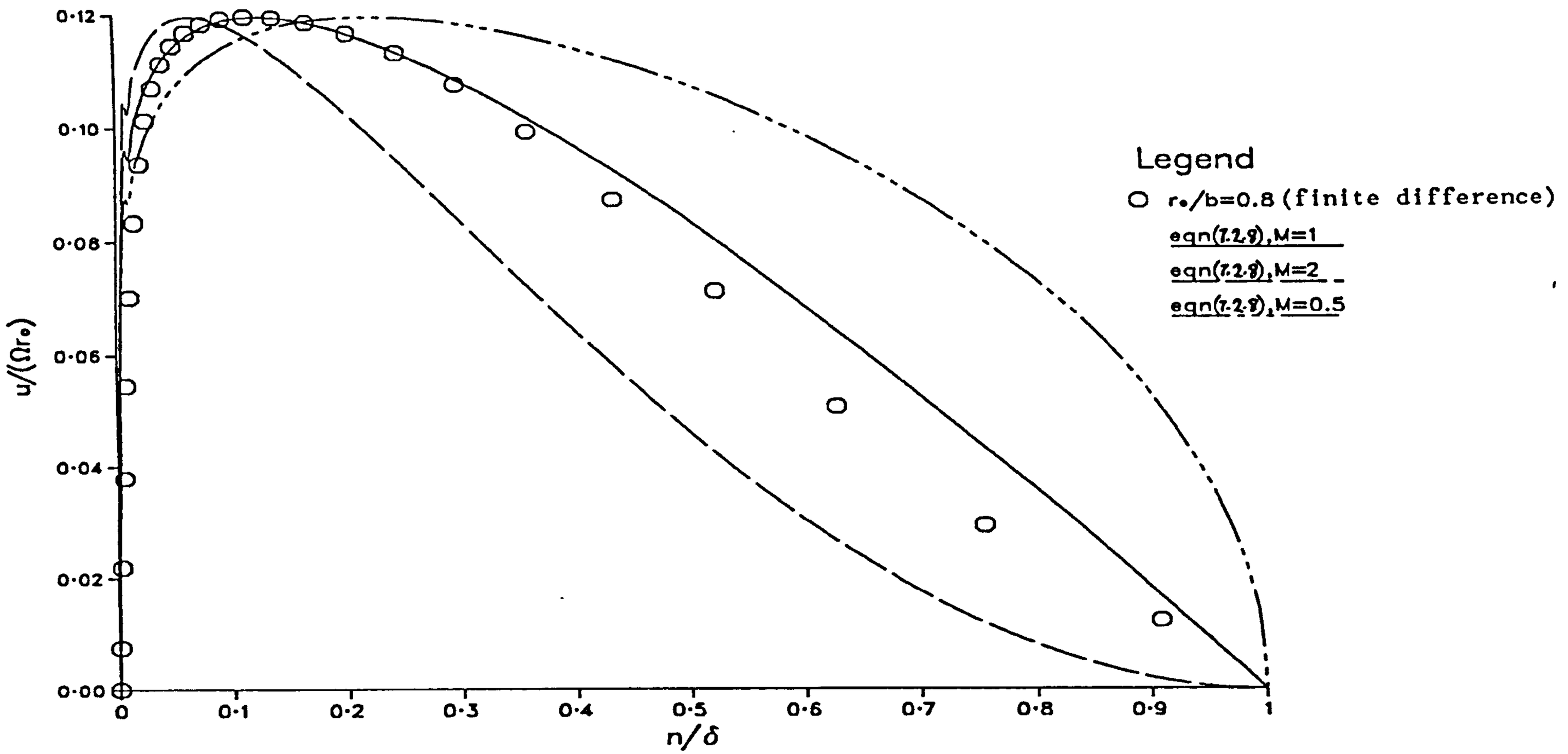

Figure 7.8(c)

Radial velocity profiles across the rotor boundary layer;
$\lambda=15°$, $Cq=6000$, $a/b=0$, $d/b=0.16$, and $Re=10^6$

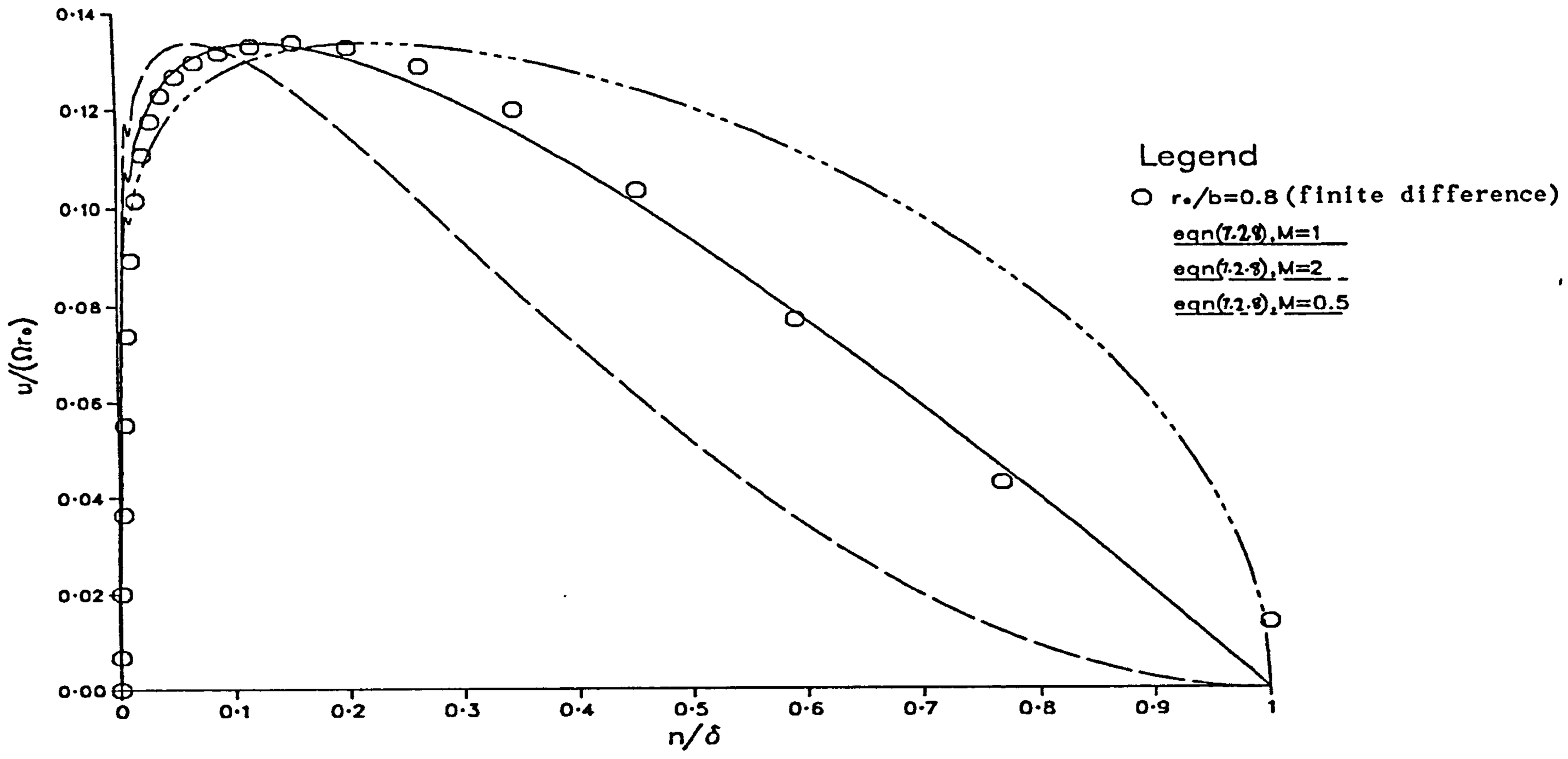

Figure 7.8(d)

Finite difference predictions for the tangential velocity at n=d/2; Cq=0, a/b=0, d/b=0.24 and Re=10^6.

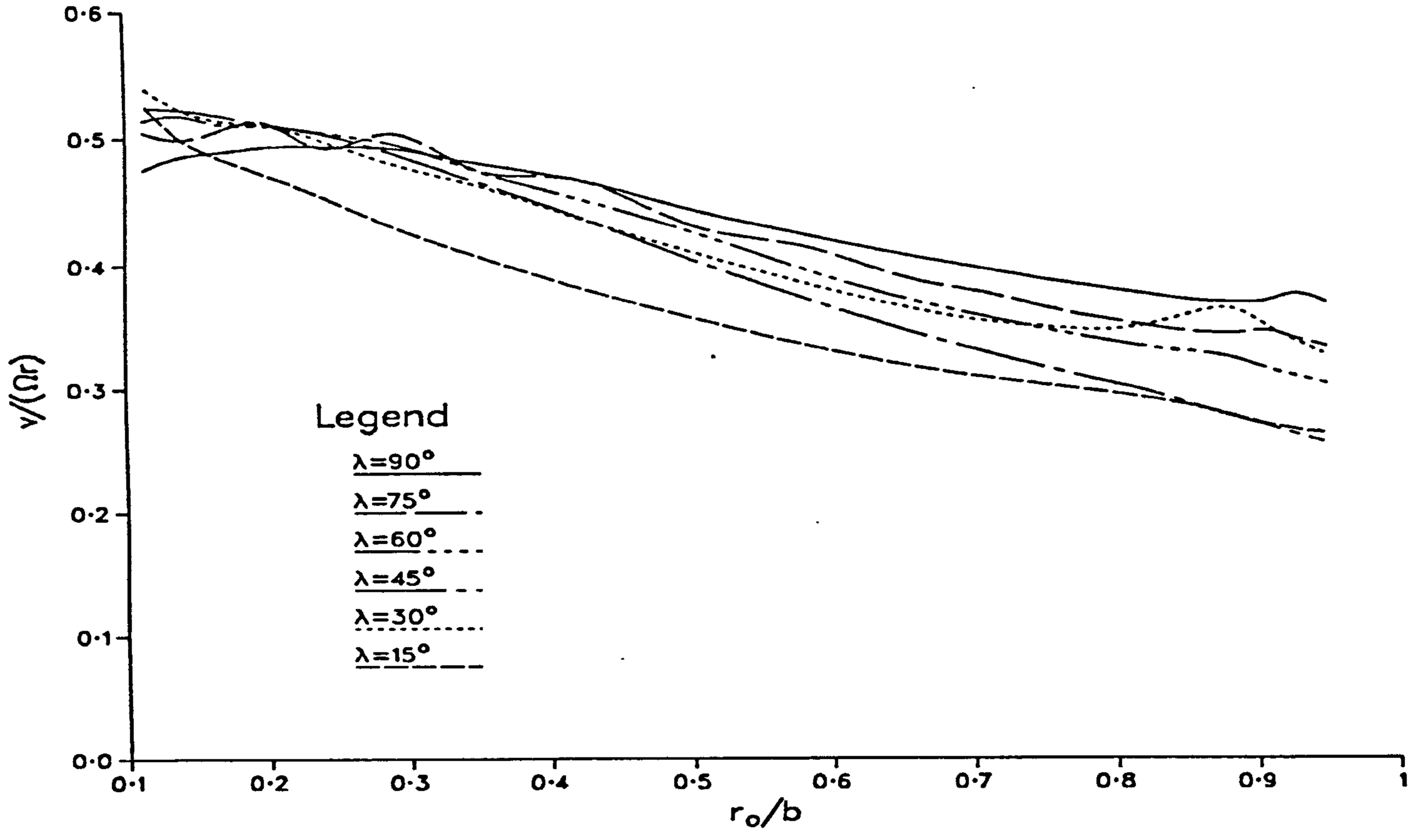

Figure 7.9(a)

Finite difference predictions for the tangential velocity at n=d/2; Cq=0, a/b=0, d/b=0.16 and Re=10^6.

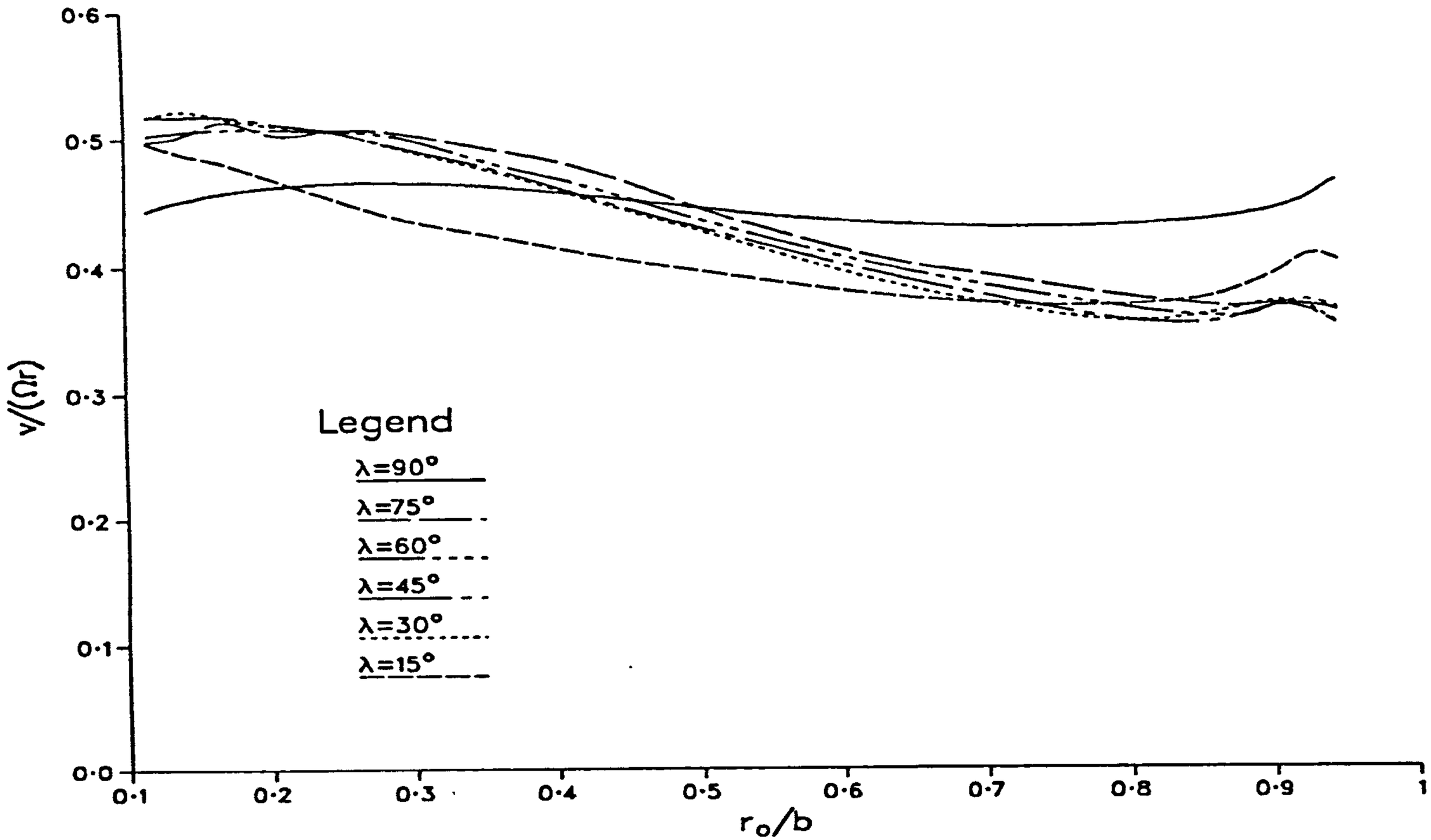

Figure 7.9(b)

Finite difference solutions for the limiting flow angle on the rotor, Cq=0, a/b=0, d/b=0.08, Re=$4*10^6$

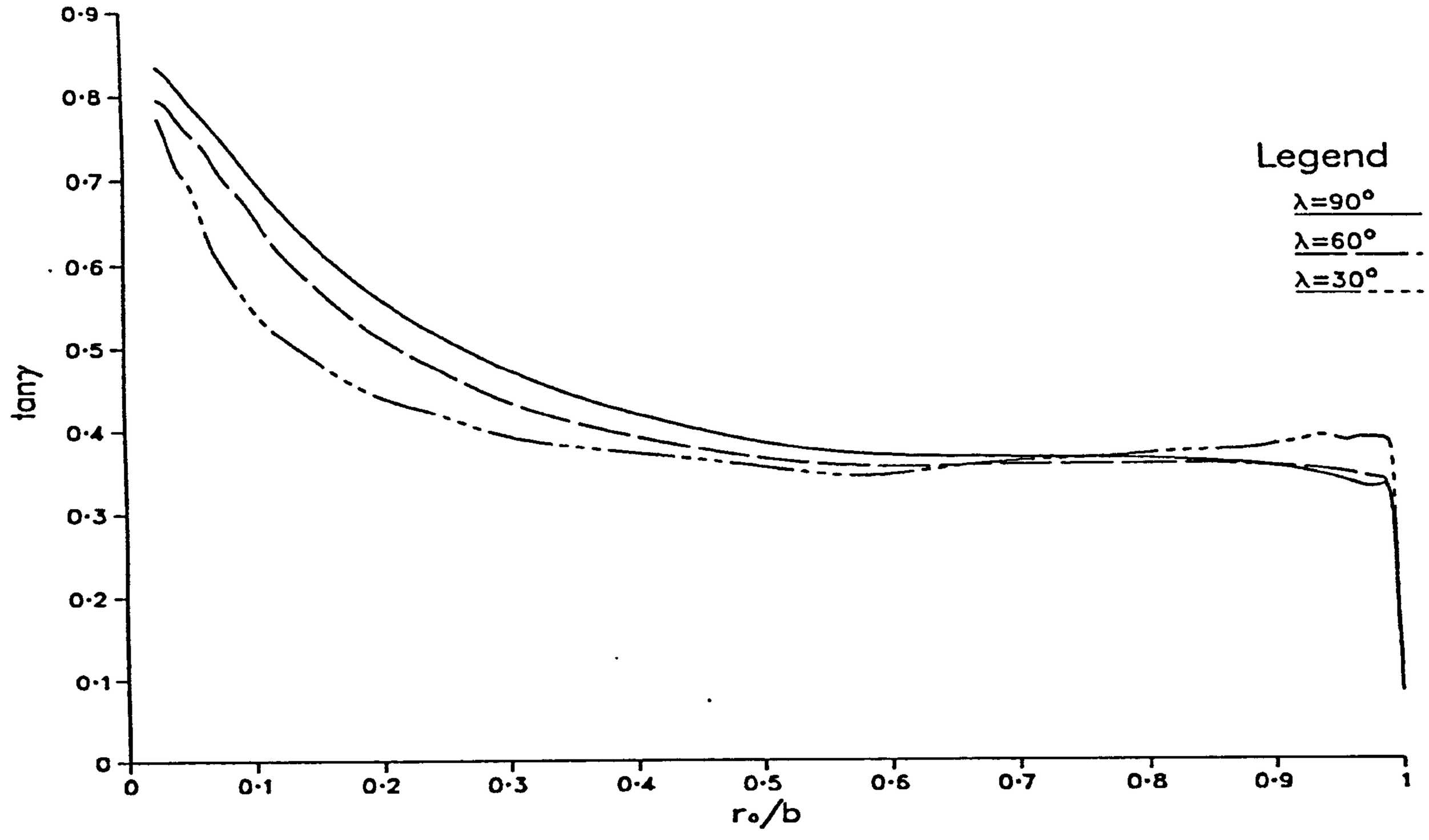

Figure 7.10(a)

Finite difference solutions for the limiting flow angle on the rotor, Cq=0, a/b=0, d/b=0.24, Re=10^6

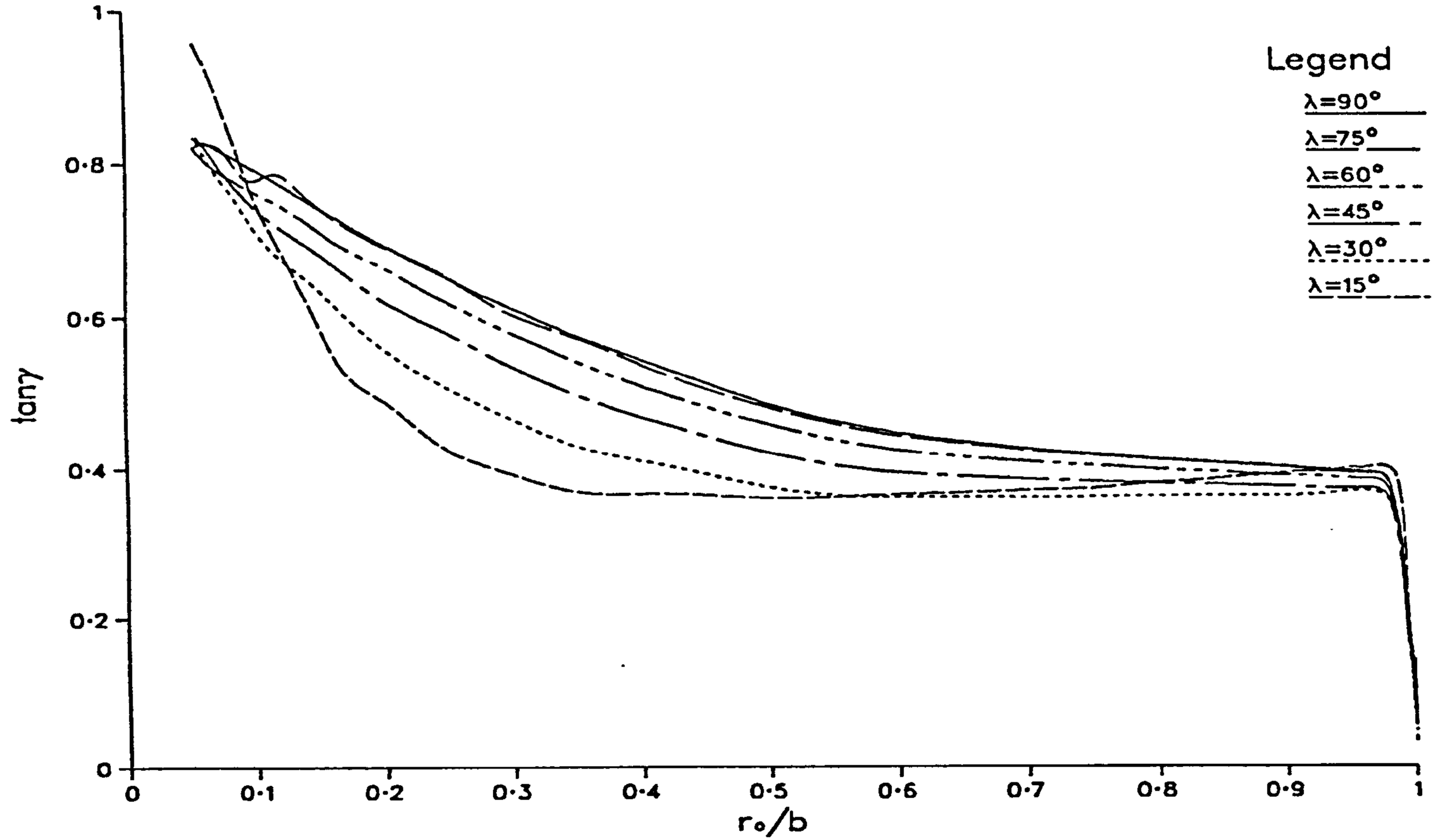

Figure 7.10(b)

Finite difference solutions for the limiting flow angle on the rotor, Cq=6000, d/b=0.16, Re=10^6

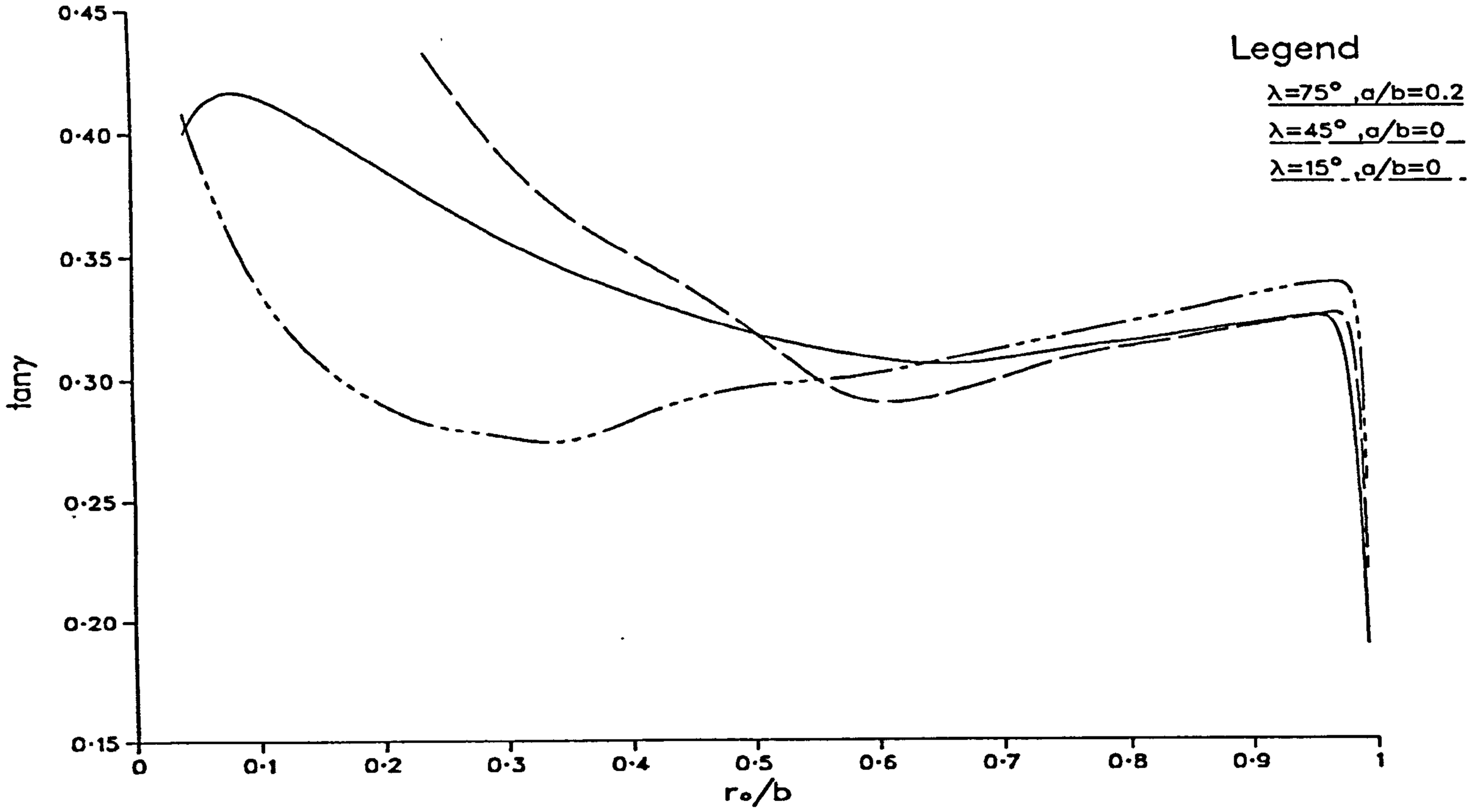

Figure 7.10(c)

Finite difference predictions for the limiting flow angle on the stator; Cq=0, a/b=0, d/b=0.08 and Re=$4*10^6$.

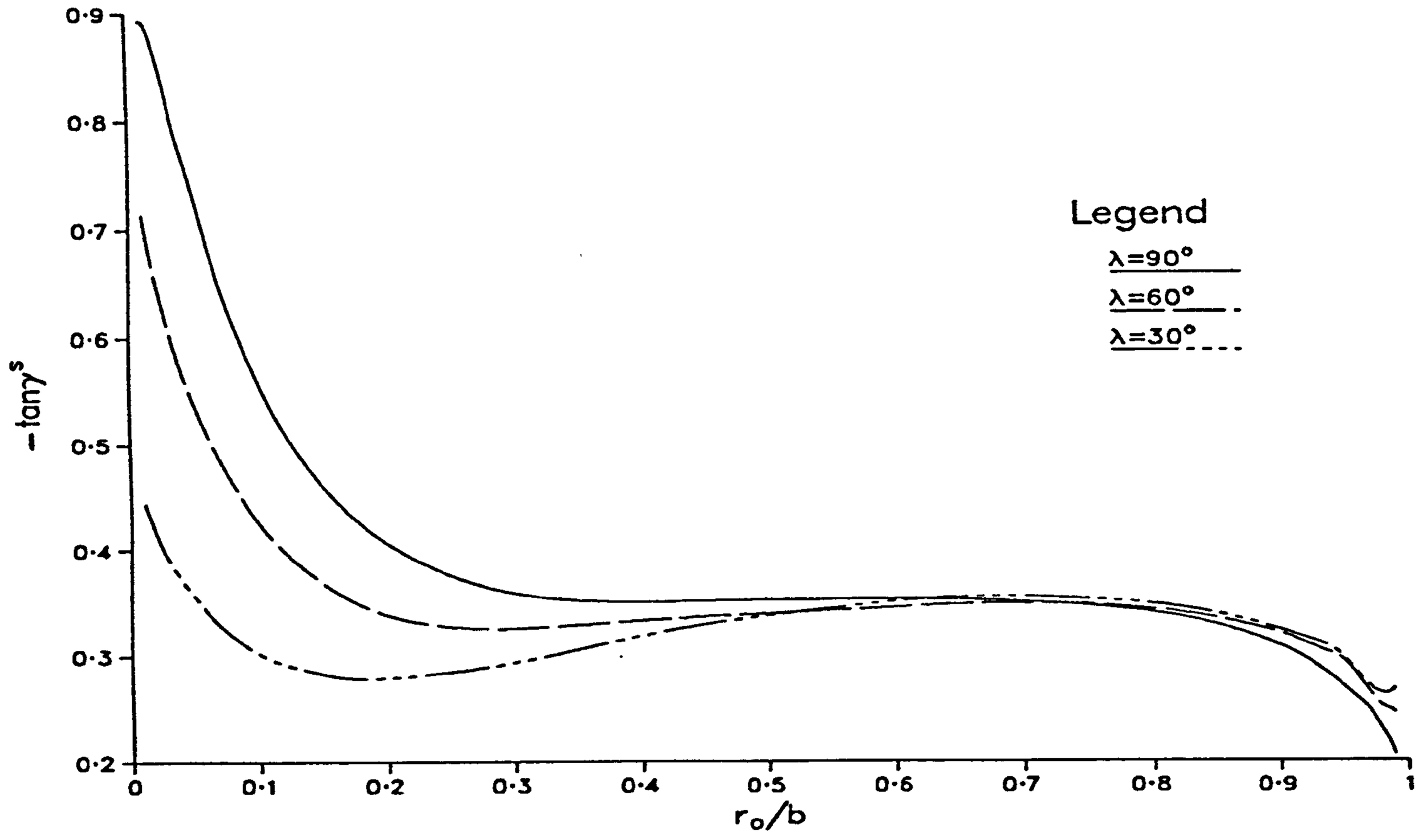

Figure 7.11(a)

Finite differnce predictions for the limiting flow angle on the stator; Cq=0, a/b=0, d/b=0.24 and Re=10^6.

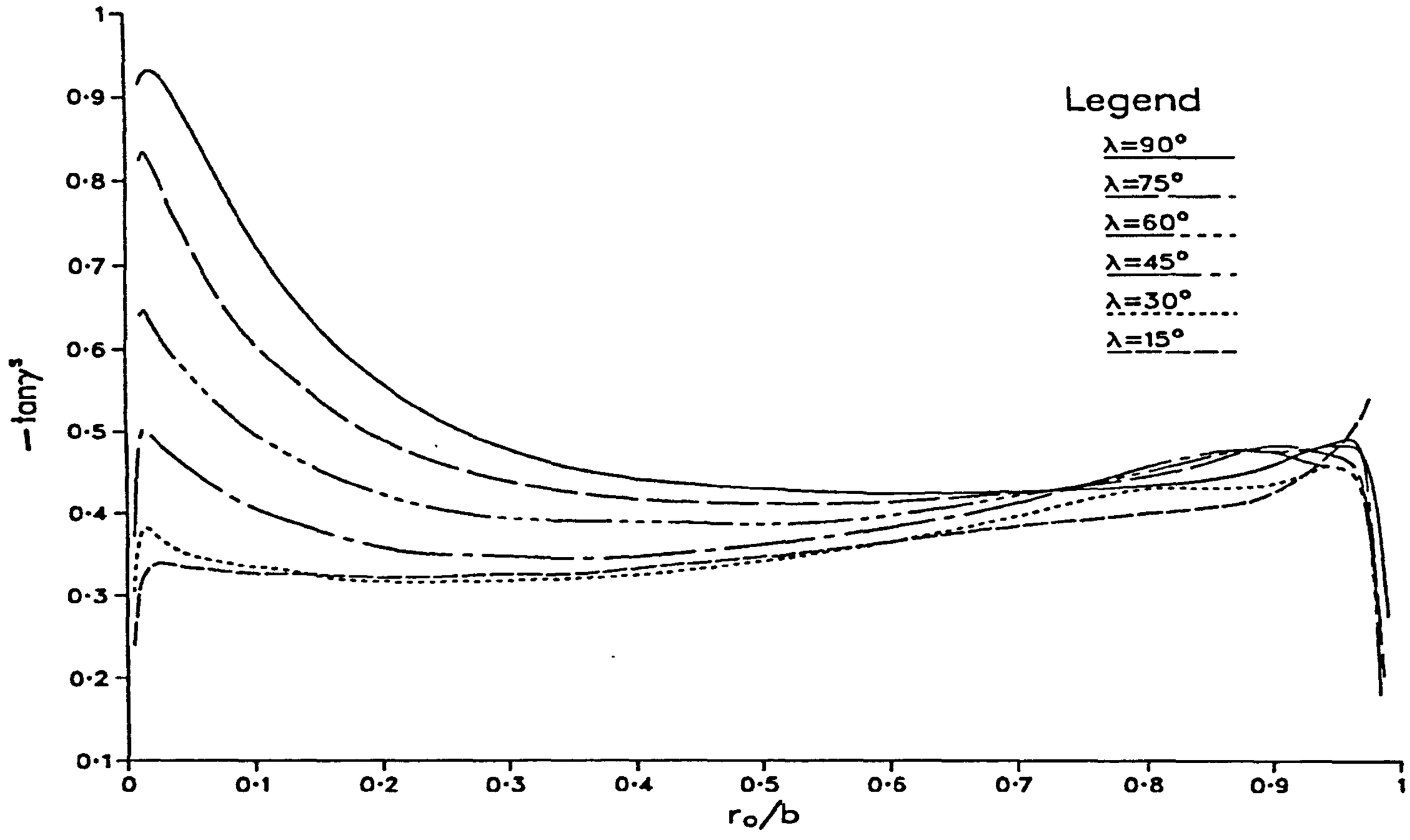

Figure 7.11(b)

Finite differnce predictions for the limiting flow angle on the stator; Cq=6000, d/b=0.16 and Re=10^6.

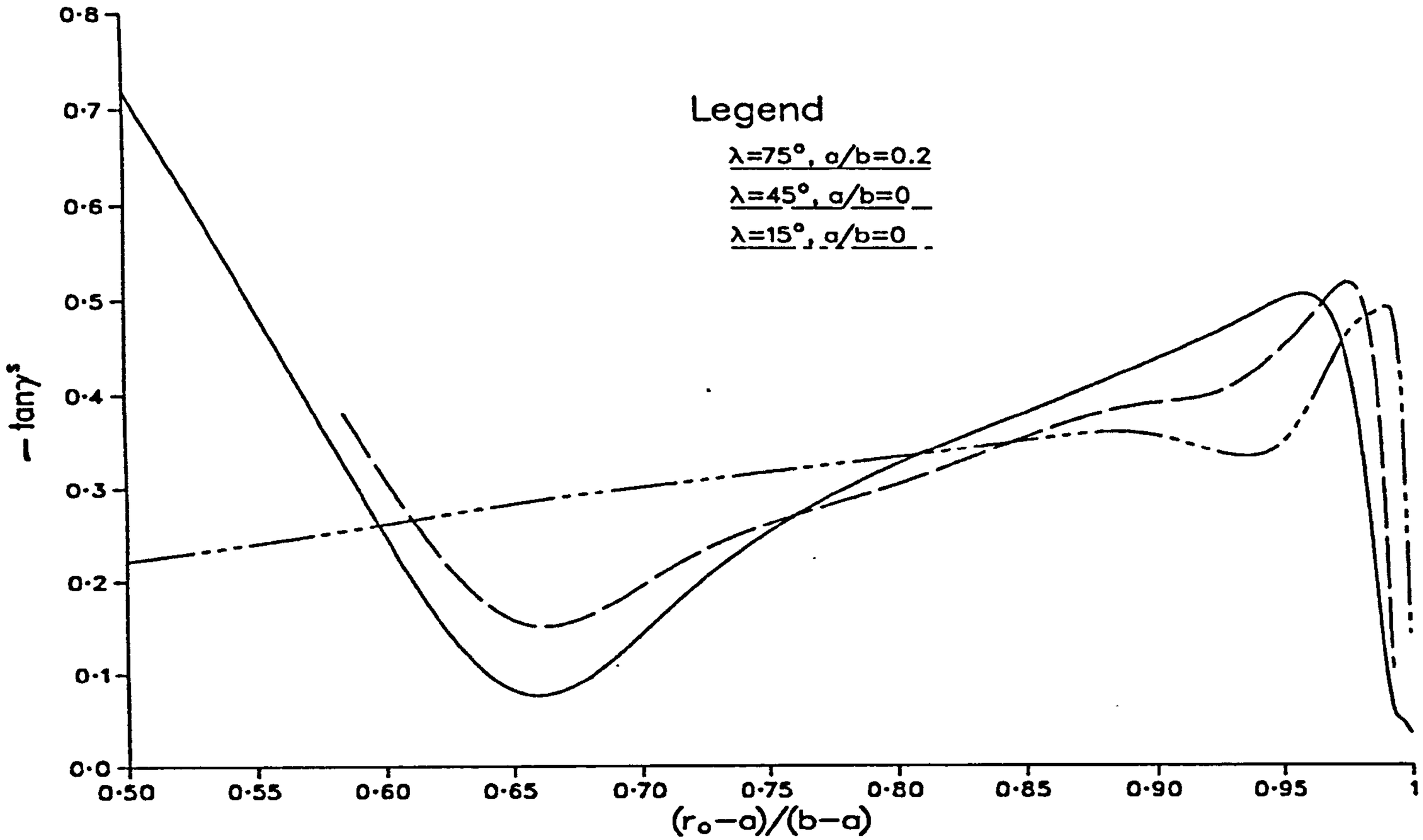

Figure 7.11(c)

Finite difference predictions of the radial velocity profiles across the stator boundary layer; $Cq=0$, $a/b=0$, $d/b=0.16$, $Re=10^6$ and $\lambda=90^{o}$.

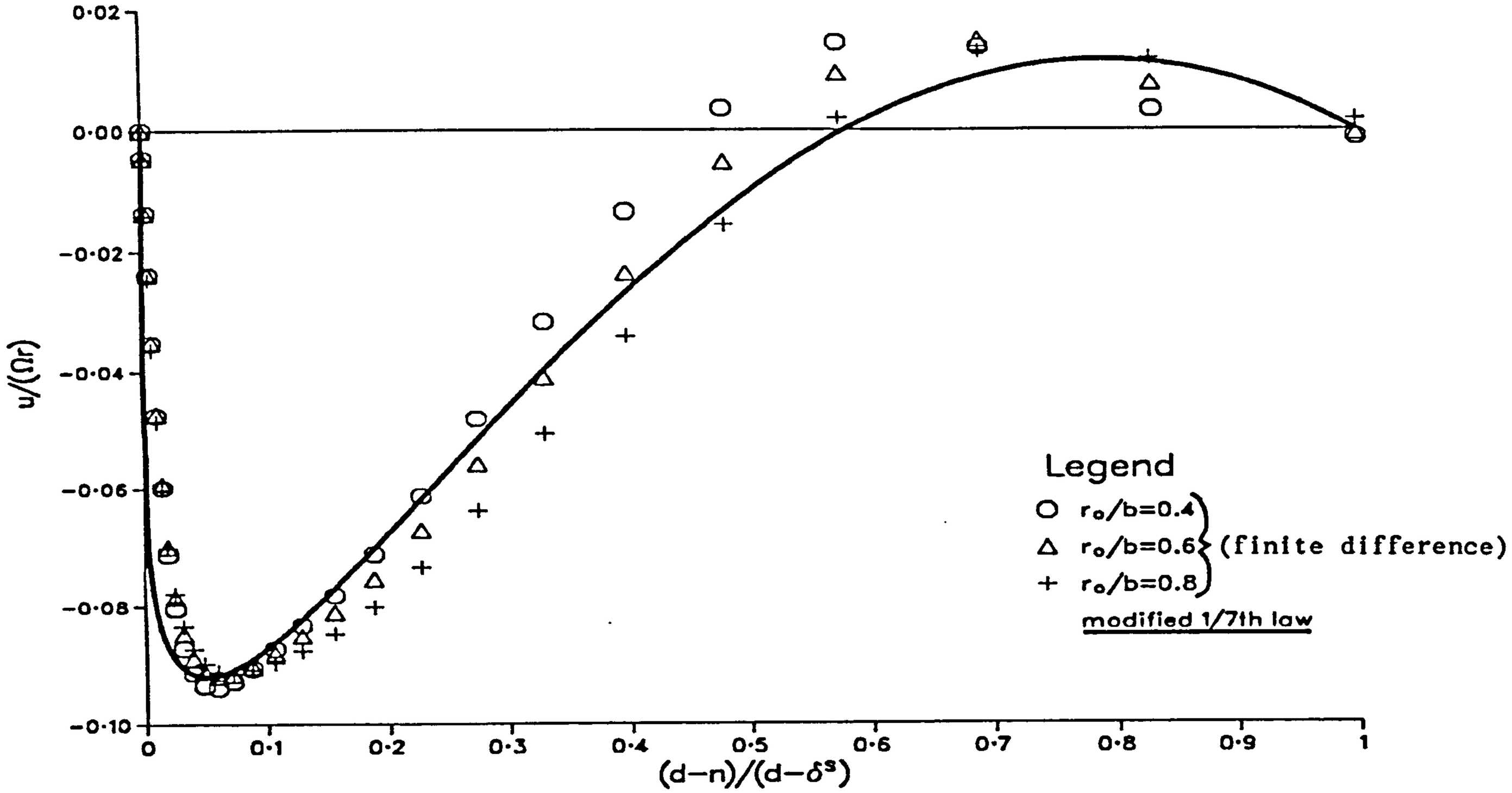

Figure 7.12(a)

Finite difference predictions for the radial velocity profiles across the stator boundary layer; Cq=0, a/b=0, d/b=0.08, Re=$4*10^6$ and $\lambda=30°$

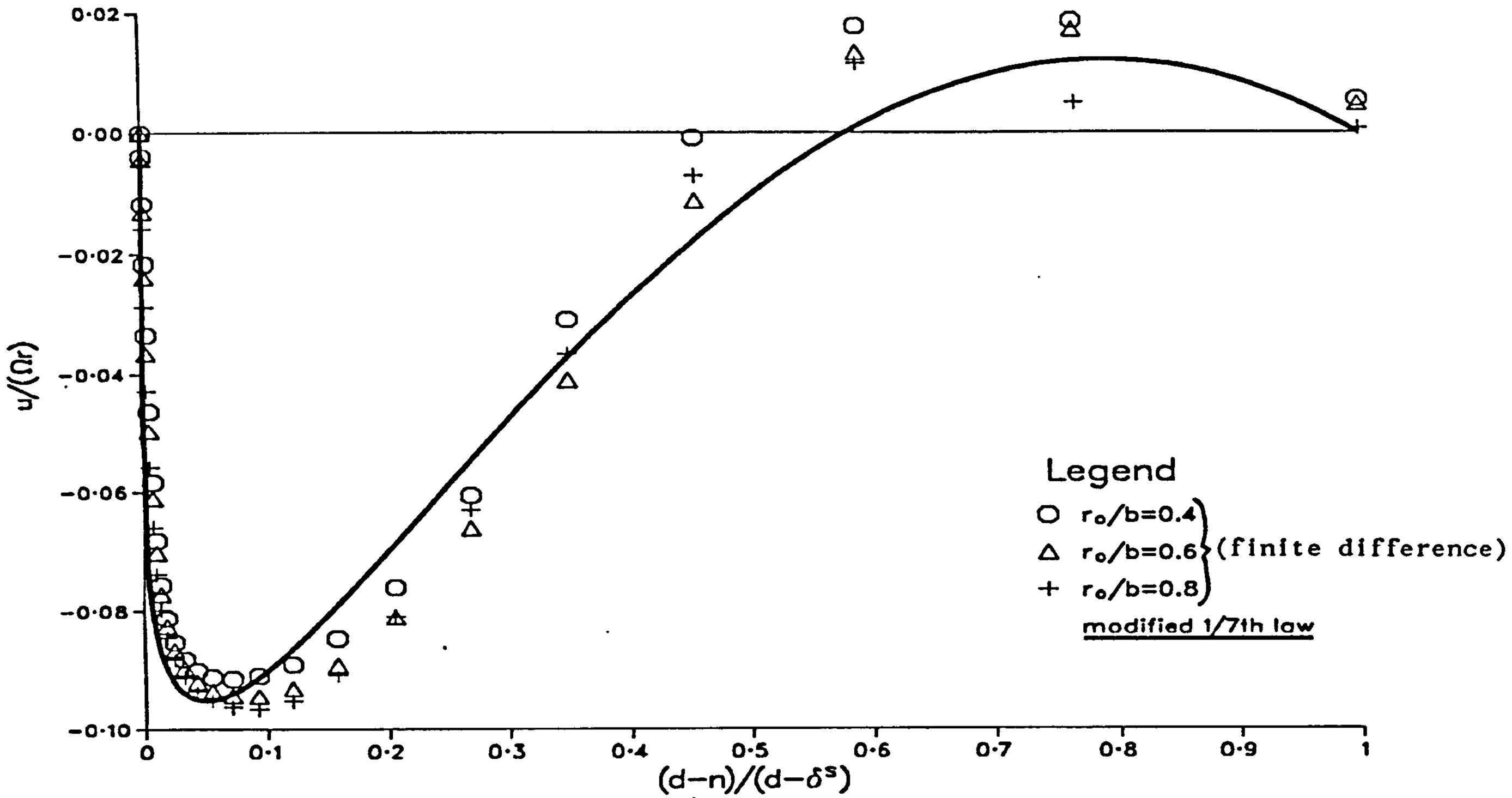

Figure 7.12(b)

Finite difference predictions for the tangential velocity profiles across the stator boundary layer; Cq=0, a/b=0, d/b=0.16, Re=10^6 and $\lambda=90^\circ$.

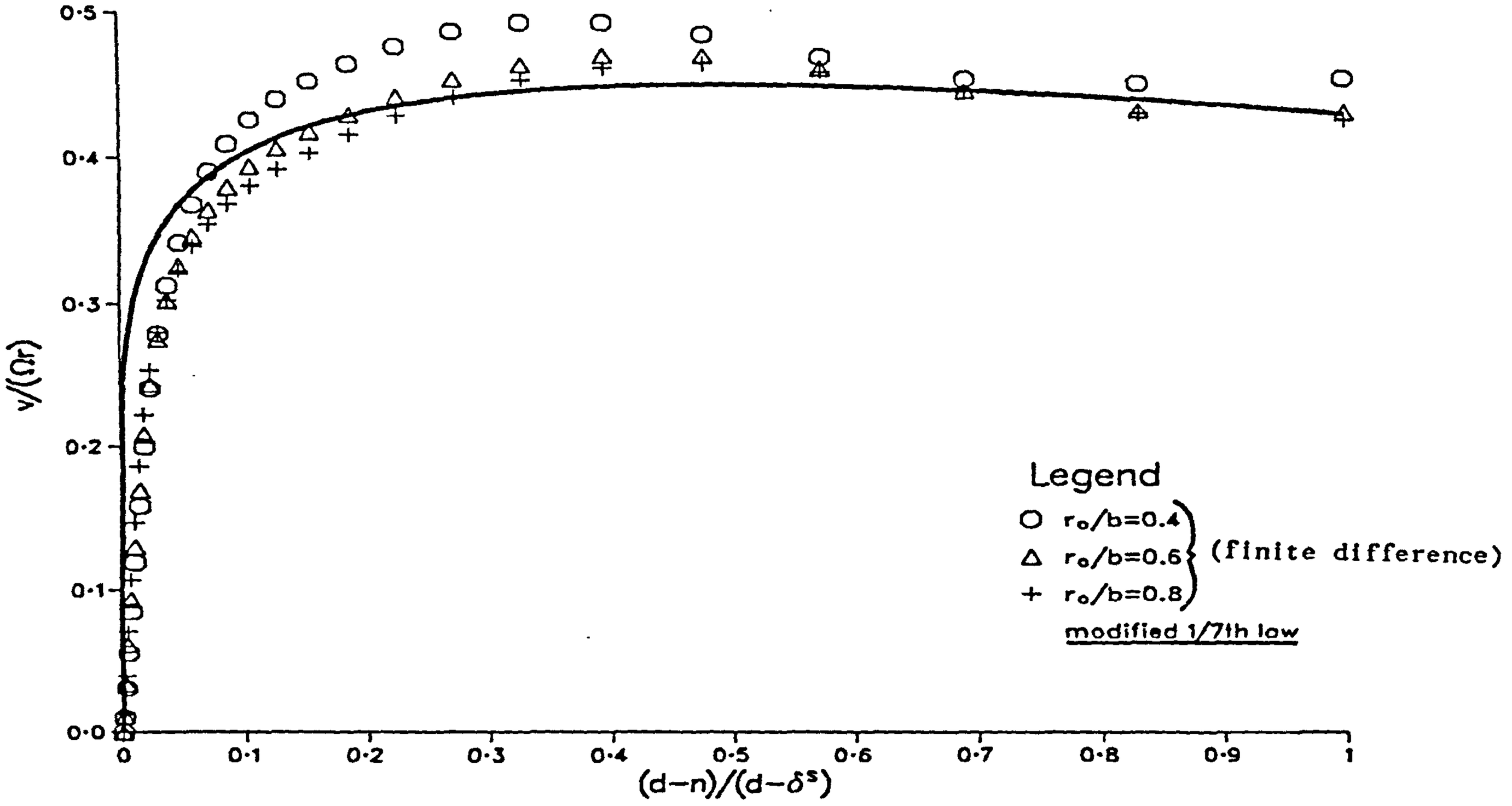

Figure 7.13(a)

Finite difference predictions for the tangential velocity profiles across the stator boundary layer;
Cq=0, a/b=0, d/b=0.08, Re=$4*10^6$ and $\lambda=30^\circ$

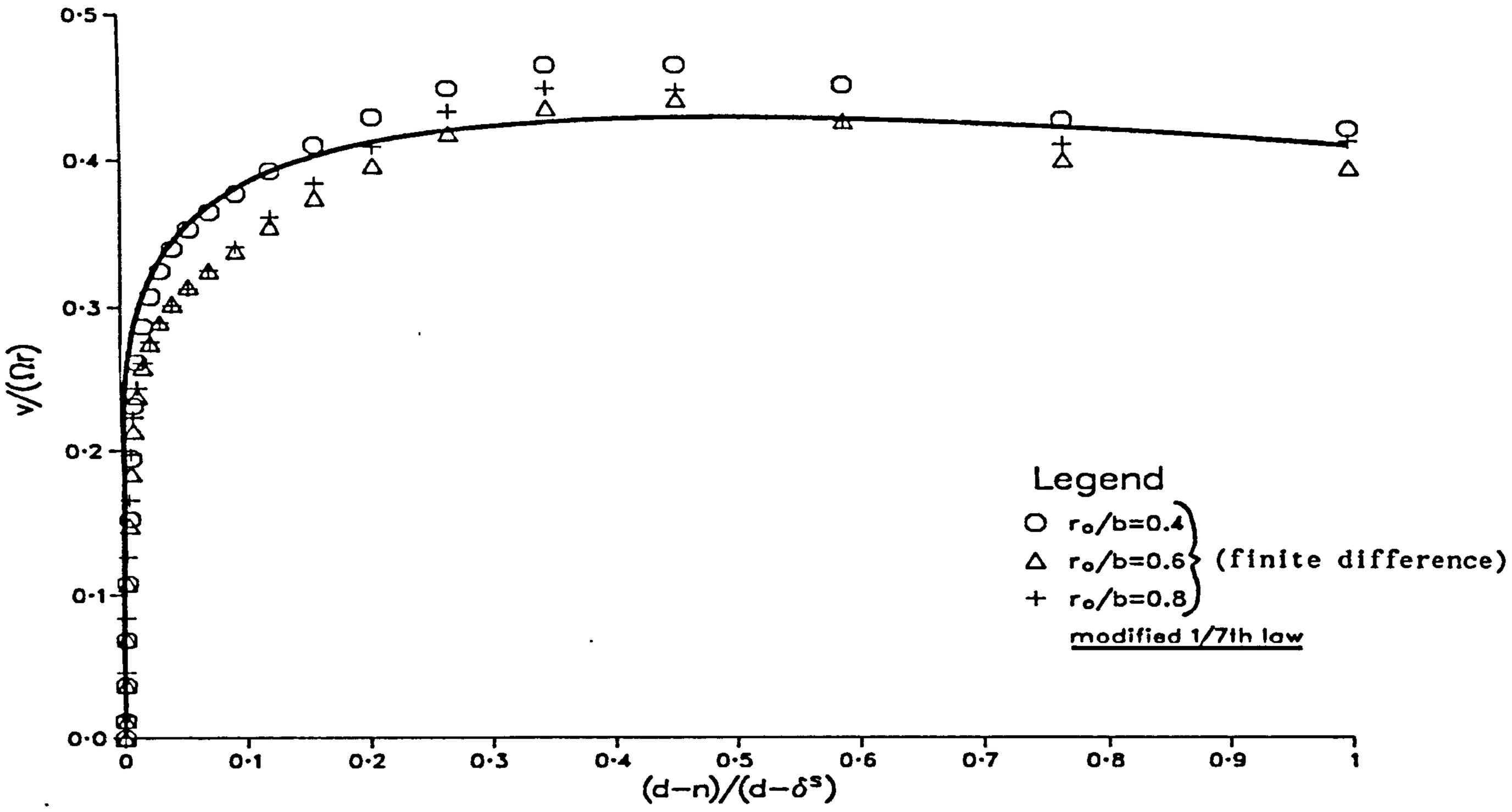

Figure 7.13(b)

A comparison of the rotor moment coefficients;
Cq=0, a/b=0, d/b=0.16 and Re=10^6.

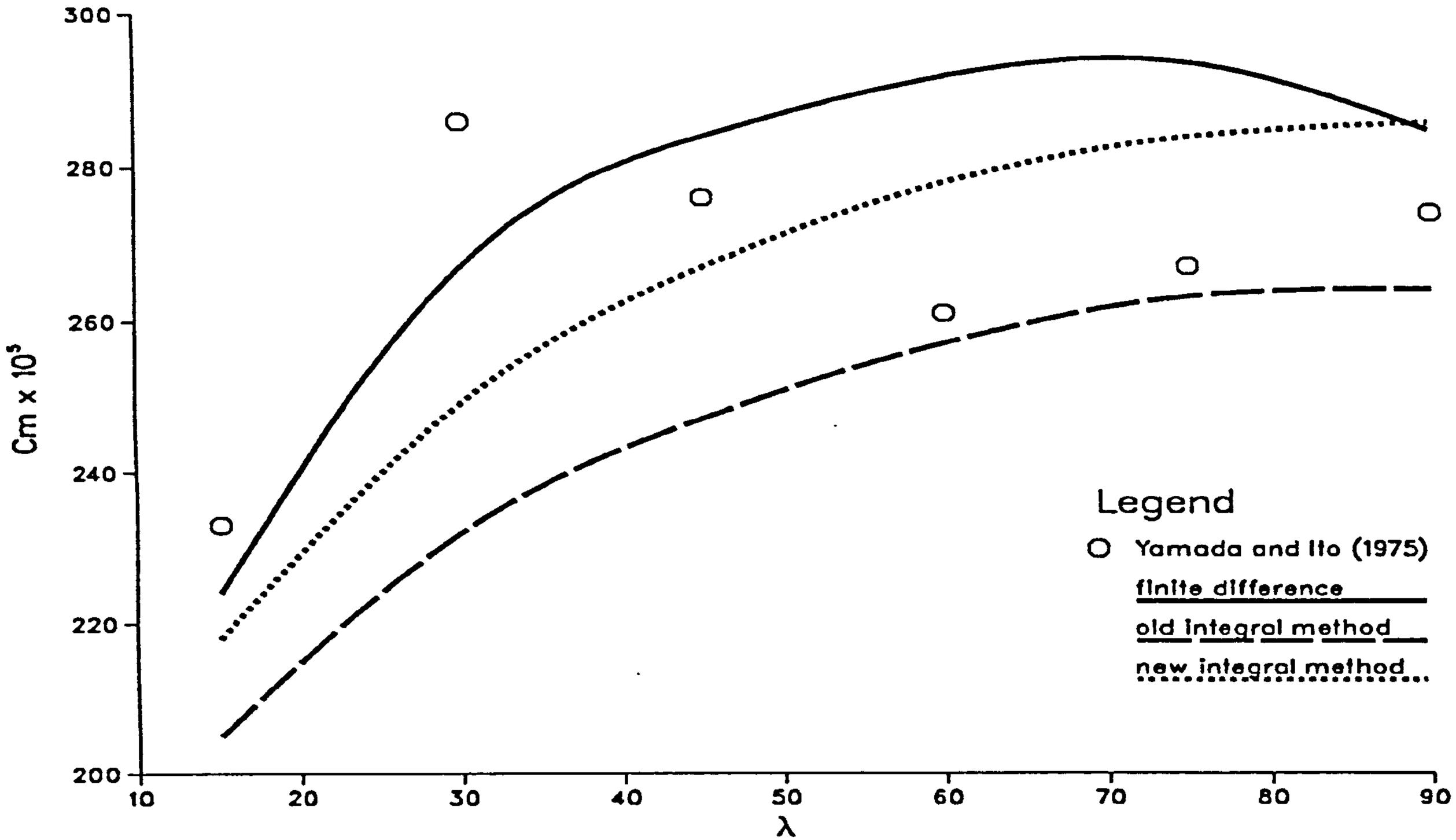

Figure 7.14(a)

A comparison of the rotor moment coefficients;
Cq=0, a/b=0, d/b=0.24 and Re=10^6.

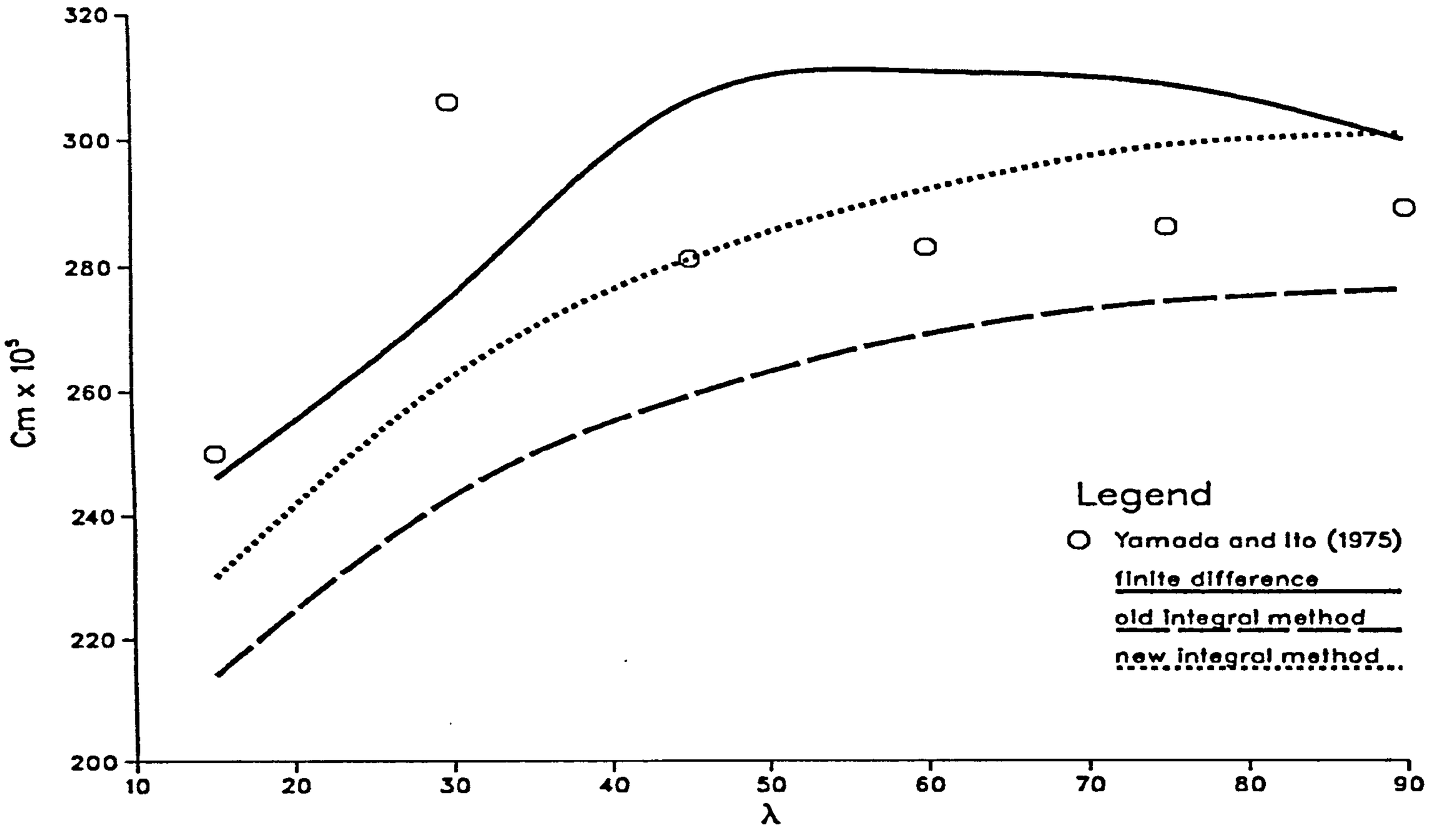

Figure 7.14(b)

A comparison of the rotor moment coefficients;
Cq=0, a/b=0, d/b=0.08 and λ=90°.

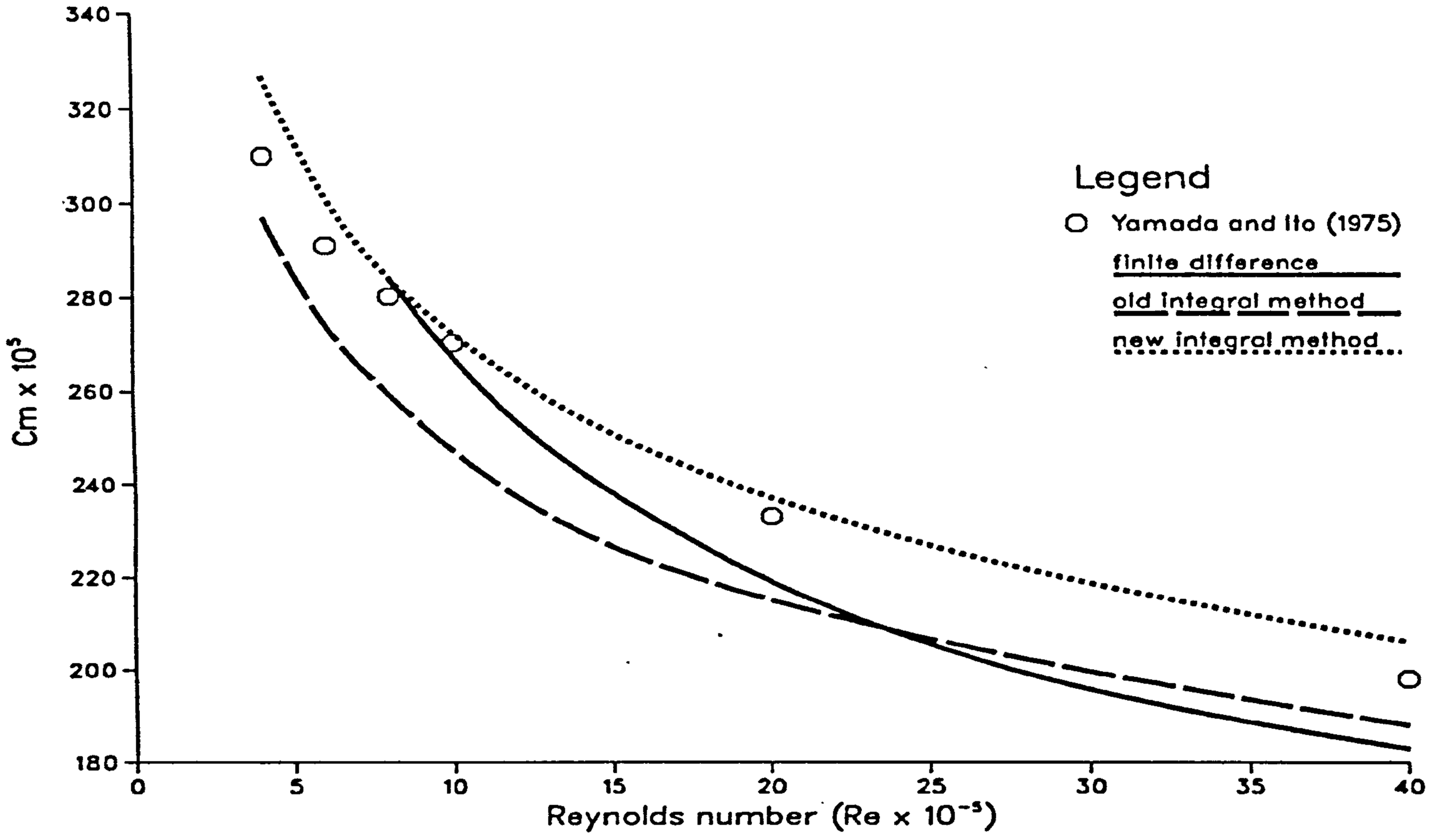

Figure 7.14(c)

A comparison of the rotor moment coefficients;
$a/b=0$, $d/b=0.16$, $Re=10^6$ and $\lambda=45°$.

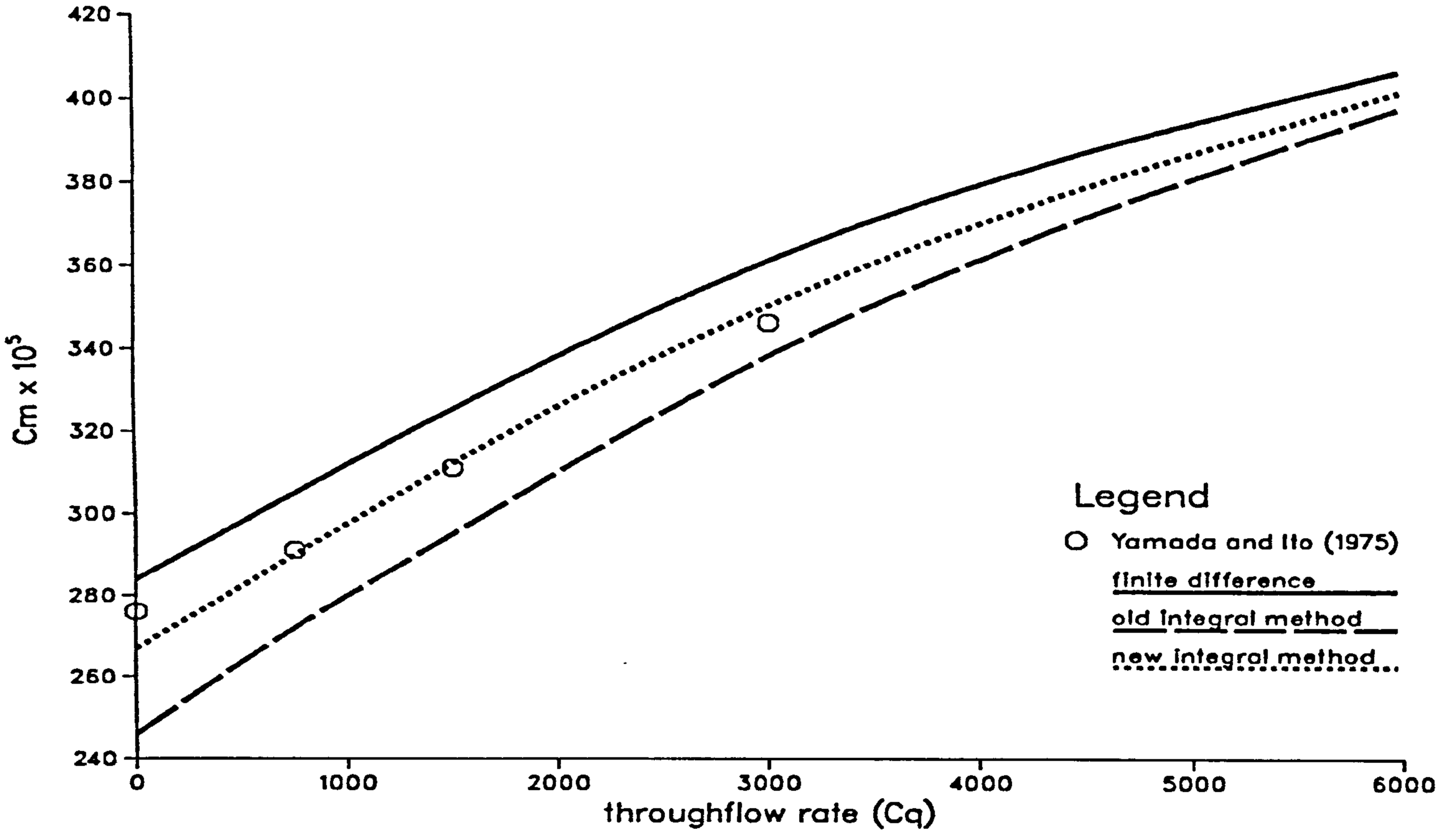

Figure 7.14(d)

A comparison of the stator moment coefficients;
Cq=0, a/b=0, d/b=0.16, and Re=10^6.

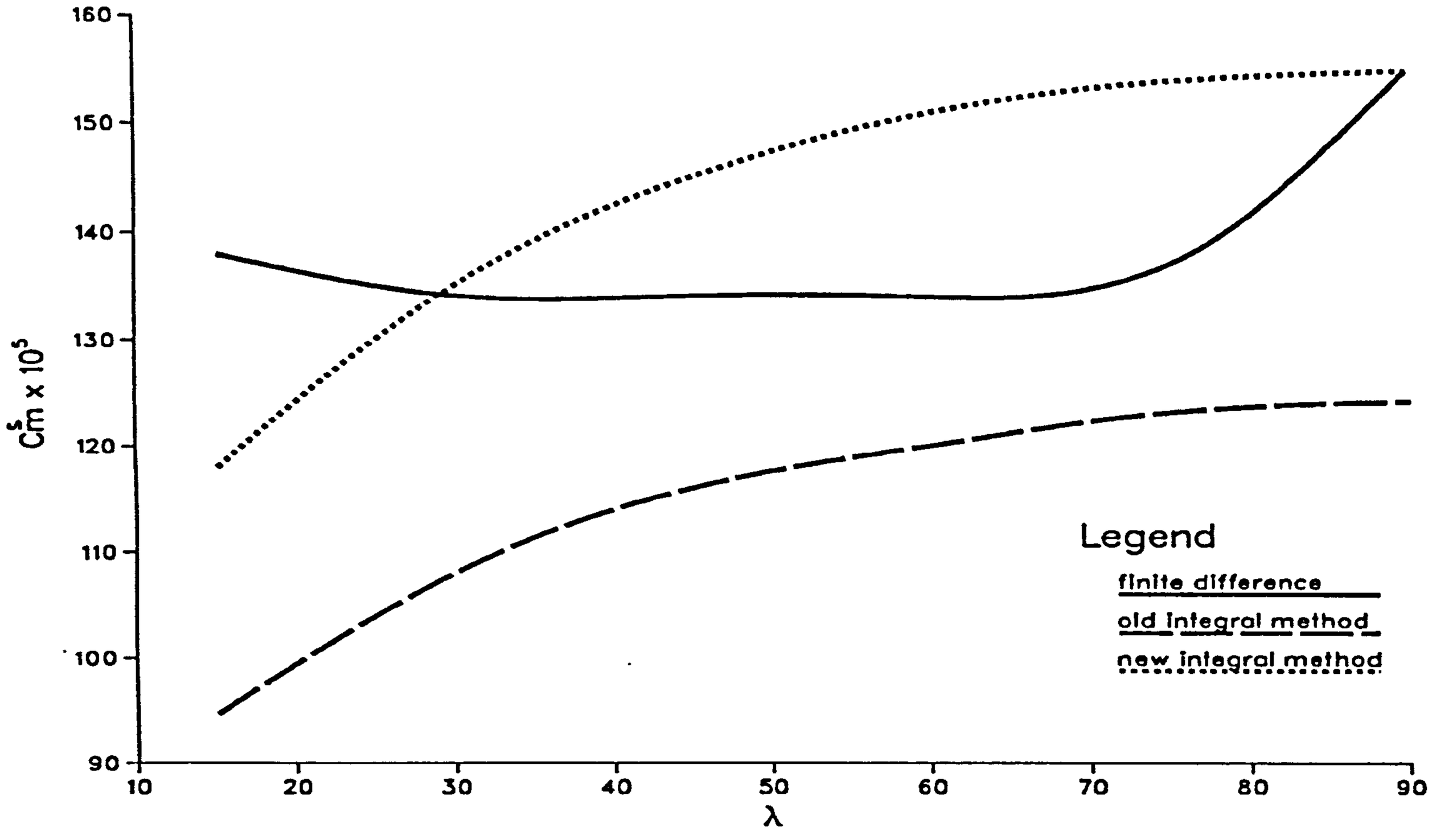

Figure 7.15(a)

A comparison of the stator moment coefficients;
$Cq=0$, $a/b=0$, $d/b=0.24$, and $Re=10^6$.

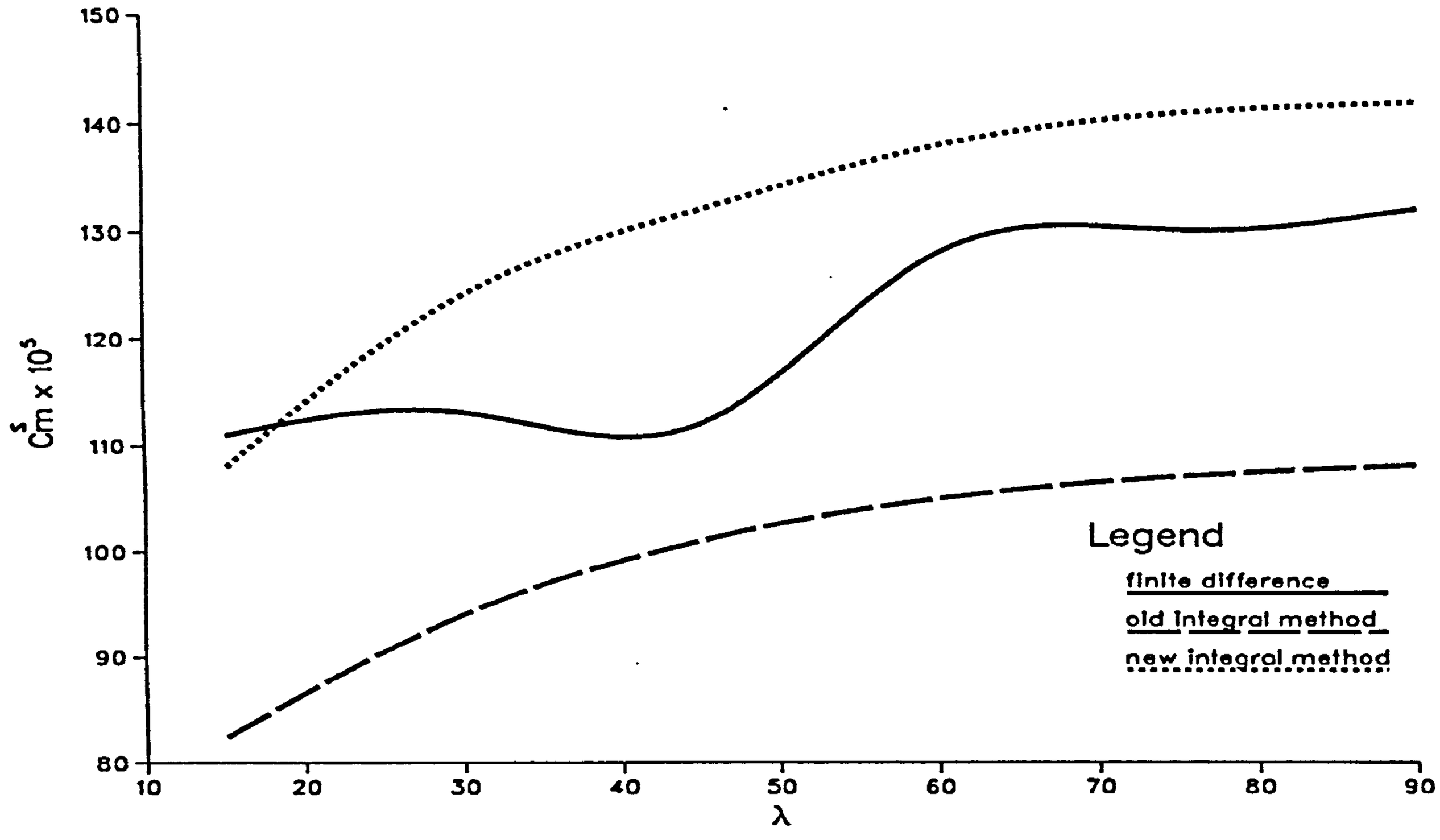

Figure 7.15(b)

A comparison of the stator moment coefficients;
Cq=0, a/b=0, d/b=0.08, and λ=90°.

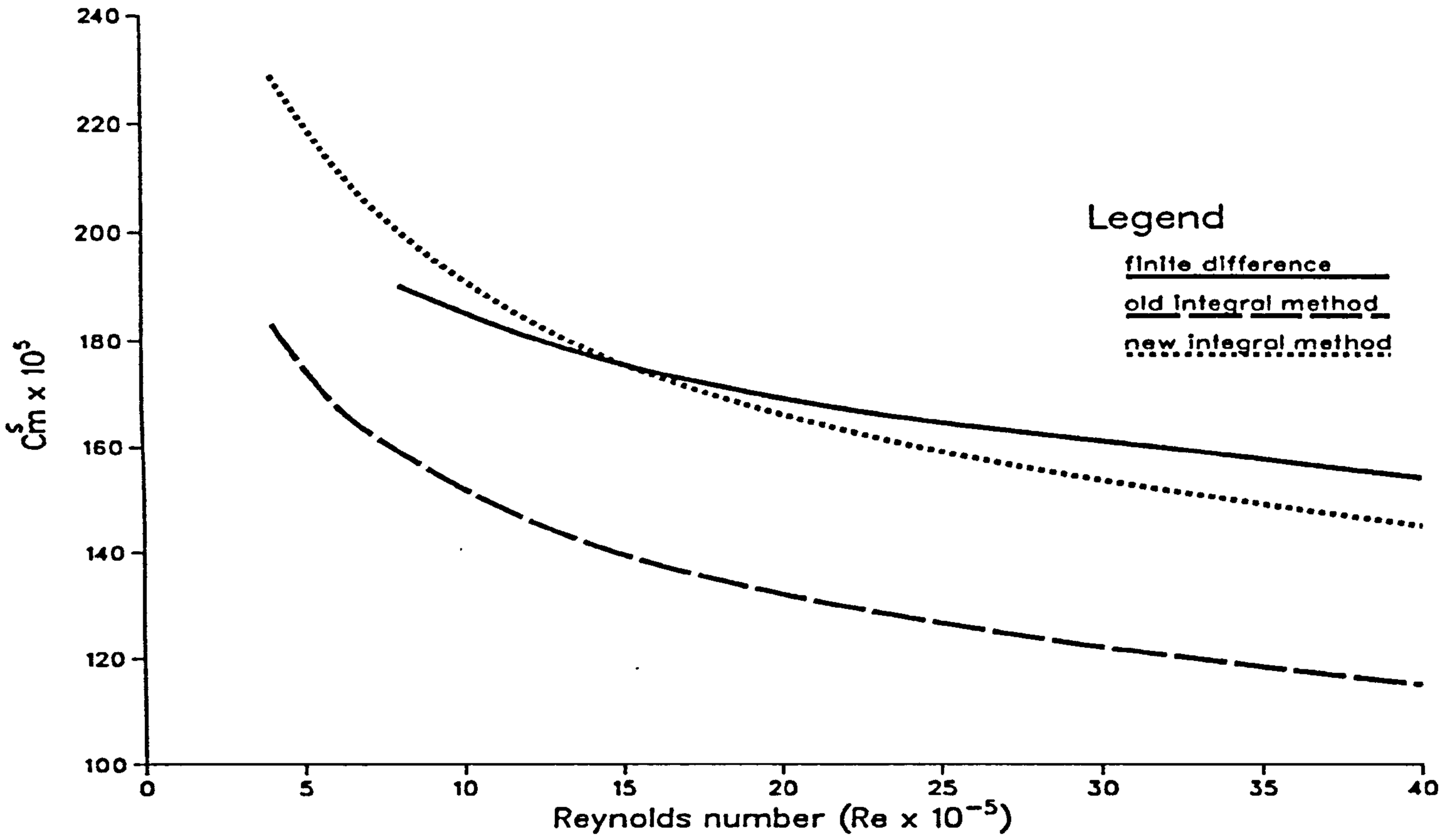

Figure 7.15(c)

A comparison of the stator moment coefficients;
$a/b=0$, $d/b=0.16$, $Re=10^6$ and $\lambda=45^\circ$.

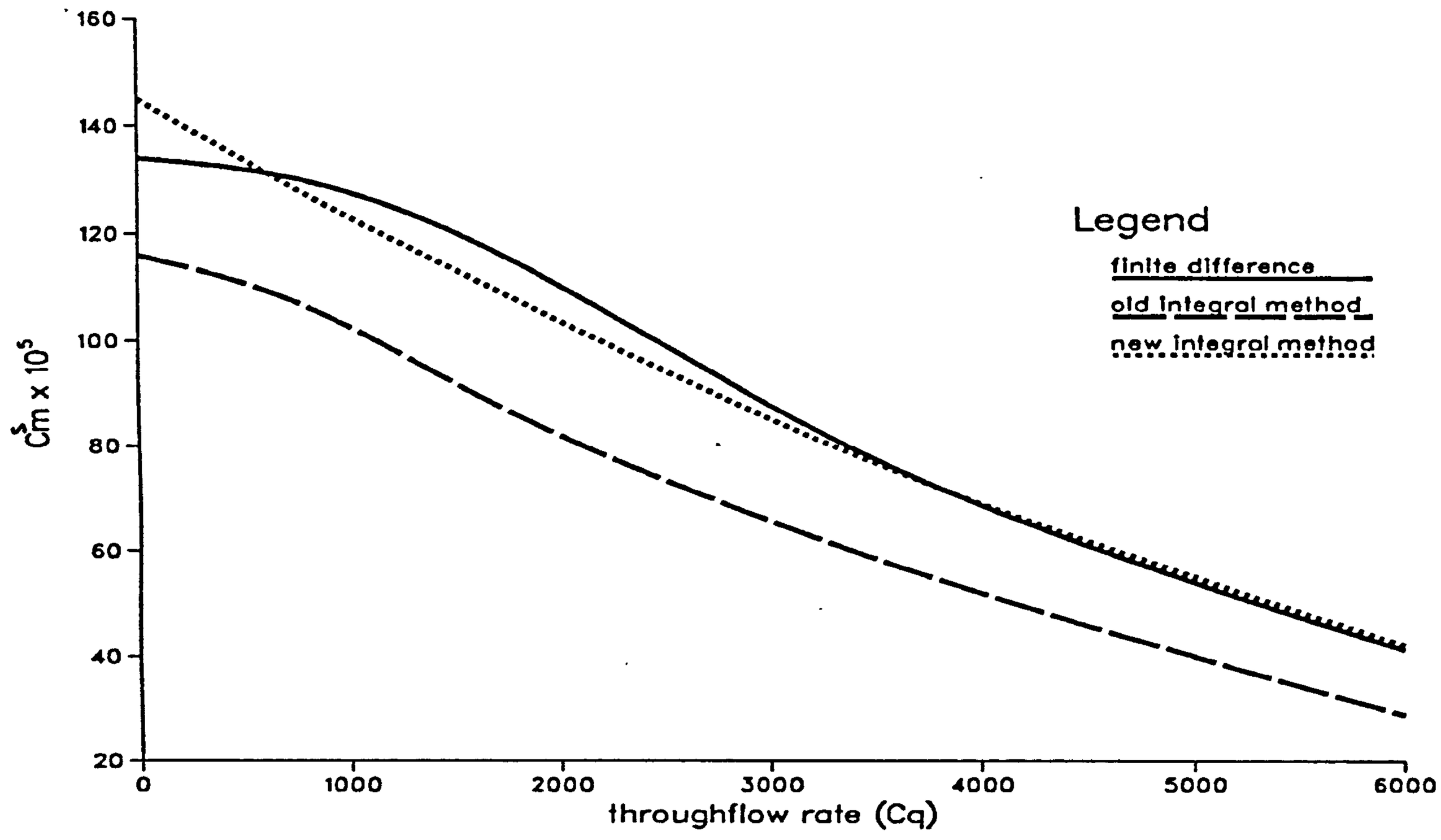

Figure 7.15(d)

A comparison of the predicted mid-axial tangential velocity;
$Cq=0$, $a/b=0$, $d/b=0.16$, $Re=10^6$ and $\lambda=90°$.

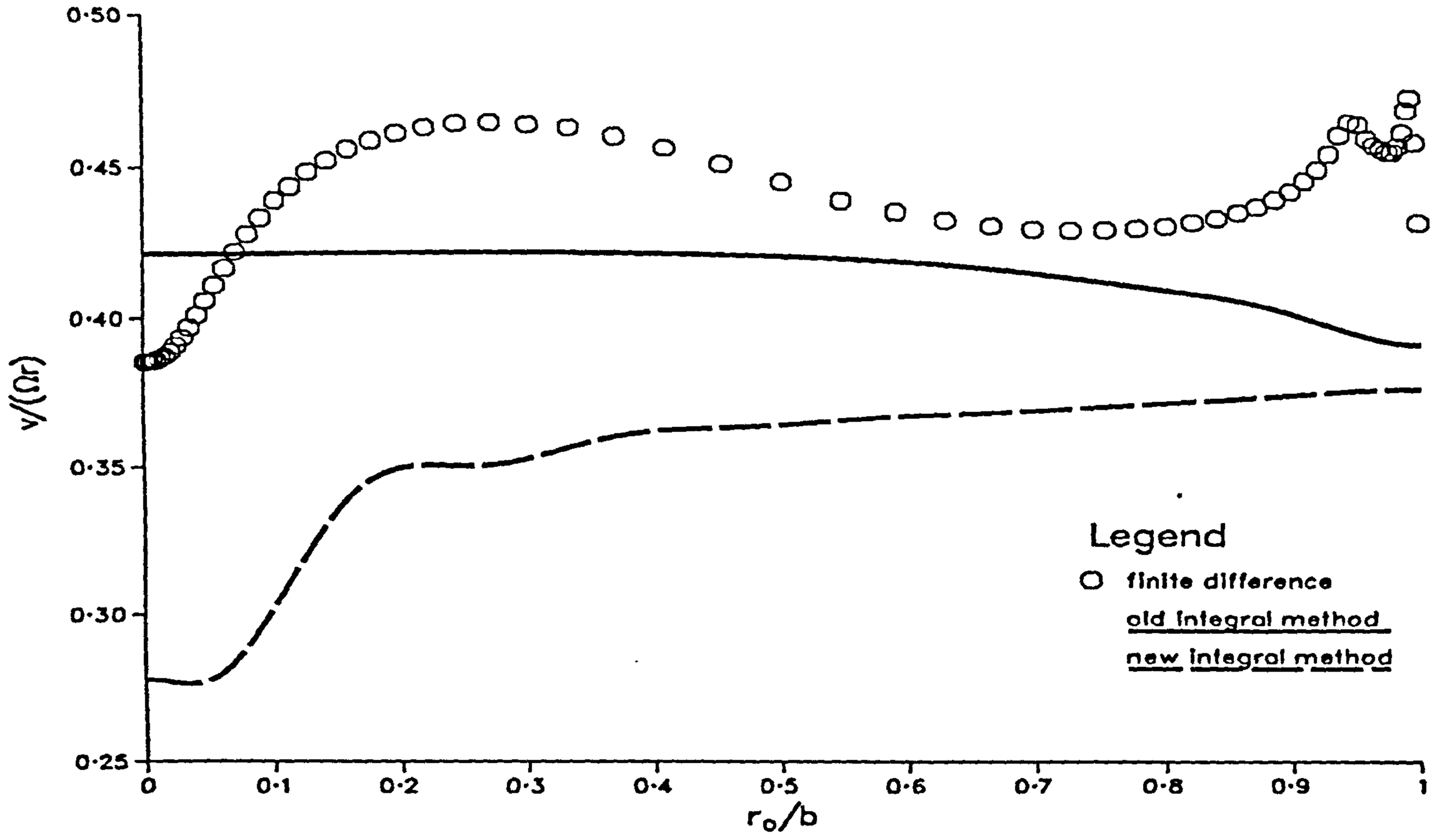

Figure 7.16(a)

A comparison of the predicted mid–axial tangential velocity;
Cq=3000, a/b=0, d/b=0.16, Re=10^6 and λ=75°

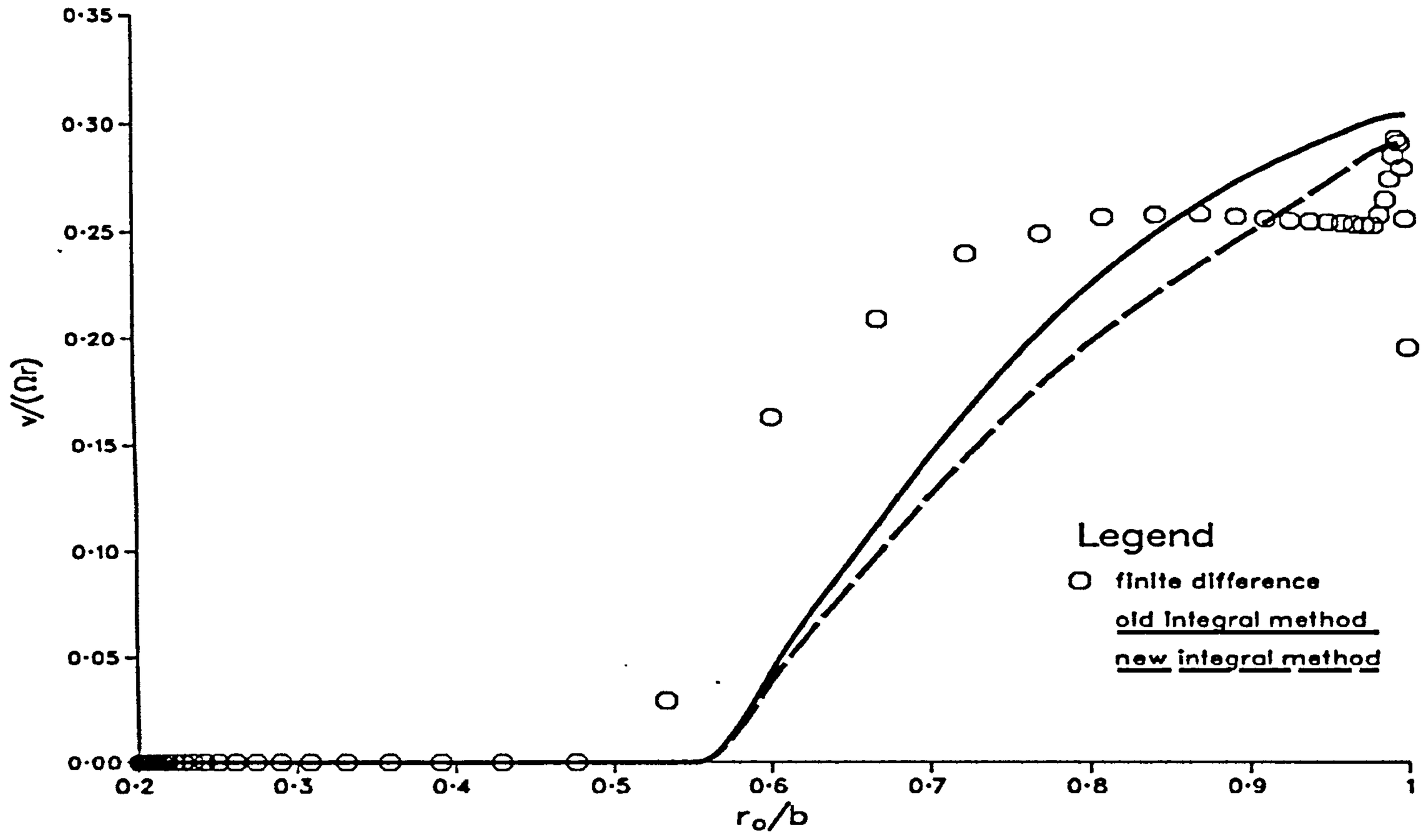

Figure 7.16(b)

Finite difference prediction for the stator surface shear stress;
Cq=3000, a/b=0, d/b=0.16 and Re=10^6 and $\lambda=45^o$

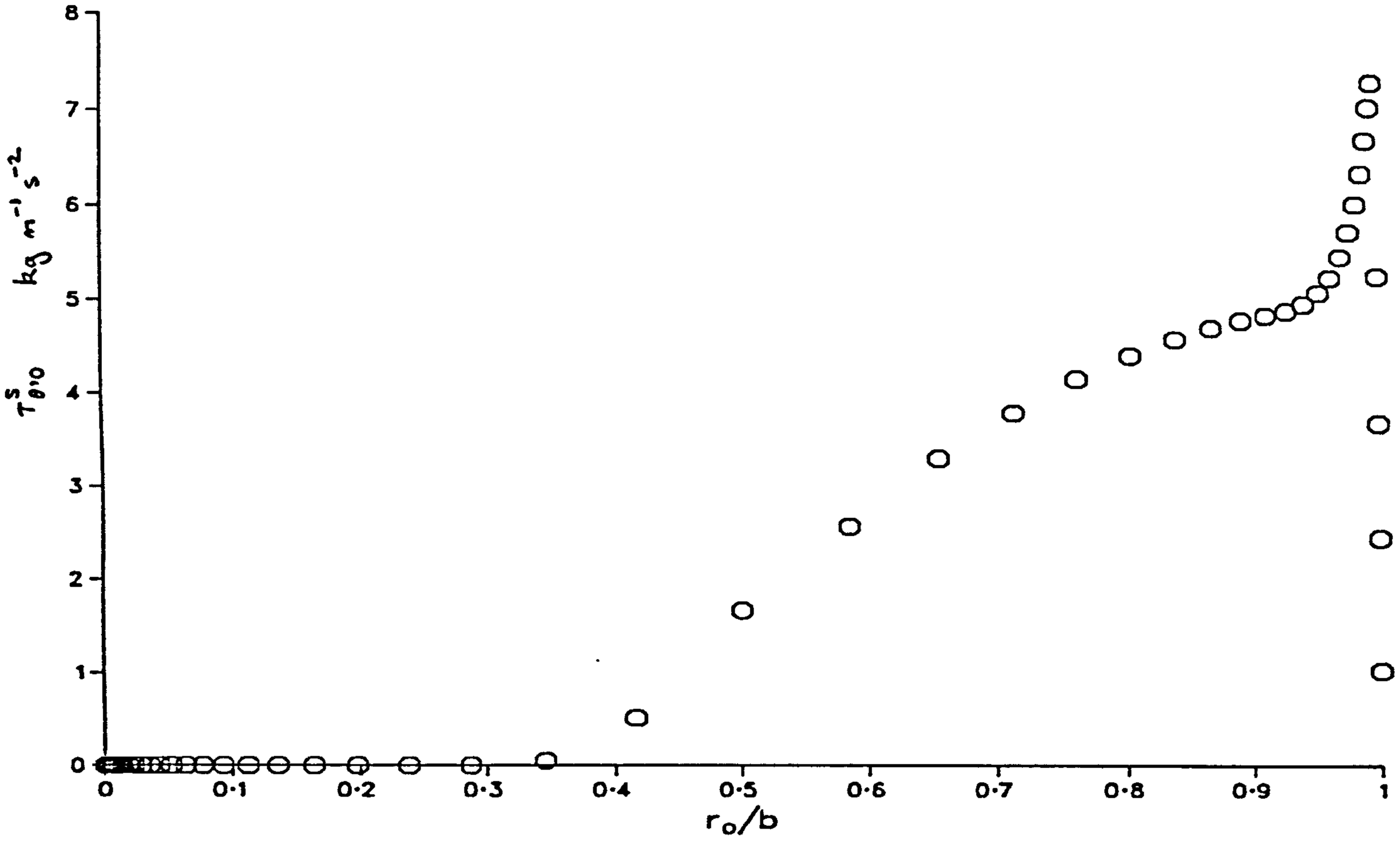

Figure 7.17

A comparison of the predicted limiting flow angle on the stator;
Cq=0, a/b=0, d/b=0.16, Re=10^6 and λ=90°.

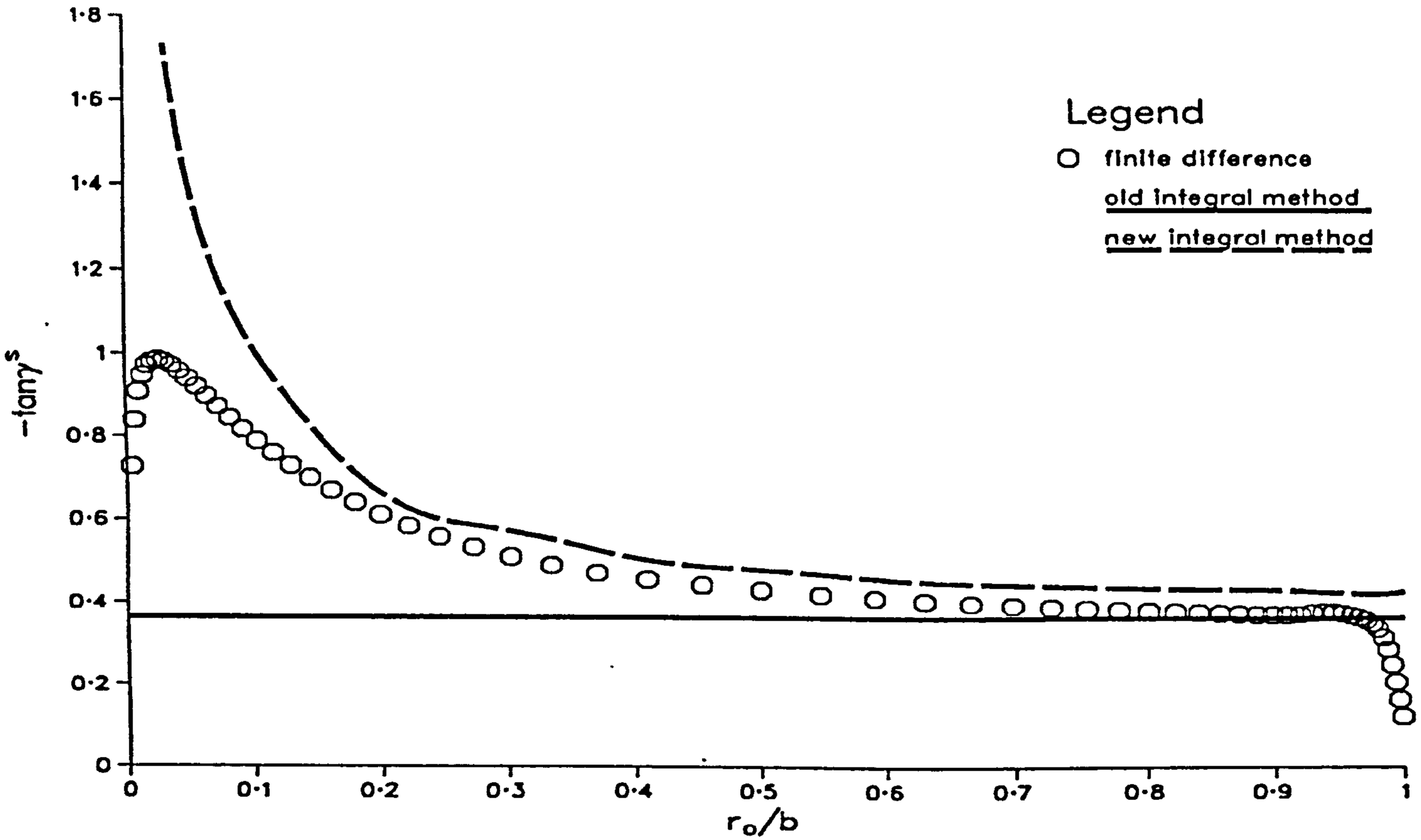

Figure 7.18(a)

A comparison of the predicted limiting flow angle on the stator;
Cq=3000, d/b=0.16 and Re=10^6.

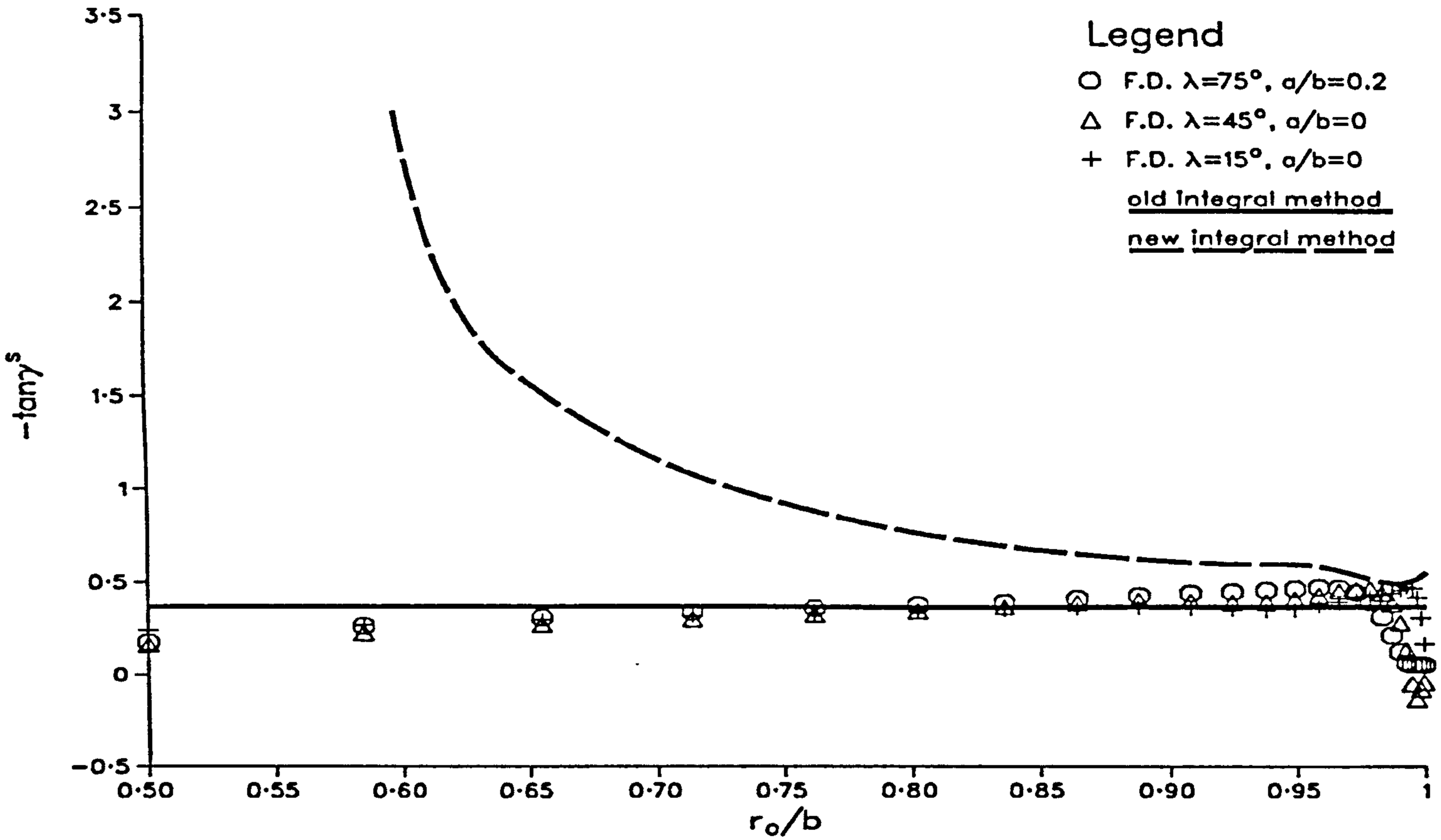

Figure 7.18(b)

The effect of the "square" shroud treatment on moment coefficient calculations; Cq=0, a/b=0, d/b=0.16, and Re=10^6.

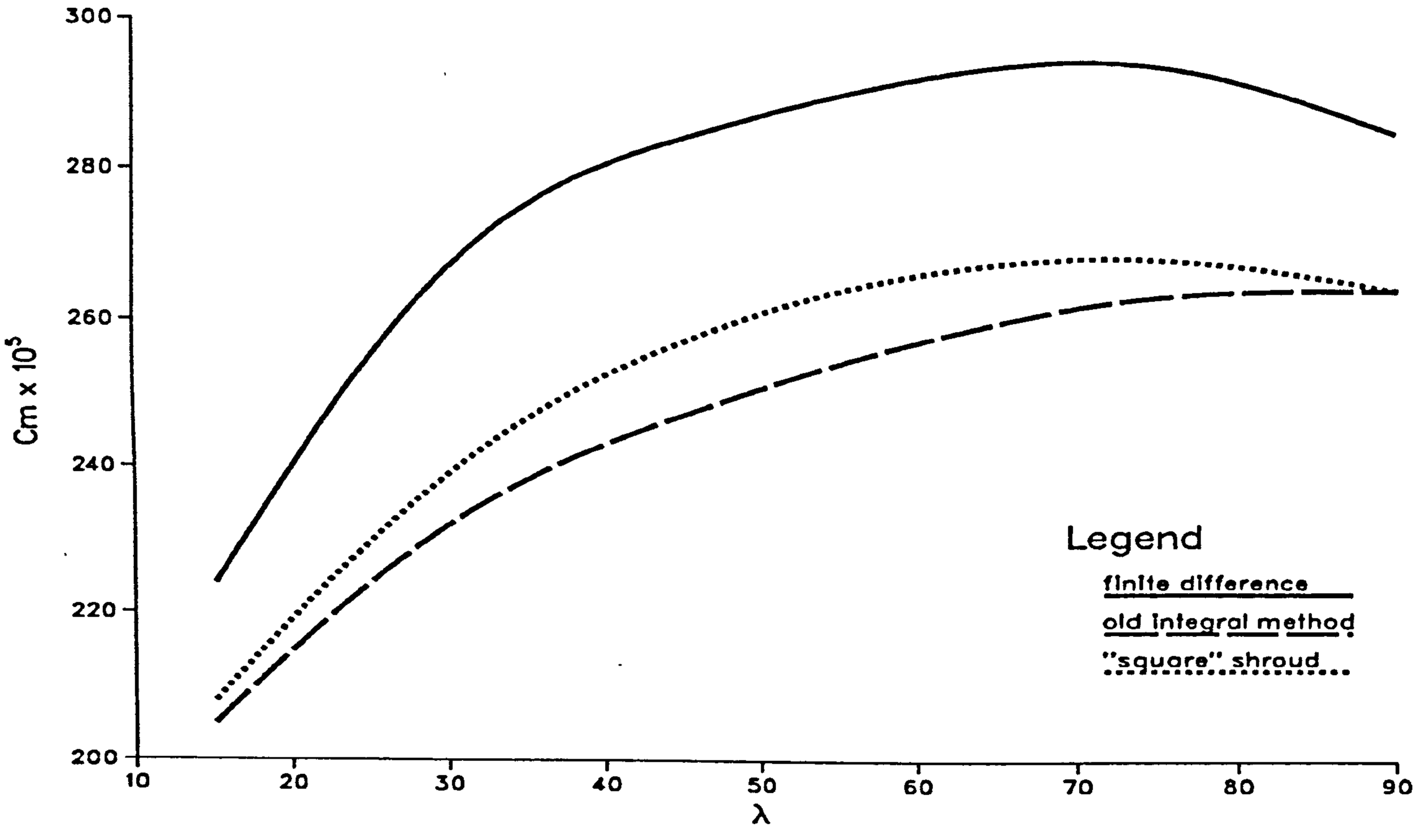

Figure 7.19(a)

The effect of the "square" shroud treatment on moment coefficient calculations; Cq=0, a/b=0, d/b=0.24, and Re=10^6.

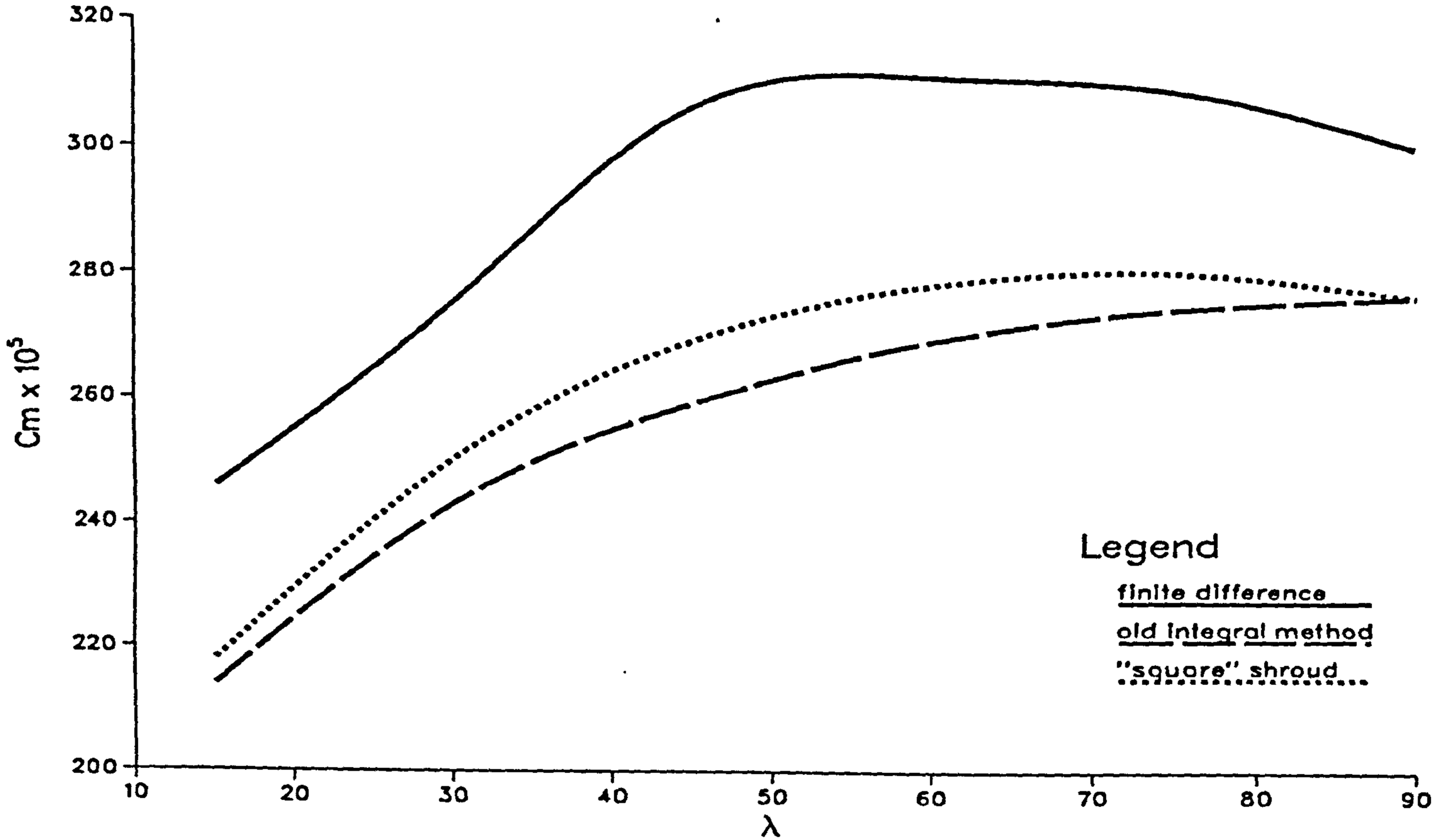

Figure 7.19(b)